

Surface Composition and Surface Tension of Ionic Liquid Systems Studied in Vacuum Using Angle-Resolved X-Ray Photoelectron Spectroscopy and a Newly Developed Pendant Drop Apparatus

**Untersuchungen der Oberflächenszusammensetzung und
Oberflächenspannung von ionischen Flüssigkeiten im Vakuum
mittels winkelaufgelöster Röntgen-
Photoelektronenspektroskopie und einer neuentwickelten
Pendant Drop-Apparatur**

Der Naturwissenschaftlichen Fakultät der
Friedrich-Alexander-Universität Erlangen-Nürnberg

zur Erlangung des Doktorgrades Dr. rer. nat.

vorgelegt von

Ulrike Paap

Als Dissertation genehmigt von der Naturwissenschaftlichen Fakultät
der Friedrich-Alexander-Universität Erlangen-Nürnberg

Tag der mündlichen Prüfung: 05.05.2023

Gutachter: Prof. Dr. Hans-Peter Steinrück

Prof. Dr. Karsten Meyer

TABLE OF CONTENTS

1.	Introduction.....	8
2.	Methods and Basics	11
2.1.	Surface/Interfacial Tension (ST/IFT)	11
2.1.1.	Axisymmetric Drop Shape Analysis (ADSA).....	11
2.1.2.	Young Equation.....	13
2.2.	Angle-Resolved X-Ray Photoelectron Spectroscopy (ARXPS).....	14
3.	Materials, Instrumentations and Experimental Details	17
3.1.	Materials and Sample Preparation.....	17
3.2.	Details on the Instruments.....	19
3.2.1.	High Vacuum Pendant Drop (PD)/Sessile Drop (SD)	19
3.2.2.	Data Evaluation PD.....	20
3.2.3.	Dual Analyzer System for Surface Analysis	22
3.2.4.	Data Evaluation ARXPS.....	24
4.	Results and Discussion.....	26
4.1.	High Vacuum Pendant Drop and Sessile Drop Setup ^[P2]	26
4.1.1.	Pendant Drop.....	26
4.1.2.	Sessile Drop.....	27
4.1.3.	PD Calibration Measurements with Water and Benzene	28
4.2.	PD Measurements of Ionic Liquid Systems in High Vacuum ^[P1-P3]	29
4.2.1.	Surface Tension of [C ₈ C ₁ Im][PF ₆] ^[P2]	30
4.2.2.	Surface Tension of [(mPEG _n) ₂ Im]I ^[P2]	32
4.2.3.	Surface Tension of Mixtures of [(mPEG ₂) ₂ Im]I and [C ₈ C ₁ Im][PF ₆] ^[P3]	34
4.3.	Surface Composition of Ionic Liquid Systems ^{[P1], [P3]}	35
4.3.1.	[m(PEG _n) ₂ Im]I (<i>n</i> = 2, 4, 6) ^[P1]	36
4.3.2.	[(mPEG ₂) ₂ Im]I, [C ₈ C ₁ Im][PF ₆] and their Mixtures ^[P3]	38
4.4.	Correlation of Surface Composition and Surface Tension of Ionic Liquid Systems ^[P3]	41
4.5.	Composition of BNCs of [C ₂ C ₁ Im][BIm ₄] ^[P4]	45
5.	Summary	48
5.1.	English Version	48
5.2.	German Version (Deutsche Zusammenfassung)	50
6.	References.....	53
7.	Acknowledgements (Danksagung).....	59
8.	Appendix.....	61
8.1	Publications	61
8.1.1.	<i>Bis</i> -polyethylene glycol-functionalized imidazolium ionic liquids: A multi-method approach towards bulk and surface properties ^[P1]	62
8.1.2.	Probing surface and interfacial tension of ionic liquids in vacuum with the pendant drop and sessile drop method ^[P2]	93

8.1.3.	Direct correlation of surface tension and surface composition of ionic liquid mixtures – A combined vacuum pendant drop and angle-resolved X-ray photoelectron spectroscopy study ^[P3]	117
8.1.4.	B/N-doped carbon sheets from a new ionic liquid with excellent sorption properties for methylene blue ^[P4]	145
8.2.	Density Calculations of Mixtures	169
8.3.	Manual.....	171

PUBLISHED PAPERS; [P1-P4] IN THE APPENDIX

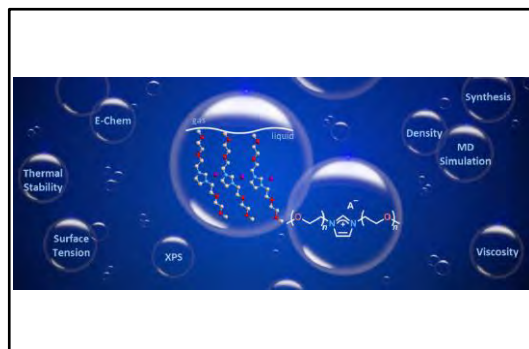
[P1] **Bis-polyethylene glycol-functionalized imidazolium ionic liquids: A multi-method approach towards bulk and surface properties**

V. Seidl, M. Bosch, U. Paap, M. Livraghi, Z. Zhai, C. R. Wick, T. M. Koller, P. Wasserscheid, F. Maier, A.-S. Smith, J. Bachmann, H.-P. Steinrück and K. Meyer

Journal of Ionic Liquids, 2, 100041 (2022)

[10.1016/j.jil.2022.100041](https://doi.org/10.1016/j.jil.2022.100041)

The author's contribution is the ARXPS investigation, data analysis and interpretation and the ARXPS section manuscript preparation.



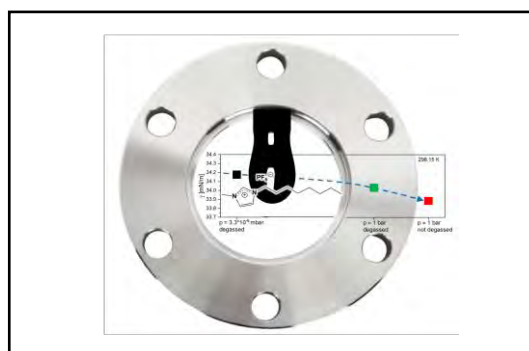
[P2] **Probing surface and interfacial tension of ionic liquids in vacuum with the pendant drop and sessile drop method**

U. Paap, B. Kreß, H.-P. Steinrück and F. Maier

International Journal of Molecular Sciences, 23, 13158 (2022)

[10.3390/ijms232113158](https://doi.org/10.3390/ijms232113158)

The author's contribution is the development, construction and evaluation of the final structure and methodology, the ARXPS and PD/SD investigation, analysis, interpretation of the data and manuscript preparation.



[P3] **Direct correlation of surface tension and surface composition of ionic liquid mixtures – A combined vacuum pendant drop and angle resolved X-ray photoelectron spectroscopy study**

U. Paap, V. Seidl, K. Meyer, F. Meier and H.-P. Steinrück

Molecules, 27, 8561 (2022)

[10.3390/molecules27238561](https://doi.org/10.3390/molecules27238561)

The author's contribution is the sample preparation, ARXPS and PD investigation, analysis, interpretation of the data and manuscript preparation.

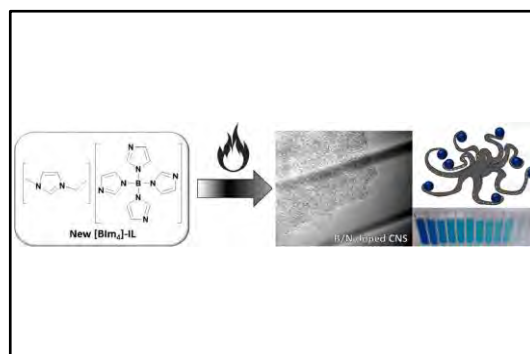


[P4] B/N-doped carbon sheets from a new ionic liquid with excellent sorption properties for methylene blue

J. Mehler, M. Ermer, U. Paap, B. S. J. Heller, F. Maier, H.-P. Steinrück, M. Hartmann, C. Korte, P. S. Schulz and P. Wasserscheid

Journal of Ionic Liquids, 1, 100004 (2021)

[10.1016/j.jil.2021.100004](https://doi.org/10.1016/j.jil.2021.100004)



The author's contribution is the ARXPS investigation, data analysis and interpretation.

TABLE OF ABBREVIATIONS

ADSA	Axysymmetric Drop Shape Analysis
ARXPS	Angle-resolved X-ray photoelectron spectroscopy
ASF	Atomic sensitivity factor
BE	Binding energy
BNC	B- and N-doped carbon
CA	Contact angle
DASSA	Dual Analyzer System for Surface Analysis
ESCA	Electron spectroscopy for chemical analysis
FEL	Fast-Entry Load-Lock
FTIR	Fourier-transform infrared spectroscopy
FWHM	Full Width at Half Maximum
HV	High vacuum
ICP-OES	Inductively coupled plasma atomic emission spectroscopy
ID	Information depth
IFT	Interfacial tension
IL	Ionic liquid
IR	Infrared
MB	Methylene blue
MD	Molecular dynamics

NMR	Nuclear magnetic resonance
PD	Pendant drop
PEG	Polyethylene glycol
RAS-LIF	Reactive atom scattering with laser-induced fluorescence
SCLS	Surface core level shift
SD	Sessile drop
ST	Surface tension
UHV	Ultra-high vacuum
XPS	X-ray photoelectron spectroscopy
XRD	X-ray diffraction

1. INTRODUCTION

Ionic liquids (ILs) are salts characterized by a low melting point, often liquid below room temperature, a negligible vapor pressure and have attracted great interest in research and industry over the last two decades.^[1-7] They are typically composed of strongly asymmetric and weakly coordinating ions, and their properties can be tailored over a wide range, making them interesting for many applications.^[3,8-10] Apart from other advantages, it is this almost uncountable possibility of adapting their physico-chemical properties by adequate and independent choice among many available anions and cations with specific molecular sub-units, which has earned ILs the term “designer solvents”.^[11,12] Mixing of two or more pure known ILs^[13-15] is an extension of this designer concept and a simple preparation route for new IL systems. However, the resulting properties of the mixture often deviate significantly from those of the individual ILs and do not follow ideal mixing rules. The deviations are related to the complex interplay of various long- and short-range interactions between the ions in the mixture.^[13,14] This leads to rather complex structures on the nanoscale in the bulk of pure ILs and IL mixtures.^[16,17] A prediction of the situation for ions at interfaces of the IL with a solid or with the gas phase is even more difficult. Mixtures containing fluorinated chains are an example, where a preferential enrichment of these moieties at the surface has been observed.^[18-21] The surface layer composition of ILs is determined by the preferential orientation of the ions to the gas (or vacuum) side to minimize the surface free energy, which is then directly reflected in the experimentally observed surface tension (ST).^[22]

As already discussed at the beginning of the last century by Hardy^[23] and Langmuir^[24,25], the break in symmetry at the surface of a liquid can lead to very distinct preferential orientation and segregation effects of molecules close to the liquid-gas interface. Langmuir studied a series of fatty acid solutions in water and observed for lower concentrations that the hydrocarbon chains lie flat on the water surface. With increasing concentration of the solution, the fatty acid molecules in the surface layer become more densely packed until the surface is saturated by the hydrocarbon chains arranged vertically while the ST levels off.^[25] This demonstrates that changes in ST often are very different from changes in bulk composition and the ST cannot be derived from ideal mixing rules. Langmuir also reported in his review “Forces Near the Surfaces of Molecules” that for all pure

organic liquids comprised of molecules with long alkyl tails, such as *n*-hexane and *n*-hexanol, the STs are almost equal, and therefore, independent of the hydrocarbon length. He inferred that the forces along the entire length of the alkyl part of the molecule are nearly uniform. The surface tension values of aliphatic alcohols explained Langmuir by splitting the surface tension into independently acting contributions of tail (hydrocarbon-chain) and head (hydroxyl) groups.^[26] The long tails are predominantly covering the outer surface leading to very similar ST values. For liquids with shorter alkyl chains, the hydroxyl groups are also significantly exposed to the gas phase resulting in ST changes. Thus, the ST of these hydrocarbons is attributed to the result of independent contributions from the molecular units that are exposed on average to the outer surface;^[26,27] this concept was also referred to as “Langmuir principle” elucidating the ST of pure $[C_nC_1Im][Tf_2N]$ ionic liquids.^[22]

While several groups have extensively studied the surfaces and interfaces of pure ILs under the well-defined conditions of ultrahigh vacuum,^[6,28-38] the analysis on the surface composition of IL mixtures with surface science techniques is a rather new field.^[20,34,39-43] ST at the macroscopic level arises from the fact that molecules in the bulk and at the surface have very different local environments and thus different interactions. Apart from the fact that ST of ILs is the focus of interest of many experimental and theoretical groups,^[44-47] it is also of great importance for many IL applications, including gas release and adsorption, coating and wetting, and multiphase catalysis phenomena at the liquid-gas interface.^[46] The ST of a liquid depends on the chemical composition of the surface layer and is therefore sensitive to contaminants or the gaseous environment.^[48,49] Surface science methods under ultraclean vacuum conditions are well suited for studying the intrinsic surface properties of ILs due to their extremely low vapor pressures.^[28-31,50] These methods allow one to characterize the surface composition and the molecular arrangement of cations and anions with high accuracy, which in turn sets the stage for investigating the surface tension of well-characterized and well-defined clean surfaces. The correlation between macroscopic surface tension and microscopic surface structure can then be used to adjust the surface properties for specific experiments in basic research, such as using liquid mixtures, or for targeted applications in industry.^[P2]

This thesis starts with the development and calibration of a new pendant drop (PD)/sessile drop (SD) setup to determine the intrinsic ST/IFT of ILs under vacuum conditions to minimize the risk of possible surface contamination.^[P2] Subsequently, temperature-dependent ST measurements from 370 K down to 295 K on the pure ILs [C₈C₁Im][PF₆] and [m(PEG_n)₂Im]I ($n = 2, 4, 6$),^[P2] as well as mixtures of these two ILs containing 4.5, 9.6, 19.4, and 49.8 mol% [C₈C₁Im][PF₆] are presented.^[P3] Along with their ST values, the surface composition of these ILs and their mixtures is discussed as determined from temperature-dependent angle-resolved X-ray photoelectron spectroscopy (ARXPS) in 0° and 80° emission in a temperature range from 370 K down to 230 K in ultra-high vacuum (UHV)^[P1,P3] in the so-called DASSA setup^[51]. In particular, ARXPS was used to verify the purity of the IL systems employed analyzing all elements present (except hydrogen and helium), and to reveal changes in stoichiometry at the surface as compared to the bulk. Then, applying the Langmuir principle, a quantitative correlation between the surface tension and the surface composition of IL mixtures is established, even for very complex ions, which allows for predicting the ST of IL mixtures based on their surface composition determined by ARXPS. Conversely, the ST value measured for an IL mixture at a given temperature under clean conditions can also be used to derive the composition at the outer surface.^[P3]

Finally, as an independent side project, porous carbonaceous materials doped with heteroatoms are discussed. These materials are highly tunable, stable and have a large surface area, possess interesting adsorptive properties and show a great potential for catalysis, energy conversion/storage, optoelectronic and sensing applications.^[52-56] A very popular class of pyrolysis precursors are ILs, as their thermal stability and low volatility provide high yields for carbonization. Due to the wide variety of cation-anion combinations, the amount of types of doping heteroatoms in the final product can be controlled.^[57,58] B- and N-doped carbon (BNC) materials based on a new 1-ethyl-3-methylimidazolium tetrakis(1-imidazolyl)borate ([C₂C₁Im][BIm₄]) precursor were characterized by means of X-ray photoelectron spectroscopy (XPS) to provide information about composition and bonding configuration of these BNCs obtained under different pyrolysis conditions.^[P4]

2. METHODS AND BASICS

2.1. SURFACE/INTERFACIAL TENSION (ST/IFT)

The central part of the experiments presented in this thesis are surface tension measurements using the pendant drop (PD) method, a macroscopic thermodynamic method of surface science. In this thesis, measured tensions at gas-liquid and at vacuum-liquid boundaries are both referred to “surface tension (ST)”. For liquid-liquid and liquid-solid boundaries, the expression “interfacial tension (IFT)” is used. The following basics also apply to liquid-liquid interfaces. For more details, see Ref. [59-62] and Appendix 8.3.

2.1.1. AXISYMMETRIC DROP SHAPE ANALYSIS (ADSA)

The most important part for accurate PD ST/IFT measurements is the exact determination of the shape of a hanging (=pendant) drop.^[63-66] In 1805, Young^[67] developed the quantitative theory of surface tension in general, which was completed by Laplace^[68] with respect to the mathematical description in the following year. The resulted Young–Laplace equation is a nonlinear partial differential equation that describes the capillary pressure difference (dp) sustained across the interface between the liquid and a gas phase (or across the interface between two immiscible liquid phases) due to the surface (or the interfacial) tension γ . It is defined as^{[P2],[60,62]}

$$dp = \gamma \left(\frac{1}{R_1} + \frac{1}{R_2} \right) \quad (1)$$

where R_1 and R_2 are the radii of curvature of a curved surface. For more details see Appendix 8.3.

In 1881, Worthington suggested that the ST of a liquid can be determined from the shape of a hanging drop, which is deformed by gravity.^[69-71] Bashford and Adams published 1883 numerical tables for the approximate solutions of the axially symmetric Young-Laplace equation.^[72] There, the drop shape is defined by a single dimensionless quantity representing the ratio of gravitational and interfacial forces and is specified by

$$\beta = d\rho g \frac{R_0^2}{\gamma} \quad (2)$$

Note that R_0 is the curvature radius of the drop at its apex and $d\rho$ the difference in mass densities of drop and surrounding medium.^[72] In 1947, Merrington and Richardson defined β as ‘Bond number’.^[73] When the bond number can be accurately determined from the drop shape, the surface (interfacial) tension can be directly obtained from the density, gravitational force and drop size. However, this proved to be challenging for some systems, especially for drops strongly elongated due to a low surface tension with only R_0 as characteristic drop shape parameter.

In 1938, Andreas et al. demonstrated an improved approach to determine γ from the aspherical drop shape based on the value $S = d_s/d_e$, which is the ratio of the maximum drop diameter, d_e , and the drop diameter, d_s , measured at a distance d_e from the apex.^[74] This method is named the “Method of selected planes” and is illustrated in Figure 1. The ratio S is then compared with tables calculated experimentally by Andreas et al., which correlates the bond number and interfacial tension. These tables were further improved over time by numerical integration of the Young-Laplace equation.^[74,75]

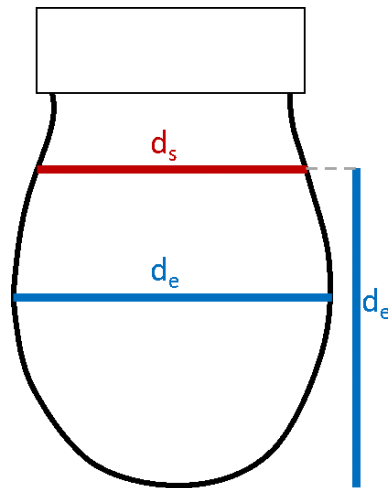


Figure 1: Illustration of the “Method of selected planes” from Ref. [74] using the ratio $S = d_s/d_e$ as characteristic descriptor for the pendant drop shape. The maximum drop diameter d_e (blue) and the drop diameter d_s (red) at the distance d_e above the apex are shown. Adapted from [P2] under license CC BY 4.0.

The Young-Laplace equation is still used today to derive γ . However, today’s standard programs for calculating the surface tension are based on the ADSA algorithm (axisymmetric drop shape analysis) developed by Neumann et al.^[63,76-80] The software for

this algorithm uses an image-processing technique that automatically detects the edge of the drop.^[81] Subsequently, the ST/IFT is calculated from the final drop profile using a numerical method,^[79,81] which is based on an optimization process.^[77,79] In this process, a set of Laplacian curves (theoretical curves) are fitted to the experimental profile. Before the fitting process, theoretical curves are generated by integrating the Young-Laplace equation (Equation 1) for the given values of surface tension and curvature at the apex of the drop.^[77,79] To fit the Laplacian profile to the experimental profile, an iterative solution procedure based on numerical solvers is necessary.^[79] As the results of the numerical solvers, the optimization parameters are obtained, which give the best fit between the measured profile and a Laplacian curve. Other surface/interface properties such as drop volume, surface area and contact angle are then determined from the selected Laplacian curve.^[77,79]

2.1.2. YOUNG EQUATION

To determine the wetting of a liquid on a solid, the sessile drop (SD) method is used as a standard approach. In this method, a droplet is placed on a solid surface. From the simple slope, the interaction of the droplet with the solid surface and the resulting wetting behavior can be determined. The droplet shape of a liquid L on a solid surface S in a gas phase G can be described by the Young equation

$$\gamma_{SG} = \gamma_{SL} + \gamma_{LG} \cos \Theta \quad (3)$$

This equation is based on the force balance at the three-phase contact line in the direction parallel to the surface, which is illustrated in Figure 2. In this equation, γ_{SG} is the surface free energy of the solid, γ_{SL} the interfacial tension between liquid and solid, $\gamma_{LG} = \gamma$ the surface tension of the liquid and $\cos \Theta$ the wetting/contact angle (CA).^[59-62,82] $\gamma_{SG} - \gamma_{SL}$ is also termed “wetting tension”.^[61] For more details see Ref. [59-62,82].

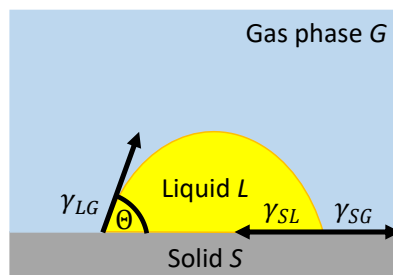


Figure 2: Contact angle of a liquid on a solid surface.

2.2. ANGLE-RESOLVED X-RAY PHOTOELECTRON SPECTROSCOPY (ARXPS)

Another central analytical method of this thesis is angle-resolved X-ray photoelectron spectroscopy (ARXPS). This very surface-sensitive technique is performed under ultra-high vacuum (UHV) conditions, it will be shortly described here; for more details, see Ref. [83-86].

X-ray photoelectron spectroscopy (XPS) is based on the external photoelectric effect, which was found by Hertz and Hallwachs in 1887^[87] and 1888^[88], proved by Lenard in 1894^[89] and interpreted by Einstein in 1905^[90]. A schematic illustration of the photoelectric effect is shown in Figure 3.

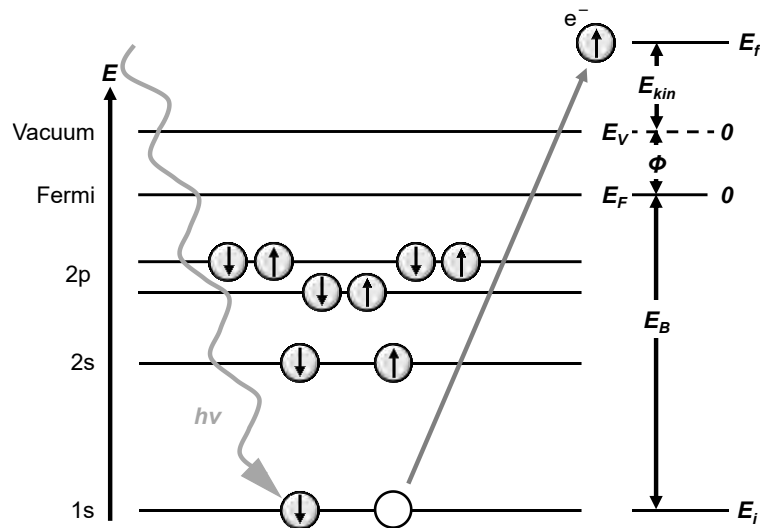


Figure 3: Scheme of the external photoelectric effect.

A sample is irradiated with photons of a specific energy $h\nu$ and photoelectrons are emitted. The emitted electrons are detected by an electrostatic analyzer as a function of their kinetic energy E_{kin} . With excitation of the electrons from the initial E_i to the final state of energy E_f , conservation of energy applies:

$$E_f = E_i + h\nu \quad (4)$$

The binding energy E_B is typically referenced to the Fermi energy E_F . The kinetic energy E_{kin} of an electron in free space is related to the vacuum level E_V , which differs from the Fermi energy by the work function Φ . The work function is a location-dependent quantity, which can vary and thus also the vacuum level. Because the kinetic energy is measured

via the analyzer, the work function of the analyzer Φ_{an} is also included in the measurement. Taking the work function of the analyzer into account by calibrating the analyzer to the Fermi energy of a metal sample, the binding energy is given by:

$$E_B = h\nu - E_{kin} - \Phi_{an} \quad (5)$$

Note that this relationship strictly applies to conductive samples electrically connected to the electron analyzer only without sample charging, which implies a common Fermi energy of both, sample and analyzer.

XPS yields characteristic energies for the respective elements and their core levels, whose exact values also depend on the chemical environment of the electron-emitting atom. Therefore, XPS is also known as Electron Spectroscopy for Chemical Analysis (ESCA). For more details on XPS, see Ref. [83-86].

The high surface-sensitivity of XPS arises from the large cross-section for inelastic scattering of the excited electrons while traveling in matter. The inelastic mean free path length (IMFP, λ) typically ranges from few angstroms to nanometers depending on material density and kinetic energy (note that different core levels have distinct E_B and thus distinct E_{kin} values, which are related to different λ values).^[91-95] ARXPS as one specific form of XPS allows for probing the near-surface region of a sample with different surface sensitivity by detecting electrons under different emission angles. As it is illustrated in Figure 4, the change in surface sensitivity with electron emission angle can be understood as follows: a higher peak intensity in the more surface-sensitive 80° measurement indicates a higher concentration of this elements in the outermost layers as compared to the more volume-sensitive measurement at 0° and vice versa. Thus, the changes in peak intensities with emission angle allows for the determination of surface enrichment and orientation effects. The contribution to the measured XPS signal in intensity follows an exponential behavior. Thereby, the intensity I_d at a depth d relative to the intensity I_0 at the IL/vacuum interface ($d = 0$) for different emission angels can be expressed by the Beer-Lambert law^[96,97]:

$$\frac{I_d}{I_0} = e^{-\frac{d}{\lambda \cdot \cos \vartheta}} \quad (6)$$

where ϑ is the emission angle of the photoelectrons relative to the surface normal (see Figure 4 left). Figure 4 (right) illustrates the exponential decrease of the contribution

from depth d in surface-sensitive ARXPS at different emission angles. The resulting intensities to the XPS signal at normal and grazing emission are given accordingly for 0° in black and for 80° in red.

The information depth (ID) of ARXPS is defined as

$$ID = 3\lambda \cdot \cos(\vartheta) \quad (7)$$

For organic matter, ID is around 7 to 9 nm at 0° (more bulk sensitive), while at 80° (surface-sensitive), ID decreases down to 1 - 1.5 nm. For the 80° measurement, more than 80% of the total core level intensity originates solely from the outermost layer.^[22]

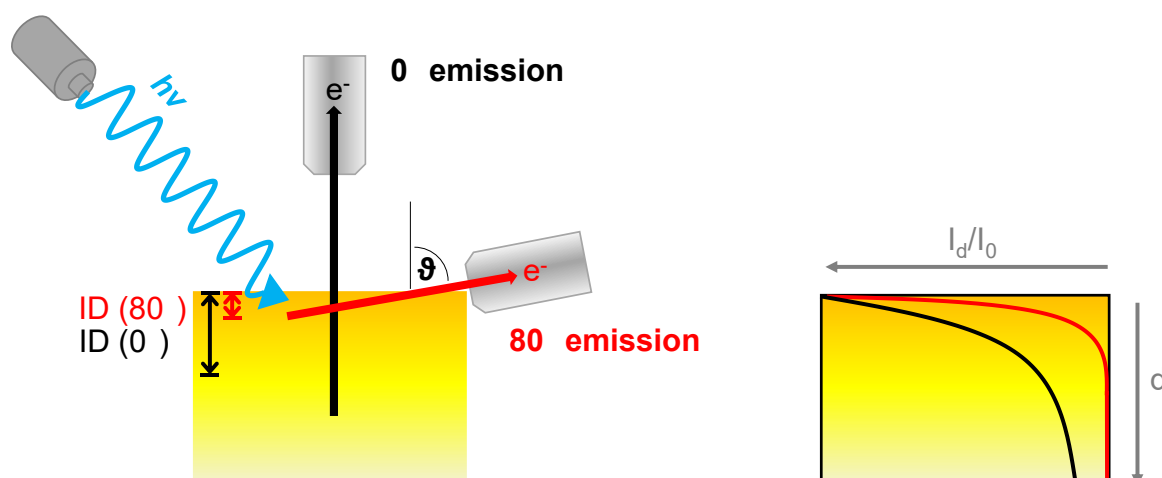


Figure 4: Left: Schematic representation of ARXPS recordings at an emission angle of $\vartheta = 0^\circ$ and 80° relative to the surface normal of the sample. The length of the arrows within the sample (black: 0° , red: 80°) represents the path length of the electrons of 3λ in the material, and thus, the resulting information depth ID at 0° (black) and 80° (red). Right: Exponential decrease of the intensity I_d for the emission angles of 0° (black) and 80° (red) of a signal from a depth d in relation to the intensity I_0 at the IL/vacuum interface.

3. MATERIALS, INSTRUMENTATIONS AND EXPERIMENTAL DETAILS

3.1. MATERIALS AND SAMPLE PREPARATION

Table 1 provides an overview of the ILs investigated in this work using ARXPS and PD/SD, including abbreviations, molecular structure and IUPAC name. All calibration fluids and ILs studied in this thesis were analyzed without further purification.

All liquid samples investigated with ARXPS were prepared on a molybdenum sample holder with a film thickness of 0.1 to 0.5 mm and degassed for at least 12 h in the fast-entry load-lock of our vacuum chamber prior to UHV ARXPS analysis. ^{[P1-P3][51]}

For all ST studies with the PD method, the reservoir was filled with 1 to 1.5 ml of the investigated liquid. ST studies under vacuum conditions were performed at a chamber background pressure in the low 10^{-6} mbar range. Before ST investigations were performed, the PD chamber was heated to at least 363 K and the ILs were degassed for at least 12 h after reaching this temperature. ^[P2,P3]

Surface tension calibration measurements were performed with Millipore water H₂O (resistivity 18.2 M Ω ·cm) and with benzene C₆H₆ (purity 99.7%) purchased from Merck at room temperature ($T_{\text{H}_2\text{O}} = 295.45$ K and $T_{\text{C}_6\text{H}_6} = 295.15$ K) and ≈ 1 bar ambient pressure.

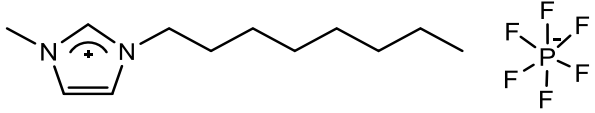
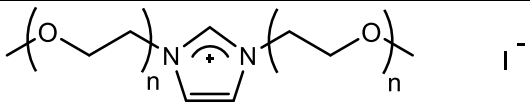
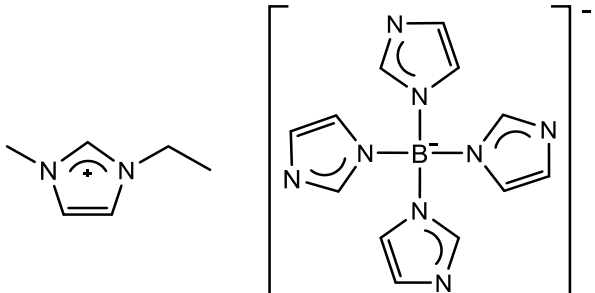
UHV ARXPS as well as surface tension measurements in high vacuum (HV) and in air were performed with 1-methyl-3-octylimidazolium hexafluorophosphate [C₈C₁Im][PF₆] (purity 99%) purchased from IoLiTec and used as delivered. ARXPS measurements were carried out at temperatures from 363 K down to around 233 K. ^[P3] The HV surface tension was measured from 360 K down to 295 K. ^[P2,P3] Then, the chamber was vented with air and the surface tension of the HV-degassed IL was investigated in the same temperature range at ambient pressure of ≈ 1 bar. For comparison, the surface tension of the initial, non-degassed [C₈C₁Im][PF₆] was also studied at a pressure of ≈ 1 bar in a similar temperature range. ^[P2]

UHV ARXPS and HV ST measurements were also performed for 1,3-bis(polyethylene glycol)imidazolium iodide [m(PEG_n)₂Im]I with ($n = 2, 4, 6$) synthesized by V. Seidl according to [P1] and mixtures of [C₈C₁Im][PF₆] and [(mPEG₂)₂Im]I with 4.5, 9.6, 19.4, and 49.8 mol% [C₈C₁Im][PF₆] content. The mixtures were prepared in total amount of one to three grams by weighing [C₈C₁Im][PF₆] in [(mPEG₂)₂Im]I, stirring and waiting overnight. ^[P3] First, ARXPS investigations of [m(PEG_n)₂Im]I with ($n = 2, 4, 6$) were performed at

room temperature (≈ 298 K).^[P1] For $[\text{C}_8\text{C}_1\text{Im}][\text{PF}_6]$, $[\text{m}(\text{PEG}_2)_2\text{Im}]\text{I}$ ^[P1,P3] and the mixtures, ARXPS measurements were recorded at temperatures from 363 K down to around 238/233 K,^[P3] where the onset of sample charging in ARXPS indicated solidification.^[51] ST studies for all pure ILs $[\text{m}(\text{PEG}_n)_2\text{Im}]\text{I}$ with ($n = 2, 4, 6$)^[P2] and mixtures of $[\text{C}_8\text{C}_1\text{Im}][\text{PF}_6]$ in $[\text{m}(\text{PEG}_2)_2\text{Im}]\text{I}$ ^[P3] were performed under HV conditions from around 370 K down to 290 K.

B- and N-doped carbons (BNCs) were synthesized by J. Mehler using 1-ethyl-3-methyl-imidazolium tetrakis-(1-imidazolyl)borate $[\text{C}_2\text{C}_1\text{Im}][\text{BIm}_4]$ mixed with an eutectic mixture of NaCl and ZnCl_2 and heated to pyrolysis temperatures of 1073, 1173 and 1273 K (800, 900 and 1000°C) according to [P4]. The porous BNCs were analyzed by XPS at an emission angle of 0° at ≈ 298 K. Here, a double-sided adhesive Cu foil was glued to the molybdenum sample holder and the BNCs were spread evenly on this foil with a spatula. Excess BNC was tapped off the sample holder. These samples were also degassed for at least 12 h in the fast-entry load-lock of our vacuum chamber prior to UHV ARXPS analysis.

Table 1: Overview of abbreviations, molecular structures and IUPAC names of the investigated reference liquids and ILs.

Abbreviation	Molecular Structure	IUPAC Name
$[\text{C}_8\text{C}_1\text{Im}][\text{PF}_6]$		1-methyl-3-octylimidazolium hexafluorophosphate
$[\text{m}(\text{PEG}_n)_2\text{Im}]\text{I}$ ($n = 2, 4, 6$)		1,3-bis(polyethylene glycol)imidazolium iodide
$[\text{C}_2\text{C}_1\text{Im}][\text{BIm}_4]$		1-ethyl-3-methylimidazolium tetrakis-(1-imidazolyl)borate

3.2. DETAILS ON THE INSTRUMENTS

3.2.1. HIGH VACUUM PENDANT DROP (PD)/SESSILE DROP (SD)

The pendant drop method is one of the most popular standard techniques to determine surface tension. For the determination of the contact angle, the sessile drop method is used as standard technique. Commonly PD/SD measurements are performed under non-vacuum conditions^[46], in various gas atmospheres or under different pressure conditions. In a standard setup with a syringe operating under ambient pressure, the 1 bar pressure acting at the pendant drop surface allows for pushing out from or drawing back into the vertically mounted cannula by moving the syringe stamp. This enables an easy adjustment of a constant and stable drop volume. When measuring in vacuum, no such external pressure acts at the droplet surface. This implies that the liquid can only be pushed out, while no negative pressure difference can be generated by retracting back the syringe stamp.

A detailed description of our new PD/SD chamber is given in Chapter 4.1.1, and only the basic details of the general setup are provided here. Figure 5 shows a photograph (left) and a drawing (right) of the HV PD/SD chamber developed in this thesis and used to acquire all the ST data shown herein. This setup enables us to study ST/CA on well-defined and well-characterized clean surfaces.^[P2]

The new high vacuum PD/SD setup (see Figure 5) is mounted in a small stainless steel vacuum six-way cubic cross as vacuum chamber. It operates in the pressure range from atmosphere (≈ 1 bar) to HV (10^{-7} mbar), and in a temperature range from room temperature to about 400 K. The chamber is pumped by a turbomolecular pump (Pfeiffer, HiPace 80), which is connected to an oil-free scroll pump (Pfeiffer, HiScroll 6). To vary the pressure or introduce a specific gas atmosphere, the gate valve to the pumps is closed, and the chamber can be either vented with air, or gases can be introduced by a fine dosing valve. The pressure is recorded with a multi-range pirani/cold cathode gauge (Pfeiffer, PKR 251). Attached heating tapes allow for uniform baking of the chamber, degassing of the liquids, and temperature-dependent measurements. In this thesis, PD measurements were performed in a temperature range of 370 K down to 290 K. Optical images of the pendant or sessile drops are recorded through a CF40 window using a high-speed camera (DataPhysics, iDS, UI-3350CP-M-GL R2).^[P2] The drops are illuminated from the back by a diffuse LED light screen, mounted on the opposite window for accurate imaging.^{[P2],[66,98]} A

cover with minimum sized rectangular opening (10 mm x 25 mm) is positioned at the illumination flange (that is, between the light source and the drop), to reduce reflections from the metallic walls inside the cross. All ST measurements were performed with camera setting of 16 for contrast and 12 for brightness.^[P2]

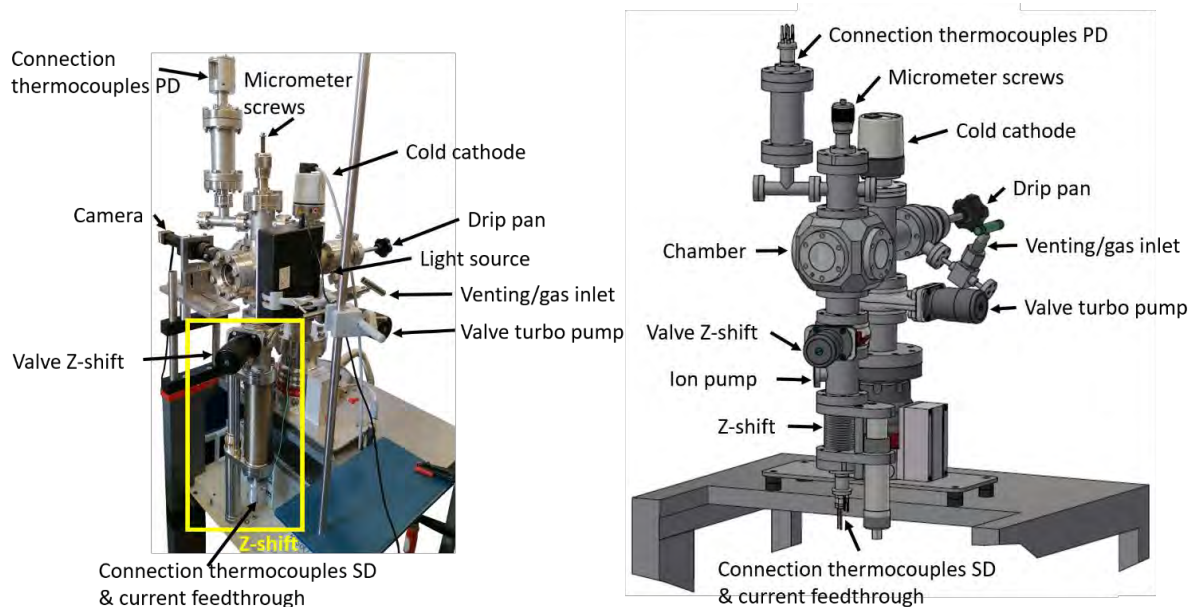


Figure 5: Photograph (left) and drawing (right) of the whole vacuum PD/SD system with attached z-shift of the SD assembly. Adapted from [P2] under license CC BY 4.0.

3.2.2. DATA EVALUATION PD

Surface tension studies were performed using a stainless-steel capillary with outer and inner capillary diameters of 2.02 mm and 0.50 mm, respectively. Two twisted stainless steel wires (0.2 mm) were inserted into the cannula to increase the contact area. Videos for surface tension investigations of the pendant drops were recorded with a high speed camera (4 frames per second). For the surface tension evaluation, 5 to 10 frames per drop were used. To ensure the reproducibility of the data, 5 drops were formed at a fixed temperature (with a maximum temperature drift of ± 1 K). The corresponding axisymmetric drop shape analysis (ADSA) of the drop shape and the self-consistent solution of the Young-Laplace equation was evaluated using the software SCA 22/15 (surface and interfacial tension; version 5.0.35) from DataPhysics.^[P2,P3] This software numerically solves the Young-Laplace equation in a self-consistent way with respect to manually set reference lines (see Figure 6).^[P2]

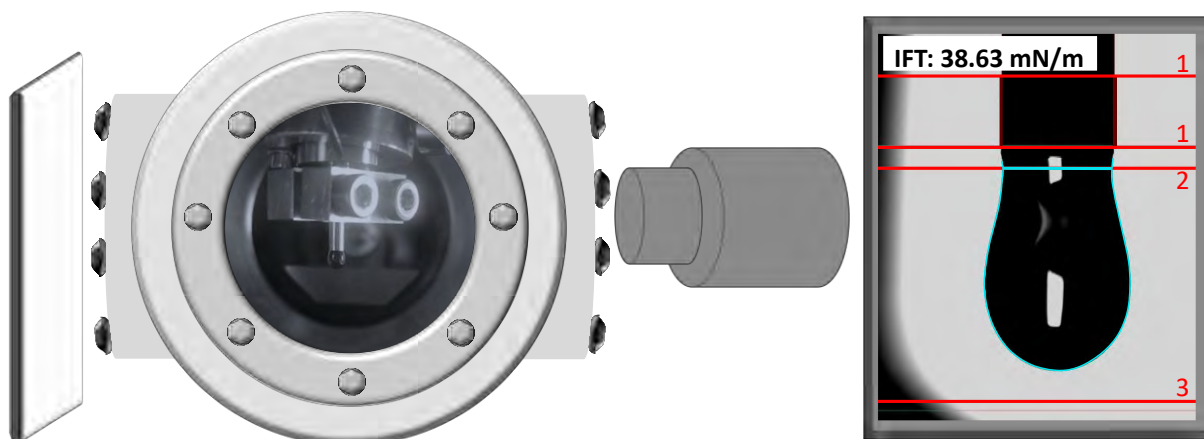


Figure 6: Left: PD configuration for ST measurements with diffuse light source (left), chamber with drop (middle) and camera (right). Right: Drop image with manually set reference lines for evaluation of surface tension (red, 1: magnification lines, 2: cannula end line, 3: boundary line) and received contour lines (turquoise). Adapted from [P2] under license CC BY 4.0.

Table 2: Densities [g/cm^3] and their literature references for the calibration liquids water and benzene. Adapted in parts from [P2] under license CC BY-NC 4.0. Temperature-dependent density parameters for pure $[\text{C}_8\text{C}_1\text{Im}][\text{PF}_6]$ and $[(\text{mPEG}_2)_2\text{Im}]\text{I}$ with references. The density of their mixtures containing 4.5, 9.6, 19.4 and 49.8 mol% $[\text{C}_8\text{C}_1\text{Im}][\text{PF}_6]$ is calculated from the mixing ratio of the two pure ILs. For information on density calculation, see Appendix 8.2. The densities for the surface tension evaluation at different temperatures are determined as $\rho = \rho_0 + \rho_1 \cdot T + \rho_2 \cdot T^2$ (temperature in K). Adapted in parts from [P3] under license CC BY-NC 4.0.

Calibration Liquids			
	T [K]	ρ [g/cm^3]	Literature
MP-water	295.45	0.9990	[99]
Benzene	295.15	0.8767	[100]
Ionic Liquids			
	ρ_0 [g/cm^3]	ρ_1 [$\text{g}/\text{cm}^3 \cdot \text{K}$]	ρ_2 [$\text{g}/\text{cm}^3 \cdot \text{K}^2$]
$[\text{C}_8\text{C}_1\text{Im}][\text{PF}_6]$	1.61	$-1.59 \cdot 10^{-3}$	$1.21 \cdot 10^{-6}$
49.8 mol%	1.65	$-1.30 \cdot 10^{-3}$	$7.39 \cdot 10^{-7}$
19.4 mol%	1.69	$-1.24 \cdot 10^{-3}$	$6.40 \cdot 10^{-7}$
9.6 mol%	1.71	$-1.22 \cdot 10^{-3}$	$6.07 \cdot 10^{-7}$
4.5 mol%	1.72	$-1.21 \cdot 10^{-3}$	$5.91 \cdot 10^{-7}$
$[(\text{mPEG}_2)_2\text{Im}]\text{I}$	1.72	$-1.20 \cdot 10^{-3}$	$5.70 \cdot 10^{-7}$
$[(\text{mPEG}_4)_2\text{Im}]\text{I}$	1.60	$-1.13 \cdot 10^{-3}$	$4.77 \cdot 10^{-7}$
$[(\text{mPEG}_6)_2\text{Im}]\text{I}$	1.56	$-1.14 \cdot 10^{-3}$	$4.89 \cdot 10^{-7}$

A list of densities used for ST evaluation and the corresponding literature are given in Table 2.^[P1-P3] For information on density calculation, see Appendix 8.2.

For all systems investigated as a function of temperature, the ST was successfully fitted by a linear regression

$$\gamma_{calc} = \gamma_0 + \gamma_1 \cdot T \quad (8)$$

where γ_0 and γ_1 are the fitting coefficients and T the temperature in Kelvin.^[P2,P3]

Further information on the software can be found in [P2] and in Appendix 8.3. Detailed descriptions of the data evaluation of the measured liquids are given in [P2] and [P3].

3.2.3. DUAL ANALYZER SYSTEM FOR SURFACE ANALYSIS

In conventional ARXPS, measurements are performed by either tilting the sample or rotating the analyzer to change electron detection angle, particularly to achieve grazing emission with increasing surface sensitive information, as described in Chapter 2.2. In contrast, the unique Dual Analyzer System for Surface Analysis (DASSA),^[51] which was developed in our group together with Omicron NanoTechnology with focus on ARXPS investigations of macroscopic ionic liquid samples, two electron analyzers mounted for normal (0°) and grazing (80°) emission angle operate simultaneously while the sample is maintained in a horizontal geometry. Figure 7 depicts a scheme of the DASSA, which was used to acquire all of the ARXPS data presented in this work.

The DASSA setup consists of preparation chamber, analysis chamber and fast-entry load-lock (FEL) system. A sputtering gun (SPECS IQE 11/35), quadrupole mass spectrometer (QMS; HIDEN HAL 3F 511), and low energy electron diffraction system (LEED; Omicron) are installed in the preparation chamber. The samples are introduced into the FEL system via a nitrogen-filled inert box, degassed for at least 12 h, and then transferred to the manipulator in the preparation chamber. The manipulator head has two sample stages, a low-temperature stage with liquid nitrogen cooling and radiation heating, and a high-temperature stage with electron bombardment heating. Note that in this thesis, mainly the low-temperature sample stage was used due to the temperature range from

363 K down to 233 K. The sputtering gun (for Ar⁺ bombardment) mounted in the preparation chamber is used for cleaning the molybdenum reservoirs and for occasional surface cleaning of the IL samples under investigation.

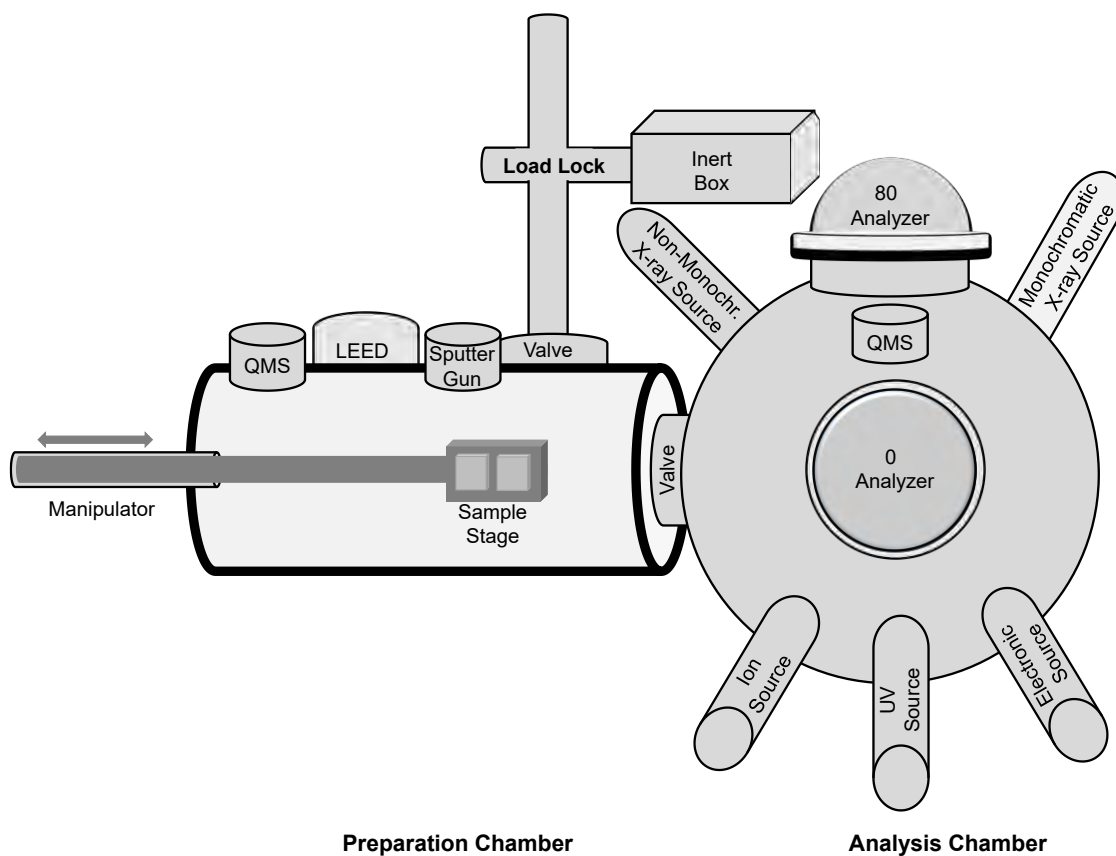


Figure 7: Schematic representation of the DASSA setup with the three main parts: Preparation Chamber (left), Analysis Chamber (right) and the Loading Lock (top). The assembled components of the three chambers are indicated.

The two identical hemispherical ARGUS electron analyzers with emission angles of 0° and 80° relative to the surface normal are mounted in the analysis chamber. This geometry allows simultaneous acquisition of XP spectra (Software: MATRIX T3.2) at normal (0°) and grazing (80°) emission from the same sample spot, reducing X-ray exposure time. The sample is kept in a horizontal position to avoid dripping of macroscopic liquid samples. A monochromatic Al K α X-ray source (Omicron XM 1000; $h\nu = 1486.6$ eV, 238 W power) is mounted in a “magic angle” configuration with respect to both analyzers. Survey scans are recorded with a pass energy of 150 eV, while a pass energy of 35 eV is used for region scans, resulting in a total energy resolution of 0.4 eV. In addition, a dual non-monochromatic X-ray source (Omicron DAR 400) with Mg K α ($h\nu = 1253.6$ eV) and Al K α ($h\nu = 1486.6$ eV) radiation, a QMS (Pfeiffer Vacuum PrismaPlus QMG 220), an electron

source for charge compensation (Omicron CN 10), an ultraviolet source (Omicron HIS 13) and an ion source (Omicron FIG 05) are connected to the analysis chamber, but were not used in this thesis. Further details are described in Ref. [51].

3.2.4. DATA EVALUATION ARXPS

All XPS data were analyzed using the CasaXPS software (version 2.3.16Dev6). A two-point linear background was subtracted for all peaks, except for the I 3d region, where a three-point linear background was used. Fitting was performed using pseudo-Voigt functions (product of Gaussian and Lorentzian with 30% Lorentzian contribution).^[P3] Atomic sensitivity factors (ASFs) relative to F 1s were applied for the quantitative analysis of the core levels.^[102] The specific core levels and the associated ASFs used in this work are listed in Table 3.

Table 3: ASFs applied to peak intensities for measurements performed in this work using the DASSA setup.

Core Level	ASF (DASSA)
F 1s	1.00
I 3d _{5/2}	6.17
O 1s	0.67
N 1s	0.46
C 1s	0.30
P 2p	0.46
B 1s	0.15

For the spin-orbit split P 2p_{1/2} and 2p_{3/2} core levels, the intensity ratio was set to 1:2, the separation of both peaks to 0.90 eV with the same full width at half maximum (FWHM). For pure [C₈C₁Im][PF₆], the C 1s region was fitted with three peaks for C₂, C_{hetero} and C_{alkyl}. The C₂ and C_{hetero} peaks are separated by 0.90 eV, have an intensity ratio of 1:4, and FWHMs of 1:1.1; C₂ and C_{alkyl} have equal FWHM. In case of pure [(mPEG₂)₂Im]I, the C 1s region was fitted with two peaks, C₂ and C_{hetero}, with a peak separation of 0.87 eV and a ratio of 1:12. For C_{hetero}, the FWHM was 1.19 times that of the C₂ peak. The C 1s region of the mixtures was fitted considering the different peak positions, peak widths of the pure ILs and the corresponding mixing ratios and resulting atomic ratios. The C_{alkyl} signals

in the mixtures are small for low $[\text{C}_8\text{C}_1\text{Im}][\text{PF}_6]$ content. Therefore, an additional constraint for unambiguous fitting was used, namely a fixed peak separation of the C_{hetero} and the C_{alkyl} peaks of 1.59 eV in 0° and 1.46 eV in 80° .^[P3]

In order to visualize depletion/enrichment effects by direct comparison and to account for an overall reduced signal intensity for the grazing emission geometry, all 80° spectra were scaled up by a common geometry factor. This factor is chosen in such way that the sum of the weighted intensities of all core-levels obtained at 0° and 80° are identical according to an established procedure.^{[P1,P3],[18,51]} In addition, the energy scales of all 80° spectra were shifted slightly by -0.1 eV so that the N 1s peaks in 80° of the common imidazolium head group fall on the N 1s peaks in 0° .^[P3]

For the BNCs determination of $[\text{C}_2\text{C}_1\text{Im}][\text{BIm}_4]$, only the 0° data were considered and analyzed. The N 1s and C 1s regions were fitted with three peaks. The peak with the highest binding energy is due to the satellite features of the N and C atoms in an aromatic configuration. In the N 1s region, the C-N and B-N peaks were fitted with a separation of 2.1 eV and FWHMs of 1.1:1. The C-N and C-C peak are separated by 1.7 eV and have FWHMs of 1.7:1 in the C 1s region. The B 1s region was fitted with two peaks B-O and B-N, separated by 1.4 eV and have equal FWHM.^[P4]

4. RESULTS AND DISCUSSION

Four peer-reviewed articles were published as part of this thesis and are summarized in this chapter. Further experimental details are given in the corresponding publications [P1] - [P4].

4.1. HIGH VACUUM PENDANT DROP AND SESSILE DROP SETUP^[P2]

This chapter mainly focuses on the the PD/SD chamber (see Chapter 3.2.1), which was developed, built and put in operation in course of this thesis in 2021. In addition, the main features of the chamber, the pendant drop and sessile drop sample system, and calibration and reference measurements of the PD system are also presented here. Additional ST results are presented in Chapter 4.2 and 4.4. For more details on the setup, problems and solutions, as well as data evaluation, see [P2] and Appendix 8.3.

4.1.1. PENDANT DROP

Once a pendant drop is formed in vacuum, the liquid drop and the liquid in the cannula are retained only by capillary forces counteracting gravitational forces; otherwise, the liquid would simply drip out of the syringe. To ensure that the capillary forces are comparable to those of gravity in order to obtain suitable stable hanging drops for the measurements, a stainless steel capillary with outer and inner capillary diameters of $\varnothing_o = 2.02$ mm and $\varnothing_i = 0.50$ mm, respectively, turned out to be suitable for IL measurements. To increase the contact area and thus the capillary forces within the cannula, two twisted stainless steel wires (0.2 mm diameter) are inserted into the cannula. Figure 8a shows the new PD syringe setup, which is made of stainless steel. It consists of a stationary reservoir with degassing holes, a replaceable cannula and a stamp that can be moved vertically with a micrometer screw-drive. Liquid tightness between the stamp and the reservoir, and between the cannula and the reservoir, is achieved by viton seals mounted on the stamp and between the cannula and the reservoir. The entire assembly is mounted on a CF 40 flange (see Figure 8b) so that the tip of the cannula ends in the center of the six-way cross after assembly.^[P2]

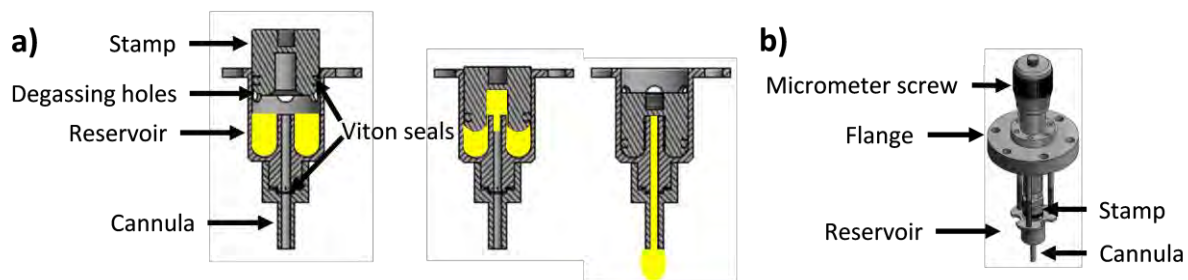


Figure 8: Concept and construction for vacuum drop formation: a) Inner part in vacuum consisting of a stamp, reservoir with degassing holes and cannula (inside the cannula, inserted twisted wires increase capillary forces). The stamp is pushed in the reservoir to press the liquid into the cannula and forms a drop at its end. b) Complete setup with the micrometer screw that moves the stamp in vertical direction. Adapted from [P2] under license CC BY 4.0.

First, the liquid under investigation is filled into the setup's reservoir in air. The setup is then attached to the PD chamber via the CF 40 flange and the chamber including the reservoir is carefully pumped down with the stamp retracted, i.e. with the reservoir degassing holes open. Pumping and degassing of the sample is performed for at least 12 h at chamber temperatures of 340 to 370 K to remove all volatile species from the liquid. The temperature is verified by two independent type K-thermocouples, which are mounted next to the cannula tip. When the final vacuum is reached and the sample is completely degassed, the stamp is slowly moved down into the reservoir, closing the degassing holes before touching the liquid surface. The stamp pushes the liquid into the cannula, and a drop of growing size is formed slowly at the end of the cannula (see Figure 8a). Just before a targeted drop reaches its maximum size, the stamp must be pushed back a little, otherwise liquid from the reservoir will still be pressed into the cannula and the drop will fall off very quickly. When the drop detaches from the cannula, it is collected in a glass vessel located in an extra tube attached to the chamber below the cannula. Video recordings are made of the formed drops.^[P2]

4.1.2. SESSILE DROP

Our system can also be used to perform sessile drop measurements on ultra-clean surfaces. For these measurements, a cannula with a smaller outer diameter of $\varnothing_o = 1.05$ mm (inner diameter: $\varnothing_i = 0.5$ mm) is used to obtain a suitable small size of the formed droplets.^[P2] In order to neglect the influence of gravitational force and to obtain reproducible

data, the volume of a sessile drop should be 0.5 to 10 μl , according to literature.^[103-108] After pumping the chamber and degassing the liquid in the reservoir, some preliminary drops are first formed and disposed in a small drip pan (see Figure 6) that can be placed under the cannula. This is followed by the actual deposition of the droplets on a solid sample (e.g. a well-prepared single crystal surface), which is fixed onto specially designed SD sample holders for solid samples as shown in Appendix 8.3. The sample holder is mounted on a z-shift manipulator of a vacuum suitcase. The suitcase is attached to the bottom flange of the PD/SD chamber via a gate valve and pumped by a small ion getter pump.^[P2] The vacuum suitcase allows for the transfer of well-prepared samples via the FEL chamber from DASSA^[51] (see Section 3.2.3) to the PD/SD chamber without breaking the vacuum. Conversely, it also allows for vacuum-transfer of deposited sessile drops without air contact to DASSA for further XPS analysis in terms of sample composition and purity. To deposit a drop on the solid sample surface, the gate valve is opened and the sample is moved with the z-shift to the target position under the cannula. After the droplet is deposited, the contact angle (CA) is determined by taking pictures with the PD/SD camera. A resistive pBN heater (Neyco, PCPBNP05, $\Phi = 12.7$ mm, resistance: 5-7 Ohm, maximum power: 80 W) mounted beneath the sample holder in the z-shift allows for simultaneous sample heating up to 800 K to perform temperature-dependent CA measurements.^[P2]

4.1.3. PD CALIBRATION MEASUREMENTS WITH WATER AND BENZENE

Surface tension calibration measurements were performed using Millipore water (resistivity 18.2 MW \cdot cm) at room temperature (295.45 K, ST literature value at this temperature is 72.34 mN/m^[109]) at 1 bar ambient pressure. To find the optimum conditions and positions for the light source and the high-speed camera relative to the setup and to calibrate the whole system, images were acquired with different contrast and brightness settings in the SCA 22/15 software from DataPhysics. The density value for water of 0.9990 g/cm³ was used.^[99] An optimized surface tension value of 72.40 ± 0.06 mN/m deviates by less than 0.1% from the literature value at camera contrast and brightness settings of 16 and 12 and at slightly lower or rather higher brightness without further refinement needed.^[P2]

To crosscheck the calibration, ST measurements were also performed using the settings derived from water (see above) for benzene in air at room temperature

($p \approx 1$ bar, 295.15 K). The surface tension values were determined using the density for benzene at this temperature and compared with the values from Ref. [100]. These were obtained under equilibrium conditions of benzene vapor pressure. We could not achieve these equilibrium conditions in our setup. The surface tension of 28.85 ± 0.03 mN/m determined by us is slightly higher than the literature value (28.62 mN/m at 295.15 K^[110]). This deviation of 0.8% is within the statistical uncertainty range of $\pm 2\%$ typically observed for surface tensions measured with the PD method.^[46,111] The slightly higher surface tension value of benzene compared to the literature can be attributed in part to the higher benzene vapor pressure and non-equilibrium conditions in our setup. The formed benzene drops evaporate slowly during image acquisition, resulting in a decrease in the drop volume and a more spherical drop shape.^[P2] As our system is manually operated, no μL could be added to the drop to compensate for evaporation loss, as is often done in literature.^[98,112,113] This evaporation problem is not relevant to our targeted measurements of ILs, since our system was designed for surface tension measurements of non-volatile liquids.^[P2]

4.2. PD MEASUREMENTS OF IONIC LIQUID SYSTEMS IN HIGH VACUUM^[P1-P3]

The aim of this chapter is to obtain a fundamental understanding of the intrinsic surface tensions of liquids and their mixtures. For this purpose, the intrinsic surface tensions must be accurately determined under well-defined and ultra-clean conditions, that is, at best in HV.^[P2]

In [P2], we studied the surface tension of two different pure ILs, one is the standard IL $[\text{C}_8\text{C}_1\text{Im}][\text{PF}_6]$ and the other is the newly synthesized ILs $[(\text{mPEG}_n)_2\text{Im}]\text{I}$ ($n = 2, 4, 6$). Investigations of $[\text{C}_8\text{C}_1\text{Im}][\text{PF}_6]$ were first performed in high vacuum ($3.3 \cdot 10^{-6}$ mbar), then degassed and non-degassed in air (≈ 1 bar) in the temperature range from 360 K down to 295 K and compared with literature values. Subsequently, the $[(\text{mPEG}_n)_2\text{Im}]\text{I}$ ILs were studied as a function of temperature in high vacuum^[P2] and compared with surface tension measurements at 1 bar inert argon atmosphere with a conventional PD setup performed by Ziwen Zhai. Information on the latter measurement in argon atmosphere, as well as other characterization methods of $[(\text{mPEG}_n)_2\text{Im}]\text{I}$ can be found in [P1] and are not discussed here.^[P1] For more details to this study, see [P2].

In the first part of [P3], we investigated the temperature dependence (from 363 K down to 300 K) of the surface tension of [(mPEG₂)₂Im]I and [C₈C₁Im][PF₆] mixtures with 4.5, 9.6, 19.4, and 49.8 mol% [C₈C₁Im][PF₆] content under ultra-clean HV conditions at a pressure in low 10⁻⁶ mbar. We compare the ST obtained from the measurements with the ST of the ideal behavior to determine the correlation with the surface composition in Chapter 4.4. The studied mixtures consist of ILs with different anions and cations. Further experimental details can be found in Subchapter 4.3.2 on surface composition, in Chapter 4.4 on the correlation of surface composition and surface tension, and [P3].

4.2.1. SURFACE TENSION OF [C₈C₁IM][PF₆]^[P2]

For temperature-dependent PD measurements in high vacuum and degassed in air, [C₈C₁Im][PF₆] was inserted into the PD reservoir and degassed under HV conditions as described in Chapters 3.1 and 4.1.1. First, the surface tension was measured at a pressure of 3.3·10⁻⁶ mbar from 360 K down to 295 K; then the chamber was vented with air and the ST of the HV-degassed IL was measured in the same temperature range at an ambient pressure of ≈1 bar. For comparison, the ST of the original, non-degassed [C₈C₁Im][PF₆] was also measured at a pressure of ≈1 bar in a similar temperature range. For evaluation, the temperature-dependent density of dried [C₈C₁Im][PF₆] from Ref. [101] (see Section 3.2.2, Table 2) was used for all data sets. In all cases, we observed a linear decrease of ST with increasing temperature values (see Figure 9a), which was fitted by Equation 8 (see Chapter 3.2.2). With the corresponding coefficients and this equation, the surface tension were calculated for 298 K (see Table 4) and plotted for the different measurement conditions (see Figure 9b).

For the degassed IL at 298 K in air under ambient pressure, the ST value is 34.03 mN/m, which agrees to within 0.24% with the one obtained in Ref. [114] using the Wilhelmy Plate method at similar conditions (33.95 mN/m for degassed [C₈C₁Im][PF₆], ambient pressure, 298 K). Comparing this value with those measured by Freire et al. using the Du Noüy ring method (34.87 mN/m for degassed [C₈C₁Im][PF₆], ambient pressure, 298 K, Ref. [44]), it differs by about 2%. When comparing the different absolute ST values of different groups, deviations of several % are common.^[46,111] However, much smaller relative changes in ST caused, e.g., by a change in water content, can be detected with high accuracy when an identical device is used as it is the case of the present work. Thus, the

changes in the ST values of the degassed IL in HV (34.18 mN/m at 298 K), of the degassed IL in air (34.03 mN/m) and of the non-degassed IL in air (33.89 mN/m) are indeed significant. The ST was systematically lower for the degassed IL at atmospheric pressure in air and lowest for the non-degassed IL in air (see Figure 9b, Table 4). The difference in density between vacuum and gas phase should give an effect of less than 0.1% = 0.03 mN/m. These systematic reduced ST values are mainly attributed to the residual water content of the non-degassed IL or the additional water absorption by the degassed IL after venting the chamber. Note that a quantitative determination of water content could not be performed in these experiments. Nevertheless, the measurement method is accurate enough to detect a clear influence of the different water content on the surface tension.^[P2]

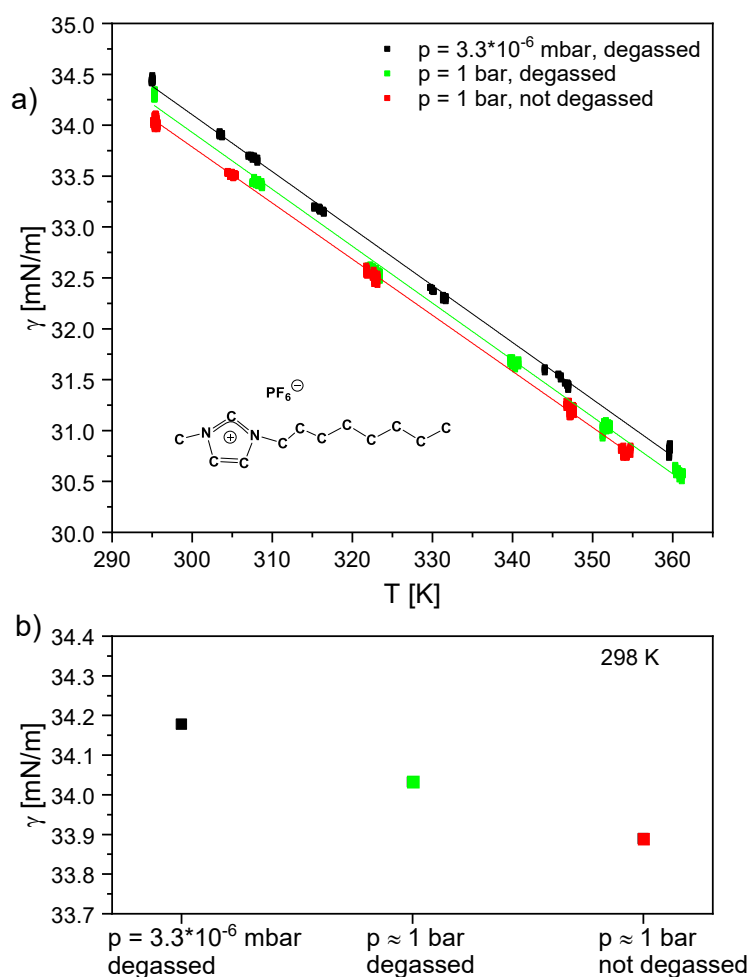


Figure 9: Surface tension values of $[C_8C_1Im][PF_6]$ in vacuum and in air (≈ 1 bar) under degassed and non-degassed conditions. (a) The temperature-dependent ST is determined using the density of dried $[C_8C_1Im][PF_6]$ from Ref. [101]. (b) Calculated surface tension values for the three different conditions at 298 K based on the linear fits of (a) using Equation 8. Adapted from [P2] under license CC BY 4.0.

Table 4: Surface tension values of $[C_8C_1Im][PF_6]$ at $T = 298$ K under degassed and non-degassed conditions at different pressures. Coefficients of the linear fits to the data according to Equation 8. The surface tension is calculated using the temperature-dependent density of dried $[C_8C_1Im][PF_6]$ from Ref. [101]. Reproduced from [P2] under license CC BY 4.0.

Condition	p [mbar]	γ [mN/m] ($T = 298$ K)	γ_0 [mN/m]	γ_1 [mN/m·K ⁻¹]	γ [mN/m] from Ref. [114] ($T = 298$ K)
Degassed	$3.3 \cdot 10^{-6}$	34.18	50.67	-0.0553	
Degassed	$1.0 \cdot 10^3$	34.03	50.69	-0.0559	33.95
Non-degassed	$1.0 \cdot 10^3$	33.89	50.32	-0.0551	

4.2.2. SURFACE TENSION OF $[(MPEG_n)_2Im]I$ [P2]

As a next step, we also investigated the temperature-dependent ST of a new class of $[(MPEG_n)_2Im]I$ salts, with symmetric polyethylene glycol (PEG)-chains at the imidazolium cation of increasing lengths ($n = 2, 4, 6$) in HV at a low pressure of $5 \cdot 10^{-6}$ mbar (see Figure 10). The density and subsequently the surface tensions in an inert argon atmosphere of 1 bar using a conventional PD setup was studied by Ziwen Zhai.^[P1] The purity of the ILs and the absence of surface contaminations were also verified by nuclear magnetic resonance (NMR) and ARXPS, respectively. The latter method is explained in more detail in Subchapter 4.3.1. An overview of all measurement methods and the characterization of these ILs can be found in [P1]. The temperature-dependent ST data are linearly fitted according to Equation 8 (Chapter 3.2.2). The corresponding fitting parameters in Table 5 are presented together with the resulting surface tension values in HV at 298 K for the three ILs with different PEG-chain lengths (dashed vertical line in Figure 10). They agree very well with the surface tension values under 1 bar argon^[P1] measured with a standard PD setup. The very small deviation between the two setups, with an average of 0.5% (see Table 5), is attributed to the careful calibration procedure of both instruments with water. Compared to the calibration measurements with benzene (see Chapter 4.1.3 and [P2]), drop changes due to evaporation have no influence on the determined surface tension.^[P2]

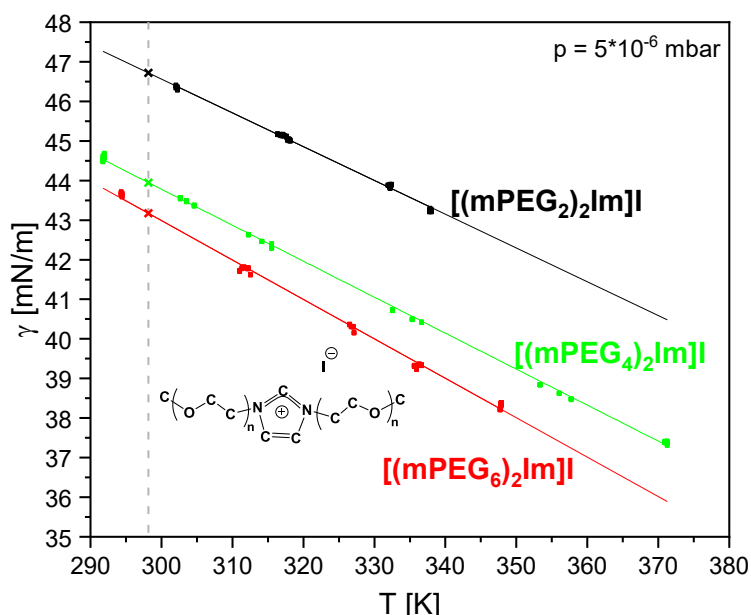


Figure 10: Surface tension values of $[(m\text{PEG}_n)_2\text{Im}]\text{I}$ with $n = 2, 4, 6$ measured in vacuum at different temperatures. The crosses at 298 K (dashed line) represent the calculated surface tension values based on the linear fits according to Equation 8. Adapted from [P2] under license CC BY 4.0.

Table 5: Surface tension values of $[(m\text{PEG}_n)_2\text{Im}]\text{I}$ with $n = 2, 4, 6$ at $T = 298$ K measured in vacuum. Coefficients of the linear fits to the data according to Equation 8. Comparison to literature data measured under 1 bar Ar atmosphere.^[P1] Reproduced from [P2] under license CC BY 4.0.

IL	γ [mN/m] at 5 · 10 ⁻⁶ mbar (T = 298 K)	γ_0 [mN/m]	γ_1 [mN/m · K ⁻¹]	γ [mN/m] from [P1] at 1 bar Ar (T = 298 K)
$[(m\text{PEG}_2)_2\text{Im}]\text{I}$	46.72	72.17	-0.0854	46.26
$[(m\text{PEG}_4)_2\text{Im}]\text{I}$	43.95	71.05	-0.0909	43.94
$[(m\text{PEG}_6)_2\text{Im}]\text{I}$	43.17	72.87	-0.0996	42.96

A linear decrease in surface tension is again observed with increasing temperature. When comparing the different ILs, a decrease in surface tension with increasing PEG_n-chain length n is evident. The surface tension decreases from 46.72 mN/m for PEG₂ to 43.95 mN/m for PEG₄ and to 43.17 mN/m for PEG₆ at 298 K (see Table 5), which is a decrease by -5.9% when increasing the PEG-chain length from 2 to 4, and only by -1.8% when increasing the PEG-chain length from 4 to 6.^[P2] In addition to our PD measurements in HV, we also perform ARXPS measurements in UHV. The latter clearly reveal a preferential orientation of the PEG-chains towards the surface and a depletion of the

iodine anion; both become more pronounced with increasing chain length, which is described in more detail in Subchapter 4.3.1.^[P1] The significant ST decrease from PEG₂ to PEG₄ and the moderate decrease from PEG₄ to PEG₆ can be explained by the Langmuir principle in which the surface tension is related to the outermost surface composition.^[22] Above a certain PEG-chain length, the surface layer is more or less completely saturated with PEG-chain constituents, so that the surface tension flattens out.^[P2] An analogous behavior was also reported for [C_nC₁Im][Tf₂N] ILs with different alkyl chain lengths,^[22] where ARXPS measurements also exhibited an orientation of the alkyl chains towards the surface. For this IL class, more or less constant ST values were observed above a certain alkyl chain length due to saturation of the outer surface with aliphatic carbon.^[P2]

4.2.3. SURFACE TENSION OF MIXTURES OF [(mPEG₂)₂Im]I AND [C₈C₁Im][PF₆]^[P3]

In addition, temperature-dependent PD measurements were performed for [(mPEG₂)₂Im]I and [C₈C₁Im][PF₆] mixtures containing 4.5, 9.6, 19.4, and 49.8 mol% [C₈C₁Im][PF₆] in vacuum (low 10⁻⁶ mbar range). Figure 11 shows a linear decrease of the surface tensions for the pure ILs (open squares), as already described in Subchapters 4.2.1 and 4.2.2, and their mixtures (full squares) with increasing temperature, fitted by Equation 8 (see Chapter 3.2.2). The ST of the mixtures decreases with increasing content of [C₈C₁Im][PF₆]. Comparing the ST values calculated at 298 K from Equation 8, the highest value of $\gamma = 46.72$ mN/m is found for pure [(mPEG₂)₂Im]I and the lowest value of 34.18 mN/m for [C₈C₁Im][PF₆]. The values for the mixtures are in between. Remarkably, the change in ST is more pronounced at lower [C₈C₁Im][PF₆] contents, decreasing from 46.72 for 0 mol% to 44.67 for 4.5 mol% (by -2.05 mN/m) and further to 43.16 mN/m for 9.6 mol% (by -1.51 mN/m). It finally decreases only from 37.72 mN/m for 49.8 mol% to 34.16 mN/m for 100 mol% (by -3.56 mN/m). As it is clear from Figure 11, the same trend is observed for all studied temperatures.^[P3] Thus, the ST of the mixtures does not follow the ideal behavior, which would result from the ST values γ_i of the pure ILs weighted with the corresponding bulk mole fractions x_i and the following equation

$$\gamma_{T,mixture}(x) = \gamma_{T,[(mPEG_2)_2Im]I} \cdot x_{[(mPEG_2)_2Im]I} + \gamma_{T,[C_8C_1Im][PF_6]} \cdot x_{[C_8C_1Im][PF_6]} \quad (9)$$

In Figure 11, the non-ideal character is also evident from the fact that the lines for the measured data (solid lines) clearly fall below the ideal characteristics (dashed lines).

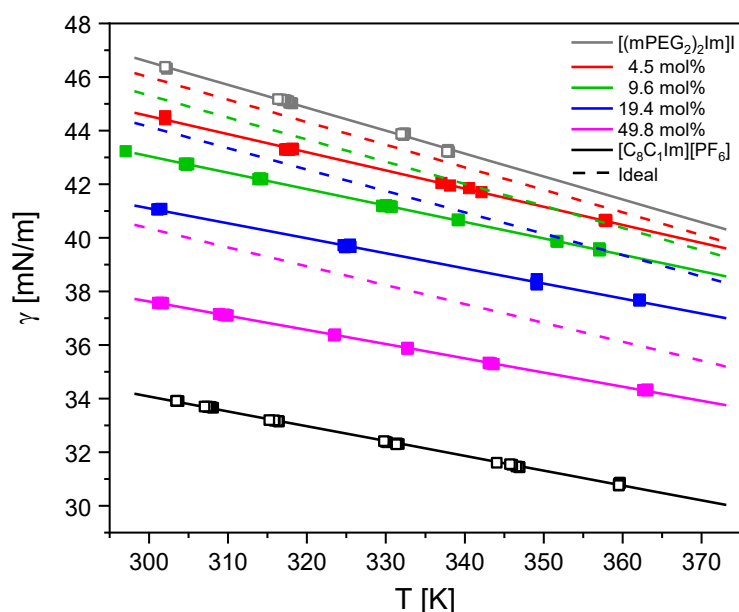


Figure 11: The surface tension values measured by the PD method in HV are shown as open and filled squares, along with their linear fits (lines) using Equation 8, compared with the surface tension expected for ideal behaviour of different mixtures (dashed lines). Obviously, the measured surface tension deviates strongly from the ideal mixing rules of all mixtures and temperatures. Reproduced from [P3] under license CC BY 4.0.

4.3. SURFACE COMPOSITION OF IONIC LIQUID SYSTEMS^{[P1], [P3]}

Both, ILs and polyethylene glycols (PEGs) are known for their physiological and chemical properties, such as low vapor pressure, low toxicity, and high chemical and thermal stability.^[115-117] PEGs are approved for use in biotechnology, medicine, drug discovery and food.^[116,117] PEG ILs offer a hydrophilic alternative to mainly established hydrophobic ILs (substituted in the cation with alkyl and/or aryl groups), as they exhibit altered physico-chemical properties but no significant changes in reactivity.^[118-120] Therefore, they find application as electrolytes in electronic devices^[121-125] and as solvents or catalysts in organic processes.^[126]

In [P1], a series of *bis*-mPEG_{*n*}-substituted imidazolium-based ILs with different anions (I, OMs, PF₆ and Tf₂N) and PEG_{*n*}-chain lengths (*n* = 2, 3, 4, 5, 6) were synthesized and experimentally investigated with respect to melting temperature, thermal stability, density, viscosity, surface tension, electrochemical potential window and electrical conductivity. In addition, the surface behavior and orientation of the [(mPEG_{*n*})₂Im]I (*n* = 2, 4, 6) ILs were analyzed using ARXPS and these results were compared with corresponding molecular dynamics (MD) simulations. In the following Chapter 4.3.1, the focus is on the ARXPS studies of the [(mPEG_{*n*})₂Im]I (*n* = 2, 4, 6) ILs, with different chain lengths in the

cation and the same anionic head group, at room temperature. For details of the synthesis, characterization and MD simulations performed by the co-authors, see the peer-reviewed article.^[P1]

In the second part of [P3], temperature-dependent effects (down to solidification temperature) of the surface composition of $[(m\text{PEG}_2)_2\text{Im}]^+$, $[\text{C}_8\text{C}_1\text{Im}][\text{PF}_6]$ and various mixtures of both ILs consisting of with very different anions and cations were analyzed. These investigations were performed under ultra-clean UHV conditions in a pressure range of $8 \cdot 10^{-11}$ to $1.5 \cdot 10^{-9}$ mbar using ARXPS. In Chapter 4.3.2, the focus is on the temperature-dependent surface composition – particularly on the O_{PEG} signals of the O 1s and on the C_{alkyl} signals of the C 1s regions at 80° – in order establish a correlation with the macroscopic surface tension values, will be presented in Chapter 4.4 (for further details, see [P3]).

4.3.1. $[(m\text{PEG}_n)_2\text{Im}]^+$ ($n = 2, 4, 6$)^[P1]

For the three $[(m\text{PEG}_n)_2\text{Im}]^+$ salts ($n = 2, 4, 6$), ARXP spectra were recorded for all relevant core levels I 3d_{5/2}, O 1s, N 1s, C 1s (and Si 2p, not shown here) at 298 K (see Figure 12).

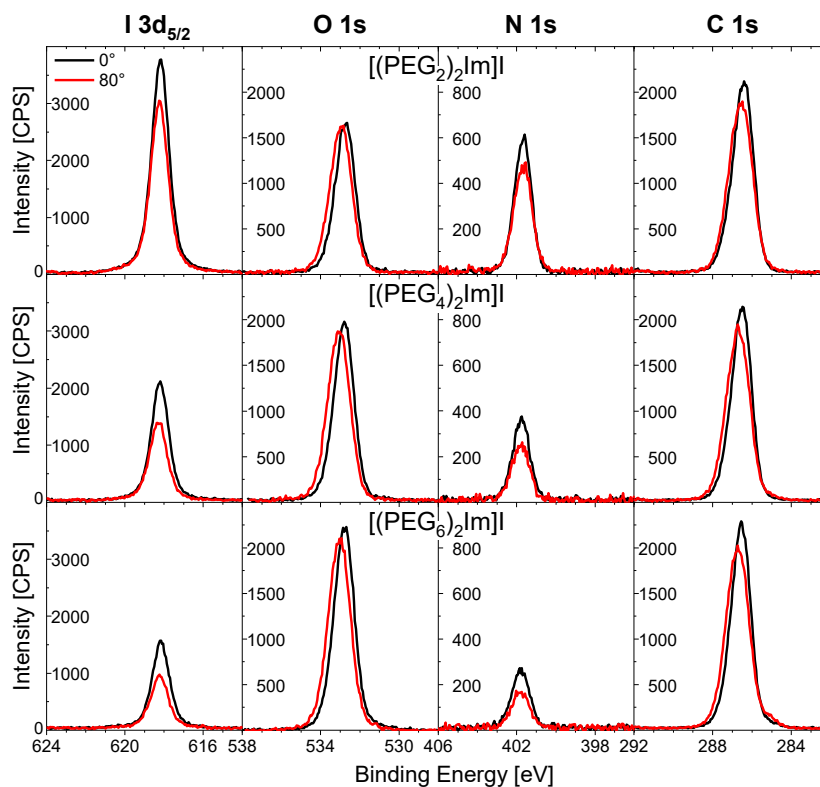


Figure 12: ARXP spectra for $[(m\text{PEG}_n)_2\text{Im}]^+$ with $n = 2$ (top row), 4 (middle), 6 (bottom) recorded under 0° (black) and 80° (red) emission angle at 298 K. Reproduced from [P1] under license CC BY-NC-ND 4.0.

The binding energies (BEs) of I 3d_{5/2} and N 1s are identical at 0° and 80°, while the O 1s and C 1s levels are slightly shifted by 0.3 ± 0.1 eV to higher binding energy at 80°. The I 3d_{5/2} and N 1s peaks at 0° (black) have much higher intensity than at 80° (red). This indicates a depletion of the corresponding atoms at the outermost surface, which becomes more pronounced with increasing chain length, as shown in Figure 13, where the ratios of the composition values, n(80°)/n(0°) are plotted. Fitting the peaks of the O 1s and C 1s signals shows a broadening of the peaks associated with the shifts in binding energy.^[P1]

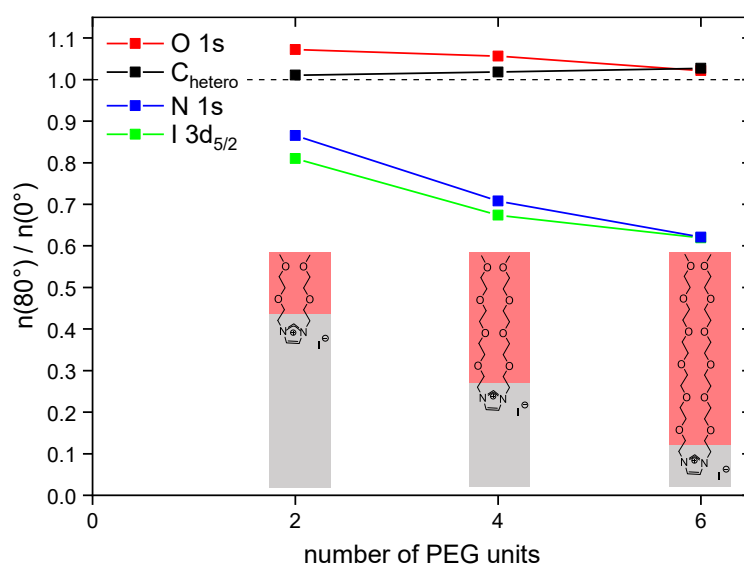


Figure 13: Composition ratios $n(80^\circ)/n(0^\circ)$ for the individual atoms derived from the corresponding intensities 80° and 0° for O 1s (red), C_{hetero} (black), N 1s (blue), and I 3d_{5/2} (green) for the [(mPEG_n)₂Im]I salts (n = 2, 4, 6). With increasing chain length, the thickness of the surface layer with the preferentially enriched PEG-chains (light red) also increases, and thus, the ionic moieties are further away from the outer surface. Same data as shown in [P1]. Reproduced from [P1] under license CC BY-NC-ND 4.0.

Taking into account the increase in peak width, the plot of chain signals in Figure 13 exhibits an 80°/0° ratio above 1, and consequently, an excess of O and C_{hetero}. Notably, two carbons of the imidazolium ring and two adjacent carbons also contribute to the C_{hetero} peak. This small excess of chain signals at 80° and the simultaneous decrease in N 1s and I 3d_{5/2} is caused by a pronounced enrichment of the PEG-chains at the outer surface due to their preferential orientation toward vacuum. As a result, these chains attenuate the 80° signals of the underneath ionic moieties, i.e., the N 1s signal of the positively charged imidazolium ring and the I 3d_{5/2} signal of the anion. The peak broadening and the shift of the O 1s and C 1s peaks to higher binding energy at 80° (see Figure 12) can be

explained by the fact that the PEG-chain atoms at the outer surface, in contrast to the ionic constituents, experience an anisotropic environment with IL neighbors on one side and vacuum on the other. This leads to a surface core level shift (SCLS) to higher binding energy. The very similar behavior of the I and N signals in Figure 13 indicates that both the anion and the imidazolium ring are approximately the same distance from the outer surface. Despite this strong enrichment of the PEG-chains, the $80^\circ/0^\circ$ ratios in Figure 13 for the O 1s and C_{hetero} signals each show somewhat larger value than the nominal value of one. This is due to the fact that the number of O and C_{hetero} atoms in the chains (14) far exceeds the number of I and N atoms (3). Thus, no significant enrichment, but a pronounced depletion can be observed. Whether one or both PEG-chains are enriched on the surface cannot be clearly determined with ARXPS. A very strong damping effect of the I $3d_{5/2}$ and N 1s signals at 80° was already observed for the shortest PEG-chain ($n = 2$), and is even more pronounced for longer chains. These observations indicate that most likely both chains of a single cation are preferentially oriented toward the vacuum. Our ARXPS results were confirmed by MD simulations from the group of Ana-Sunčana Smith. Furthermore, the simulations clearly show that a considerable part of cations in the surface layer are oriented such that both chains are oriented towards vacuum.^[P1]

4.3.2. [(mPEG₂)₂Im]I, [C₈C₁Im][PF₆] AND THEIR MIXTURES^[P3]

The O 1s and C 1s regions of the pure ILs and the corresponding mixtures at 298 K for emission angles of 0° and 80° are shown in Figure 14. Again, for the pure [(mPEG₂)₂Im]I (Figure 14, bottom), the SCLS is observed in the O_{PEG} peak of the O 1s region and the C_{hetero} peak in the surface-sensitive 80° spectra compared to the bulk-sensitive 0° spectra, as already described above and discussed in more detail in [P1]. In mixtures, the SCLSs are also observable for the O_{PEG} peak, indicating the presence of the PEG-chains at the surfaces, but to a lesser extent, which will be discussed below. The SCLS in the C_{hetero} signal is less pronounced because the atoms of the imidazolium ring also contribute to this peak. Both SCLSs can be attributed to the preferential orientation of the PEG-chains towards the surface, as already discussed in more detail in [P1] and in the Subchapter 4.3.1. With increasing [C₈C₁Im][PF₆] content in the mixture, a decrease in O_{PEG} intensity at 0° and an even stronger decrease at 80° is observed for the mixtures in contrast to pure [(mPEG₂)₂Im]I.

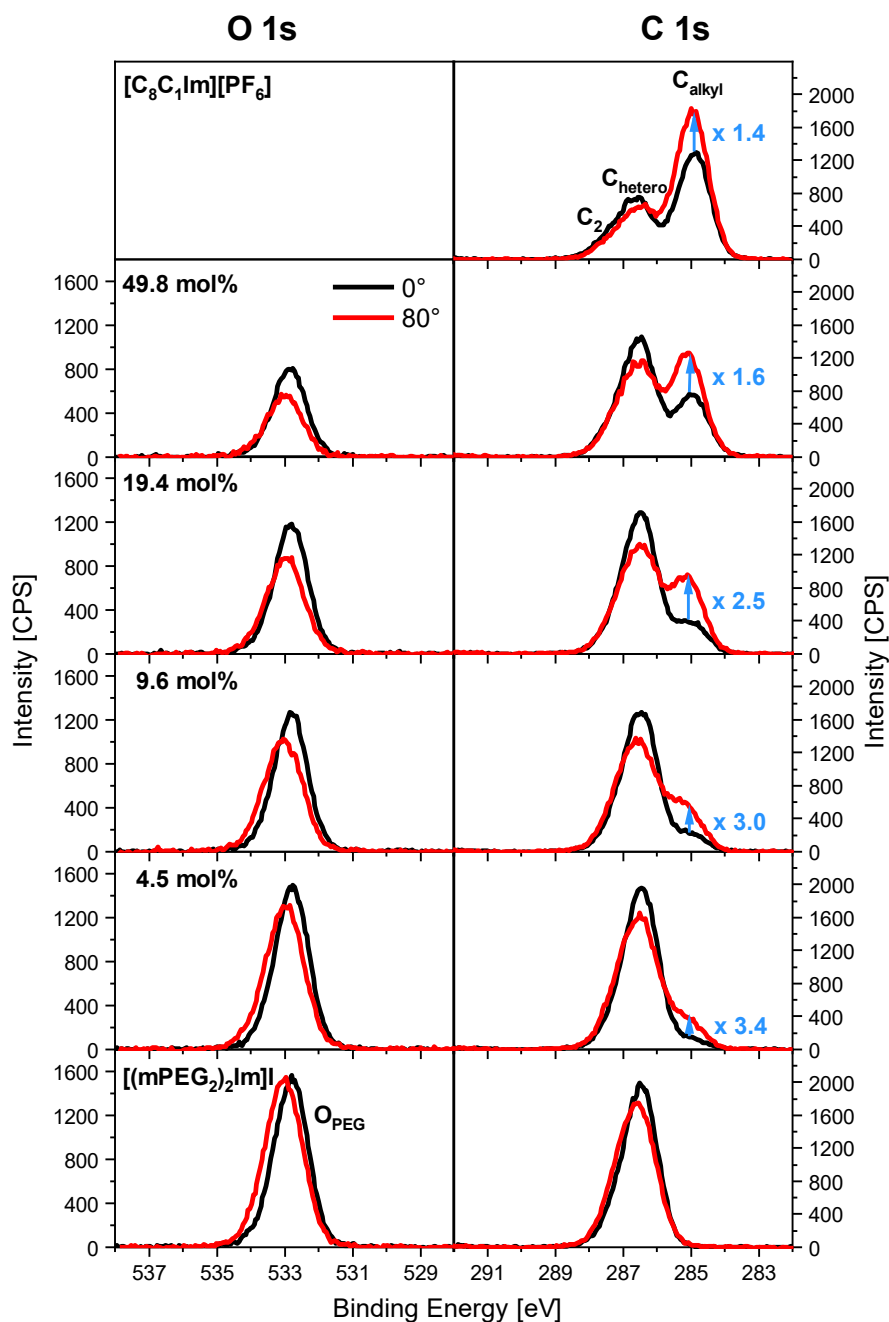


Figure 14: ARXP spectra of the O 1s and C 1s region at 0° (black) and 80° (red) emission of pure $[C_8C_1Im][PF_6]$, pure $[(mPEG_2)_2Im]I$, and different mixtures of these ILs, recorded at $T = 298$ K. The relative increases in C_{alkyl} intensity with change of emission angle from 0° to 80° are given by the blue numbers. Adapted from [P3] under license CC BY 4.0.

The C 1s spectrum at 80° for pure $[C_8C_1Im][PF_6]$ shows a lower intensity of the C_2/C_{hetero} peaks, but a significantly higher intensity of the C_{alkyl} peak compared to 0°. This indicates an orientation of the alkyl chains of the cation towards the vacuum, while the C_2/C_{hetero} atoms are oriented towards the bulk,^[P3] as observed for many $[C_8C_1Im]^+$ cation

ILs.^[127] For the mixtures, this behavior is also present, but the C_{alkyl} enrichment at the surface is stronger for a lower $[\text{C}_8\text{C}_1\text{Im}][\text{PF}_6]$ content and at the same time, the C_2 and C_{hetero} depletion is less pronounced (see factors shown in blue in Figure 14). This is attributed to a different degree of enrichment and depletion of the C_{alkyl} and PEG-chains in the different mixtures (for the C_2 and C_{hetero} signals, again consider the contribution of the different cations; the C_{alkyl} signal originates exclusively from the $[\text{C}_8\text{C}_1\text{Im}]^+$ cation).^[P3]

Temperature-dependent measurements to study surface enrichment and depletion as well as orientation effects of the pure ILs and mixtures were performed from 363 K down to 238 / 233 K. Figure 15 shows the quantitative analysis of the C_{alkyl} and O_{PEG} data. The $n(80^\circ)/n_{\text{nominal}}$ ratio for C_{alkyl} of the pure $[\text{C}_8\text{C}_1\text{Im}][\text{PF}_6]$ (black squares) shows a weak decrease from 1.48 at 223 K to 1.32 at 363 K. This is attributed to the more randomly oriented $[\text{C}_8\text{C}_1\text{Im}]^+$ cations at the surface at higher temperature. In contrast, the mixtures display a very pronounced decrease in the $n(80^\circ)/n_{\text{nominal}}$ ratio for C_{alkyl} with increasing temperatures. This is explained by the loss of selective surface enrichment of the alkyl chains relative to the PEG-chains (see discussion below), which is a loss in preferential segregation of the $[\text{C}_8\text{C}_1\text{Im}]^+$ cations at increased temperatures. The ratio change with temperature is most pronounced for the 4.5 mol% mixture, where the $n(80^\circ)/n_{\text{nominal}}$ ratio for C_{alkyl} decreases from around 10 down to 2.7 in the temperature range of 238 K up to 363 K.^[P3]

In case of pure $[(\text{mPEG}_2)_2\text{Im}]\text{I}$, the normalized O_{PEG} content (grey squares) at the surface measured in 80° shows a very weak decrease from 1.17 to 1.15 with increasing temperature (see Figure 15).^[P3]

The mixtures, however, exhibit a clearly continuous increase of the O content at the surface with increasing temperature. The 4.5 mol% $[\text{C}_8\text{C}_1\text{Im}][\text{PF}_6]$ mixture e.g. increases from 0.86 K to 1.09 K in the temperature range from 238 K up to 363 K. This behavior reflects the increasing PEG-chain contribution at the surface, which goes along with the loss in alkyl chain signal (described above).^[P3] As previously discussed for pure ILs and IL mixtures,^[18,39] the generally observed loss in alkyl chain enrichment in ARXPS with increasing temperature is attributed to the loss in surface order as an entropic effect.^[P3]

All other core level intensities of the anions and the imidazolium head groups show small changes with temperature (see [P3]), which is to be expected because they are preferentially depleted from the outer surface.^[P3]

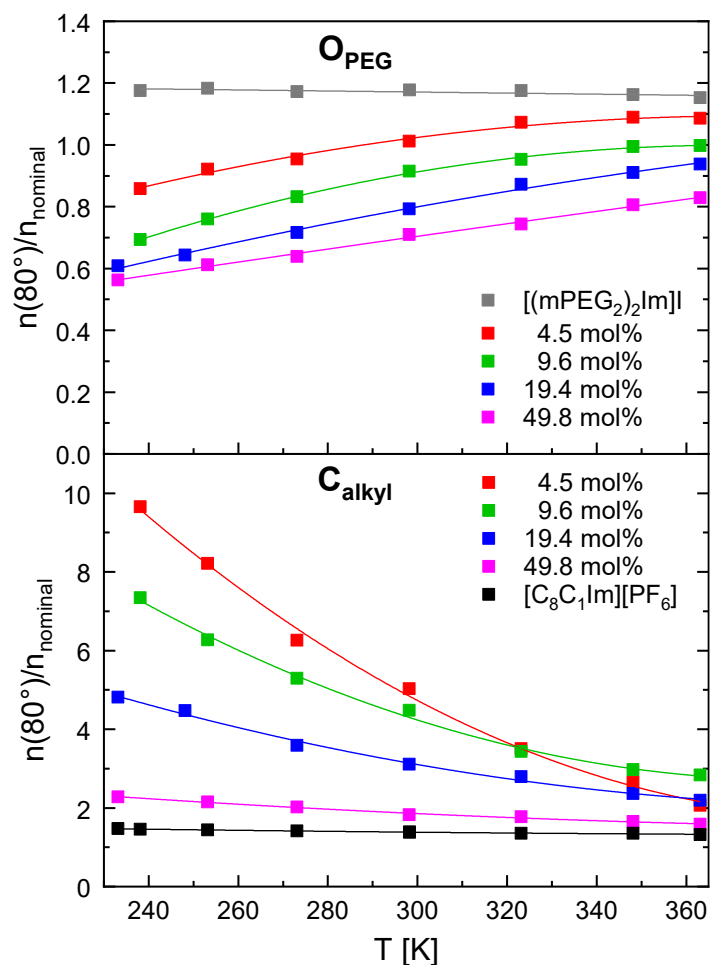


Figure 15: O_{PEG} (top) and C_{alkyl} (bottom) normalized content $n(80^\circ)/n_{nominal}$, derived from the corresponding 80° intensities and their nominal atomic numbers of O_{PEG} and C_{alkyl} for the pure ILs and mixtures at different temperatures. Adapted from [P3] under license CC BY 4.0.

4.4. CORRELATION OF SURFACE COMPOSITION AND SURFACE TENSION OF IONIC LIQUID SYSTEMS^[P3]

While macroscopically the ST is the observable change in free energy per unit area, at the microscopic level the ST arises from the fact that molecules in the bulk and at the surface, i.e., at the boundary to vacuum (or a gas phase), have very different local environments and thus different interactions. As already shown, one can predict the correct surface tension trend along the n -alkyl imidazolium ILs with increasing chain length n by combining structural data from ARXPS experiments with MD simulations.^[22] In addition, our group already reported on mixtures of ILs with common $[PF_6]^-$ anion and imidazolium cations

carrying either short butyl or partially fluorinated butyl chains^[18,128] by combining conventional ST measurements (PD under 1 bar argon) and ARXPS experiments. A similar approach was successfully employed by the McKendrick group.^[20,21] They used reactive atom scattering with laser-induced fluorescence (RAS-LIF) in combination with MD and ST measurements to study mixtures of ILs with different alkyl chain lengths in the cation and also with partially fluorinated chains at room temperature. From the obtained RAS-LIF signals, they were able to derive a quantitative analysis of the alkyl content on the surface, originating mainly from the alkyl residues on the outer surface. From the underrepresentation of the alkyl signals, they indirectly deduced a preferential surface enrichment of the fluorine chains in the mixtures, which allowed then to describe the observed ST values of the mixture using the Langmuir concept, already described in Chapter 1 and briefly explained in Chapter 4.2.^[20,21]

The final part of [P3] addresses the combination of ST measurements performed under ultraclean vacuum conditions (see Chapter 4.2) and ARXPS in ultra-high vacuum (see Subchapter 4.3.2) of [(mPEG₂)₂Im]I, [C₈C₁Im][PF₆] and mixtures of both ILs with 4.5, 9.6, 19.4, and 49.8 mol% [C₈C₁Im][PF₆] content. From the ARXPS signals of the octyl chains, a clear preferential surface enrichment of the [C₈C₁Im]⁺ cations and of the PEG-chains, a simultaneous depletion of the [(mPEG₂)₂Im]⁺ cations in the mixtures can be deduced. As discussed in this Chapter 4.4, this non-stoichiometric surface behavior is also reflected in the measured surface tension values. It will be demonstrated that the simple Langmuir concept links the surface tension and surface composition of IL mixtures in a quantitative way, even for very complex ions.^[P3]

To correlate the surface tension results with the ARXPS data, the ST data at 298 K in Figure 16a are linked to the corresponding atomic O_{PEG} and C_{alkyl} contents in Figure 16b as determined from the 80° ARXP spectra. The latter are normalized to the number of corresponding atoms in the ion, i.e., seven C_{alkyl} atoms in [C₈C₁Im][PF₆] and four O_{PEG} atoms in [(mPEG₂)₂Im]I. In Figure 16b, the C_{alkyl} signal (gray circles) represents the surface concentration of the alkyl-chains of the [C₈C₁Im]⁺ cation and the O_{PEG} signal (red circles) represents the surface concentration of the PEG-chains of the [(mPEG₂)₂Im]⁺ cation. Ideally, a linear concentration dependence is expected (gray and red solid lines for C_{alkyl} and O_{PEG}, respectively). However, a significant deviation is evident, as the measured C_{alkyl} data are above the gray ideal line and the O_{PEG} data are well below the ideal line. This

reflects the above-mentioned preferential enrichment of the alkyl-chains and depletion of the PEG-chains in the mixtures at the surface. An ideal behavior of the ST would correspond to a linear decrease with increasing $[\text{C}_8\text{C}_1\text{Im}][\text{PF}_6]$ content (black solid line in Figure 16a). The fact that the ST values of all mixtures fall below the ideal line with a much stronger decrease in the ideal behavior at low $[\text{C}_8\text{C}_1\text{Im}][\text{PF}_6]$ contents, is attributed to the strong preferential enrichment and depletion effects that occur at the liquid-vacuum interface, which were derived from the $[\text{C}_8\text{C}_1\text{Im}]^+$ - and $[(\text{mPEG}_2)_2]^+$ -chain signals in ARXPS (see Subsection 4.3.2).^[P3]

Next, we apply the Langmuir principle approach for pure ILs^[22] to the binary IL mixtures studied in this thesis. For this purpose, the groups of $[(\text{mPEG}_2)_2\text{Im}]\text{I}$ (O_{PEG}) and $[\text{C}_8\text{C}_1\text{Im}][\text{PF}_6]$ (C_{alkyl}) measured in 80° ARXPS, which are predominantly present on the outer surface (see Subchapter 4.3.2), and thus mainly contribute to the ST of the pure ILs, are used to represent the effective surface mole fractions of the corresponding IL in the mixture. Instead of the ideal mixing behavior of Equation 9, the surface tension of a mixture with a certain bulk composition x at temperature T is estimated from $n_{\text{OPEG},80^\circ}(x)$ and $n_{\text{Calkyl},80^\circ}(x)$, that is, the number of O_{PEG} and C_{alkyl} atoms, respectively, as derived from the temperature-dependent 80° ARXP spectra:^[P3]

$$\gamma_{T,\text{ARXPS } 80^\circ}(x) = \frac{\gamma_{T,[(\text{mPEG}_2)_2\text{Im}]\text{I}} \cdot \frac{n_{\text{OPEG},80^\circ}(x)}{4} + \gamma_{T,[\text{C}_8\text{C}_1\text{Im}][\text{PF}_6]} \cdot \frac{n_{\text{Calkyl},80^\circ}(x)}{7}}{\frac{n_{\text{OPEG},80^\circ}(x)}{4} + \frac{n_{\text{Calkyl},80^\circ}(x)}{7}} \quad (10)$$

In this equation, $\gamma_{T,[(\text{mPEG}_2)_2\text{Im}]\text{I}}$ and $\gamma_{T,[\text{C}_8\text{C}_1\text{Im}][\text{PF}_6]}$ are the temperature-dependent surface tension values of pure $[(\text{mPEG}_2)_2\text{Im}]\text{I}$ and $[\text{C}_8\text{C}_1\text{Im}][\text{PF}_6]$, respectively.

Figure 17 shows the ST values of the mixtures derived from the 80° ARXPS using Equation 10 for selected temperatures (circles for 298, 323, 348, 363 K). The extremely good agreement between calculated and measured ST of the mixtures is about 1% deviation with a maximum deviation of 1.7% for one data point. This indicates that the ARXPS 80° geometry (signals are integrated over the topmost one nm) appears to be sensitive enough to detect the deviations of the surface mole fraction from the bulk composition.^[P2]

Compared to the RAS-LIF method (see top section),^[20,21] in the ARXPS method, all elements can be analyzed, and so in our case the enrichment of the alkyl chains and the de-

pletion of the PEG-chains were studied. In addition, we were able to perform surface composition and surface tension studies over a wide temperature range and under well-defined vacuum conditions, which allowed for the acquisition of very reliable data sets.^[P3]

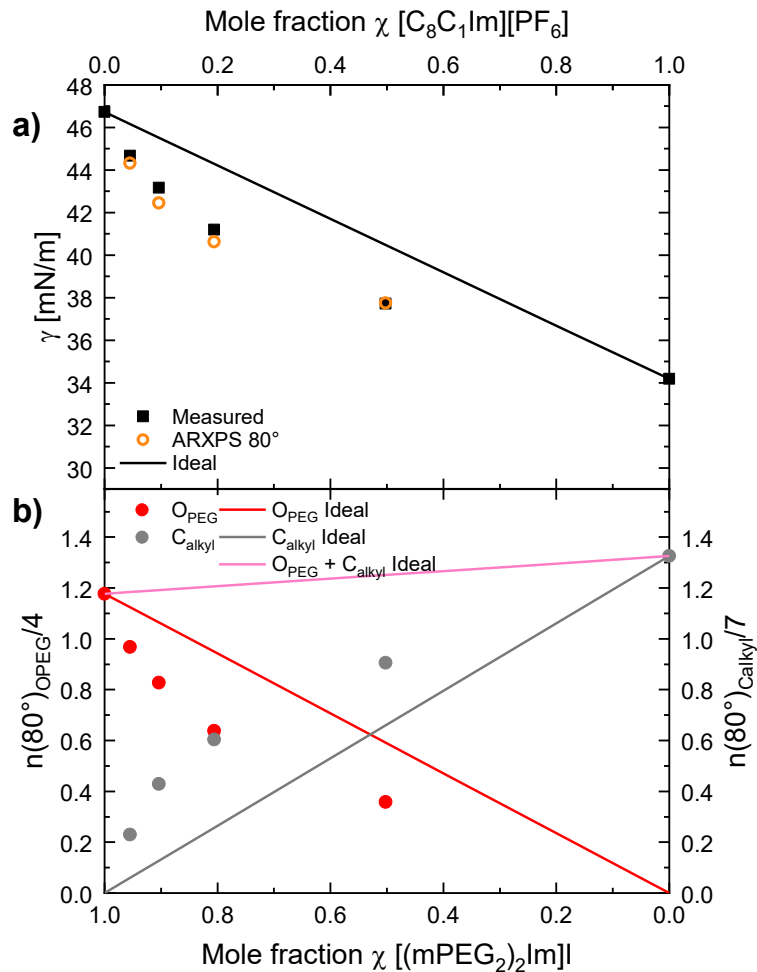


Figure 16: a) Surface tension values of the pure ILs and their mixtures at 298 K (black squares), determined from PD measurements in Chapter 4.2.3 (Figure 11), combined with the surface tension values calculated from the 80° ARXPS data according to Equation 10 (open orange circles) as a function of the bulk mole fraction. The surface tension of ideal mixtures without enrichment/depletion effects is shown as a black line for comparison. b) Number of atoms, $n(80^\circ)$, determined from ARXPS data at 80° normalized to the number of corresponding atoms in the IL for O_{PEG} (red circles) and for C_{alkyl} (gray circles) for the pure IL and for the mixtures at 298 K as a function of the bulk mole fraction. The ideal behavior, i.e., the expected changes without the presence of surface enrichment/depletion effects is shown by the straight lines. Adapted from [P3] under license CC BY 4.0.

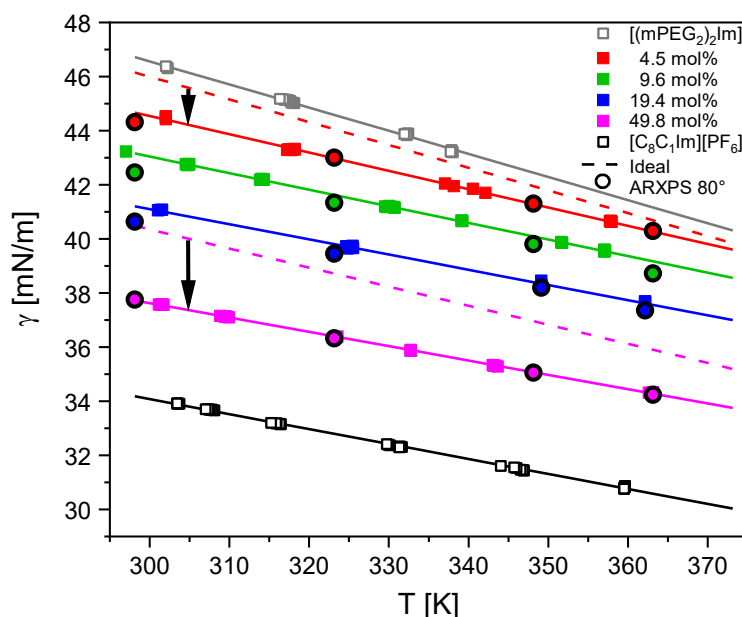


Figure 17: Surface tension values measured by the PD method (open and full squares), their linear fits (lines) using Equation 8, and the ST values calculated from the 80° ARXPS data (filled circles) using Equation 10 are shown. For comparison, the ideal behavior for the ST of the 4.5 and 49.8 mol% mixtures is plotted according to Equation 9 (dotted lines; a comparison for all mixtures is shown in Figure 12 in Subchapter 4.2.3). Adapted from [P3] under license CC BY 4.0.

4.5. COMPOSITION OF BNCs OF [C₂C₁Im][BIM₄]^[P4]

In [P4], B- and N-doped carbon (BNC) materials with [C₂C₁Im][BIM₄] as a precursor were characterized with different techniques, e.g. elemental analysis, inductively coupled plasma atomic emission spectroscopy (ICP-OES), gas sorption, infrared (IR) spectroscopy, Raman spectroscopy, XPS, X-ray diffraction (XRD) and microscopy. After the material characterization, the materials were tested in the adsorptive removal of pollutant methylene blue (MB). In this chapter, the XPS studies are discussed in detail and only the 0° emission spectra for BNC-800, BNC-900 and BNC-1000 are shown here, where the number corresponds to the pyrolysis temperature. For further characterization and studies on the catalytic activity of the BNCs performed by the co-authors, see [P4].

The composition and bonding configuration of BNC investigations by XPS at 0° (see Figure 18) show essentially the same bonding situation as Fourier-transform infrared spectroscopy (FTIR), according to literature binding energy values.^[129] Species associated with B-N (B 1s at 191.2 eV, N 1s at 398.7 eV), C-N (C 1s at 286.6 eV, N 1s at 400.8 eV), and C-C bonds (C 1s at 284.7 eV) are present and confirm the results from the

complementary FTIR spectra. Both XPS and FTIR also reveal that the BNC materials consist of carbon domains with boron and nitrogen incorporations. The absence of characteristic signals in C 1s (expected at 284.1 eV) and B 1s (expected at 190.4 eV) allows us to exclude C-B bonds. However, a very small amount of oxidized boron is also visible in the B 1s region at higher BEs (192.6 eV) for all three BNC materials. Boron-oxygen bonds are attributed to the oxophilic nature of unsaturated boron in defects and have also been observed in other BNC materials prepared via pyrolysis.^[130]

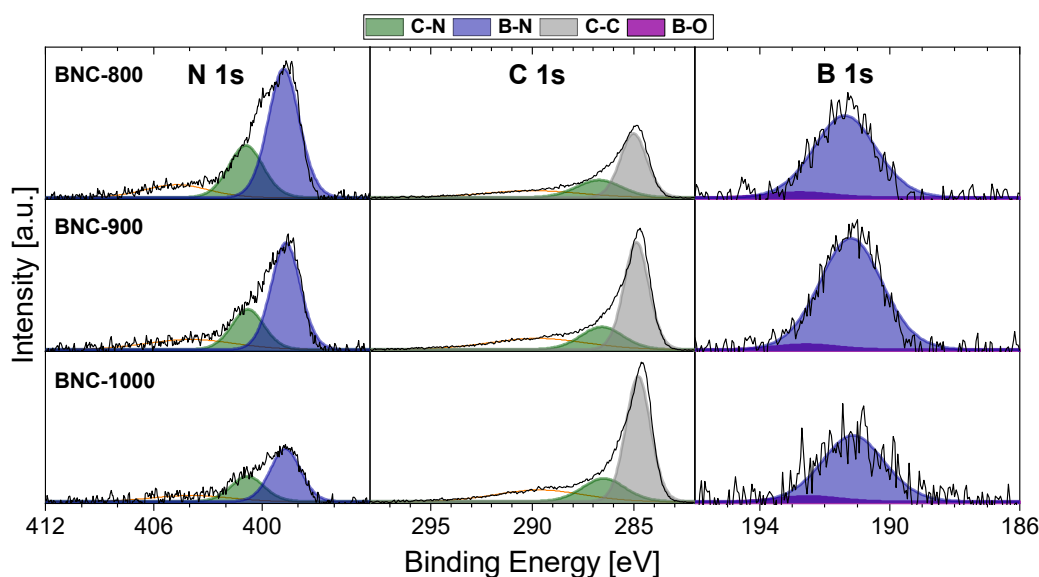


Figure 18: XP spectra of N 1s, C 1s and O 1s of BNC-800 (first row), BNC-900 (second row), and BNC-1000 (third row). Intensity scales within one column are equal. Green, blue and grey are the signals related to C-N, B-N and C-C. A small B-O contribution is marked in magenta. The broad peaks (orange) at higher BE in the N 1s and C 1s region are due to satellite features of N and C atoms in an aromatic configuration. Reproduced from [P4] under license CC BY 4.0.

In Figure 18, all N 1s and C 1s spectra of the samples studied here show a broad peak shifted to higher BE (orange peaks), which can be attributed to satellites of aromatically bound carbon and nitrogen. In comparison to the overall bulk composition as given by elemental analysis, the composition derived from the more surface sensitive XPS analysis (sum of all species within one region) reveals a quite good agreement of the relative C-N-B content for BNC-800 and BNC-1000; only BNC-900 shows a boron content slightly too high. Considering the B : N ratio of the B-N-related XP signals (blue peaks in Figure 18) and the absence of B bound to C, we assume that in BNC-800, mainly BN_3 sites and the N at C-N sites (green peaks) are incorporated into the carbon domains. While the boron content remains more or less constant at 900 °C, the nitrogen starts to burn mainly at C-N

sites and converts C-N carbon into C-C carbon, as can be seen from the increase in the C-C peaks (grey peaks in Figure 18). Compared to 900 °C, the pyrolysis done at 1000 °C releases even more nitrogen and also boron as it is evident from the pronounced decrease in N 1s and B 1s intensities, which is associated with the increased conversion to C-C carbon. The lower B : N \approx 1 : 2 ratio of the B-N signals in BNC-1000 as compared to B : N \approx 1 : 3 in BNC-800 (attributed to BN₃) is also an indication that preferentially boron nitride configurations are formed in the near-surface region at 1000 °C.^[P4]

5. SUMMARY

5.1. ENGLISH VERSION

The focus of this thesis is to gain a deeper understanding in surfaces of pure and mixed ionic liquid (IL) systems. The concept of mixing two (or even more) pure ILs provides an elegant and simple way for preparing new, fine-tuned and well-adapted IL materials for dedicated applications. In particular at surfaces and interfaces, however, the related properties often deviate from simple mixing rules due to non-ideal behavior. Hence, surfaces of pure ionic liquids and of IL mixtures were investigated using angle-resolved X-ray photoelectron spectroscopy (ARXPS) and pendant drop (PD) measurements to access information on surface composition and surface tension, respectively. The ARXPS experiments are performed in ultra-high vacuum (UHV) and provide information from the first 7 to 9 nm in 0° emission, and down to the topmost 1 to 1.5 nm in 80° emission. Preferential enrichment and depletion of ions at the surface as well as molecular orientation in the outermost surface layer are directly reflected by intensity changes of IL-derived signals with emission angle. PD measurements are performed in high vacuum (HV) providing intrinsic surface tension values without the risk of surface-active contaminants or an influence of a gas atmosphere.

Since PD measurements in vacuum were not available at the beginning of this dissertation, the first main part of this thesis is therefore the development, description and calibration of a new high vacuum pendant drop/sessile drop setup, where measurements can be performed in the pressure range from 10^{-7} mbar up to 1 bar. Control measurements are performed with Millipore water and benzene. Particularly, the surface tension (ST) values of Millipore water investigated in our new chamber compared to literature values are in extremely good agreement with deviations smaller than 0.1%.^[P2]

Next, first measurements of pure ILs and mixtures at different pressures and degassing conditions are investigated, as these provide information about the influence of these variables on ST with very high accuracy. The STs of $[C_8C_1Im][PF_6]$ in vacuum, degassed and non-degassed are studied. Compared to the vacuum measurements of the degassed IL, we observed a significant decrease in surface tension when measured in air. This decrease is attributed to the uptake of water from the surrounding atmosphere.^[P2]

Temperature-dependent surface tension values under HV of $[m(\text{PEG}_n)_2\text{Im}]^+\text{I}^-$ ILs with different polyethylene glycol (PEG)-chain lengths ($n = 2, 4, 6$) are presented next,^[P2] showing very good agreement with previously published data of these ILs measured under 1 bar Ar^[P1] in a completely different setup. The reported decrease in surface tension with increasing chain length is confirmed by our vacuum data and is attributed to an increasing enrichment of the PEG-chains at the surface; this chain enrichment is directly observed in ARXPS at 298 K. A consequence of the PEG-chain enrichment is the surface depletion of the imidazole ring of the cation as deduced from the N 1s signal and of the anion as deduced from the I 3d_{5/2} signal. The strong damping effect for the I 3d_{5/2} and N 1s signals at 80° is already observed for the shortest PEG-chain ($n = 2$), and is even more pronounced for the longer chains ($n = 4$ and 6). This indicates that both chains of a single cation are indeed preferentially oriented toward the vacuum side. Our ARXPS results confirm MD simulations, which also show that a significant part of cations in the surface layer are oriented such that both chains are oriented towards vacuum.^[P1]

For the IL mixture experiments, we selected $[m(\text{PEG}_2)_2\text{Im}]^+\text{I}^-$ and $[\text{C}_8\text{C}_1\text{Im}]^+[\text{PF}_6]^-$ due to their very different ST values of 46.72 mN/m and 34.18 mN/m, respectively. The values for the mixtures are found to lay in-between those of the pure ILs but strongly deviate from simple ideal mixing rules. In particular, the experimentally ST values of the mixtures are systematically shifted towards the values of $[\text{C}_8\text{C}_1\text{Im}]^+[\text{PF}_6]^-$, which indicates a stronger enrichment of alkyl groups at the surface, again confirmed by our ARXPS results. The latter show a strong selective enrichment of the alkyl-chains of the $[\text{C}_8\text{C}_1\text{Im}]^+$ cation and a simultaneous depletion of PEG-chains of the $[m(\text{PEG}_2)_2\text{Im}]^+$ cation for all mixtures, which is most pronounced at the lowest $[\text{C}_8\text{C}_1\text{Im}]^+[\text{PF}_6]^-$ content. We then apply a simple Langmuir approach based on the ARXPS-derived surface composition, which allows us to predict and to reproduce the experimentally measured ST with a very high accuracy. On the one hand, this approach provides a microscopic basis for the macroscopic surface tension by the information obtained from ARXPS, and on the other hand, information about surface enrichment effects in mixtures can now be derived from the deviation of the ST data obtained by the PD method from the ideal behavior.^[P3]

In the last part of this thesis, the XPS characterization of B- and N-doped carbon materials (BNC) obtained by pyrolysis at 800, 900 and 1000 °C of $[\text{C}_2\text{C}_1\text{Im}]^+[\text{BIm}_4]^-$ as pre-

cursor are discussed. The focus of this study is on the composition and bonding configuration of the BNCs. The XPS results show that the BNC materials consist of carbon domains with boron and nitrogen inclusions^[P4] and confirm the results shown in previous Fourier-transform infrared spectroscopy (FTIR) studies.^[129] In addition, a conversion of C-N bonds to C-C carbons with increasing pyrolysis temperature is directly reflected in the corresponding XP spectra in the N 1s and C 1s regions.^[P4]

5.2. GERMAN VERSION (DEUTSCHE ZUSAMMENFASSUNG)

Ein Schwerpunkt dieser Arbeit ist es, ein tieferes Verständnis der Oberflächen von ionischen Flüssigkeiten (IL) und von IL-Mischungen zu erlangen. Das Konzept des Mischens zweier (oder sogar mehrerer) reiner ILs bietet eine elegante und einfache Möglichkeit zur Herstellung neuer, fein abgestimmter und gut angepasster IL-Materialien für spezielle Anwendungen. Insbesondere an Oberflächen und Grenzflächen weichen die damit verbundenen Eigenschaften jedoch häufig von den einfachen Mischungsregeln ab, da sie sich nicht ideal verhalten. Daher wurden Oberflächen von reinen ionischen Flüssigkeiten und von IL-Mischungen mittels winkelaufgelöster Röntgenphotoelektronenspektroskopie (ARXPS) und Pendant Drop-Messungen (PD) untersucht, um Informationen über die Oberflächenzusammensetzung bzw. die Oberflächenspannung zu erhalten. Die im Ultrahochvakuum (UHV) durchgeführten ARXPS-Experimente liefern Informationen über die ersten 7 bis 9 nm bei 0°-Emission und über die obersten 1 bis 1,5 nm bei 80°-Emission. Die bevorzugte An- und Abreicherung von Ionen an der Oberfläche sowie die molekulare Orientierung in der äußersten Oberflächenschicht spiegeln sich direkt in den Intensitätsänderungen der IL-Gruppensignale mit dem Emissionswinkel wider. Die PD-Messungen wurden im Hochvakuum (HV) durchgeführt. Sie liefern intrinsische Oberflächenspannungswerte ohne das Risiko oberflächenaktiver Verunreinigungen oder des Einflusses einer Gasatmosphäre.

Da PD-Messungen unter Vakuumbedingungen zu Beginn dieser Dissertation noch nicht zur Verfügung standen, besteht der erste Hauptteil dieser Arbeit in der Entwicklung, Beschreibung und Kalibrierung eines neuen Hochvakuum-Pendant-Drop/Sessile-Drop-Aufbaus, mit dem Messungen im Druckbereich von 10^{-7} mbar bis 1 bar durchgeführt wer-

den können. Es werden Kontrollmessungen mit Millipore-Wasser und Benzol gezeigt. Insbesondere die Oberflächenspannungswerte (ST) von Millipore-Wasser, die in unserer neuen Kammer untersucht wurden, stimmen mit Literaturwerten sehr gut überein, wobei die Abweichungen weniger als 0,1% betragen.^[P2]

Als nächstes wurden erste Oberflächenspannungsmessungen von reinen ILs und von Mischungen bei verschiedenen Drücken und Entgasungsbedingungen durchgeführt, da diese Informationen über den Einfluss dieser Variablen auf die ST mit sehr hoher Genauigkeit liefern. Die ST von $[\text{C}_8\text{C}_1\text{Im}][\text{PF}_6]$ wurde im Vakuum, entgast und nicht entgast an Luft untersucht. Im Vergleich zu den Vakuummessungen an der entgasten IL nimmt die Oberflächenspannung bei der Messung an Luft signifikant ab, was auf die Aufnahme von Wasser aus der umgebenden Atmosphäre zurückgeführt wird.^[P2]

Im Folgenden werden temperaturabhängige Oberflächenspannungswerte unter HV von $[\text{m}(\text{PEG}_n)_2\text{Im}]\text{I}$ ILs mit unterschiedlichen Polyethylenglykol (PEG)-Kettenlängen ($n = 2, 4, 6$) vorgestellt,^[P2] die eine sehr gute Übereinstimmung mit früher veröffentlichten Daten dieser ILs zeigen, die unter 1 bar Ar^[P3] in einem völlig anderen Aufbau gemessen wurden. Die berichtete Abnahme der Oberflächenspannung mit zunehmender Kettenlänge wird durch unsere Vakuumdaten bestätigt und auf eine zunehmende Anreicherung der PEG-Ketten an der Oberfläche zurückgeführt; diese Kettenanreicherung wurde bei ARXPS-Untersuchungen bei 298 K direkt beobachtet. Eine Folge der PEG-Kettenanreicherung ist die Oberflächenabreicherung des Imidazolrings des Kations im N 1s-Signal und des Anions im I 3d_{5/2}-Signal. Der starke Dämpfungseffekt für die I 3d_{5/2}- und N 1s-Signale bei 80° wird bereits für die kürzeste PEG-Kette ($n = 2$) beobachtet und ist bei den längeren Ketten ($n = 4$ und 6) noch ausgeprägter. Aufgrund der insgesamt starken Dämpfungseffekte sind daher vermutlich beide Ketten eines einzelnen Kations vorzugsweise zur Vakuumseite hin orientiert. Unsere ARXPS-Ergebnisse werden durch MD-Simulationen bestätigt; diese zeigen auch, dass ein erheblicher Teil der Kationen in der Oberflächenschicht so orientiert ist, dass beide Ketten zum Vakuum hin ausgerichtet sind.^[P1]

Für IL-Mischungsexperimente wurden $[\text{m}(\text{PEG}_2)_2\text{Im}]\text{I}$ und $[\text{C}_8\text{C}_1\text{Im}][\text{PF}_6]$ aufgrund ihrer sehr unterschiedlichen ST-Werte von 46,72 bzw. 34,18 mN/m ausgewählt. Die ST-Werte für die Mischungen liegen zwischen denen der reinen ILs, weichen aber stark von idealen Mischungsregeln ab. Insbesondere sind die experimentellen ST-Werte der Mischungen systematisch in Richtung der Werte von $[\text{C}_8\text{C}_1\text{Im}][\text{PF}_6]$ verschoben, was auf eine

stärkere Anreicherung der Oktylketten an der Oberfläche hinweist. Letzteres wird wiederum durch unsere ARXPS-Ergebnisse bestätigt, die eine starke selektive Anreicherung der Alkylketten des $[C_8C_1Im]^+$ -Kations und eine gleichzeitige Verarmung der PEG-Ketten des $[m(PEG_2)_2Im]^+$ -Kations für alle Mischungen zeigen; diese Effekte sind in der Mischung mit dem niedrigsten $[C_8C_1Im][PF_6]$ -Anteil am stärksten ausgeprägt. Mit Hilfe eines einfachen Langmuir-Ansatzes, der auf der von ARXPS abgeleiteten Oberflächenzusammensetzung basiert, können die experimentell gemessenen ST-Werte mit sehr hoher Genauigkeit vorhergesagt und reproduziert werden. Dieser Ansatz liefert zum einen mit den aus ARXPS gewonnenen Informationen eine mikroskopische Erklärung für die makroskopische Oberflächenspannung, zum anderen können nun aus der Abweichung der mit der PD-Methode gewonnenen ST-Daten vom Idealverhalten Informationen über Oberflächenanreicherungseffekte in Gemischen abgeleitet werden.^[P3]

Im letzten Teil dieser Arbeit wird die XPS-Charakterisierung von B- und N-dotierten Kohlenstoffmaterialien (BNC) diskutiert, die durch Pyrolyse bei 800, 900 und 1000 °C von $[C_2C_1Im][BIm_4]$ als Vorprodukt erhalten wurden. Der Schwerpunkt dieser Studie liegt auf der Zusammensetzung und der Bindungskonfiguration der BNCs. Die XPS-Ergebnisse zeigen, dass die BNC-Materialien aus Kohlenstoff-Domänen mit Bor- und Stickstoffein-schlüssen bestehen^[P4] und bestätigen die Ergebnisse früherer Fourier-Transformations-Infrarotspektroskopie (FTIR)-Studien.^[129] Darüber hinaus spiegelt sich in den entsprechenden XP-Spektren in den N 1s- und C 1s-Regionen eine Umwandlung von C-N-Bindungen in C-C-Kohlenstoffe mit steigender Pyrolysetemperatur direkt wider.^[P4]

6. REFERENCES

1. Zhao, D.; Wu, M.; Kou, Y.; Min, E. Ionic liquids: applications in catalysis. *Catalysis Today* **2002**, *74*, 157-189, doi:10.1016/S0920-5861(01)00541-7.
2. Welton, T. Ionic liquids in catalysis. *Coordination Chemistry Reviews* **2004**, *248*, 2459-2477, doi:10.1016/j.ccr.2004.04.015.
3. Plechkova, N.V.; Seddon, K.R. Applications of ionic liquids in the chemical industry. *Chemical Society Reviews* **2008**, *37*, 123-150, doi:10.1039/B006677J.
4. Olivier-Bourbigou, H.; Magna, L.; Morvan, D. Ionic liquids and catalysis: Recent progress from knowledge to applications. *Applied Catalysis A: General* **2010**, *373*, 1-56, doi:10.1016/j.apcata.2009.10.008.
5. MacFarlane, D.R.; Tachikawa, N.; Forsyth, M.; Pringle, J.M.; Howlett, P.C.; Elliott, G.D.; Davis, J.H.; Watanabe, M.; Simon, P.; Angell, C.A. Energy applications of ionic liquids. *Energy & Environmental Science* **2014**, *7*, 232-250, doi:10.1039/C3EE42099J.
6. Steinrück, H.-P.; Wasserscheid, P. Ionic Liquids in Catalysis. *Catalysis Letters* **2015**, *145*, 380-397, doi:10.1007/s10562-014-1435-x.
7. Singh, S.K.; Savoy, A.W. Ionic liquids synthesis and applications: An overview. *Journal of Molecular Liquids* **2020**, *297*, 112038, doi:10.1016/j.molliq.2019.112038.
8. Pádua, A.A.; Costa Gomes, M.F.; Canongia Lopes, J.N. Molecular solutes in ionic liquids: a structural perspective. *Accounts of Chemical Research* **2007**, *40*, 1087-1096.
9. Jiang, W.; Wang, Y.; Yan, T.; Voth, G.A. A multiscale coarse-graining study of the liquid/vacuum interface of room-temperature ionic liquids with alkyl substituents of different lengths. *The Journal of Physical Chemistry C* **2008**, *112*, 1132-1139.
10. Kaur, G.; Kumar, H.; Singla, M. Diverse applications of ionic liquids: A comprehensive review. *Journal of Molecular Liquids* **2022**, *351*, 118556, doi:10.1016/j.molliq.2022.118556.
11. DESIGNER SOLVENTS. *Chemical & Engineering News Archive* **1998**, *76*, 32-37, doi:10.1021/cen-v076n013.p032.
12. Newington, I.; Perez-Arlandis, J.M.; Welton, T. Ionic liquids as designer solvents for nucleophilic aromatic substitutions. *Org Lett* **2007**, *9*, 5247-5250, doi:10.1021/ol702435f.
13. Niedermeyer, H.; Hallett, J.P.; Villar-Garcia, I.J.; Hunt, P.A.; Welton, T. Mixtures of ionic liquids. *Chemical Society Reviews* **2012**, *41*, 7780-7802, doi:10.1039/C2CS35177C.
14. Chatel, G.; Pereira, J.F.B.; Debbeti, V.; Wang, H.; Rogers, R.D. Mixing ionic liquids – “simple mixtures” or “double salts”? *Green Chemistry* **2014**, *16*, 2051-2083, doi:10.1039/C3GC41389F.
15. Clough, M.T.; Crick, C.R.; Gräsvik, J.; Hunt, P.A.; Niedermeyer, H.; Welton, T.; Whitaker, O.P. A physicochemical investigation of ionic liquid mixtures. *Chemical Science* **2015**, *6*, 1101-1114, doi:10.1039/C4SC02931C.
16. Hayes, R.; Warr, G.G.; Atkin, R. Structure and Nanostructure in Ionic Liquids. *Chemical Reviews* **2015**, *115*, 6357-6426, doi:10.1021/cr500411q.
17. Wang, Y.-L.; Li, B.; Sarman, S.; Mocci, F.; Lu, Z.-Y.; Yuan, J.; Laaksonen, A.; Fayer, M.D. Microstructural and Dynamical Heterogeneities in Ionic Liquids. *Chemical Reviews* **2020**, *120*, 5798-5877, doi:10.1021/acs.chemrev.9b00693.
18. Heller, B.S.J.; Lexow, M.; Greco, F.; Shin, S.; Partl, G.; Maier, F.; Steinrück, H.-P. Temperature-Dependent Surface Enrichment Effects in Binary Mixtures of Fluorinated and Non-Fluorinated Ionic Liquids. *Chemistry – A European Journal* **2020**, *26*, 1117-1126, doi:10.1002/chem.201904438.
19. Heller, B.S.J.; Paap, U.; Maier, F.; Steinrück, H.-P. Pronounced surface enrichment of fluorinated ionic liquids in binary mixtures with methoxy-functionalized ionic liquids. *Journal of Molecular Liquids* **2020**, *305*, 112783, doi:10.1016/j.molliq.2020.112783.
20. Smoll, E.J.; Tesa-Serrate, M.A.; Purcell, S.M.; D’Andrea, L.; Bruce, D.W.; Slattery, J.M.; Costen, M.L.; Minton, T.K.; McKendrick, K.G. Determining the composition of the vacuum-liquid interface in ionic-liquid mixtures. *Faraday Discussions* **2018**, *206*, 497-522, doi:10.1039/C7FD00175D.
21. Purcell, S.M.; Lane, P.D.; D’Andrea, L.; Elstone, N.S.; Bruce, D.W.; Slattery, J.M.; Smoll, E.J.; Greaves, S.J.; Costen, M.L.; Minton, T.K.; et al. Surface Structure of Alkyl/Fluoroalkylimidazolium Ionic-Liquid Mixtures. *The Journal of Physical Chemistry B* **2022**, *126*, 1962-1979, doi:10.1021/acs.jpcc.1c10460.
22. Shimizu, K.; Heller, B.S.J.; Maier, F.; Steinrück, H.-P.; Lopes, J.N.C. Probing the Surface Tension of Ionic Liquids Using the Langmuir Principle. *Langmuir* **2018**, *34*, 4408-4416, doi:10.1021/acs.langmuir.7b04237.

23. Hardy, W.B. The tension of composite fluid surfaces and the mechanical stability of films of fluid. *Proceedings of the Royal Society of London. Series A, Containing Papers of a Mathematical and Physical Character* **1912**, *86*, 610-635.
24. Langmuir, I. The constitution and fundamental properties of solids and liquids. Part I. Solids. *Journal of the American chemical society* **1916**, *38*, 2221-2295.
25. Langmuir, I. The constitution and fundamental properties of solids and liquids. II. Liquids. *Journal of the American chemical society* **1917**, *39*, 1848-1906.
26. Langmuir, I. Forces Near the Surfaces of Molecules. *Chemical Reviews* **1930**, *6*, 451-479, doi:10.1021/cr60024a002.
27. Langmuir, I. Nobel Lecture. Available online: NobelPrize.org, <https://www.nobelprize.org/prizes/chemistry/1932/langmuir/lecture/> (accessed on 20.10.2022).
28. Steinrück, H.-P.; Libuda, J.; Wasserscheid, P.; Cremer, T.; Kolbeck, C.; Laurin, M.; Maier, F.; Sobota, M.; Schulz, P.S.; Stark, M. Surface Science and Model Catalysis with Ionic Liquid-Modified Materials. *Advanced Materials* **2011**, *23*, 2571-2587, doi:10.1002/adma.201100211.
29. Hashimoto, H.; Ohno, A.; Nakajima, K.; Suzuki, M.; Tsuji, H.; Kimura, K. Surface characterization of imidazolium ionic liquids by high-resolution Rutherford backscattering spectroscopy and X-ray photoelectron spectroscopy. *Surface Science* **2010**, *604*, 464-469, doi:10.1016/j.susc.2009.12.023.
30. Smith, E.F.; Rutten, F.J.M.; Villar-Garcia, I.J.; Briggs, D.; Licence, P. Ionic Liquids in Vacuo: Analysis of Liquid Surfaces Using Ultra-High-Vacuum Techniques. *Langmuir* **2006**, *22*, 9386-9392, doi:10.1021/la061248q.
31. Santos, C.S.; Baldelli, S. Gas-liquid interface of room-temperature ionic liquids. *Chemical Society Reviews* **2010**, *39*, 2136-2145.
32. Iwahashi, T.; Nishi, T.; Yamane, H.; Miyamae, T.; Kanai, K.; Seki, K.; Kim, D.; Ouchi, Y. Surface Structural Study on Ionic Liquids Using Metastable Atom Electron Spectroscopy. *The Journal of Physical Chemistry C* **2009**, *113*, 19237-19243, doi:10.1021/jp9056797.
33. Lovelock, K.R.J.; Villar-Garcia, I.J.; Maier, F.; Steinrück, H.-P.; Licence, P. Photoelectron Spectroscopy of Ionic Liquid-Based Interfaces. *Chemical Reviews* **2010**, *110*, 5158-5190, doi:10.1021/cr100114t.
34. Chen, L.G.; Lerum, R.V.; Aranda-Espinoza, H.; Bermudez, H. Surfactant-Mediated Ion Exchange and Charge Reversal at Ionic Liquid Interfaces. *The Journal of Physical Chemistry B* **2010**, *114*, 11502-11508, doi:10.1021/jp106582t.
35. Steinrück, H.-P. Recent developments in the study of ionic liquid interfaces using X-ray photoelectron spectroscopy and potential future directions. *Physical Chemistry Chemical Physics* **2012**, *14*, 5010-5029, doi:10.1039/C2CP24087D.
36. Villar-Garcia, I.J.; Fearn, S.; De Gregorio, G.F.; Ismail, N.L.; Gschwend, F.J.V.; McIntosh, A.J.S.; Lovelock, K.R.J. The ionic liquid-vacuum outer atomic surface: a low-energy ion scattering study. *Chemical Science* **2014**, *5*, 4404-4418, doi:10.1039/C4SC00640B.
37. Lexow, M.; Maier, F.; Steinrück, H.-P. Ultrathin ionic liquid films on metal surfaces: adsorption, growth, stability and exchange phenomena. *Advances in Physics: X* **2020**, *5*, 1761266, doi:10.1080/23746149.2020.1761266.
38. Nakajima, K.; Lísal, M.; Kimura, K. Surfaces of Ionic Liquids. 2020; pp. 351-389.
39. Kolbeck, C.; Deyko, A.; Matsuda, T.; Kohler, F.T.U.; Wasserscheid, P.; Maier, F.; Steinrück, H.-P. Temperature-Dependent Surface-Enrichment Effects of Imidazolium-Based Ionic Liquids. *ChemPhysChem* **2013**, *14*, 3726-3730, doi:10.1002/cphc.201300719.
40. Souda, R. Surface segregation in binary mixtures of imidazolium-based ionic liquids. *Surface Science* **2010**, *604*, 1694-1697, doi:10.1016/j.susc.2010.06.016.
41. Nakajima, K.; Miyashita, M.; Suzuki, M.; Kimura, K. Surface structures of binary mixtures of imidazolium-based ionic liquids using high-resolution Rutherford backscattering spectroscopy and time of flight secondary ion mass spectroscopy. *The Journal of Chemical Physics* **2013**, *139*, 224701, doi:10.1063/1.4838376.
42. Nakajima, K.; Nakanishi, S.; Lísal, M.; Kimura, K. Surface structures of binary mixture of ionic liquids. *Journal of Molecular Liquids* **2017**, *230*, 542-549.
43. Oz, E.; Sahin, O.; Okur, H.I.; Suzer, S. Surface Propensity of Anions in a Binary Ionic-Liquid Mixture Assessed by Full-Range Angle-Resolved X-ray Photoelectron Spectroscopy and Surface-Tension Measurements. *ChemPhysChem* **2020**, *21*, 2397-2401, doi:10.1002/cphc.202000750.
44. Freire, M.G.; Carvalho, P.J.; Fernandes, A.M.; Marrucho, I.M.; Queimada, A.J.; Coutinho, J.A.P. Surface tensions of imidazolium based ionic liquids: Anion, cation, temperature and water effect. *Journal of Colloid and Interface Science* **2007**, *314*, 621-630, doi:10.1016/j.jcis.2007.06.003.
45. Gardas, R.L.; Coutinho, J.A.P. Applying a QSPR correlation to the prediction of surface tensions of ionic liquids. *Fluid Phase Equilibria* **2008**, *265*, 57-65, doi:10.1016/j.fluid.2008.01.002.

46. Tariq, M.; Freire, M.G.; Saramago, B.; Coutinho, J.A.; Lopes, J.N.C.; Rebelo, L.P.N. Surface tension of ionic liquids and ionic liquid solutions. *Chemical Society Reviews* **2012**, *41*, 829-868.
47. Luís, A.; Shimizu, K.; Araújo, J.M.M.; Carvalho, P.J.; Lopes-da-Silva, J.A.; Canongia Lopes, J.N.; Rebelo, L.P.N.; Coutinho, J.A.P.; Freire, M.G.; Pereira, A.B. Influence of Nanosegregation on the Surface Tension of Fluorinated Ionic Liquids. *Langmuir* **2016**, *32*, 6130-6139, doi:10.1021/acs.langmuir.6b00209.
48. Massoudi, R.; King, A.D. Effect of pressure on the surface tension of water. Adsorption of low molecular weight gases on water at 25.deg. *The Journal of Physical Chemistry* **1974**, *78*, 2262-2266, doi:10.1021/j100615a017.
49. Sachs, W.; Meyn, V. Pressure and temperature dependence of the surface tension in the system natural gas/water principles of investigation and the first precise experimental data for pure methane/water at 25°C up to 46.8 MPa. *Colloids and Surfaces A: Physicochemical and Engineering Aspects* **1995**, *94*, 291-301, doi:10.1016/0927-7757(94)03008-1.
50. Goodman, D.W. Model studies in catalysis using surface science probes. *Chemical Reviews* **1995**, *95*, 523-536.
51. Niedermaier, I.; Kolbeck, C.; Steinrück, H.-P.; Maier, F. Dual analyzer system for surface analysis dedicated for angle-resolved photoelectron spectroscopy at liquid surfaces and interfaces *Review of Scientific Instruments* **2016**, *87*, doi:10.1063/1.4942943.
52. Titirici, M.-M.; White, R.J.; Brun, N.; Budarin, V.L.; Su, D.S.; del Monte, F.; Clark, J.H.; MacLachlan, M.J. Sustainable carbon materials. *Chemical Society Reviews* **2015**, *44*, 250-290, doi:10.1039/C4CS00232F.
53. Su, D.S.; Perathoner, S.; Centi, G. Nanocarbons for the Development of Advanced Catalysts. *Chemical Reviews* **2013**, *113*, 5782-5816, doi:10.1021/cr300367d.
54. Zhao, S.; Wang, D.-W.; Amal, R.; Dai, L. Carbon-Based Metal-Free Catalysts for Key Reactions Involved in Energy Conversion and Storage. *Advanced Materials* **2019**, *31*, 1801526, doi:10.1002/adma.201801526.
55. Liang, C.; Li, Z.; Dai, S. Mesoporous Carbon Materials: Synthesis and Modification. *Angewandte Chemie International Edition* **2008**, *47*, 3696-3717, doi:10.1002/anie.200702046.
56. Jariwala, D.; Sangwan, V.K.; Lauhon, L.J.; Marks, T.J.; Hersam, M.C. Carbon nanomaterials for electronics, optoelectronics, photovoltaics, and sensing. *Chemical Society Reviews* **2013**, *42*, 2824-2860, doi:10.1039/c2cs35335k.
57. Paraknowitsch, J.P.; Thomas, A.; Schmidt, J. Microporous sulfur-doped carbon from thienyl-based polymer network precursors. *Chemical Communications* **2011**, *47*, 8283-8285, doi:10.1039/C1CC12272J.
58. Zhang, S.; Dokko, K.; Watanabe, M. Carbon materialization of ionic liquids: from solvents to materials. *Materials Horizons* **2015**, *2*, 168-197, doi:10.1039/C4MH00141A.
59. Evans, D.F.; Wennerström, H. *The colloidal domain: where physics, chemistry, biology, and technology meet*; Wiley-VCH, USA: 1999; Volume 2.
60. Erbil, H.Y. *Surface Chemistry*; Blackwell Publishing Ltd: 2006; Volume 1.
61. Robert J. Good, R.R.S. *Surface and Colloid Science*; Plenum Press, New York: 1979; Volume 11.
62. Paul C. Hiemenz; Rajagopalan, R. *Principle of Colloid and Surface Chemistry*; CRC Press: 1997; Volume 3.
63. Hoorfar, M.; Kurz, M.A.; Neumann, A.W. Evaluation of the surface tension measurement of axisymmetric drop shape analysis (ADSA) using a shape parameter. *Colloids and Surfaces A: Physicochemical and Engineering Aspects* **2005**, *260*, 277-285, doi:10.1016/j.colsurfa.2004.08.080.
64. Ferrera, C.; Montanero, J.M.; Cabezas, M.G. An analysis of the sensitivity of pendant drops and liquid bridges to measure the interfacial tension. *Measurement Science and Technology* **2007**, *18*, 3713-3723.
65. Saad, S.M.; Policova, Z.; Acosta, E.J.; Neumann, A.W. Range of validity of drop shape techniques for surface tension measurement. *Langmuir* **2010**, *26*, 14004-14013, doi:10.1021/la1020675.
66. Berry, J.D.; Neeson, M.J.; Dagastine, R.R.; Chan, D.Y.C.; Tabor, R.F. Measurement of surface and interfacial tension using pendant drop tensiometry. *Journal of Colloid and Interface Science* **2015**, *454*, 226-237, doi:10.1016/j.jcis.2015.05.012.
67. Young, T. III. An essay on the cohesion of fluids. *Philosophical Transactions of the Royal Society of London* **1805**, *95*, 65-87, doi:doi:10.1098/rstl.1805.0005.
68. Laplace, P.S., Marquis De. *Traité De Mécanique Céleste*. **1806**, *10*.
69. Worthington, A.M. On pendent drops. *Proceedings of the Royal Society of London* **1881**, *32*, 362-377.
70. Worthington, A.M. IV. Note on a point in the theory of pendent drops. *The London, Edinburgh, and Dublin Philosophical Magazine and Journal of Science* **1885**, *19*, 46-48, doi:10.1080/14786448508627638.

71. Ferguson, A. Photographic measurements of pendant drops. *Philos. Mag.* **1911**, *23*, 417-430.
72. Bashforth, F.; Adams, J.C. *An attempt to test the theories of capillary action by comparing the theoretical and measured forms of drops of fluid*; University Press: 1883.
73. Merrington, A.C.; Richardson, E.G. The break-up of liquid jets. *Proceedings of the Physical Society* **1947**, *59*, 1-13, doi:10.1088/0959-5309/59/1/302.
74. Andreas, J.M.; Hauser, E.A.; Tucker, W.B. Boundary tension by pendant drops. *The Journal of Physical Chemistry* **1938**, *42*, 1001-1019, doi:10.1021/j100903a002.
75. Fordham, S.; Freeth, F.A. On the calculation of surface tension from measurements of pendant drops. *Proceedings of the Royal Society of London. Series A. Mathematical and Physical Sciences* **1948**, *194*, 1-16, doi:doi:10.1098/rspa.1948.0063.
76. Cheng, P.; Li, D.; Boruvka, L.; Rotenberg, Y.; Neumann, A.W. Automation of axisymmetric drop shape analysis for measurements of interfacial tensions and contact angles. *Colloids and Surfaces* **1990**, *43*, 151-167, doi:10.1016/0166-6622(90)80286-D.
77. Río, O.I.d.; Neumann, A.W. Axisymmetric Drop Shape Analysis: Computational Methods for the Measurement of Interfacial Properties from the Shape and Dimensions of Pendant and Sessile Drops. *Journal of Colloid and Interface Science* **1997**, *196*, 136-147, doi:10.1006/jcis.1997.5214.
78. Rotenberg, Y.; Boruvka, L.; Neumann, A.W. Determination of surface tension and contact angle from the shapes of axisymmetric fluid interfaces. *Journal of Colloid and Interface Science* **1983**, *93*, 169-183, doi:10.1016/0021-9797(83)90396-X.
79. Hoorfar, M.; W. Neumann, A. Recent progress in Axisymmetric Drop Shape Analysis (ADSA). *Advances in Colloid and Interface Science* **2006**, *121*, 25-49, doi:10.1016/j.cis.2006.06.001.
80. Huh, C.; Reed, R.L. A method for estimating interfacial tensions and contact angles from sessile and pendant drop shapes. *Journal of Colloid and Interface Science* **1983**, *91*, 472-484, doi:10.1016/0021-9797(83)90361-2.
81. Hoorfar, M.; Neumann, A.W. Axisymmetric drop shape analysis (ADSA) for the determination of surface tension and contact angle. *The Journal of Adhesion* **2004**, *80*, 727-743, doi:10.1080/00218460490477684.
82. Holmberg, K. *Handbook of Applied Surface and Colloid Chemistry*; Wiley&Sons,England: 2002; Volume 1,2.
83. Hammer, H.; Hammer, K. *Grundkurs der Physik 2 5.A.*; Oldenbourg Wissenschaftsverlag: München, 1994.
84. Haken, H.; Wolf, H.C. *Molekülphysik und Quantenchemie: Einführung in die experimentellen und theoretischen Grundlagen*, Fünfte, völlig neubearbeitete und erweiterte Auflage ed.; Springer: Berlin; Heidelberg, 2006.
85. Fauster, T.; Hammer, L.; Heinz, K.; Schneider, M.A. *Oberflächenphysik*; Oldenbourg Wissenschaftsverlag: München, 2013.
86. Heide, P.v.d. X-ray Photoelectron Spectroscopy: An introduction to Principles and Practices. 2011.
87. Hertz, H. Ueber einen Einfluss des ultravioletten Lichtes auf die electriche Entladung. *Annalen der Physik* **1887**, *267*, 983-1000, doi:10.1002/andp.18872670827.
88. Hallwachs, W. Ueber den Einfluss des Lichtes auf electrostatisch geladene Körper. *Annalen der Physik* **1888**, *269*, 301-312, doi:10.1002/andp.18882690206.
89. Lenard, P. Ueber Kathodenstrahlen in Gasen von atmosphärischem Druck und im äussersten Vacuum. *Annalen der Physik* **1894**, *287*, 225-267, doi:10.1002/andp.18942870202.
90. Einstein, A. Über einen die Erzeugung und Verwandlung des Lichtes betreffenden heuristischen Gesichtspunkt. *Annalen der Physik* **1905**, *322*, 132-148, doi:10.1002/andp.19053220607.
91. Tanuma, S.; Powell, C.J.; Penn, D.R. Calculations of electron inelastic mean free paths. V. Data for 14 organic compounds over the 50–2000 eV range. *Surface and Interface Analysis* **1994**, *21*, 165-176, doi:10.1002/sia.740210302.
92. Cremer, T.; Killian, M.; Gottfried, J.M.; Paape, N.; Wasserscheid, P.; Maier, F.; Steinrück, H.-P. Physical Vapor Deposition of [EMIM][Tf2N]: A New Approach to the Modification of Surface Properties with Ultrathin Ionic Liquid Films. *ChemPhysChem* **2008**, *9*, 2185-2190, doi:10.1002/cphc.200800300.
93. Cremer, T.; Stark, M.; Deyko, A.; Steinrück, H.P.; Maier, F. Liquid/Solid Interface of Ultrathin Ionic Liquid Films: [C1C1Im][Tf2N] and [C8C1Im][Tf2N] on Au(111). *Langmuir* **2011**, *27*, 3662-3671, doi:10.1021/la105007c.
94. Cremer, T.; Wibmer, L.; Calderón, S.K.; Deyko, A.; Maier, F.; Steinrück, H.P. Interfaces of ionic liquids and transition metal surfaces—adsorption, growth, and thermal reactions of ultrathin [C1C1Im][Tf2N] films on metallic and oxidised Ni(111) surfaces. *Physical Chemistry Chemical Physics* **2012**, *14*, 5153-5163, doi:10.1039/C2CP40278E.

95. Deyko, A.; Cremer, T.; Rietzler, F.; Perkin, S.; Crowhurst, L.; Welton, T.; Steinrück, H.-P.; Maier, F. Interfacial Behavior of Thin Ionic Liquid Films on Mica. *The Journal of Physical Chemistry C* **2013**, *117*, 5101-5111, doi:10.1021/jp3115397.
96. Taccardi, N.; Grabau, M.; Debuschewitz, J.; Distaso, M.; Brandl, M.; Hock, R.; Maier, F.; Papp, C.; Erhard, J.; Neiss, C.; et al. Gallium-rich Pd-Ga phases as supported liquid metal catalysts. *Nat. Chem.* **2017**, *9*, 862-867, doi:10.1038/nchem.2822.
97. Pintori, G.; Cattaruzza, E. XPS/ESCA on glass surfaces: A useful tool for ancient and modern materials. *Optical Materials: X* **2022**, *13*, 100108, doi:10.1016/j.omx.2021.100108.
98. Saad, S.M.I.; Policova, Z.; Neumann, A.W. Design and accuracy of pendant drop methods for surface tension measurement. *Colloids and Surfaces A: Physicochemical and Engineering Aspects* **2011**, *384*, 442-452, doi:10.1016/j.colsurfa.2011.05.002.
99. Kell, G.S. Density, thermal expansivity, and compressibility of liquid water from 0. deg. to 150. deg.. Correlations and tables for atmospheric pressure and saturation reviewed and expressed on 1968 temperature scale. *Journal of Chemical and Engineering data* **1975**, *20*, 97-105.
100. Parkhurst, H.J.; Jonas, J. Dense liquids. II. The effect of density and temperature on viscosity of tetramethylsilane and benzene. *The Journal of Chemical Physics* **1975**, *63*, 2705-2709, doi:10.1063/1.431619.
101. Gardas, R.L.; Freire, M.G.; Carvalho, P.J.; Marrucho, I.M.; Fonseca, I.M.A.; Ferreira, A.G.M.; Coutinho, J.A.P. High-Pressure Densities and Derived Thermodynamic Properties of Imidazolium-Based Ionic Liquids. *Journal of Chemical & Engineering Data* **2007**, *52*, 80-88, doi:10.1021/je060247x.
102. Wagner, C.D.; Davis, L.E.; Zeller, M.V.; Taylor, J.A.; Raymond, R.H.; Gale, L.H. Empirical Atomic Sensitivity Factors for Quantitative Analysis by Electron Spectroscopy for Chemical Analysis. *Surf. Interface Anal.* **1981**, *3*, 211-225, doi:10.1002/sia.740030506.
103. Kaelble, D.H.; Cirilin, E.H. Dispersion and polar contributions to surface tension of poly(methylene oxide) and Na-treated polytetrafluoroethylene. *Journal of Polymer Science Part A-2: Polymer Physics* **1971**, *9*, 363-368, doi:10.1002/pol.1971.160090210.
104. Blythe, A.R.; Briggs, D.; Kendall, C.R.; Rance, D.G.; Zichy, V.J.I. Surface modification of polyethylene by electrical discharge treatment and the mechanism of autoadhesion. *Polymer* **1978**, *19*, 1273-1278, doi:10.1016/0032-3861(78)90304-X.
105. Fowkes, F.M.; McCarthy, D.C.; Mostafa, M.A. Contact angles and the equilibrium spreading pressures of liquids on hydrophobic solids. *Journal of Colloid and Interface Science* **1980**, *78*, 200-206, doi:10.1016/0021-9797(80)90508-1.
106. Rudawska, A.; Jacniacka, E. Analysis for determining surface free energy uncertainty by the Owen-Wendt method. *International Journal of Adhesion and Adhesives - INT J ADHES ADHES* **2009**, *29*, 451-457, doi:10.1016/j.ijadhadh.2008.09.008.
107. Vuckovac, M.; Latikka, M.; Liu, K.; Huhtamäki, T.; Ras, R.H.A. Uncertainties in contact angle goniometry. *Soft Matter* **2019**, *15*, 7089-7096, doi:10.1039/C9SM01221D.
108. Schuster, J.M.; Schvezov, C.E.; Rosenberger, M.R. Influence of Experimental Variables on the Measure of Contact Angle in Metals Using the Sessile Drop Method. *Procedia Materials Science* **2015**, *8*, 742-751, doi:10.1016/j.mspro.2015.04.131.
109. Vargaftik, N.B.; Volkov, B.N.; Voljak, L.D. International Tables of the Surface Tension of Water. *Journal of Physical and Chemical Reference Data* **1983**, *12*, 817-820, doi:10.1063/1.555688.
110. Sugden, S. VI.—The variation of surface tension with temperature and some related functions. *Journal of the Chemical Society, Transactions* **1924**, *125*, 32-41.
111. Sánchez, L.G.; Espel, J.R.; Onink, F.; Meindersma, G.W.; Haan, A.B.d. Density, Viscosity, and Surface Tension of Synthesis Grade Imidazolium, Pyridinium, and Pyrrolidinium Based Room Temperature Ionic Liquids. *Journal of Chemical & Engineering Data* **2009**, *54*, 2803-2812, doi:10.1021/je800710p.
112. Kahl, H.; Wadewitz, T.; Winkelmann, J. Surface Tension of Pure Liquids and Binary Liquid Mixtures. *Journal of Chemical & Engineering Data* **2003**, *48*, 580-586, doi:10.1021/je0201323.
113. Naser, M.A.; Permadi, A.K.; Bae, W.; Ryoo, W.; Siregar, S. A laboratory investigation of the effects of saturated steam properties on the interfacial tension of heavy-oil/steam system using pendant drop method. *Energy and Environment Research* **2015**, *5*, 94.
114. Klomfar, J.; Součková, M.; Pátek, J. Surface Tension Measurements for Four 1-Alkyl-3-methylimidazolium-Based Ionic Liquids with Hexafluorophosphate Anion. *Journal of Chemical & Engineering Data* **2009**, *54*, 1389-1394, doi:10.1021/je800895q.
115. Wasserscheid, P.; Welton, T. *Ionic liquids in synthesis*; Wiley Online Library: 2008; Volume 1.
116. Chen, J.; Spear, S.K.; Huddleston, J.G.; Rogers, R.D. Polyethylene glycol and solutions of polyethylene glycol as green reaction media. *Green Chemistry* **2005**, *7*, 64-82, doi:10.1039/B413546F.

117. Colacino, E.; Martinez, J.; Lamaty, F.; Patrikeeva, L.S.; Khemchyan, L.L.; Ananikov, V.P.; Beletskaya, I.P. PEG as an alternative reaction medium in metal-mediated transformations. *Coordination Chemistry Reviews* **2012**, *256*, 2893-2920, doi:10.1016/j.ccr.2012.05.027.
118. Kolbeck, C.; Killian, M.; Maier, F.; Paape, N.; Wasserscheid, P.; Steinrück, H.-P. Surface Characterization of Functionalized Imidazolium-Based Ionic Liquids. *Langmuir* **2008**, *24*, 9500-9507, doi:10.1021/la801261h.
119. Schrekker, H.S.; Silva, D.O.; Gelesky, M.A.; Stracke, M.P.; Schrekker, C.M.; Gonçalves, R.S. Preparation, cation-anion interactions and physicochemical properties of ether-functionalized imidazolium ionic liquids. *Journal of the Brazilian Chemical Society* **2008**, *19*, 426-433, doi:10.1590/S0103-50532008000300009.
120. Sato, T.; Masuda, G.; Takagi, K. Electrochemical properties of novel ionic liquids for electric double layer capacitor applications. *Electrochimica Acta* **2004**, *49*, 3603-3611, doi:10.1016/j.electacta.2004.03.030.
121. Döbbelin, M.; Azcune, I.; Bedu, M.; Ruiz de Luzuriaga, A.; Genua, A.; Jovanovski, V.; Cabañero, G.; Odriozola, I. Synthesis of Pyrrolidinium-Based Poly(ionic liquid) Electrolytes with Poly(ethylene glycol) Side Chains. *Chemistry of Materials* **2012**, *24*, 1583-1590, doi:10.1021/cm203790z.
122. Ganapatibhotla, L.V.N.R.; Zheng, J.; Roy, D.; Krishnan, S. PEGylated Imidazolium Ionic Liquid Electrolytes: Thermophysical and Electrochemical Properties. *Chemistry of Materials* **2010**, *22*, 6347-6360, doi:10.1021/cm102263s.
123. Zhou, Z.-B.; Matsumoto, H.; Tatsumi, K. Cyclic Quaternary Ammonium Ionic Liquids with Perfluoroalkyltrifluoroborates: Synthesis, Characterization, and Properties. *Chemistry – A European Journal* **2006**, *12*, 2196-2212, doi:10.1002/chem.200500930.
124. Xu, W.; Angell, C.A. Solvent-free electrolytes with aqueous solution-like conductivities. *Science* **2003**, *302*, 422-425, doi:10.1126/science.1090287.
125. Branco, L.C.; Rosa, J.N.; Moura Ramos, J.J.; Afonso, C.A.M. Preparation and Characterization of New Room Temperature Ionic Liquids. *Chemistry – A European Journal* **2002**, *8*, 3671-3677, doi:10.1002/1521-3765(20020816)8:16<3671::AID-CHEM3671>3.0.CO;2-9.
126. Cecchini, M.M.; Charnay, C.; De Angelis, F.; Lamaty, F.; Martinez, J.; Colacino, E. Poly(ethylene glycol)-Based Ionic Liquids: Properties and Uses as Alternative Solvents in Organic Synthesis and Catalysis. *ChemSusChem* **2014**, *7*, 45-65, doi:10.1002/cssc.201300421.
127. Kolbeck, C.; Cremer, T.; Lovelock, K.R.J.; Paape, N.; Schulz, P.S.; Wasserscheid, P.; Maier, F.; Steinrück, H.-P. Influence of Different Anions on the Surface Composition of Ionic Liquids Studied Using ARXPS. *J. Phys. Chem. B* **2009**, *113*, 8682-8688, doi:10.1021/jp902978r.
128. Koller, T.M.; Lenahan, F.D.; Schmidt, P.S.; Klein, T.; Mehler, J.; Maier, F.; Rausch, M.H.; Wasserscheid, P.; Steinrück, H.-P.; Fröba, A.P. Surface Tension and Viscosity of Binary Mixtures of the Fluorinated and Non-fluorinated Ionic Liquids [PFBMIm][PF6] and [C4C1Im][PF6] by the Pendant Drop Method and Surface Light Scattering. *International Journal of Thermophysics* **2020**, *41*, 144, doi:10.1007/s10765-020-02720-w.
129. Hao, Q.; Song, Y.; Mo, Z.; Mishra, S.; Pang, J.; Liu, Y.; Lian, J.; Wu, J.; Yuan, S.; Xu, H.; et al. Highly Efficient Adsorption of Oils and Pollutants by Porous Ultrathin Oxygen-Modified BCN Nanosheets. *ACS Sustainable Chemistry & Engineering* **2019**, *7*, 3234-3242, doi:10.1021/acssuschemeng.8b05173.
130. Portehault, D.; Giordano, C.; Gervais, C.; Senkowska, I.; Kaskel, S.; Sanchez, C.; Antonietti, M. High-Surface-Area Nanoporous Boron Carbon Nitrides for Hydrogen Storage. *Advanced Functional Materials* **2010**, *20*, 1827-1833, doi:10.1002/adfm.201000281.
131. Khalil, M.; Alyami, R.; Al-Khabbas, M. Introducing mole fraction in the density calculations of liquid-liquid solutions. *International journal of physical sciences* **2013**, *8*, 27-30.
132. Verlinde, J.; Verbeeck, R.; Thun, H. Density and Vapour Pressure of the Propylene Glycol-Water System from 15 to 50° C. *Bulletin des Sociétés Chimiques Belges* **1975**, *84*, 1119-1130.

7. ACKNOWLEDGEMENTS (DANKSAGUNG)

Ich möchte mich hiermit bei allen Personen bedanken, die mich im Laufe meiner Doktorarbeit unterstützt haben.

Mein ganz besonderer Dank gilt Herrn Professor Steinrück, für die Möglichkeit, meine Doktorarbeit am Lehrstuhl PC II durchführen zu dürfen, für die Unterstützung insbesondere für die Weitergabe seines Wissens im Bereich Oberflächenforschung und für die vielen hilfreichen Diskussionen.

Ich möchte mich auch bei Florian Maier für seine Betreuung in der IL-Gruppe, insbesondere für die Unterstützung durch fachlichen Diskussionen, Ideen und Korrekturen beim Paper schreiben, herzlich bedanken.

Ein weiterer besonderer Dank gilt Bernd Kreß, der mich beim Bau der neuen Pendant Drop/Sessile Drop Anlage sehr unterstützt hat, durch Zeichnungen, Ideen, Erklärungen, Einblicke in technische Details und viele Diskussionen. Ohne ihn wäre das Projekt in dieser Weise und so schnell nicht von statten gegangen. Ich möchte mich auch für den Einsatz bei Problemen an der DASSA herzlich bedanken.

Auf diesem Wege möchte ich mich recht herzlich bei Friedhold Wölfel und seinem Team für die schnelle Sonderanfertigung der der Pendant Drop/Sessile Drop Bauteile, ohne die diese Anlage nicht laufen würde, sowie für schnelle Reparaturen an der DASSA, bedanken.

Ein weiterer Dank gilt Hans-Peter Bäumler für seine Hilfe bei technischen und elektronischen Problemen und seiner tatkräftigen Unterstützung diese zu lösen.

Besonders möchte ich mich bei Dr. Bettina Heller und Dr. Francesco Greco bedanken. Ohne euch hätte ich die DASSA, ihre Probleme vor meiner Zeit und entsprechende Lösungen nie kennen gelernt. Danke für die Weitergabe eures Wissens in fachlicher und Anlagentechnischer weiße. Insbesondere möchte ich mich bei Dr. Bettina Heller für die Einarbeitung an dieser Anlage bedanken.

Ein weiterer Dank gilt den ehemaligen und jetzigen IL-Gruppenmitgliedern, Dr. Shungwan Shin, Dr. Matthias Lexow, Dr. Manuel Meusel, Dr. Cynthia Fernández, Dr. Simon Jaekel, Rajan Adhikari, Afra Gezmis, Daniel Hemmeter, Stephen Massicot, Majid Shaker,

Timo Talwar und Leonhard Winter für die gute Zusammenarbeit und die angenehme Arbeitsatmosphäre.

Des Weiteren möchte ich mich besonders bei Vera Seidl, Professor Meyer, Ziwen Zhai, Thomas Koller und Julian Mehler für eine angenehme und gute Kooperation bedanken. Insbesondere bei Vera Seidl und Professor Meyer für die schnellen Synthesen, die Möglichkeit, dass ich selber mal in einem AC-Labor stehen durfte und für unsere konstruktiven Gespräche. Bei Ziwen Zhai und Thomas Koller möchte ich mich für die fachlich hilfreichen Diskussionen über Oberflächenspannungen bedanken. Besonders bedanke ich mich auch bei Julian Mehler, für seine Synthesen, die fachlichen Diskussionen und eine super Zusammenarbeit.

Ich möchte mich auch bei Nicolas Wellnhofer für seine gute Zusammenarbeit und Unterstützung im Rahmen seiner Bachelorarbeit bedanken.

Bei Susana Kreß und Andrea Meixner-Wolf möchte ich mich für die schnelle und unkomplizierte Hilfe bei administrativen Fragen und bei Norman Anja Schmidt für die IT-Unterstützung bedanken.

Ein weiterer Dank gilt Andrea Buchner und Gertrud Weiß für die Unterstützung beim Bestellen von Verbrauchsmaterialien.

Ich möchte mich bei allen Mitgliedern des PC II-Lehrstuhls für eine tolle Zeit bedanken.

Abschließend möchte ich mich noch bei meiner Familie, insbesondere meinem Vater und meinen Geschwistern für ihre Unterstützung in jeder Lebenslage, sowie bei meinem Freund und bei meinen Freunden, bedanken.

8. APPENDIX

8.1 PUBLICATIONS

[P1] Bis-polyethylene glycol-functionalized imidazolium ionic liquids: A multi-method approach towards bulk and surface properties

V. Seidl, M. Bosch, U. Paap, M. Livraghi, Z. Zhai, C. R. Wick, T. M. Koller, P. Wasserscheid, F. Maier, A.-S. Smith, J. Bachmann, H.-P. Steinrück and K. Meyer

Journal of Ionic Liquids, 2, 100041 (2022)

[10.1016/j.jil.2022.100041](https://doi.org/10.1016/j.jil.2022.100041)

This article is licensed under the Creative Commons CC BY-NC-ND 4.0 license. To view a copy of the license, visit <https://creativecommons.org/licenses/by/4.0/>. Copyright © 2022 by the Authors. Published by Elsevier B.V.

[P2] Probing surface and interfacial tension of ionic liquids in vacuum with the pendant drop and sessile drop method

U. Paap, B. Krefß, H.-P. Steinrück and F. Maier

International Journal of Molecular Sciences, 23, 13158 (2022)

[10.3390/ijms232113158](https://doi.org/10.3390/ijms232113158)

This article is licensed under the Creative Commons CC BY 4.0 license. To view a copy of the license, visit <https://creativecommons.org/licenses/by/4.0/>. Copyright © 2022 by the Authors. Published by MDPI, Basel, Switzerland.

[P3] Direct correlation of surface tension and surface composition of ionic liquid mixtures – A combined vacuum pendant drop and angle resolved X-ray photoelectron spectroscopy study

U. Paap, V. Seidl, K. Meyer, F. Meier and H.-P. Steinrück

Molecules, 27, 8561 (2022)

[10.3390/molecules27238561](https://doi.org/10.3390/molecules27238561)

This article is licensed under the Creative Commons CC BY 4.0 license. To view a copy of the license, visit <https://creativecommons.org/licenses/by/4.0/>. Copyright © 2022 by the Authors. Published by MDPI, Basel, Switzerland.

[P4] B/N-doped carbon sheets from a new ionic liquid with excellent sorption properties for methylene blue

J. Mehler, M. Ermer, U. Paap, B. S. J. Heller, F. Maier, H.-P. Steinrück, M. Hartmann, C. Korte, P. S. Schulz and P. Wasserscheid

Journal of Ionic Liquids, 1, 100004 (2021)

[10.1016/j.jil.2021.100004](https://doi.org/10.1016/j.jil.2021.100004)

This article is licensed under the Creative Commons CC BY 4.0 license. To view a copy of the license, visit <https://creativecommons.org/licenses/by/4.0/>. Copyright © 2021 by the Authors. Published by Elsevier B.V.

8.1.1. BIS-POLYETHYLENE GLYCOL-FUNCTIONALIZED IMIDAZOLIUM IONIC LIQUIDS: A MULTI-METHOD APPROACH TOWARDS BULK AND SURFACE PROPERTIES^[P1]

Journal of Ionic Liquids 2 (2022) 100041



Contents lists available at ScienceDirect

Journal of Ionic Liquids

journal homepage: www.elsevier.com/locate/jil



Bis-polyethylene glycol-functionalized imidazolium ionic liquids: A multi-method approach towards bulk and surface properties



Vera Seidl^a, Michael Bosch^b, Ulrike Paap^c, Mattia Livraghi^d, Ziwen Zhai^e, Christian R. Wick^d, Thomas M. Koller^e, Peter Wasserscheid^{f,g}, Florian Maier^c, Ana-Sunčana Smith^d, Julien Bachmann^b, Hans-Peter Steinrück^c, Karsten Meyer^{a,*}

^a Department of Chemistry and Pharmacy, Inorganic Chemistry, Friedrich-Alexander-Universität Erlangen-Nürnberg (FAU), Egerlandstr. 1, 91058 Erlangen, Germany

^b Department of Chemistry and Pharmacy, Chemistry of Thin Film Materials, Interdisciplinary Center for Nanostructured Films (IZNF), Friedrich-Alexander-Universität Erlangen-Nürnberg (FAU), Cauerstr. 3, 91058 Erlangen, Germany

^c Department of Chemistry and Pharmacy, Physical Chemistry, Friedrich-Alexander-Universität Erlangen-Nürnberg (FAU), Egerlandstr. 3, 91058 Erlangen, Germany

^d Department of Physics, Institute for Theoretical Physics, PULS Group, Interdisciplinary Center for Nanostructured Films (IZNF), Friedrich-Alexander-Universität Erlangen-Nürnberg (FAU), Cauerstr. 3, 91058 Erlangen, Germany

^e Department of Chemical and Biological Engineering and Erlangen Graduate School in Advanced Optical Technologies, Institute of Advanced Optical Technologies – Thermophysical Properties (AOT-TP), Friedrich-Alexander-Universität Erlangen-Nürnberg (FAU), Paul-Gordan-Str. 8, 91052 Erlangen, Germany

^f Department of Chemical and Biological Engineering, Chemical Engineering, Friedrich-Alexander-Universität Erlangen-Nürnberg (FAU), Egerlandstr. 3, 91058 Erlangen, Germany

^g Forschungszentrum Jülich, Helmholtz-Institute Erlangen-Nürnberg for Renewable Energy (IEK 11), Egerlandstr. 3, 91058 Erlangen, Germany

ARTICLE INFO

Keywords:

Ether-based room-temperature ionic liquids
physicochemical properties
surface behavior

ABSTRACT

Adding to the versatile class of ionic liquids, we report a new series of hydrophilic polyethylene glycol-functionalized room-temperature ionic liquids, offering interesting thermo- and electrochemical behavior as well as remarkable surface properties. A scalable and generally applicable synthetic procedure for the preparation of *N,N'*-bis(polyethylene glycol)imidazolium salts, generally abbreviated as [(mPEG)_nIm][A] (*n* = 2–6, A = Γ⁻, OMS⁻, PF₆⁻, NTf₂⁻) was developed. These ionic liquids were studied concerning their thermo- and electrochemical properties, such as phase transition behavior, decomposition temperature, viscosity, and density, as well as electrical conductivity and electrochemical stability, using *i.a.* differential scanning calorimetry (DSC), thermogravimetric analysis (TGA), electrochemical impedance spectroscopy (EIS) and linear sweep voltammetry (LSV). Additionally, the surface properties were investigated by angle-resolved X-ray photoelectron spectroscopy (ARXPS) and the pendant drop method. Molecular dynamics simulations complement the studies and provide insight into the molecular structure of the ionic liquids and their specific orientation at the liquid-vacuum interface.

1. Introduction

Ionic Liquids (ILs) and polyethylene glycol (PEG) are both known to have fascinating physical and chemical properties, including non-toxicity, high thermal and chemical stability as well as low vapor pressure and high ionic conductivity (Wasserscheid and Welton, 2008, Chen et al., 2005, Colacino et al., 2012). Combining the advantages of both results in an innovative group of polyethylene glycol-functionalized ILs, which represent an appealing *hydrophilic alternative* among a large pool of well-established, mainly hydrophobic ILs, substituted with alkyl and/or aryl groups.

The so-called “PEGylation” of an IL changes its physicochemical properties without significantly altering the reactivity, in particular,

when using methylated PEG (mPEG) substituents. For instance, replacing alkyl chains by oligo ether functionalities has been shown to induce a decrease in the ILs' melting temperature and viscosity but an increase in the density and thermal stability (Kolbeck et al., 2008, Schrekker et al., 2008, Sato, Masuda, and Takagi, 2004). Hence, PEG-substituted ILs find application as solvents or catalysts in organic reactions, (Cecchini et al., 2014) and as electrolytes in electronic devices (Xu and Angell, 2003, Döbbelin et al., 2012, Ganapatibhotla et al., 2010, Branco et al., 2002, Zhou, Matsumoto, and Tatsumi, 2006). Moreover, PEG chains offer the possibility of interaction with small molecules (e.g. CO₂, SO₂) (Bara et al., 2007, Sharma et al., 2012, Yang et al., 2012) and (in)organic cations (e.g. protons, metal ions), (Winther-Jensen et al., 2010, Guo et al., 2017) which enables their application in gas separa-

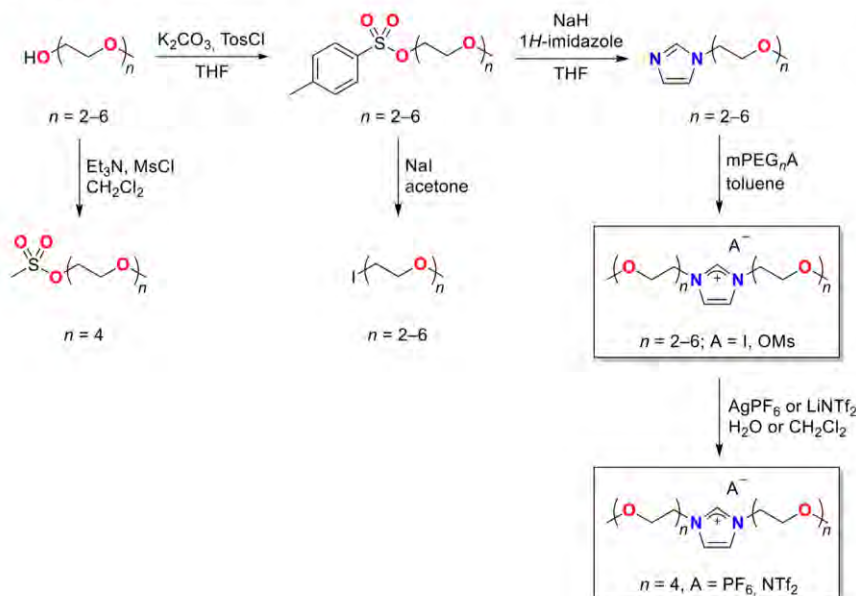
* Corresponding author.

E-mail address: karsten.meyer@fau.de (K. Meyer).

<https://doi.org/10.1016/j.jil.2022.100041>

Received 1 June 2022; Accepted 20 July 2022

2772-4220/© 2022 The Authors. Published by Elsevier B.V. This is an open access article under the CC BY-NC-ND license (<http://creativecommons.org/licenses/by-nc-nd/4.0/>).



Scheme 1. General synthetic procedure to all prepared bis-mPEG_n-functionalized ILs 1–8.

tion membranes (Bara, Noble, and Gin, 2009; Deng et al., 2016) and as reductants or stabilizers in nanoparticle synthesis (Schrekker et al., 2007; Dorjnamjin, Ariunaa, and Shim, 2008).

Although several PEG-functionalized ILs for numerous applications have been reported in the literature, their physicochemical properties are poorly understood. Especially for bis-PEG_n-substituted imidazolium-based ILs (n = repeating unit), only a few examples – often with a short PEG chain length ($n \leq 2$) and/or with terminal OH-groups (Riisager et al., 2005; Ikeda, Teshima, and Miyasaka, 2006; Jadhav et al., 2011; Jadhav et al., 2012; Jadhav et al., 2014; Zhang et al., 2014; Chavan, 2015; Chavan et al., 2016; López et al., 2019; Nagaraju et al., 2015) – are known, and their thermo- and electrochemical characterization is scarcely described. Therefore, and based on our experience with saturated and unsaturated imidazolium-based ILs, (Wang et al., 2009; Wang et al., 2011; Wang et al., 2014; Seidl et al., 2021) we here report a systematic study on a series of bis-mPEG_n-substituted imidazolium-based ILs with the general formula [(mPEG_n)₂Im][A] (Fig. 1). This study includes a generally applicable and scalable synthesis of the ILs as well as the experimental investigation of their melting temperature, thermal stability, density, viscosity, surface tension, electrochemical potential window, and electrical conductivity, described as a function of different anions ($A = I^-$, OMs^- , NTf_2^- , PF_6^-) and mPEG_n chain lengths ($n = 2-6$). In addition, the surface behavior and the orientation of selected [(mPEG_n)₂Im]I salts were studied by angle-resolved X-ray photoelectron spectroscopy (ARXPS), and the results were compared to molecular dynamics simulations of the respective ILs.

2. Results and Discussion

2.1. Synthesis

The synthetic procedure towards the bis-mPEG_n-substituted imidazolium salts reported here is depicted in Scheme 1 and is based on a series of nucleophilic substitution reactions. Starting from the primary mPEG_n alcohol, the respective mPEG_n mesylates and tosylates were synthesized in a high-yield sulfonylation reaction using a base and the corresponding sulfonyl chloride (Schrekker et al., 2008,

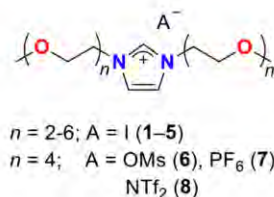


Fig. 1. Overview of the synthesized bis-mPEG_n-functionalized ILs 1–8.

Roy, Gowd, and Ramakrishnan, 2012). The *p*-toluene sulfonate derivatives were then further converted to the mPEG_n iodide in acetone (Döbbelin et al., 2012). Additionally, alkylation of 1*H*-imidazole was performed with sodium hydride as a base and *p*-toluene sulfonate derivatives as the alkylating agents (Bara et al., 2007). After purification via Kugelrohr distillation, alkylation of the mPEG_n-functionalized imidazole with the respective mPEG_n iodide in toluene yields the desired ILs 1–5. The [(mPEG₄)₂Im][OMs] (6) was obtained in a similar quaternization reaction with the methanesulfonate ester derivative, solventless at 60 °C. It is of vital importance to note that higher temperatures lead to the decomposition of the mPEG_n methanesulfonate.

Anion exchange to the [(mPEG₄)₂Im][PF₆] (7) was carried out starting from the respective iodide salt and silver hexafluorophosphate in water. However, [(mPEG₄)₂Im][NTf₂] (8) was prepared differently, using [(mPEG₄)₂Im][OMs] and lithium bis(trifluoromethanesulfonyl)imide in dry dichloromethane, which represents a less expensive and similarly effective alternative method for anion exchange to bis-mPEG-substituted ILs with hydrophobic anions.

All ILs were dried under vacuum for 5 days at 45 °C and checked for purity by CHN elemental analysis and NMR spectroscopy as well as XPS in cases of [(mPEG_n)₂Im]I ($n = 2, 4, 6$).

2.2. Molecular Model

The parametrization of [(mPEG_n)₂Im]⁺ ($n = 2, 4$; 1, 3) cations was performed utilizing the GAFF force field (Wang et al., 2004). Partial

Table 1

Transition temperatures, changes in (molar) heat capacities, enthalpies of fusion, entropies of fusion, and decomposition temperatures determined by DSC and TGA measurements of all bis-mPEG-substituted ILS 1–8. Temperatures given below were obtained by recording the onset temperatures of the 2nd heating cycle; Cr = crystalline phase, I = isotropic phase, glass = glass transition, cold cryst. = cold crystallization.

IL	Phase Transition ^{a)}	T _{transition} /°C	ΔC _p /J g ⁻¹ K ⁻¹	ΔC _{p,m} /J mol ⁻¹ K ⁻¹	ΔH _m /kJ mol ⁻¹	ΔS _m /J mol ⁻¹ K ⁻¹	T _d ^{b)} /°C
1	glass – I	–67.4	1.019	407.8	/	/	285.5
2	glass – I	–57.2	0.601	293.5	/	/	288.5
	cold cryst. Cr – I	–7.2 30.0	/	/	–34.3 33.4	129.1 110.0	
3	glass – I	–67.0	1.247	718.8	/	/	287.7
4	glass – I	–66.2	1.310	870.6	/	/	284.7
5	glass – I	–66.0	1.605	1208.1	/	/	288.5
6	glass – I	–64.0	1.350	735.3	/	/	337.2
7	glass – I	–59.5	0.615	365.6	/	/	n.d. ^{b)}
8	glass – I	–66.6	1.172	855.2	/	/	n.d. ^{b)}

^{a)} DSC and TGA traces of all compounds can be found in the Supporting Information (Fig. S2–S6).

^{b)} because of HF formation and subsequent damage to the thermocouple, thermal stability was not determined for fluorine containing compounds.

atomic charges were derived by means of the RESP method, utilizing the RED.M.V tools, (Dupradeau et al., 2010, Pigache, Gieplak, and Dupradeau, 2004) with input molecular geometries optimized by Gaussian 16 (Frisch et al., 2016) at the HF/6-31G(d) (Ditchfield, Hehre, and Pople, 1971, Hehre, Ditchfield, and Pople, 1972, Francel, Pietro, and Hehre, 1982, Rassolov et al., 2001) level of theory. Given the large conformational space of mPEG_n side chains, a representative set of conformations was used in both cases. Specifically, six conformers were initially optimized for *n* = 1. Each of them was later replicated three times, by first adding side-chain atoms in an all-extended manner to obtain [(mPEG₂)₂Im]⁺, and then rotating some of the newly added bonds to produce extra conformations. After optimizations, these eighteen structures served as input for the RESP charge derivations. Similarly, each *n* = 2 structure was then extended to *n* = 4, replicated and finally mutated to yield a pool of thirty-six conformers to parametrize [(mPEG₂)₄Im]⁺ (for details, see Section 2.1.1). The parametrization of iodide was taken from Migliorati et al. (Migliorati et al., 2015).

In order to make a liquid with a vacuum interface in molecular dynamics (MD) simulations, first, cubic boxes were assembled containing 1400 [(mPEG_n)₂Im]I pairs, amounting to 63000 and 102200 atoms, for *n* = 2, 4, respectively. Simulations were conducted using GROMACS 2019.5 (Pronk et al., 2013, Abraham et al., 2015). An elaborate equilibration procedure, including both annealing and relaxation in the NPT ensemble, was applied to each system, allowing the density to reach steady state. Concomitantly, ionic liquid-vacuum (LV) interfaces were established by introducing appropriately sized vacuum slabs along the *z*-axis. The newly created LV systems were then further annealed and equilibrated in the NVT ensemble, at temperatures of 303, 317, 333 and 338 K for *n* = 2 and 303, 330, 350 and 370 K for *n* = 4. Final production runs comprised 300 ns (for details, see Vučemilović-Alagić et al. (Vučemilović-Alagić et al., 2019) and Supporting Information).

2.3. Phase Transition Behavior

The phase transition behavior and the corresponding parameters, such as the changes in (molar) heat capacity (ΔC_p, ΔC_{p,m}), molar enthalpy (ΔH_m) and entropy of fusion (ΔS_m) were determined by differential scanning calorimetry (DSC), and are summarized in Table 1.

All reported ILS 1–8 are liquid at or near room temperature and, by definition, are, thus, described as room-temperature ILS (RTILs). Because of the mPEG chains' high flexibility, the crystallization process in all ILS 1–8 is suppressed upon cooling, which results in a supercooled liquid and, finally, a glassy state is obtained between –67.4 and –57.2 °C. Generally, the corresponding change in molar heat capacity, ΔC_{p,m}, strongly increases with longer mPEG_n chain lengths, indicating enhanced rotational freedom. Within the series of different counterions, ΔC_{p,m} decreases as follows: [NTf₂]⁻ > [OMs]⁻ > I⁻ > [PF₆]⁻. Moreover, [(mPEG₃)₂Im]I exhibits an additional cold crystallization event

during the heating process at –7.2 °C (ΔH_m = –34.3 kJ mol⁻¹), preceding its melting at 30.0 °C (ΔH_m = 33.4 kJ mol⁻¹). Thermochemical features, such as glass transitions and cold crystallization processes, have also been literature-reported for other mPEG-substituted imidazolium salts; nevertheless, ΔC_{p,m} values are reported to be lower (Ganapatibhotla et al., 2010, Kouwer and Swager, 2007, Branco et al., 2002, Zhou, Matsumoto, and Tatsumi, 2004, Schrekker et al., 2008).

2.4. Thermal Stability

The thermal stability was established by the determination of the onset temperature of thermogravimetric analysis (TGA) measurements (Table 1).

The decomposition temperature of all iodide salts 1–5 ranges between 284.7 and 288.5 °C, which is similar to other *mono*-mPEG-substituted imidazolium iodides (Ganapatibhotla et al., 2010). Hence, and contrasting to the chain length dependency of alkyl-substituted ILS, (Cao and Mu, 2014) the influence of the mPEG chain length is negligible. Because of possible protective inter- and intramolecular interactions of the PEG chains' oxygen atoms with the imidazolium moiety, (Fei et al., 2007, Shimizu et al., 2013, Luo et al., 2010, Zeng et al., 2019) the nucleophilic attack of the counterion is expected to be hindered. This nucleophilic attack is most likely responsible for the ILS' thermochemical degradation (Chan, Chang, and Grimmer, 1977). As a consequence of the protective Im–O interactions, the thermal stability of the here reported ILS 1–5 is higher than that of comparable alkyl-substituted halide salts (Damilano et al., 2020). The [(PEG₄)₂Im][OMs] (6) exhibits a decomposition temperature of 337.2 °C and is thermally more stable than the closely related [(mPEG₂)₂Im][OMs] (Schrekker et al., 2008, Schrekker et al., 2007).

2.5. Liquid Density

Temperature-dependent density measurements of [(mPEG_n)₂Im]I (*n* = 2, 4, 6) (1, 3, 5) were performed between 10 and 90 °C (283 and 363 K) in order to study the influence of the mPEG chain length. As expected, and according to Fig. 2 (left), the liquid density decreases with increasing temperature. Moreover, longer substituents in the bis-mPEG-functionalized ILS induce a lowering in density: Notably, the density decreases by ~7.4% from [(mPEG₂)₂Im]I to [(mPEG₄)₂Im]I, and only by 3.4% from [(mPEG₄)₂Im]I to [(mPEG₆)₂Im]I. This trend of converging densities or molar volumes with increasing mPEG side chains is also reported for 1-mPEG_n-3-methyl- and 1-alkyl-3-methylimidazolium-based ILS for varying side chains, (Ganapatibhotla et al., 2010, Zhou, Matsumoto, and Tatsumi, 2004, Schrekker et al., 2008, Dzyuba and Bartsch, 2002, Ghatee et al., 2010) and reflects the increasing contribution of the ILS' side chain length to their density. Based on the densities and the molecular weights of the bis-mPEG_n-based ILS, the derived mo-

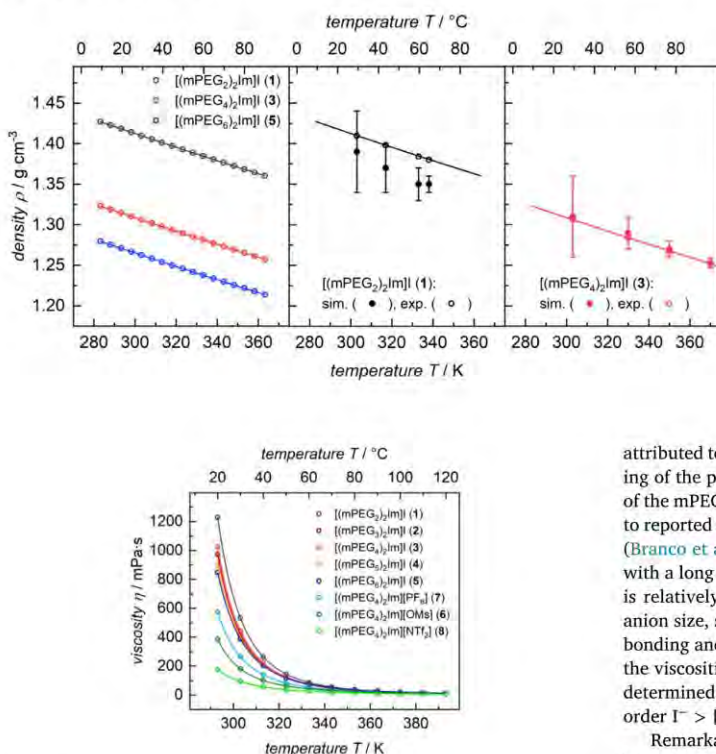


Fig. 3. Temperature-dependent viscosity (η) of ILs 1–8. Solid lines represent the best fits of experimental data according to the Vogel-Tammann-Fulcher equation $\eta = \eta_0 \exp [B/(T-T_0)]$. Complete data and fit parameters can be found in the Supporting Information (Table S2 and S3).

lar volume V_m shows a linear increase with increasing total number of the mPEG units, *i.e.* $2n$, at all temperatures considered here.

The linear slope of V_m as a function of $2n$ allows us, for example, to calculate the molar volume of the single PEG unit ($-\text{CH}_2\text{CH}_2\text{O}-$) at 25 °C as $38.9 \text{ cm}^3 \text{ mol}^{-1}$.

For comparison, the density of pure PEG-400, featuring eight PEG units, is between 1.126 and 1.077 g cm^{-3} in the temperature range from 20 to 80 °C, (Sequeira et al., 2019) which is about 13% lower than the values for $[(\text{mPEG}_6)_2\text{Im}]$ with the longest side chains in this work. From the density data and the molar mass of PEG-400, an estimation for the V_m value for the PEG unit of about $40 \text{ cm}^3 \text{ mol}^{-1}$ at 25 °C can be derived, which agrees well with the aforementioned value deduced from the IL densities. Here, the influence of the two PEG head groups ($-\text{CH}_3$ vs. $-\text{OH}$) can be neglected.

A good agreement can be observed between the experimental and MD-derived density data (Fig. 2, right). The difference between the simulated and experimental values never exceeds 0.03 g cm^{-3} , with most experimental data points lying within the error bars of the simulation results.

2.6. Viscosity

The temperature-dependent viscosity of the RTILs 1–8 (Fig. 3) was determined between 20 and 120 °C (293 and 393 K). It decreases exponentially with increasing temperature, and converges to values between 6 and 13 mPa s at 120 °C. At room temperature (Table 2), all iodide salts 1–5 provide viscosities between 846 and 1229 mPa s, generally becoming less viscous with longer mPEG_{*n*} chain length. This might be

Fig. 2. Temperature-dependent density (ρ) based on experiments for ILs 1, 3 and 5 (left) and simulated density values for 1 and 3 (middle and right; experimental values for the exact temperatures of the MD calculations were calculated from the respective fit in the left graph). Solid lines represent the best fits of experimental data according to a second-order polynomial equation $\rho_{\text{calc}}(T) = \rho_0 + \rho_1 T + \rho_2 T^2$. Complete data and fit parameters can be found in the Supporting Information (Table S4 and S5).

attributed to reduced Coulombic interactions due to an enhanced shielding of the positively charged imidazolium moiety by Im–O interactions of the mPEG side chain. The chain length dependency of 1–5 is contrary to reported *mono*-mPEG_{*n*}-substituted ILs with short chain length ($n \leq 3$), (Branco et al., 2002, Guo et al., 2017) but similar to imidazolium salts with a long mPEG_{*n*} chain ($n > 6$), for which the chain lengths' influence is relatively small (Ganapatibhotla et al., 2010). Because of modified anion size, symmetry and charge distribution, the strength of hydrogen bonding and Coulombic interactions seems to be attenuated. Therefore, the viscosities of $[(\text{mPEG}_4)_2\text{Im}][\text{A}]$ ($\text{A} = \text{PF}_6^-, \text{OMs}^-, \text{NTf}_2^-$) (6–8) are determined to be lower than the comparable iodide salt and follow the order $\text{I}^- > [\text{PF}_6]^- > [\text{OMs}]^- > [\text{NTf}_2]^-$.

Remarkably, all *bis*-mPEG_{*n*}-functionalized ILs 1–8 are found to be more viscous than reported *mono*-PEGylated imidazolium salts (Ganapatibhotla et al., 2010, Zhang et al., 2014, Branco et al., 2002, Zhou, Matsumoto, and Tatsumi, 2004). A reason for this might be enhanced Van-der-Waals interactions between the mPEG chains of the larger and less flexible imidazolium cations as well as a reduced rotational freedom (Tang, Baker, and Zhao, 2012).

2.7. Electrical Conductivity

The electrical conductivity, κ , of $[(\text{mPEG}_n)_2\text{Im}][\text{A}]$ (1–8) (Table 3) was determined using electrochemical impedance spectroscopy (EIS) at room temperature, and varies between 0.59 and 0.10 mS cm^{-1} . Despite the decreasing viscosity, which should favor higher conductivities, the iodide salts 1–5 become less conductive with longer mPEG chain length. This might be explained by an increased molecular weight and molar volume of the ILs, which reduces the effective ion concentration; thus, leading to lower overall conductivity (Ganapatibhotla et al., 2010). Replacing iodide with $[\text{PF}_6]^-$ or $[\text{NTf}_2]^-$ as the counterion increases the conductivity from 0.16 mS cm^{-1} (for 3) up to 0.59 mS cm^{-1} (for 8). The $[(\text{mPEG}_4)_2\text{Im}][\text{OMs}]$ IL (7) yields values close to the analogous iodide salt. However, comparable 1-mPEG-3-methylimidazolium salts show higher conductivities than the *bis*-mPEG-ILs 1–8 reported herein, but the values converge with longer mPEG chain length (Ganapatibhotla et al., 2010, Zhang et al., 2014, Lall-Ramnarine et al., 2017, Donato et al., 2007, Chen et al., 2016).

2.8. Electrochemical Stability

The electrochemical stability of all *bis*-mPEG_{*n*}-functionalized imidazolium salts 1–8 (Fig. 4, Table 3), determined by linear sweep voltammetry (LSV) (Fig. S9), is cathodically limited by the reduction of the imidazolium core, followed by various degradation steps at negative potentials (De Vos, Maton, and Stevens, 2014). The oxidation of the counterion at positive potentials defines the anodic limit (Matsumoto, Sakaabe, and Tatsumi, 2005). All iodide salts 1–5 exhibit

Table 2
Viscosity data (η) of ILs 1–8 at 20 °C, density data (ρ) of ILs 1, 3, 5 at 20 °C, and surface tension (γ) of ILs 1, 3, 5 at 30 °C.

#	IL	η at 20 °C / mPa s	ρ at 20 °C / g cm ⁻³	γ at 30 °C / mN m ⁻¹
1	[(mPEG ₂) ₂ Im]I	1229.0	1.4184	45.92
2	[(mPEG ₃) ₂ Im]I	972.6	/	/
3	[(mPEG ₄) ₂ Im]I	1023.3	1.3146	43.47
4	[(mPEG ₆) ₂ Im]I	900.3	/	/
5	[(mPEG ₆) ₂ Im]I	846.8	1.2710	42.63
6	[(mPEG ₄) ₂ Im][OMs]	384.9	/	/
7	[(mPEG ₄) ₂ Im][PF ₆]	573.8	/	/
8	[(mPEG ₄) ₂ Im][NTf ₂]	176.1	/	/

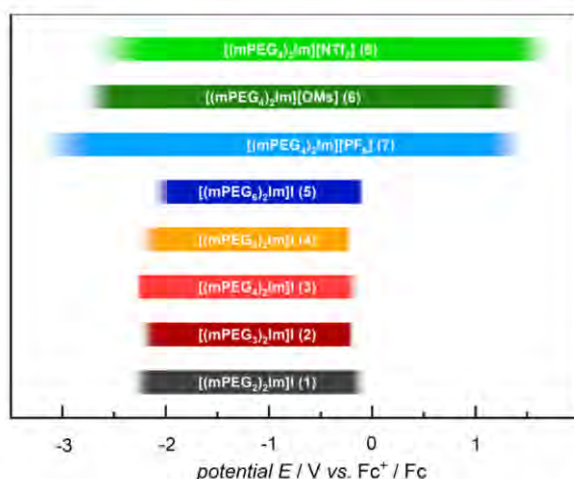


Fig. 4. Electrochemical window of all bis-mPEG_n-functionalized imidazolium salts 1–8. Faded colors represent the experimental uncertainty.

electrochemical windows of approximately 2 V width and are limited anodically by the low oxidation potential of the iodide counterion. The exchange of the anion can not only improve the anodic but also the cathodic limit, which enlarges the electrochemical window of the mesylate, bis(trifluoromethylsulfonyl)imide and hexafluorophosphate salts 6–8 up to 4.4 V (for 5). The lower cathodic limit might be explained by the anions' impact on the ion-pair strength of the IL (De Vos, Maton, and Stevens, 2014). Among others, the ion-pairing is influenced by the hydrogen bonding of the C(2)–H moiety to the anion and can be correlated to the chemical shift of the corresponding signal in the proton NMR spectrum (Fig. S1). Nevertheless, interactions between the electrode surface and any functional groups of the ILs or contaminants cannot be neglected and could also influence the electrochemical window.

Within the cyclic voltammogram (CV) of 1–5 (Fig. S10–S11), a large reduction peak can be detected on the reverse scan after reaching the anodic limit. This results from the reduction of triiodide, which was generated on the forward scan at the anodic limit, to iodide (Ejigu et al., 2011). Moreover, unidentified redox events within RTILs 6–8 most likely result from the reduction of oxygen or water on the platinum electrode. This also agrees with the observation of a possible decomposition process when adding moisture-sensitive cobaltocene (O'Mahony et al., 2008, Montiel et al., 2018, Lee et al., 2013).

2.9. Surface Tension

Measurements of the temperature-dependent surface tension, γ , of [(mPEG₂)₂Im]I (1), [(mPEG₄)₂Im]I (3) and [(mPEG₆)₂Im]I (5) (Fig. 5, Table 2) were performed between 30 and 90 °C (303 and 363 K) and show a typical trend of decreasing surface tensions with higher temper-

atures (Kolbeck et al., 2010, Koller et al., 2015). Notably, the surface tension decreases upon elongation of the mPEG_n-substituents in the ILs. In detail, the surface tensions of 1 and 3 between 30 and 90 °C differ by 5.6 to 9.1%, whereas the surface tensions of 3 and 5 differ by only ~2.3%.

A similar trend has also been observed for 1-alkyl-3-methylimidazolium-based ILs, in which a saturation of the surface tension could be achieved for sufficiently long chains (Kolbeck et al., 2010, Koller et al., 2015). Here, ARXPS measurements showed that the alkyl side chains are preferentially orientated toward the gas phase, (Kolbeck et al., 2010) which enabled the correlation between surface tension and surface composition, according to Langmuir's principle (Shimizu et al., 2018). For the bis-mPEG_n-functionalized ILs, reported herein, ARXPS data indicate an enrichment of the PEG side chains at the outer IL surface, accompanied by the depletion of the ionic head groups (see Section 2.10). Therefore, the contributions of the ionic sublayer to the surface tension are gradually reduced with increasing number of mPEG units. This behavior can be explained by the increasing mean distance between the ionic moieties and the IL surface – primarily induced by electrostatic interactions between the charged groups – resulting in a reduced electrostatic potential acting on the surface. The predominant coverage of the outer surface by the mPEG-functionalities is also reflected by considering the experimental surface tensions values for PEG-200, PEG-400 and PEG-600 (Beiranvand, Najibi, and Shahraki, 2020). These data, obtained at atmospheric pressure at 20 or 23 °C, show comparable values between 40.0 and 41.5 mN m⁻¹ and are only slightly lower than the γ_{calc} value of 43.4 mN m⁻¹ for [(mPEG₆)₂Im]I (5) obtained by extrapolation of the surface tensions' linear fit to 23 °C.

The surface tension was also studied using MD simulations (for further details, see Supporting Information). For [(mPEG₄)₂Im]I (3), the general temperature-dependent linear decrease of the experimentally obtained surface tensions is recovered (Fig. 5, right). However, the trend is not seen for $n = 2$ (1), although the experimental data fall basically within the uncertainty of the simulation results. This behavior of surface tension in simulations of [(mPEG₂)₂Im]I is likely due to this IL's sluggish dynamics, particularly at low temperatures, as reflected by its high viscosity as well. This causes significant difficulties in sampling capillary waves with large (and very slow) wavelength, and leads to the underestimation of the surface tension at low temperatures.

2.10. Angle-Resolved X-ray Photoelectron Spectroscopy (ARXPS)

For the three [(mPEG_n)₂Im]I salts ($n = 2, 4, 6$) (1, 3, 5), ARXP spectra were recorded for all relevant core levels (I 3d_{5/2}, O 1s, N 1s, C 1s) at room temperature (Fig. 6). Additionally, the Si 2p region was checked (Fig. S14) for typical surface-active contaminations, such as silicones (e.g. vacuum grease) (Steinrück, 2012). The lack of those signals also proves the high purity of the [(mPEG_n)₂Im]I ILs synthesized in this work. The binding energies and the quantitative composition values obtained for the two detection angles are provided in Table 4. For the three ILs, the binding energies at 0° are identical within the experimental uncertainty of ±0.2 eV, yielding values of 618.2 eV for the I 3d_{5/2}, 401.7 eV for N 1s, 532.8 eV for O 1s, and 286.5 eV for C 1s (denoted as

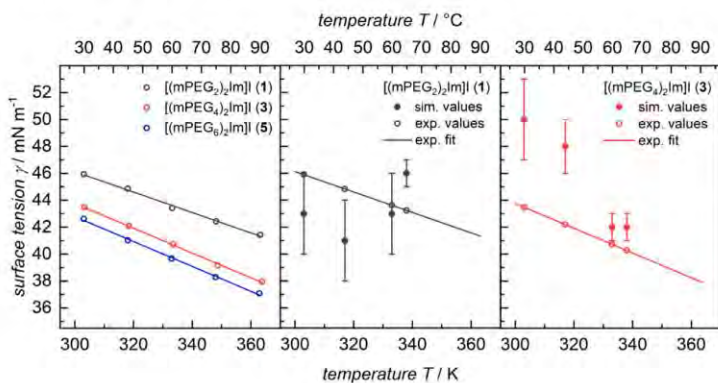


Fig. 5. Temperature-dependent surface tension (γ) based on experiments for ILs 1, 3 and 5 in an argon atmosphere of 0.1 MPa (left), and simulated surface tension values for 1 and 3 (middle and right; experimental values for the exact temperatures of the calculation were calculated from the respective fit in the left graph). Solid lines represent the best fit of experimental data according to the linear equation $\gamma_{\text{calc}}(T) = \gamma_0 + \gamma_1 T$. Complete data and fit parameters can be found in the Supporting Information (Table S7 and S8).

Table 3
Electrical conductivity (κ) and electrochemical window (EW) of [(mPEG_n)₂Im][A] (1–8).

IL	κ / mS cm ⁻¹	Electrochemical Window at 23 °C vs. Fc ⁺ /Fc ⁽¹⁾		
		Anodic Limit / V	Cathodic Limit / V	Total EW / V
1	0.18	-0.1	-2.3	2.2
2	0.17	-0.2	-2.2	2.0
3	0.15	-0.2	-2.3	2.1
4	0.12	-0.2	-2.2	2.0
5	0.10	-0.1	-2.1	2.0
6	0.16	1.3	-2.7	4.0
7	0.23	1.4	-3.0	4.4
8	0.59	1.6	-2.5	4.1

^{a)} electrochemical windows were determined at a limiting current of 5 mA cm⁻²

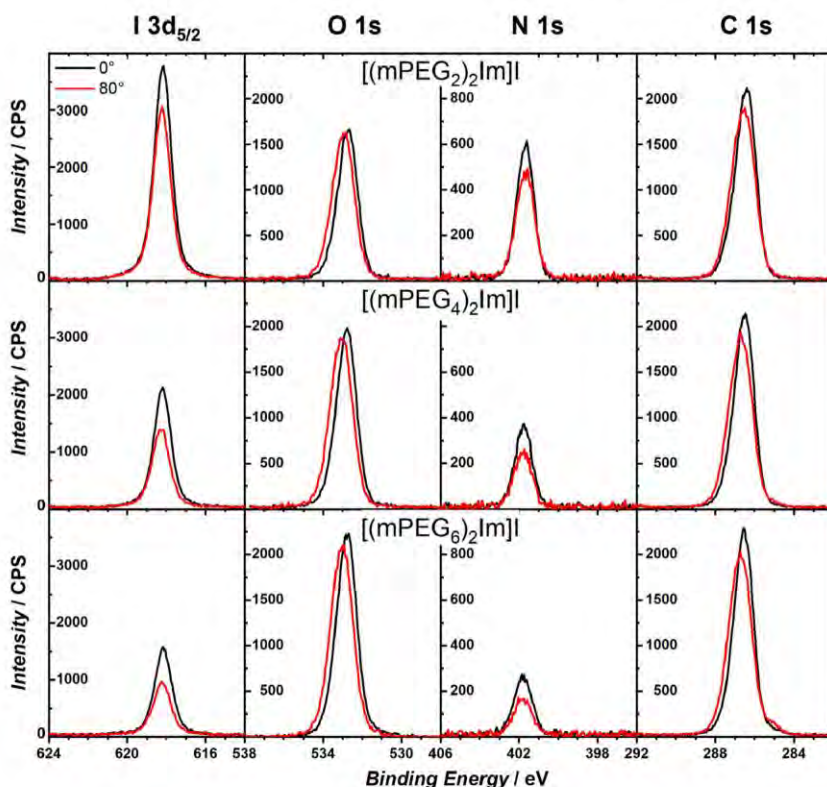


Fig. 6. Room-temperature ARXP spectra for [(mPEG_n)₂Im]I (1, 3, 5) with $n = 2$ (top row), 4 (middle), 6 (bottom) recorded under 0° (black, bulk sensitive) and 80° (red, surface sensitive) emission angle.

Table 4

Quantitative analysis of [(mPEG_n)₂Im]I with $n = 2, 4, 6$ (1, 3, 5). To derive the number of atoms from the 0° and the 80° spectra with respect to the nominal content. ASF factors from Niedermaier et al. (Niedermaier et al., 2016) were applied.

	I 3d _{5/2}	O 1s	N 1s	C ₂	C _{hetero}	C _{alkyl} ^{a)}
Atomic Sensitivity Factor (ASF) relative to ASF _{I 3s} = 1.00	6.17	0.67	0.46	0.30	0.30	0.30
[(mPEG₂)₂Im]I						
0° Binding Energy/eV	618.2	532.8	401.7	287.3	286.4	
80° Binding Energy/eV	618.4	533.1	401.8	287.6	286.7	
Nominal	1	4	2	1	12	
n(0°)	0.98	4.29	1.91	0.99	11.8	0.00
n(80°)	0.80	4.36	1.66	0.99	11.9	0.00
n(80°)/n(0°)	0.81	1.07	0.87		1.01	
[(mPEG₄)₂Im]I						
0° Binding Energy/eV	618.2	532.8	401.8	287.4	286.5	
80° Binding Energy/eV	618.4	533.2	401.9	287.6	286.8	285.1
Nominal	1	8	2	1	20	
n(0°)	0.90	8.54	1.93	0.98	19.6	0.00
n(80°)	0.61	9.02	1.36	1.00	20.0	0.18
n(80°)/n(0°)	0.68	1.06	0.71		1.01	
[(mPEG₆)₂Im]I						
0° Binding Energy/eV	618.2	532.8	401.8	287.4	286.6	284.7
80° Binding Energy/eV	618.3	533.2	401.9	287.7	286.8	285.1
Nominal	1	12	2	1	28	
n(0°)	0.86	13.2	1.90	0.97	27.1	0.41
n(80°)	0.53	13.4	1.18	1.00	27.9	0.85
n(80°)/n(0°)	0.62	1.02	0.62		1.03	

^{a)} attributed to a very small carbon contamination of unknown origin (see also Fig. S13).

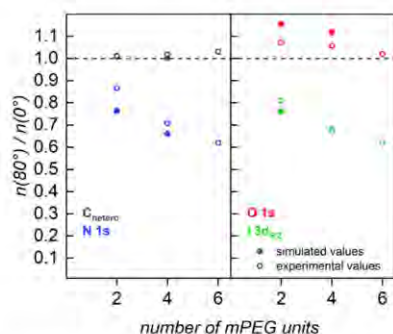


Fig. 7. Composition ratios $n(80^\circ)/n(0^\circ)$ for the individual atoms, as derived from the corresponding 80° and 0° O 1s (red), C_{hetero} 1s (black), N 1s (blue), I 3d_{5/2} (green) intensities for the [(mPEG_n)₂Im]I ILs ($n = 2, 4, 6$), and compared experimental and simulated composition ratios $n(80^\circ)/n(0^\circ)$ for 1 and 3.

C_{hetero} in Table 4). The small signal at 287.4 eV (denoted as C₂) originates from the C(2) carbon of the imidazolium ring. While the I 3d_{5/2} and N 1s binding energies are identical in 0° and 80°, the O 1s and C 1s levels at 80° are slightly shifted to higher binding energy by 0.3 ± 0.1 eV. As it will be discussed later, we attribute this differential shift to the orientation of the PEG chains at the surface pointing preferentially towards the vacuum.

The detailed comparison of the different core level signals at 0° and 80° emission in Fig. 6 shows characteristic changes. The I 3d_{5/2} and N 1s peaks at 80° (red) have significantly lower intensity than at 0° (black), which indicates a depletion of the corresponding atoms from the outermost surface. This depletion effect becomes more pronounced for increasing chain length, as evident from Table 4 and Fig. 7, where we plotted the ratios of the composition values, $n(80^\circ)/n(0^\circ)$, as open symbols. For [(mPEG₂)₂Im]I, [(mPEG₄)₂Im]I, and [(mPEG₆)₂Im]I, the 80°/0° ratios decrease from 0.81 to 0.67 to 0.62 for the I 3d_{5/2} levels, and from 0.87 to 0.71 to 0.62 for the N 1s levels, respectively. Peak fitting of the O 1s and C 1s signals reveals a broadening of the peaks, which comes along with the binding energy shifts mentioned above.

Considering the increase in peak width, the quantitative analysis of the chain signals reveals an 80°/0° ratio above 1, and, thus, an excess of O (by ~5%) and C_{hetero} (by ~2%); note that two carbons of the imidazolium ring and two carbon atoms next to it also contribute to the C_{hetero} peak) for all [(mPEG_n)₂Im]I ILs in Table 4. This small excess of chain signals at 80°, along with the concomitant decrease of the N 1s and I 3d_{5/2}, is attributed to a pronounced enrichment of the mPEG chains at the outer surface due to their preferential orientation towards the vacuum. As a consequence, these chains attenuate the 80° signals of the ionic moieties underneath (that is, nitrogen of the positively charged imidazolium ring and the iodide anion signal). This preferential chain enrichment also allows us to explain the peak broadening and shifts of the C 1s and O 1s peaks towards higher binding energy at 80°. In contrast to the ionic moieties, particularly the mPEG chain atoms at the outer surface experience an anisotropic environment with IL neighbors on one side and vacuum on the other side. This leads to an overall surface core level shift to higher binding energy. The very similar behavior of the I and N signals leads us to conclude that both, the anion and imidazolium ring, have about the same distance to the outer surface. Notably, despite this strong enrichment of the PEG chains, the 80°/0° ratios for the O 1s and C_{hetero} 1s signals both show only a weak increase. This observation is attributed to the fact that – even for the smallest [(mPEG₂)₂Im]I – the number of the O and C_{hetero} atoms in the chains (14) by far exceeds the number of I and N atoms (3). Therefore, only a pronounced depletion of the latter and no significant enrichment of the former is observable.

Interestingly, in an earlier study of our group addressing [(mPEG₃)C₁Im][NTf₂], an imidazolium-based IL with only one mPEG_n ($n = 3$) chain, a methyl group and the bulkier bis(trifluoromethylsulfonyl)imide ([NTf₂]⁻) anion, we observed an attenuation of the imidazolium N 1s signal similar to that observed here for [(mPEG₂)₂Im]I. At the same time, this earlier study showed a slight decrease of the C_{hetero} signals and a pronounced enrichment of the anion's F 1s signals, (Lovell et al., 2009) which contrasts with the results in the present study. This is likely due to the fact that the smaller iodide anion in the bis-mPEG-ILs allows for a better confinement of the ionic units in a sub-surface layer that is then covered by a more closely packed PEG surface layer.

Finally, we wish to emphasize that ARXPS cannot unambiguously deduce whether one or both of the PEG chains are enriched at the surface.

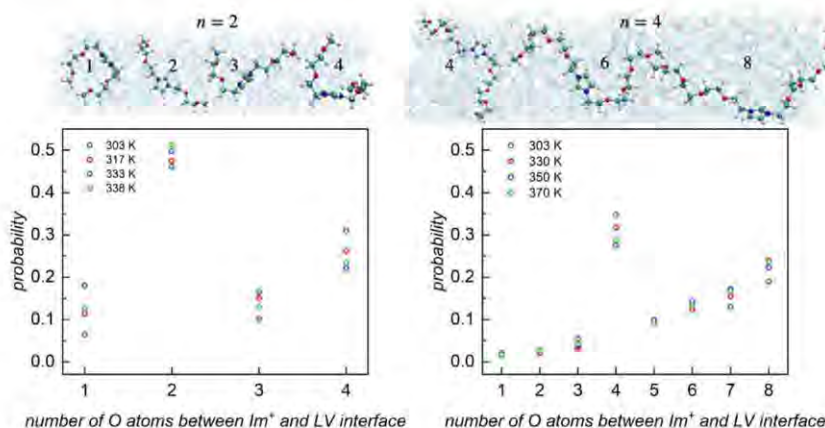


Fig. 8. Bottom: Probability to observe, within the LV interface, a cation conformation having between one and four oxygen atoms positioned between the imidazolium ring and the IL surface ($n = 2$, left) and between one and eight oxygen atoms with such property ($n = 4$, right). Temperature-dependence appears weak, particularly for $n = 4$. Top: Views of the LV interfaces of both liquids, showcasing the midpoint conformations of the most crowded clusters, obtained as outlined in the text. These structures are oriented so that the z-axis points upward; the numeral close to each of them is the number of oxygen atoms above the imidazolium ring, as analyzed in the bottom panels.

Nevertheless, the strong damping effect for the I $3d_{5/2}$ and N 1s signals in 80° already observed for the shortest PEG chain ($n = 2$) and the very pronounced effects for the longer chains ($n = 4$ and 6) indicate that, indeed, both chains of an individual cation are preferentially oriented towards the vacuum side. Our findings were corroborated by a comparison with molecular dynamics simulations (data included in Fig. 7), exhibiting a good agreement with the experimental data, as explained in Section 2.11.

2.11. Determining the Organization of the Interface Using Molecular Dynamics Simulations

In order to characterize the configurational space of the cations' PEG side chains at the ionic liquid-vacuum (LV) interface, we determined the number of cations with a specific number of oxygen atoms positioned between the imidazolium rings' center of mass and the interface. More precisely, for $n = 2$, we considered all cations found within 0.8 nm of the LV surface, and counted how many of them showed one, two, three, or four oxygen atoms located above the ring (and below the LV surface). Analogously, for $n = 4$, we looked at all cations found within 1.5 nm of the LV interface, and determined how many of them had between one and eight oxygen atoms dwelling above the imidazolium (Fig. 8). Subsequently, and in order to obtain a visual understanding of which structures were most likely associated with each number of oxygen atoms lying above the ring, we clustered each set of conformations using the rmsd-based method proposed by Daura et al. (Daura et al., 1999) (for details see Fig. S25).

For compound 1 ($n = 2$), the probability to observe a single upward chain (i.e. only two oxygen atoms between the imidazolium and the surface) is the highest and close to 0.5. At 303 K, the cumulative probability of observing both chains upward oriented (three and four oxygen atoms) is also approx. 0.5, but it does not exceed 0.4 at higher temperatures, unveiling a general preference for all-extended conformations. The situation looks different for $n = 4$. In this case, the probability of finding a single surface-oriented chain never exceeds 0.35, while the cumulative probability of finding both (at least five oxygen atoms) reaches or surpasses 0.5 (at all temperatures). Thus, for $n = 4$, the surface enrichment of fully coiled PEG chains is about equally probable as that of partially coiled ones, and more pronounced than for $n = 2$, in agreement with the experiment (at room temperature). Accordingly, we conclude that the experimentally observed enrichment of PEG chains at room temperature is confirmed: for both liquids, the probability to find no surface-oriented chains is always the smallest and remains below 0.1 at 303 K. This conclusion is also in direct accordance with our analysis of interfacial normal number density profiles (Fig. S25) for both liquids.

3. Conclusion

In this study, we present a general procedure for a scalable method to prepare a new class of hydrophilic imidazolium salts with methylated polyethylene glycol (mPEG_n) substituents. These ILs, namely [(mPEG_n)₂Im][A] ($n = 2-6$, A = I⁻, OMs⁻, PF₆⁻, NTF₂⁻) (1-8), are liquid at room temperature and were thoroughly characterized concerning their physico- and electrochemical properties as well as their surface behavior. In particular, all ILs show interesting thermal properties, such as glass transition and cold crystallization processes as well as relatively high decomposition temperatures of around 286 °C for the iodide salts 1-5; the thermal stability of the mesylate salt 6 is even higher (337 °C). The viscosity of all ILs 1-8 is determined between 1229 and 176 mPa s at room temperature, and decreases with increasing chain length of the mPEG_n substituent. The same trend can be observed when considering the liquid density data at room temperature (1.42-1.27 g cm⁻³ for 1, 3 and 5). Moreover, [(mPEG_n)₂Im]I (1-5) exhibit electrochemical stability and offer an electrochemical window of around 2 V. This range can be increased up to 4.4 V by the exchange of the counterion e.g. to the hexafluorophosphate salt 7. Similarly, the electrical conductivities of the ILs 1-5 are shown to be moderate, with values ranging from 0.18 to 0.10 mS cm⁻¹ that decrease upon elongating the mPEG_n chain length. However, the anion exchange to [NTF₂]⁻ induces a higher conductivity of 0.59 mS cm⁻¹.

In addition, the surface properties were characterized concerning the influence of the mPEG_n chain length ($n = 2, 4, 6; 1, 3, 5$). The surface tensions of these ILs were determined between 45.92 and 42.63 mN m⁻¹. The similarity of these values to the surface tension of pure polyethylene glycol with comparable chain length suggests a surface enrichment of the cation's mPEG_n chains at the gas-liquid interface. This is also deduced from the experimental observation that the ARXP spectra of all relevant core levels (I $3d_{5/2}$, O 1s, N 1s, C 1s) show characteristic changes in the signal intensities in the bulk- and surface-sensitive geometries (i.e. 0° and 80°). In particular, the I $3d_{5/2}$ and N 1s peaks at 80° have significantly lower intensity than at 0° (black), which indicates a depletion of the corresponding atoms from the outermost surface.

In order to obtain more insight into the conformations of the IL's cations at the liquid-vacuum interface, molecular dynamics simulations were performed. To validate the quality of the force field description, density, ARXPS and surface tension values were computed and compared to experimental data, finding sound agreement for the first two properties and at least acceptable accordance for the third one. MD simulations were then used to derive the probabilities of specific orientations of the mPEG_n side chains. For $n = 2$, a predilection for partially coiled conformations emerged, while for $n = 4$, an about equal prob-

ability of partially and fully coiled structures was identified. In both cases, the experimentally observed enrichment of the cations' mPEG_n substituents was confirmed.

4. Materials and Methods

4.1. General Considerations

Dry solvents were purified using a two-column solid-state solvent purification system (Glasscontour System, Irvine, CA), transferred to a Straus flask without exposure to air and stored over activated molecular sieves. 3,6-dioxaheptyl *p*-toluenesulfonate (mPEG₂Tos), 3,6,9-trioxadecyl *p*-toluenesulfonate (mPEG₃Tos), 3,6,9,12-tetraoxatridecyl *p*-toluenesulfonate (mPEG₄Tos), 3,6,9,12,15-pentaoxaheptadecyl *p*-toluenesulfonate (mPEG₅Tos), 3,6,9,12,15,18-hexaoxaononadecyl *p*-toluenesulfonate (mPEG₆Tos), 3,6,9,12-tetraoxatridecyl methanesulfonate (mPEG₄OMs), as well as 3,6-dioxaheptyl iodide (mPEG₂I), 3,6,9-trioxadecyl iodide (mPEG₃I), 3,6,9,12-tetraoxatridecyl iodide (mPEG₄I), 3,6,9,12,15-pentaoxaheptadecyl iodide (mPEG₅I), 3,6,9,12,15,18-hexaoxaononadecyl iodide (mPEG₆I) were synthesized according to literature procedures (Döbbelin et al., 2012; Roy, Gowd, and Ramakrishnan, 2012; Liu, Scharbert, and Holm, 1991; O'Driscoll et al., 2015). All other reagents were obtained from commercial sources and used without further purification. For all characterization methods under inert gas the ILs were dried *in vacuo* for 24 hours and further degassed by evacuating and refilling the samples three times with inert gas prior to the measurement.

Elemental analysis results were obtained from the Analytical Laboratories at the Friedrich-Alexander-Universität Erlangen-Nürnberg (FAU) (Erlangen, Germany), using Euro EA 3000 (Euro Vector) and EA 1108 (Carlo-Elba) elemental analyzers. Commercial laboratories refuse samples that contain fluorine as it destroys the elemental analyzers. Besides this practical problem, fluorine often causes substantial variations from the expected masses (Marcó et al., 2003).

NMR spectra were recorded at room temperature on a JEOL ECX 400 or ECZ 400S instrument at 400.18 and 399.79 MHz for ¹H and at 100.62 and 100.53 MHz for ¹³C NMR, respectively. ¹⁹F and ³¹P NMR spectra were recorded on a JEOL ECX 400 instrument operating at 376.54 and 162.00 MHz, respectively. Deuterated solvents used for NMR spectroscopy were obtained under argon and stored over activated molecular sieves. All prepared solutions were filtered into the NMR tube prior to measurement. The chemical shifts, δ , are calculated in ppm in relation to the applied magnetic field. The solvent residual signals of incomplete deuterated solvent molecules were used as internal reference for the ¹H NMR spectra as well as the solvent signals for ¹³C NMR spectral data (Fulmer et al., 2010). For ¹⁹F and ³¹P NMR data, chemical shifts were referenced by the Delta v4.3 or v5.0.5 software provided by JEOL Ltd NMR. NMR multiplicities are abbreviated as follows: s = singlet, d = doublet, t = triplet, q = quartet, quin = quintet, sept = septet, m = multiplet, br = broad, and coupling constants, *J*, are given in Hz.

Melting points and glass transition temperatures were determined by differential scanning calorimetry (DSC) using a Netzsch DSC 204 F1 Phoenix equipped with a τ -sensor and a CC200F1 controller ($\Delta T < \pm 1$ °C, $\Delta H < \pm 3\%$). The samples (30–50 mg) were prepared using an aluminum pan and measured with a heating rate of 5 K min⁻¹ and three repeating cycles for each measurement. For the determination of the melting points, the onset temperatures were used.

Thermogravimetric analysis (TGA) was carried out on a Setsys Evolution 18 machine from Setaram industries or on a TA instrument SDT 2960 Simultaneous DSC-TGA. Therefore, 20–30 mg of samples were prepared in a glass or platinum crucible and measured in the range of 25–700 °C, with a heating rate of 5 K min⁻¹. ΔT values are determined lower than ± 1.5 °C, given by the temperature error range for the thermocouple (Platinel II) of both TGA machines.

Electrochemical measurements were carried out with Gamry Interface 1000/1010E potentiostats in a nitrogen-filled propylene glove

box (Sylatech GmbH) using a setup of home-made microelectrodes (Fig. S8) with platinum for the working and auxiliary electrodes and silver as a pseudo-reference electrode. Thin films were deposited on a cleaned glass substrate by sputtering (CRC 622 model, Torr International, Inc.) or evaporation (Angstrom Engineering Covap). First, a 3–5 nm thick titanium (99.99%, Stanford Advanced Materials) adhesion layer (5 sccm Ar, 7.75 W cm⁻², RF) was sputtered, followed by a platinum (99.99%, Stanford Materials) layer of approximately 100 nm (5 sccm Ar, 7.75 mA cm⁻², DC). The platinum layer was then used as an adhesion layer for the evaporation of a silver (99.99%, Angstrom Engineering) pseudo-reference electrode. Approximately 100 nm of silver were deposited by thermal evaporation. The electrode area was defined by a laser-patterned Kapton mask, which was partially removed after the thin film depositions. For electrochemical measurements, approximately 10 μ L of the compound and a fresh electrode were used. Linear sweep and cyclic voltammetry studies were employed to investigate the electrochemical window and potentiostatic electrochemical impedance spectroscopy to determine the electrical conductivity κ . As internal references, solutions of cobaltocene (98%, abcr) or ferrocene (99%, Alfa Aesar) in dry acetonitrile (99.9%, ACROS Organics) were prepared and added to the ionic liquid, while all voltammetry results have been converted to V vs. Fe⁺/Fc (Connelly and Geiger, 1996; Shiddiky et al., 2009; Lewandowski, Waligora, and Galinski, 2013). Electrochemical windows were determined from linear sweep voltammograms in positive and negative direction from 0 V vs. Ag at a limiting current of 5 mA cm⁻¹ and later referenced to ferrocene. The electrical conductivity κ is derived from the resistivity ρ , which is calculated from the solution resistance R_s (Eq. 1). Assuming a simplified Randles circuit (which combines the double-layer capacitance C_{dl} in parallel with the charge transfer resistance, R_{ct} , and in series with the solution resistance R_s), R_s is the main resistive component at high frequencies in electrochemical impedance spectroscopy of an electrolyte, so the impedance *Z* measured at high frequency is equal to R_s . The cell constant C_{cell} of the electrode setup was determined with potassium chloride solution with a defined conductivity (Wasserscheid and Welton, 2008; Pratt et al., 2001).

$$\kappa = \frac{1}{\rho} \text{ with } \rho = \frac{R_s}{C_{cell}} \quad (\text{eq. 1})$$

Electrochemical impedance spectroscopy was performed from 0.1 Hz up to 1 MHz at 0 V vs. open circuit potential in a two-electrode configuration with an AC amplitude of 10 mV, *Z* values were taken at 100 kHz ($\Delta Z < 10\%$).

Viscosity measurements (η) were performed in a range of 20–120 °C ($\Delta T < 1$ °C) in steps of 10 °C and a shear rate of 100 m⁻¹ using a Haake Mars 60 rheometer (35 mm cone plate).

The **liquid density (ρ)** was measured at atmospheric pressure of 0.1 MPa with the vibrating-tube densimeter DMA 5000 from Anton Paar. The instrument was checked successfully with air as well as degassed and deionized water before and after each measurement series. After their preparation, the samples were injected *via* plastic syringes into the densimeter. For each IL, two measurement sets with individual samples were performed at a temperature range from 10–90 °C and in a reverse way in step of 5 °C. According to the temperature dependent liquid viscosity data, the experimental density data were corrected regarding instrument-specific viscosity effects using the corresponding models for the related ranges in η . Considering the complete experimental procedures, expanded relative uncertainties ($k = 2$) of 0.02% for the measured density data are obtained. Within combined uncertainties, agreement between the four different data sets measured for each substance can be found. The density data reported in this work represent the averages of the measurement data collected during the individual runs.

For **angle-resolved X-ray photoelectron spectroscopy (ARXPS) measurements**, thin IL films with roughly 0.1 mm thickness of the [(mPEG_n)₂Im]⁺ ILs ($n = 2, 4, 6$) were spread onto a flat molybdenum support and introduced into ultra-high vacuum for at least 18 hours to remove any volatile residues. As preventive measure, the ILs were then

additionally sputtered under mild conditions (Ar^+ , 0.3 keV, 10 μA , 5 min) in order to remove residual surface contaminations, e.g. adsorbed hydrocarbons while exposing the ILs to air during XPS sample preparation. Using a monochromated Al K_{α} X-ray source ($h\nu = 1486.6$ eV, 238 W), the ARXP spectra at 0° (normal emission) and 80° (grazing emission) were recorded at room temperature simultaneously with two identical hemispherical ARGUS-type electron analyzers (Niedermaier et al., 2016) at a pass energy of 35 eV for high-resolution core level spectra resulting in an overall energy resolution of 0.4 eV. Depending on the kinetic energy of the excited photoelectrons, the information depth ID of ARXPS in organic matter is around 7 to 9 nm in 0° (more bulk sensitive), while for 80° (surface-sensitive), ID decreases down to 1–1.5 nm; for the latter, more than 80% of the total core level intensity originates solely from the outermost IL layer (Shimizu et al., 2018). The changes in peak intensities with emission angle thus allow us to extract surface enrichment and orientation effects. The quantitative analysis of the ARXP spectra is based on established fitting procedures; in particular, for fitting the C 1s signal of the cation, a binding energy separation for the so-called C_2 and C_{hetero} peak of 0.87 eV is imposed (for the assignment of the carbon atoms and an example of peak fitting, see Fig.s S12 and S13). Using well-calibrated atomic sensitivity factors, the accurate atomic composition within the corresponding ID can be deduced from the fitting within a typical experimental uncertainty of 5% (Niedermaier et al., 2016).

The surface tension (γ) was obtained with the help of the pendant-drop (PD) method. For this, two different sample cells made of stainless steel and providing optical access were used. Details of the first cell including the peripheral system for sample handling can be found in Jander et al., (Jander et al., 2021) while the second cell is based on the same concept as the first one and includes further optical accesses for future intended measurements by surface light scattering (SLS). To validate the second sample cell and to check the reproducibility of the measurements, both cells were used in connection with same samples of [(mPEG₂)₂Im]I. For investigations of [(mPEG₄)₂Im]I and [(mPEG₆)₂Im]I, only the second sample cell was employed. Before the measurements, each used sample cell was flushed with argon and thermostated to the desired temperature. The temperature control of the sample cell is achieved by resistance heating and controlled by a Pt100 resistance probe. The reported temperature is measured in the gas phase by a second calibrated Pt100 resistance probe in close vicinity of the outlet of the capillary, where the droplets are formed. Over the entire temperature range, the expanded uncertainty ($k = 2$) of the reported temperatures associated with the surface tensions is 0.02 K. The pressure inside the sample cell was measured with a calibrated pressure transmitter with an expanded uncertainty ($k = 2$) of 5 kPa. Once temperature and pressure were stabilized within ± 0.01 K and ± 1 kPa, respectively, over all investigated states, droplets were formed at the tip of a capillary made of stainless steel with an outer diameter of 1.567 ± 0.010 mm. This capillary was inserted into the sample cell from the top and connected to a gas-tight glass syringe containing the IL samples via a fine-tuning valve. For each thermodynamic state, five droplets of [(mPEG₂)₂Im]I and [(mPEG₄)₂Im]I as well as three droplets of [(mPEG₆)₂Im]I were produced. After 10 min of equilibrium time, five photographs were taken for each droplet over time intervals of 10 to 30 s. The images of PDs were recorded by a monochromatic CMOS camera (UI-3280CP-M-GL, IDS GmbH) equipped with a manual focus-control objective (FL-BC7528-9M-F2.8/75mm, RICOH). A collimated homogeneous illumination source of the camera was realized by a monochromatic LED with a wavelength of 470 nm in combination with lenses and a diffuser. The image analysis based on the axisymmetric drop shape analysis (ADSA) is performed by a self-developed algorithm (Kersch et al., 2022). Here, the best match between the identified actual droplet contour and the theoretical profile given by the Young-Laplace (YL) equation (Rusanov and Prokhorov, 1996) is considered to determine the surface tension γ of the investigated ILs. For the conversion from the pixel to the metric scale, the outer diameter of the capillary was used. As further input parameters for solving the YL equation, the density of the gas

phase ρ_{gas} and of the liquid phase ρ are required. The latter was calculated by the fit of our experimental data according to the linear fit of the surface tension data while ρ_{gas} was obtained from the density data of argon at the corresponding temperature and pressure given by the REFPROP database (Lemmon, Huber, and McLinden, 2018). For all three ILs, measurements were performed from 303.15 to 363.15 K in steps of 15 K at an argon pressure of about 0.1 MPa. After the investigation at the highest temperature, repetition measurements at 318.15 K showed agreement clearly within the measurement uncertainty with the previous result, which confirms the reproducibility of the measurement. For each thermodynamic state, the reported surface tensions represent mean averages of the individual surface tensions obtained from the totally 15 or 25 droplets. Considering the uncertainties of the input quantities and the calibration procedure, the relative expanded uncertainty ($k = 2$) for the measured surface tensions can be stated with 2%, which is in line with our previous measurements on several reference fluids covering a broad surface tension range (Jander et al., 2021).

4.2. Synthesis

4.2.1. General Synthetic Route to 1-(Polyethylene glycol)imidazole (A-E)

In a flame-dried Schlenk flask, 1H-imidazole was dissolved in dry THF and cooled in an ice-bath. Sodium hydride (1.3 equiv) was added in portions and the suspension was stirred for 1 hour at 0°C . Then, the corresponding mPEG_nTos (1.1 equiv) was added and the reaction mixture was stirred at room temperature overnight. Water was added slowly until no hydrogen evolved and the solvent was removed under reduced pressure. The residue was taken up in dichloromethane and brine, the phases were separated and the aqueous phase was extracted with dichloromethane. The combined organic phases were dried with MgSO_4 , filtered and the solvent was removed *in vacuo* to give the desired product. If necessary, the product can be further purified by Kugelrohr distillation or filtration through alumina to remove traces of impurities.

mPEG₂Im (A). The general procedure was followed starting from 1H-imidazole (1.20 g, 17.6 mmol), NaH (0.550 g, 22.9 mmol, 1.3 equiv) and mPEG₂Tos (5.32 g, 19.4 mmol, 1.1 equiv) in THF (20 mL). Purification by Kugelrohr distillation (3.5×10^{-2} mbar/ 240°C) gives the desired product A as a colorless oil (5.21 g, 13.0 mmol, 74%).

¹H NMR (400 MHz, chloroform-*d*₁) δ (ppm) = 7.53 (s, 1 H, Im-H), 7.04 (s, 1 H, Im-H), 6.99 (s, 1 H, Im-H), 4.12 (t, ³J_{HH} = 5.2 Hz, 2 H, NCH₂), 3.74 (t, ³J_{HH} = 5.2 Hz, 3 H, NCH₂CH₂), 3.60–3.55 (m, 2 H, PEG-CH₂), 3.53–3.49 (m, 2 H, PEG-CH₂), 3.37 (s, 3 H, OCH₃); ¹³C NMR (101 MHz, chloroform-*d*₁) δ (ppm) = 137.4, 129.1, 119.3, 71.7, 70.5, 70.5, 58.9, 46.9.

mPEG₃Im (B). The general procedure was followed starting from 1H-imidazole (0.477 g, 7.01 mmol), NaH (0.219 g, 9.12 mmol, 1.3 equiv) and mPEG₃Tos (2.79 g, 7.71 mmol, 1.1 equiv) in THF (20 mL). Purification by Kugelrohr distillation (2.3×10^{-2} mbar/ 210°C) yields the desired product B as a colorless oil (1.13 g, 5.27 mmol, 75%).

¹H NMR (400 MHz, chloroform-*d*₁) δ (ppm) = 7.53 (s, 1 H, Im-H), 7.03 (s, 1 H, Im-H), 6.99 (s, 1 H, Im-H), 4.10 (t, ³J_{HH} = 5.2 Hz, 2 H, NCH₂), 3.74 (t, ³J_{HH} = 5.2 Hz, 2 H, NCH₂CH₂), 3.67–3.64 (m, 2 H, PEG-CH₂), 3.62–3.59 (m, 4 H, PEG-CH₂), 3.56–3.52 (m, 2 H, PEG-CH₂), 3.38 (s, 3 H, OCH₃); ¹³C NMR (101 MHz, chloroform-*d*₁) δ (ppm) = 137.4, 129.1, 119.3, 71.8, 70.6, 70.5, 70.4, 58.9, 46.9.

mPEG₄Im (C). The general procedure was followed starting from 1H-imidazole (0.481 g, 7.06 mmol), NaH (0.220 g, 9.18 mmol, 1.3 equiv) and mPEG₄Tos (2.80 g, 7.76 mmol, 1.1 equiv) in THF (20 mL). The desired product C was obtained after purification by Kugelrohr distillation (1.7×10^{-2} mbar/ 210°C) as a yellowish oil (1.65 g, 6.38 mmol, 90%).

¹H NMR (400 MHz, chloroform-*d*₁) δ (ppm) = 7.49 (s, 1 H, Im-H), 6.98 (s, 1 H, Im-H), 6.95 (s, 1 H, Im-H), 4.06 (t, ³J_{HH} = 5.2 Hz, 2 H, NCH₂), 3.70 (t, ³J_{HH} = 5.2 Hz, 2 H, NCH₂CH₂), 3.61–3.54 (m, 10 H, PEG-CH₂), 3.52–3.48 (m, 2 H, PEG-CH₂), 3.33 (s, 3 H, OCH₃); ¹³C NMR (101 MHz, chloroform-*d*₁) δ (ppm) = 137.3, 129.0, 119.3, 71.7, 70.5, 70.4, 70.3, 70.3, 58.8, 46.9.

mPEG₅Im (D). The general procedure was followed starting from 1H-imidazole (0.323 g, 4.74 mmol), NaH (0.148 g, 6.16 mmol, 1.3 equiv) and mPEG₅Tos (2.12 g, 5.55 mmol, 1.1 equiv) in THF (20 mL). Filtration through a plug of neutral alumina (dichloromethane/1% methanol) yields the desired product **D** as a yellowish oil (1.32 g, 4.38 mmol, 92%).

¹H NMR (400 MHz, chloroform-*d*₁) δ (ppm) = 7.50 (s, 1 H, Im-H), 6.99 (s, 1 H, Im-H), 6.96 (s, 1 H, Im-H), 4.07 (t, ³J_{HH} = 5.2 Hz, 2 H, NCH₂), 3.70 (t, ³J_{HH} = 5.1 Hz, 2 H, NCH₂CH₂), 3.64–3.55 (m, 14 H, PEG-CH₂), 3.52–3.48 (m, 2 H, PEG-CH₂), 3.33 (s, 3 H, OCH₃); ¹³C NMR (101 MHz, chloroform-*d*₁) δ (ppm) = 137.4, 129.0, 119.3, 71.8, 70.5, 70.5, 70.4, 70.4, 70.4, 70.4, 58.9, 46.9.

mPEG₆Im (E). The general procedure was followed starting from 1H-imidazole (0.289 g, 4.24 mmol), NaH (0.132 g, 5.51 mmol, 1.3 equiv), and mPEG₆Tos (2.10 g, 4.66 mmol, 1.1 equiv). After filtration through a plug of neutral alumina (dichloromethane/1% methanol), the desired product was obtained as a yellowish oil (1.41 g, 4.08 mmol, 96%).

¹H NMR (400 MHz, chloroform-*d*₁) δ (ppm) = 7.62 (s, 1 H, Im-H), 7.05 (s, 1 H, Im-H), 7.02 (s, 1 H, Im-H), 4.13 (t, ³J_{HH} = 5.1 Hz, 2 H, NCH₂), 3.75 (t, ³J_{HH} = 5.2 Hz, 2 H, NCH₂CH₂), 3.66–3.59 (m, 18 H, PEG-CH₂), 3.55–3.52 (m, 2 H, PEG-CH₂), 3.37 (s, 4 H, OCH₃); ¹³C NMR (101 MHz, chloroform-*d*₁) δ (ppm) = 137.4, 129.0, 119.3, 71.8, 70.6, 70.4, 70.4, 58.9, 46.9.

4.2.2. General Procedure to Bis-mPEG_n-imidazolium Iodide 1–5

The respective 1-(polyethylene glycol)imidazole and mPEG_nI (2 equiv) were dissolved in toluene and heated to 60 °C for 48 hours. After cooling to room temperature, the phases were separated and the residue was washed with toluene. For ionic liquids, which are soluble in toluene, the solvent was removed under reduced pressure and the residue was washed with hot *n*-hexane. If necessary, the product can be further purified by the extraction with water from a dichloromethane solution. Then, the water was removed and the desired ionic liquid was dried for 3 days at 50 °C before use.

[(mPEG₂)₂Im]I (1). The general procedure was followed starting from **A** (2.07 g, 12.2 mmol) and mPEG₂I (5.59 g, 24.3 mmol, 2 equiv) in toluene (10 mL) to obtain the desired product **1** as a brownish oil (4.38 g, 10.9 mmol, 90%).

¹H NMR (400 MHz, chloroform-*d*₁) δ (ppm) = 10.02 (s, 1 H, Im-H), 7.56 (s, 1 H, Im-H), 7.55 (s, 1 H, Im-H), 4.57 (t, ³J_{HH} = 4.7 Hz, 4 H, NCH₂), 3.94 (t, ³J_{HH} = 4.7 Hz, 4 H, NCH₂CH₂), 3.72–3.64 (m, 4 H, PEG-CH₂), 3.57–3.50 (m, 4 H, PEG-CH₂), 3.37 (s, 6 H, OCH₃); ¹³C NMR (101 MHz, chloroform-*d*₁) δ (ppm) = 136.6, 122.7, 71.5, 70.3, 68.6, 58.9, 49.8; EA, calculated for C₁₃H₂₅IN₂O₄ (found): C, 39.01% (39.15%); H, 6.30% (6.33%); N, 7.00% (6.87%).

[(mPEG₃)₂Im]I (2). The general procedure was followed starting from **B** (1.09 g, 5.09 mmol) and mPEG₃I (2.79 g, 10.2 mmol, 2 equiv) in toluene (10 mL) to yield the desired product **2** as a brownish oil (2.12 g, 4.34 mmol, 85%).

¹H NMR (400 MHz, chloroform-*d*₁) δ (ppm) = 9.84 (s, 1 H, Im-H), 7.62 (s, 1 H, Im-H), 7.62 (s, 1 H, Im-H), 4.55 (t, ³J_{HH} = 4.7 Hz, 4 H, NCH₂), 3.92 (t, ³J_{HH} = 4.7 Hz, 4 H, NCH₂CH₂), 3.71–3.66 (m, 4 H, PEG-CH₂), 3.65–3.60 (m, 8 H, PEG-CH₂), 3.56–3.51 (m, 4 H, PEG-CH₂), 3.36 (s, 6 H, OCH₃); ¹³C NMR (101 MHz, chloroform-*d*₁) δ (ppm) = 136.6, 122.8, 71.7, 70.2, 70.1, 68.7, 58.8, 49.7 ppm; EA, calculated for C₁₇H₃₃IN₂O₆ (found): C, 41.81% (41.88%); H, 6.81% (6.92%); N, 5.74% (6.00%).

[(mPEG₄)₂Im]I (3). The general procedure was followed starting from **C** (1.62 g, 6.26 mmol) and mPEG₄I (3.98 g, 12.5 mmol, 2 equiv) in toluene (10 mL) to give the desired product **3** as a brownish oil (3.32 g, 5.76 mmol, 92%).

¹H NMR (400 MHz, chloroform-*d*₁) δ (ppm) = 9.88 (s, 1 H, Im-H), 7.63 (s, 1 H, Im-H), 7.63 (s, 1 H, Im-H), 4.54 (pseudo-t, ³J_{HH} = 4.7 Hz, 4 H, NCH₂), 3.92 (pseudo-t, ³J_{HH} = 4.7 Hz, 4 H, NCH₂CH₂), 3.69–3.61 (m, 20 H, PEG-CH₂), 3.56–3.51 (m, 4 H, PEG-CH₂), 3.35 (s, 6 H, OCH₃); ¹³C NMR (101 MHz, chloroform-*d*₁) δ (ppm) = 136.8, 122.9, 71.8,

70.4, 70.3, 70.3, 70.2, 68.7, 58.9, 49.8; EA, calculated for C₂₁H₄₁IN₂O₈ (found): C, 43.75% (43.78%); H, 7.17% (7.40%); N, 4.86% (5.55%).

[(mPEG₅)₂Im]I (4). The general procedure was followed starting from **D** (1.25 g, 4.13 mmol) and mPEG₅I (2.99 g, 8.25 mmol, 2 equiv) in toluene (10 mL) yielding the desired product **4** as a brownish oil (2.70 g, 4.06 mmol, 98%).

¹H NMR (400 MHz, chloroform-*d*₁) δ (ppm) = 9.70 (s, 1 H, Im-H), 7.65 (s, 1 H, Im-H), 7.65 (s, 1 H, Im-H), 4.53 (pseudo-t, ³J_{HH} = 4.7 Hz, 4 H, NCH₂), 3.90 (pseudo-t, ³J_{HH} = 4.7 Hz, 4 H, NCH₂CH₂), 3.67–3.58 (m, 28 H, PEG-CH₂), 3.52–3.48 (m, 4 H, PEG-CH₂), 3.33 (s, 6 H, OCH₃); ¹³C NMR (101 MHz, chloroform-*d*₁) δ (ppm) = 136.8, 122.9, 71.8, 70.4, 70.4, 70.3, 70.3, 70.3, 70.2, 68.7, 58.9, 49.7; EA, calculated for C₂₅H₄₉IN₂O₁₀ (found): C, 45.18% (44.63%); H, 7.43% (7.57%); N, 4.22% (4.76%).

[(mPEG₆)₂Im]I (5). The general procedure was followed starting from **E** (1.25 g, 3.59 mmol) and mPEG₆I (2.92 g, 7.19 mmol, 2 equiv) in toluene (10 mL) to obtain the desired product **5** as a brownish oil (2.60 g, 3.45 mmol, 96%).

¹H NMR (400 MHz, chloroform-*d*₁) δ (ppm) = 9.73 (s, 1 H, Im-H), 7.64 (s, 1 H, Im-H), 7.64 (s, 1 H, Im-H), 4.54 (pseudo-t, ³J_{HH} = 4.7 Hz, 4 H, NCH₂), 3.91 (pseudo-t, ³J_{HH} = 4.7 Hz, 4 H, NCH₂CH₂), 3.68–3.59 (m, 32 H, PEG-CH₂), 3.50–3.54 (m, 4 H, PEG-CH₂), 3.35 (s, 6 H, OCH₃); ¹³C NMR (101 MHz, chloroform-*d*₁) δ (ppm) = 136.8, 122.9, 71.8, 70.5, 70.4, 70.4, 70.3, 70.3, 70.2, 68.8, 58.9, 49.8; EA, calculated for C₂₉H₅₇IN₂O₁₂ (found): C, 46.28% (45.76%); H, 7.63% (7.74%); N, 3.72% (4.22%).

4.2.3. Synthesis of [(mPEG_n)₂][OMs] (6)

A mixture of mPEG_nIm (**C**) (0.615 g, 2.38 mmol) and mPEG_nOMs (1.02 g, 3.57 mmol, 1.5 equiv) were heated to 60 °C for 48 hours. After cooling to room temperature the mixture was washed with diethyl ether (8 × 10 mL). The product was extracted with dichloromethane (10 mL), filtered and the solvent was removed under reduced pressure. The desired product **6** was further dried for 3 days at 50 °C *in vacuo* to yield a yellowish oil (1.25 g, 2.30 mmol, 96%).

¹H NMR (400 MHz, chloroform-*d*₁) δ (ppm) = 9.80 (s, 1 H, Im-H), 7.53 (s, 1 H, Im-H), 7.52 (s, 1 H, Im-H), 4.48 (pseudo-t, ³J_{HH} = 4.7 Hz, 4 H, NCH₂), 3.86 (pseudo-t, ³J_{HH} = 4.7 Hz, 4 H, NCH₂CH₂), 3.65–3.58 (m, 20 H, PEG-CH₂), 3.54–3.50 (m, 4 H, PEG-CH₂), 3.34 (s, 6 H, OCH₃), 2.80 (s, 3 H, SCH₃); ¹³C NMR (101 MHz, chloroform-*d*₁) δ (ppm) = 137.6, 122.7, 71.7, 70.4, 70.3, 70.3, 70.1, 69.0, 58.8, 49.4, 39.4; EA, calculated for C₂₂H₄₄N₂O₁₁S (found): C, 48.52% (46.23%); H, 8.14% (8.02%); N, 5.14% (5.39%); S 5.89% (5.49).

4.2.4. Synthesis of [(mPEG_n)₂][PF₆] (7)

[(mPEG₄)₂Im]I (3) (0.503 g, 0.873 mmol) was dissolved in water (10 mL), AgPF₆ (0.360 g, 1.42 mmol, 1.6 equiv) was added and the reaction mixture was stirred at room temperature for 24 hours in the dark. The resulting suspension was diluted with dichloromethane (60 mL) and the phases were separated and the aqueous phase was extracted with dichloromethane (3 × 10 mL). The combined organic phases were filtered and washed again with water (4 × 10 mL). The organic phase was dried with MgSO₄, filtered and the solvent was removed *in vacuo* to give the desired product **5** as a yellowish oil (0.398 g, 0.670 mmol, 77%).

¹H NMR (400 MHz, chloroform-*d*₁) δ (ppm) = 8.78 (s, 1 H, Im-H), 7.50 (s, 1 H, Im-H), 7.49 (s, 1 H, Im-H), 4.36 (pseudo-t, ³J_{HH} = 4.7 Hz, 4 H, NCH₂), 3.86 (pseudo-t, ³J_{HH} = 4.7 Hz, 4 H, NCH₂CH₂), 3.68–3.59 (m, 20 H, PEG-CH₂), 3.56–3.51 (m, 4 H, PEG-CH₂), 3.34 (s, 6 H, OCH₃); ¹³C NMR (101 MHz, chloroform-*d*₁) δ (ppm) = 136.4, 122.8, 71.8, 70.4, 70.3, 70.3, 70.2, 70.2, 68.5, 58.8, 49.7; ¹⁹F NMR (377 MHz, chloroform-*d*₁) δ (ppm) = -72.42 (d, ¹J_{PF} = 710.1 Hz, PF₆⁻); ³¹P NMR (162 MHz, chloroform-*d*₁) δ (ppm) = -143.76 (sept, ¹J_{PF} = 710.2 Hz, PF₆⁻); EA, calculated for C₂₁H₄₁F₆N₂O₈P (found): C, 42.43% (42.20%); H, 6.95% (6.95%); N, 4.71% (5.06%).

4.2.5. Synthesis of [(mPEG₄)₂[NTf₂]⁻] (8)

A solution of [(mPEG₄)₂] [OMs] (6) (0.489 g, 0.898 mmol) were placed in a flame-dried Schlenk flask and dissolved in dry dichloromethane (15 mL). Then, LiNTf₂ (0.515 g, 1.80 mmol, 2 equiv) was added and the suspension was stirred for 3 days at room-temperature. The precipitate was filtered off and the organic phase was washed with water (4 × 15 mL). The organic phase was dried with MgSO₄, filtered, and the solvent was removed under reduced pressure. The desired product 8 was further dried *in vacuo* at 50 °C for 3 days to give a yellowish oil (0.501 g, 0.686 mmol, 76%).

¹H NMR (400 MHz, chloroform-*d*₁) δ (ppm) = 8.91 (s, 1 H, Im-H), 7.53 (s, 1 H, Im-H), 7.52 (s, 1 H, Im-H), 4.38 (t, ³J_{HH} = 4.7 Hz, 4 H, NCH₂), 3.86 (t, ³J_{HH} = 4.7 Hz, 4 H, NCH₂CH₂), 3.69–3.59 (m, 20 H, PEG-CH₂), 3.56–3.51 (m, 4 H, PEG-CH₂), 3.34 (s, 6 H, OCH₃); ¹³C NMR (101 MHz, chloroform-*d*₁) δ (ppm) = 136.60 (s), 123.07 (s), 119.88 (q, ¹J_{CF} = 322.1 Hz, N(SO₂CF₃)₂), 71.88 (s), 70.48 (s), 70.40 (s), 70.37 (s), 70.34 (s), 70.30 (s), 68.69 (s), 58.93 (s), 49.83 (s); ¹⁹F NMR (377 MHz, chloroform-*d*₁) δ (ppm) = -78.77 (s, N(SO₂CF₃)₂); EA, calculated for C₂₅H₄₁F₉N₃O₁₂S₂ (found): C, 37.86% (37.61%); H, 5.66% (5.13%); N, 5.76% (5.24%); S, 8.79% (8.60%).

Declaration of Competing Interest

The authors declare that they have no known competing financial interests or personal relationships that could have appeared to influence the work reported in this paper.

Acknowledgements

Funded by the Deutsche Forschungsgemeinschaft (DFG, German Research Foundation) – Project-IDs 431791331 – SFB 1452, BA4277/11-1, 377472739/GRK 2423/1-2019 FRASCAL, and the Bundesministerium für Bildung und Forschung (BMBF, German Federal Ministry of Education and Research) – Grant 03HY1051.

Supplementary materials

Supplementary material associated with this article can be found, in the online version, at doi:10.1016/j.jil.2022.100041.

References

- Abraham, M.J., Murtola, T., Schulz, R., Páll, S., Smith, J.C., Hess, B., Lindahl, E., 2015. SoftwareX 1-2, 19.
- Bara, J.E., Gabriel, C.J., Lessmann, S., Carlisle, T.K., Finotello, A., Gin, D.L., Noble, R.D., 2007. Ind. Eng. Chem. Res. 46, 5380.
- Bara, J.E., Noble, R.D., Gin, D.L., 2009. Ind. Eng. Chem. Res. 48, 4607.
- Beiranvand, F., Najibi, S.H., Shahraiki, B.H., 2020. Iranian J. Oil Gas Sci. Technol. 9, 26.
- Branco, L.C., Rosa, J.N., Ramos, J.J.M., Afonso, C.A.M., 2002. Chem. Eur. J. 3, 3671.
- Branco, L.C., Rosa, J.N., Ramos, J.J.M., Afonso, C.A.M., 2002. Chem. Eur. J. 3, 3671.
- Cao, Y., Mu, T., 2014. Ind. Eng. Chem. Res. 53, 8651.
- Cecchini, M.M., Charnay, C., De Angelis, F., Lamaty, F., Martinez, J., Colacino, E., 2014. ChemSusChem 7, 45.
- Chan, B.K.M., Chang, N., Grimmitt, M.R., 1977. Aust. J. Chem. 30, 2005.
- Chavan, S.N., 2015. D. Mandal, RSC Adv. 5, 64821.
- Chavan, S.N., Tiwari, A., Nagaiah, T.C., Mandal, D., 2016. Phys. Chem. Chem. Phys. 18, 16116.
- Chen, J., Spear, S.K., Huddleston, J.G., Rogers, R.D., 2005. Green Chem 7, 64.
- Chen, Z., Huo, Y., Cao, J., Xu, L., Zhang, S., 2016. Ind. Eng. Chem. Res. 55, 11589.
- Colacino, E., Martinez, J., Lamaty, F., Patrikeeva, L.S., Khemchyan, L.L., Ananikov, V.P., Beletskaya, I.P., 2012. Coord. Chem. Rev. 256, 2893.
- Connelly, N.G., Geiger, W.E., 1996. Chem. Rev. 96, 877.
- Damilano, G., Kalebic, D., Binnebens, K., Dehaen, W., 2020. RSC Adv. 10, 21071.
- Daura, K.G.X., Jaun, B., Seebach, D., van Gunsteren, W.F., Mark, A.E., 1999. Angew. Chem. Int. Ed. 38, 236.
- De Vos, N., Maton, C., Stevens, C.V., 2014. ChemElectroChem 1, 1258.
- Deng, J., Bai, L., Zeng, S., Zhang, X., Nie, Y., Deng, L., Zhang, S., 2016. RSC Adv. 6, 45184.
- Ditchfield, R., Hehre, W.J., Pople, J.A., 1971. J. Chem. Phys. 54, 724.
- Döbbelin, M., Azcune, I., Bedu, M., Ruiz de Luzuriaga, A., Genua, A., Jovanovski, V., Cabañero, G., Odriozola, I., 2012. Chem. Mater. 24, 1583.
- Donato, R.K., Migliorini, M.V., Benvegnú, M.A., Dupont, J., Gonçalves, R.S., Schrekker, H.S., 2007. J. Solid State Electrochem. 11, 1481.
- Dorjnamjin, D., Ariunaa, M., Shim, Y.K., 2008. Int. J. Mol. Sci. 9, 807.
- Dupradeau, F.Y., Pigache, A., Zaffran, T., Savineau, C., Lelong, R., Grivel, N., Lelong, D., Rosanski, W., Cieplak, P., 2010. Phys. Chem. Chem. Phys. 12, 7821.

- Dzyuba, S.V., Bartsch, R.A., 2002. ChemPhysChem 3, 161.
- Ejigu, A., Lovelock, K.R.J., Licence, P., Walsh, D.A., 2011. Electrochim. Acta 56, 10313.
- Fei, Z., Ang, W.H., Zhao, D., Scopelliti, R., Zvereva, E.E., Katsyuba, S.A., Dyson, P.J., 2007. J. Phys. Chem. B 111, 10095.
- Francl, M.M., Pietro, W.J., Hehre, W.J., 1982. J. Chem. Phys. 77, 3654.
- Frisch, M.J., Trucks, G.W., Schlegel, H.B., Scuseria, G.E., Robb, M.A., Cheeseman, J.R., Scalmani, G., Barone, V., Petersson, G.A., Nakatsuji, H., Li, X., Caricato, M., Marenich, A.V., Bloino, J., Janesko, B.G., Gomperts, R., Mennucci, B., Hratchian, H.P., Ortiz, J.V., Izmaylov, A.F., Sonnenberg, J.L., Williams-Young, D., Ding, F., Lipparini, F., Egidi, F., Goings, J., Peng, B., Petrone, A., Henderson, T., Ranasinghe, D., Zakrzewski, V.G., Gao, J., Rega, N., Zheng, G., Liang, W., Hada, M., Ehara, M., Toyota, K., Fukuda, R., Hasegawa, J., Ishida, M., Nakajima, T., Honda, Y., Kitao, O., Nakai, H., Vreven, T., Throssell, K., Montgomery Jr, J.A., Peralta, J.E., Ogliaro, F., Bearpark, M.J., Heyd, J.J., Brothers, E.N., Kudin, K.N., Staroverov, V.N., Keith, T.A., Kobayashi, R., Normand, J., Raghavachari, K., Rendell, A.P., Burant, J.C., Iyengar, S.S., Tomasi, J., Cossi, M., Millam, J.M., Klene, M., Adamo, C., Cammi, R., Ochterski, J.W., Martin, R.L., Morokuma, K., Farkas, O., Foresman, J.B., 2016. Gaussian 16, Revision C.01.
- Fulmer, G.R., Miller, A.J.M., Sherden, N.H., Gottlieb, H.E., Nudelman, A., Stoltz, B.M., Bercaw, J.E., Goldberg, K.I., 2010. Organometallics 29, 2176.
- Ganapatibhotla, L.V.N.R., Zheng, J., Roy, D., Krishnan, S., 2010. Chem. Mat. 22, 6347.
- Ghatee, M.H., Zare, M., Moosavi, F., Zolghadr, A.R., 2010. J. Chem. Eng. Data 55, 3084.
- Guo, X., Yao, W., Chen, Y., Fan, J., Zhao, Y., Wang, J., 2017. J. Mol. Liq. 236, 308.
- Hehre, W.J., Ditchfield, R., Pople, J.A., 1972. J. Chem. Phys. 56, 2257.
- Ikedo, N., Teshima, K., Miyasaka, T., 2006. Chem. Commun. 1733.
- Jadhav, V.H., Jeong, H.-J., T, L.S., Sohn, M.-H., Kim, D.W., 2011. Org. Lett. 13, 2502.
- Jadhav, V.H., Kim, J.-Y., Chi, D.Y., Lee, S., Kim, D.W., 2014. Tetrahedron 70, 533.
- Jadhav, V.H., Lee, S.B., Jeong, H.-J., Lim, S.T., Sohn, M.-H., Kim, D.W., 2012. Tetrahedron Lett 53, 2051.
- Jander, J.H., Schmidt, P.S., Giraudet, C., Wasserscheid, P., Rausch, M.H., Fröba, A.P., 2021. Int. J. Hydrog. Energy 46, 19446.
- Kerscher, M., Jander, J.H., Junwei, J., Martin, M.M., Wolf, M., Preuster, P., Rausch, M.H., Wasserscheid, P., Koller, T.M., Fröba, A.P., 2022. Int. J. Hydrog. Energy.
- Kolbeck, C., Killian, M., Maier, F., Paape, N., Wasserscheid, P., Steinrück, H.-P., 2008. Langmuir 24, 9500.
- Kolbeck, C., Lehmann, J., Lovelock, K.R.J., Cremer, T., Paape, N., Wasserscheid, P., Fröba, A.P., Maier, F., Steinrück, H.-P., 2010. J. Phys. Chem. B 114, 17025.
- Koller, T.M., Rausch, M.H., Pohako-Esko, K., Wasserscheid, P., Fröba, A.P., 2015. J. Chem. Eng. Data 60, 2665.
- Kouwer, P.H.J., Swager, T.M., 2007. J. Am. Chem. Soc. 129, 14042.
- Lall-Ramnarin, S.L., Zhao, M., Rodriguez, C., Fernandez, R., Zmich, N., Fernandez, E.D., Dhiman, S.B., Castner, E.W., Wishart, J.F., 2017. J. Electrochem. Soc. 164, H5247.
- Lee, J., Murugappan, K., Arrigan, D.W.M., Silvester, D.S., 2013. Electrochim. Acta 101, 158.
- Lemmon, E.W., Huber, M.L., McLinden, M.O., 2018. National Institute of Standards and Technology.
- Lewandowski, A., Waligora, L., Galinski, M., 2013. J. Solut. Chem. 42, 251.
- Liu, H.Y., Scharbert, B., Holm, R.H., 1991. J. Am. Chem. Soc. 113, 9529.
- López, F.I., Domínguez, J.M., Miranda, A.D., Trejo-Durán, M., Alvarado-Méndez, E., Vázquez, M.A., 2019. Opt. Mater. 96, 109276.
- Lovelock, K.R.J., Kolbeck, C., Cremer, T., Paape, N., Schulz, P.S., Wasserscheid, P., Maier, F., Steinrück, H.-P., 2009. J. Phys. Chem. B 113, 2854.
- Luo, S., Zhang, S., Wang, Y., Xia, A., Zhang, G., Du, X., Xu, D., 2010. J. Org. Chem. 75, 1888.
- Marcó, A., Compañó, R., Rubio, R., Casals, I., 2003. Microchim. Acta 142, 13.
- Matsumoto, H., Sakaebe, H., Tatsumi, K., 2005. J. Power Sources 146, 45.
- Migliorati, V., Serva, A., Aquilanti, G., Olivi, L., Pascarelli, S., Mathon, O., D'Angelo, P., 2015. Phys. Chem. Chem. Phys. 17, 2464.
- Montiel, M.A., Solla-Gullon, J., Montiel, V., Sanchez-Sanchez, C.M., 2018. Phys. Chem. Chem. Phys. 20, 19160.
- Nagaraju, G., Manjunath, K., Sarkar, S., Gunter, E., Teixeira, S.R., Dupont, J., 2015. Int. J. Hydrog. Energy 40, 12209.
- Niedemaier, I., Kolbeck, C., Steinrück, H.-P., Maier, F., 2016. Rev. Sci. Instrum. 87, 045105.
- O'Driscoll, L.J., Welsh, D.J., Bailey, S.W.D., Visontai, D., Frampton, H., Bryce, M.R., Lambert, C.J., 2015. Chem. Eur. J. 21, 3891.
- O'Mahony, A.M., Silvester, D.S., Aldous, L., Hardacre, C., Compton, R.G., 2008. J. Chem. Eng. Data 53, 2884.
- Pigache, A., Cieplak, P., Dupradeau, F., 2004. Abstracts Of Papers Of The American Chemical Society 227, U1011.
- Pratt, K.W., Koch, W.F., Wu, Y.C., Berezansky, P.A., 2001. Pure Appl. Chem. 73, 1783.
- Pronk, S., Pall, S., Schulz, R., Larsson, P., Bjelkmar, P., Apostolov, R., Shirts, M.R., Smith, J.C., Kasson, P.M., van der Spoel, D., Hess, B., Lindahl, E., 2013. Bioinformatics 29, 845.
- Rassolov, V.A., Ratner, M.A., Pople, J.A., Redfern, P.C., Curtiss, L.A., 2001. J. Comput. Chem. 22, 976.
- Riisager, A., Fehrmann, R., Berg, R.W., van Hal, R., Wasserscheid, P., 2005. Phys. Chem. Chem. Phys. 7, 3052.
- Roy, R.K., Gowd, E.B., Ramakrishnan, S., 2012. Macromolecules 45, 3063.
- Rusanov, A.I., Prokhorov, V.A., 1996. Interfacial tensiometry. Elsevier, Amsterdam.
- Sato, T., Masuda, G., Takagi, K., 2004. Electrochim. Acta 49, 3603.
- Schrekker, H.S., Gelesky, M.A., Stracke, M.P., Schrekker, C.M., Machado, G., Teixeira, S.R., Rubim, J.C., Dupont, J., 2007. J. Colloid Interface Sci. 316, 189.
- Schrekker, H.S., Silva, D.O., Gelesky, M.A., Stacke, M.P., Schrekker, C.M., Gonçalves, R.S., Dupont, J., 2008. J. Braz. Chem. Soc. 19, 426.
- Schrekker, H.S., Silva, D.O., Gelesky, M.A., Stracke, M.P., Schrekker, C.M., Gonçalves, R.S., Dupont, J., 2008. J. Braz. Chem. Soc. 19, 426.

- Seidl, V., Sternberg, M., Heinemann, F.W., Schmiele, M., Unruh, T., Wasserscheid, P., Meyer, K., 2021. *Cryst. Growth Des.* 21, 6276.
- Sequeira, M.C.M., Pereira, M.F.V., Avelino, H.M.N.T., Caetano, F.J.P., Fareira, J.M.N.A., 2019. *Fluid Phase Equilibria* 496, 7.
- Sharma, P., Choi, S.-H., Park, S.-D., Baek, I.-H., Lee, G.-S., 2012. *Chem. Eng. J.* 181-182, 834.
- Shiddiky, M.J.A., Torriero, A.A.J., Zhao, C., Burgar, I., Kennedy, G., Bond, A.M., 2009. *J. Am. Chem. Soc.* 131, 7976.
- Shimizu, K., Bernardes, C.E., Triolo, A., Canongia Lopes, J.N., 2013. *Phys. Chem. Chem. Phys.* 15, 16256.
- Shimizu, K., Heller, B.S.J., Maier, F., Steinrück, H.P., Canongia Lopes, J.N., 2018. *Langmuir* 34, 4408.
- Steinrück, H.P., 2012. *Phys. Chem. Chem. Phys.* 14, 5010.
- Tang, S., Baker, G.A., Zhao, H., 2012. *Chem. Soc. Rev.* 41, 4030.
- Vucemilovic-Alagic, N., Banhatti, R.D., Stepic, R., Wick, C.R., Berger, D., Gaimann, M.U., Baer, A., Harting, J., Smith, D.M., Smith, A.S., 2019. *J. Colloid Interface Sci.* 553, 350.
- Wang, J., Wolf, R.M., Caldwell, J.W., Kollman, P.A., Case, D.A., 2004. *J. Comput. Chem.* 25, 1157.
- Wang, X., Heinemann, F.W., Yang, M., Melcher, B.U., Fekete, M., Mudring, A.V., Wasserscheid, P., Meyer, K., 2009. *Chem. Commun.* 7405.
- Wang, X., Sternberg, M., Kohler, F.T.U., Melcher, B.U., 2014. *P. Wasserscheid, K. Meyer, RSC Adv.* 4, 12476.
- Wang, X., Vogel, C.S., Heinemann, F.W., Wasserscheid, P., Meyer, K., 2011. *Cryst. Growth Des.* 11, 1974.
- Wasserscheid, P., Welton, T., 2008. *Ionic Liquids in Synthesis*, 1st edn. Wiley-VCH, Weinheim.
- Winther-Jensen, B., Fraser, K., Ong, C., Forsyth, M., MacFarlane, D.R., 2010. *Adv. Mater.* 22, 1727.
- Xu, W., Angell, C.A., 2003. *Science* 302, 422.
- Yang, Z.Z., He, L.N., Song, Q.W., Chen, K.H., Liu, A.H., Liu, X.M., 2012. *Phys. Chem. Chem. Phys.* 14, 15832.
- Zeng, H.J., Johnson, M.A., Ramdihal, J.D., Sumner, R.A., Rodriguez, C., Lall-Ramnarine, S.I., Wishart, J.F., 2019. *J. Phys. Chem. A* 123, 8370.
- Zhang, J., Fang, S., Qu, L., Jin, Y., Yang, L., Hirano, S.-i., 2014. *Ind. Eng. Chem. Res.* 53, 16633.
- Zhou, Z.B., Matsumoto, H., Tatsumi, K., 2004. *Chem. Eur. J.* 10, 6581.
- Zhou, Z.B., Matsumoto, H., Tatsumi, K., 2006. *Chem. Eur. J.* 12, 2196.

SUPPORTING INFORMATION

Bis-Polyethylene Glycol-Functionalized Imidazolium Ionic Liquids: a Multi-Method Approach Towards Bulk and Surface Properties

Vera Seidl,^[a] Michael Bosch,^[b] Ulrike Paap,^[c] Mattia Livraghi,^[d] Ziwen Zhai,^[e] Christian Wick,^[d] Thomas M. Koller,^[e] Peter Wasserscheid,^[f,g] Florian Maier,^[c] Ana-Sunčana Smith,^[d] Julien Bachmann,^[b] Hans-Peter Steinrück,^[c] Karsten Meyer^{[a]*}

^[a] Department of Chemistry and Pharmacy, Inorganic Chemistry, Friedrich-Alexander-Universität Erlangen-Nürnberg (FAU), Egerlandstr. 1, 91058 Erlangen

^[b] Department of Chemistry and Pharmacy, Chemistry of Thin Film Materials, Interdisciplinary Center for Nanostructured Films (IZNF), Friedrich-Alexander-Universität Erlangen-Nürnberg (FAU), Cauerstr. 3, 91058 Erlangen

^[c] Department of Chemistry and Pharmacy, Physical Chemistry, Friedrich-Alexander-Universität Erlangen-Nürnberg (FAU), Egerlandstr. 3, 91058 Erlangen

^[d] Department of Physics, Institute for Theoretical Physics, PULS Group, Interdisciplinary Center for Nanostructured Films (IZNF), Friedrich-Alexander-Universität Erlangen-Nürnberg (FAU), Cauerstr. 3, 91058 Erlangen

^[e] Department of Chemical and Biological Engineering and Erlangen Graduate School in Advanced Optical Technologies, Institute of Advanced Optical Technologies – Thermophysical Properties, Friedrich-Alexander-Universität Erlangen-Nürnberg (FAU), Paul-Gordan-Str. 8, 91052 Erlangen

^[f] Department of Chemical and Biological Engineering, Chemical Engineering, Friedrich-Alexander-Universität Erlangen-Nürnberg (FAU), Egerlandstr. 3, 91058 Erlangen

^[g] Forschungszentrum Jülich, Helmholtz-Institute Erlangen-Nürnberg for Renewable Energy (IEK 11), Egerlandstr. 3, 91058 Erlangen, Germany

Contents

1	NMR Spectroscopy	2
2	Differential Scanning Calorimetry	2
3	Thermogravimetric Analysis	4
4	Viscosity	4
5	Liquid Density	6
6	Electrochemical Measurements	7
7	Angle-Resolved X-ray Photoelectron Spectroscopy (AR-XPS)	9
8	Surface Tension	10
9	Molecular Dynamics Simulations	11

SUPPORTING INFORMATION

1 NMR Spectroscopy

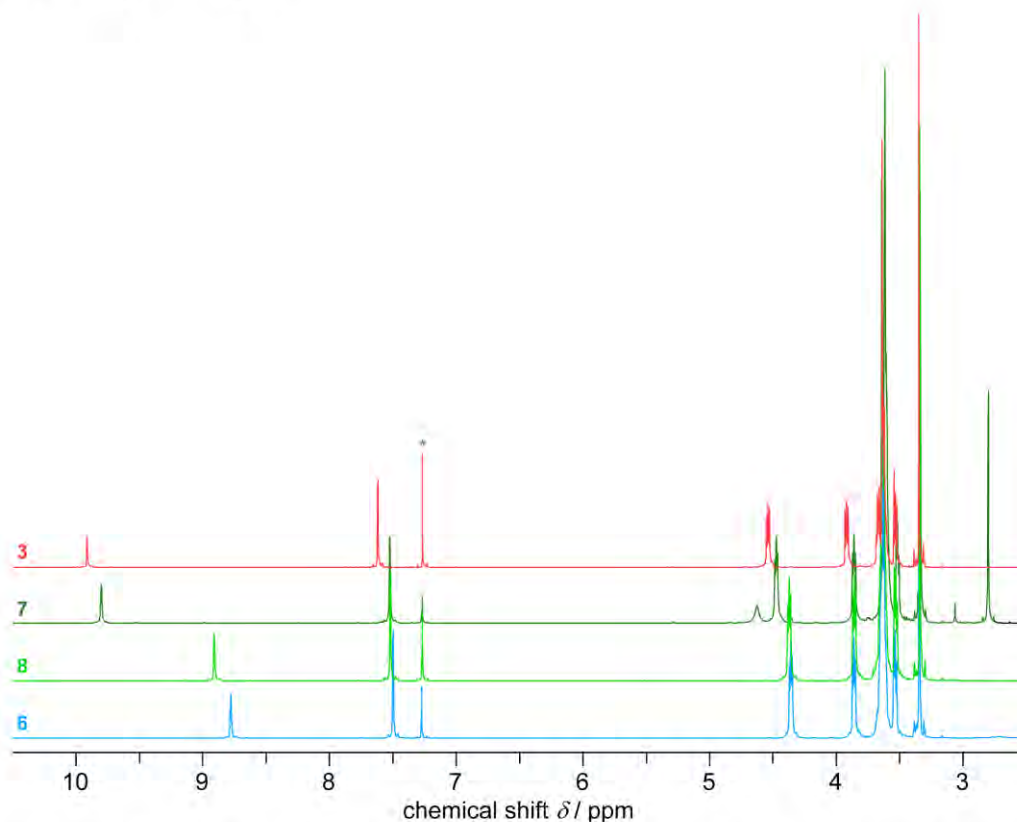


Figure S1. Compared ^1H NMR spectra of $[(\text{mPEG}_4)_2\text{Im}]\text{I}$ (**3**), $[(\text{mPEG}_4)_2\text{Im}][\text{PF}_6]$ (**6**), $[(\text{mPEG}_4)_2\text{Im}][\text{OMs}]$ (**7**), $[(\text{mPEG}_4)_2\text{Im}][\text{NTf}_2]$ (**8**), measured in chloroform- d_1 at 400 MHz at room temperature. Solvent residual signals are marked with an asterisk (*).

2 Differential Scanning Calorimetry

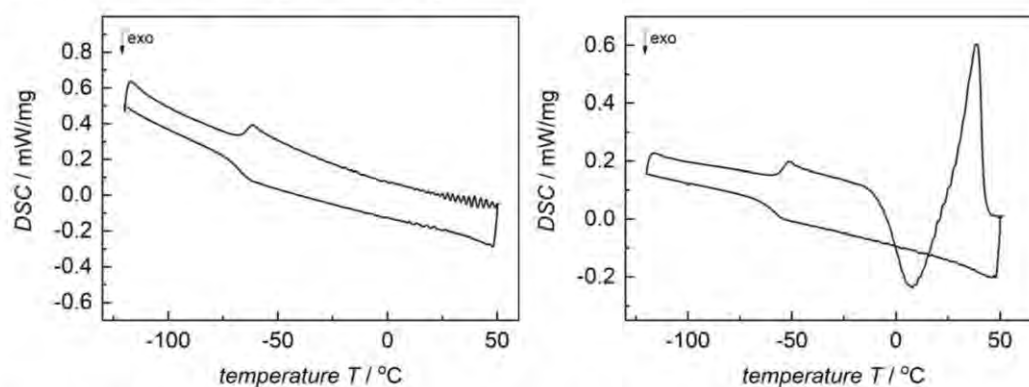


Figure S2. DSC traces of $[(\text{mPEG}_2)\text{Im}]\text{I}$ (**1**) (left) and $[(\text{mPEG}_2)\text{Im}]\text{I}$ (**2**) (right); data obtained during 2nd heating cycle are shown. Onset temperatures ($^{\circ}\text{C}$) were determined at heating/cooling rates of 5 K min^{-1} (N_2 atmosphere, Al-pan). Exothermic peaks point downwards.

S2

SUPPORTING INFORMATION

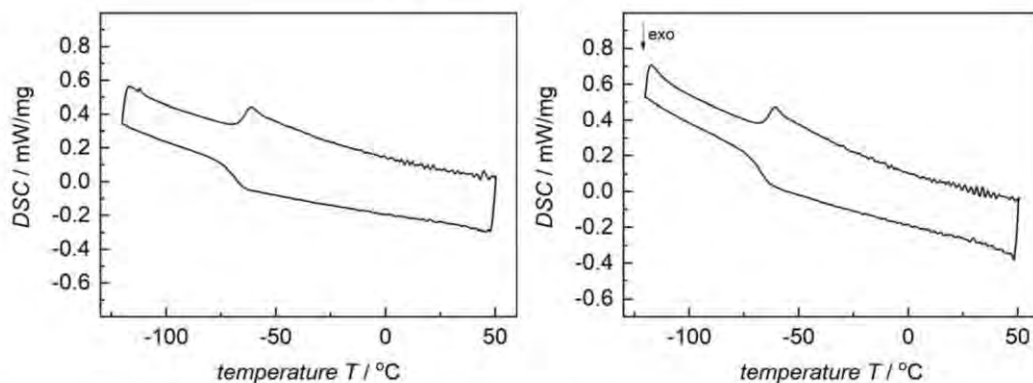


Figure S3. DSC traces of [(mPEG₄)Im]I (**3**) (left) and [(mPEG₅)Im]I (**4**) (right); data obtained during 2nd heating cycle are shown. Onset temperatures (°C) were determined at heating/cooling rates of 5 K min⁻¹ (N₂ atmosphere, Al-pan). Exothermic peaks point downwards.

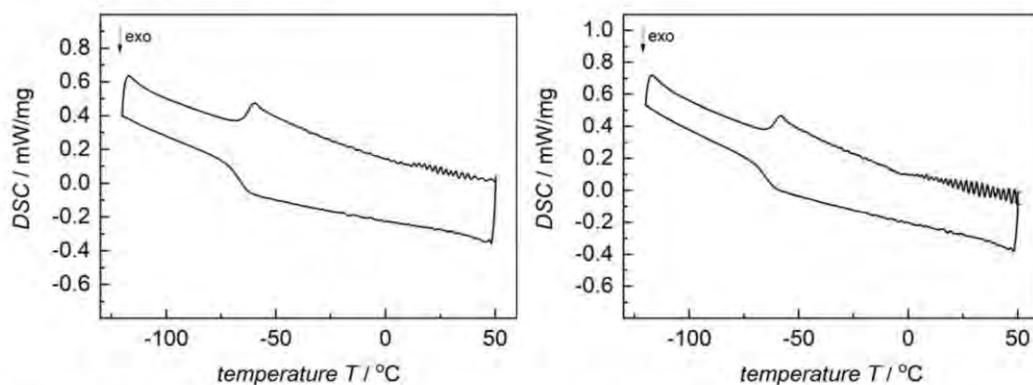


Figure S4. DSC traces of [(mPEG₆)Im]I (**5**) (left) and [(mPEG₄)Im][OMs] (**6**) (right); data obtained during 2nd heating cycle are shown. Onset temperatures (°C) were determined at heating/cooling rates of 5 K min⁻¹ (N₂ atmosphere, Al-pan). Exothermic peaks point downwards.

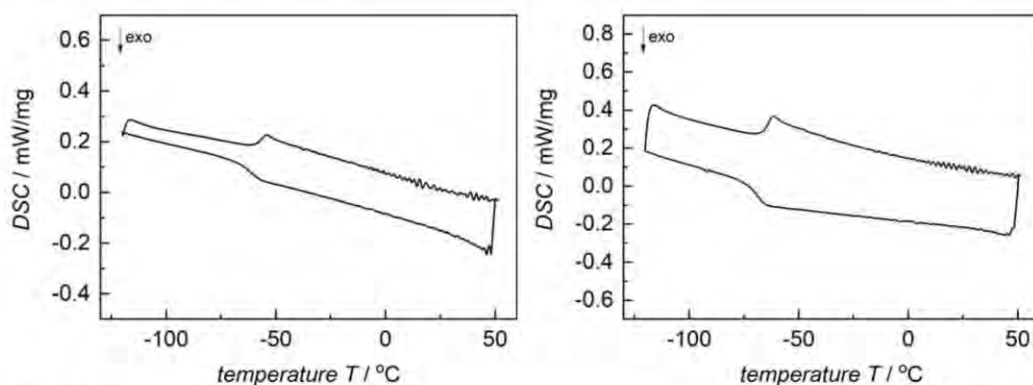


Figure S5. DSC traces of [(mPEG₄)Im][PF₆] (**7**) (left) and [(mPEG₄)Im][NTf₂] (**8**) (right); data obtained during 2nd heating cycle are shown. Onset temperatures (°C) were determined at heating/cooling rates of 5 K min⁻¹ (N₂ atmosphere, Al-pan). Exothermic peaks point downwards.

SUPPORTING INFORMATION

3 Thermogravimetric Analysis

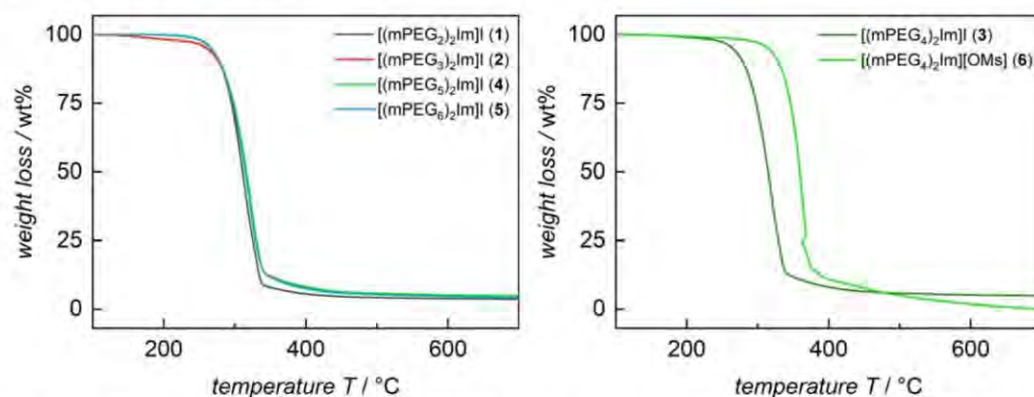


Figure S6. Thermograms of [(mPEG_n)₂Im]I (*n* = 2, 3, 5, 6) (**1**, **2**, **4**, **5**) (left) and [(mPEG₄)₂Im][A] (A = Γ⁻, OMs⁻) (**3**, **6**) (right). Heating rate of 5 K min⁻¹ (N₂ atmosphere).

4 Viscosity

Table S1. Temperature-dependent viscosity data (η) of [(mPEG_n)₂Im]I (*n* = 2–6) (**1**–**5**) at atmospheric pressure of 0.1MPa.

T / K	Viscosity η / mPa s				
	[(mPEG ₂) ₂ Im]I (1)	[(mPEG ₃) ₂ Im]I (2)	[(mPEG ₄) ₂ Im]I (3)	[(mPEG ₅) ₂ Im]I (4)	[(mPEG ₆) ₂ Im]I (5)
293.14	1229.0	972.6	1023.3	900.3	846.8
303.14	533.1	422.1	444.0	402.5	387.2
313.13	262.1	210.1	221.5	206.7	202.5
323.13	143.5	116.9	123.9	117.7	117.7
333.13	86.18	71.14	49.98	73.37	74.32
343.13	55.42	46.54	34.74	49.09	50.28
353.13	37.85	32.26	25.45	34.59	35.78
363.13	27.15	23.52	19.46	25.53	26.61
373.13	20.43	17.87	15.31	19.72	20.65
383.13	15.89	14.10	12.40	15.65	16.50
393.13	12.67	11.35	49.98	12.74	13.51

SUPPORTING INFORMATION

Table S2. Temperature-dependent viscosity data (η) of [(mPEG₄)₂Im][A] (A = OMs⁻, PF₆⁻, NTf₂⁻) (**6–8**) at atmospheric pressure of 0.1MPa.

T / K	Viscosity η / mPa s		
	[(mPEG ₄) ₂ Im][OMs] (6)	[(mPEG ₄) ₂ Im][PF ₆] (7)	[(mPEG ₄) ₂ Im][NTf ₂] (8)
293.14	384.9	573.8	176.1
303.14	182.2	263.9	93.61
313.13	100.2	140.1	56.10
323.13	61.65	81.88	36.40
333.13	41.71	52.45	25.30
343.13	30.27	35.78	18.50
353.13	23.26	25.68	14.14
363.13	18.71	19.30	11.10
373.13	15.51	15.10	9.02
383.13	13.13	12.13	7.63
393.13	11.36	9.93	6.38

Table S3. Fit coefficient of Vogel-Tammann-Fulcher equation $\eta = \eta_0 \cdot \exp[B/(T-T_0)]$ for viscosity data of IL **1–8**.

IL	η_0 / mPa s	B / K	T ₀ / K	R ²	AARD / % ^{a)}
[(mPEG ₂) ₂ Im]I (1)	0.092	983.40	189.70	0.999	2.952
[(mPEG ₃) ₂ Im]I (2)	0.138	849.37	197.20	0.999	2.113
[(mPEG ₄) ₂ Im]I (3)	0.178	808.40	199.75	0.999	1.806
[(mPEG ₅) ₂ Im]I (4)	0.216	777.88	199.81	1.000	1.504
[(mPEG ₆) ₂ Im]I (5)	0.267	748.51	200.30	1.000	1.143
[(mPEG ₄) ₂ Im][OMs] (6)	0.802	443.91	221.22	0.999	2.365
[(mPEG ₄) ₂ Im][PF ₆] (7)	0.248	694.62	203.45	1.000	0.825
[(mPEG ₄) ₂ Im][NTf ₂] (8)	0.323	566.11	203.28	1.000	0.336

^{a)} Average absolute relative deviation between the experimental η data and the correlation.

SUPPORTING INFORMATION

5 Liquid Density

Table S4. Temperature-dependent liquid density (ρ) of [(mPEG_n)₂Im]I ($n = 2, 4, 6$) (**1, 3, 5**) at an argon pressure of 0.1 MPa.^{a)}

[(mPEG ₂) ₂ Im]I (1)		[(mPEG ₄) ₂ Im]I (3)		[(mPEG ₆) ₂ Im]I (5)	
T / K	$\rho / \text{g cm}^{-3}$	T / K	$\rho / \text{g cm}^{-3}$	T / K	$\rho / \text{g cm}^{-3}$
283.15	1.4271	283.15	1.3230	283.15	1.2796
288.15	1.4228	288.15	1.3188	288.15	1.2753
293.15	1.4184	293.15	1.3146	293.15	1.2710
298.15	1.4141	298.15	1.3103	298.15	1.2668
303.15	1.4098	303.16	1.3061	303.16	1.2625
308.16	1.4055	308.16	1.3019	308.16	1.2583
313.16	1.4013	313.16	1.2977	313.16	1.2541
318.16	1.3970	318.16	1.2935	318.16	1.2499
323.16	1.3928	323.16	1.2894	323.16	1.2459
328.16	1.3887	328.16	1.2854	328.16	1.2418
333.16	1.3847	333.16	1.2813	333.16	1.2378
338.16	1.3806	338.17	1.2773	338.16	1.2338
343.16	1.3765	343.16	1.2733	343.16	1.2297
348.15	1.3725	348.15	1.2693	348.16	1.2257
353.15	1.3685	353.15	1.2653	353.16	1.2217
358.15	1.3645	358.15	1.2614	358.16	1.2177
368.15	1.3604	363.15	1.2574	363.16	1.2138

^{a)} The expanded uncertainties ($k = 2$) for temperature and pressure are 0.01 K and 3 kPa, respectively. For the density, the relative expanded uncertainty ($k = 2$) is 0.02%.

Table S5. Fit coefficients of the second-order polynomial $\rho_{\text{calc}}(T) = \rho_0 + \rho_1 T + \rho_2 T^2$ for temperature-dependent liquid density data $\rho_{\text{calc}}(T)$ of [(mPEG_n)₂Im]I ($n = 2, 4, 6$) (**1, 3, 5**).

IL	$\rho_0 / \text{g cm}^{-3}$	$\rho_1 / \text{g cm}^{-3} \text{K}^{-1}$	$\rho_2 / \text{g cm}^{-3} \text{K}^{-2}$	R^2	AARD / % ^{a)}
[(mPEG ₂) ₂ Im]I (1)	1.7215	$-1.2009 \cdot 10^{-3}$	$5.7002 \cdot 10^{-7}$	1.000	0.0024
[(mPEG ₄) ₂ Im]I (3)	1.6043	$-1.1282 \cdot 10^{-3}$	$4.7691 \cdot 10^{-7}$	0.999	0.0027
[(mPEG ₆) ₂ Im]I (5)	1.5624	$-1.1376 \cdot 10^{-3}$	$4.8934 \cdot 10^{-7}$	1.000	0.0027

^{a)} Average absolute relative deviation between the experimental ρ data and the correlation.

SUPPORTING INFORMATION

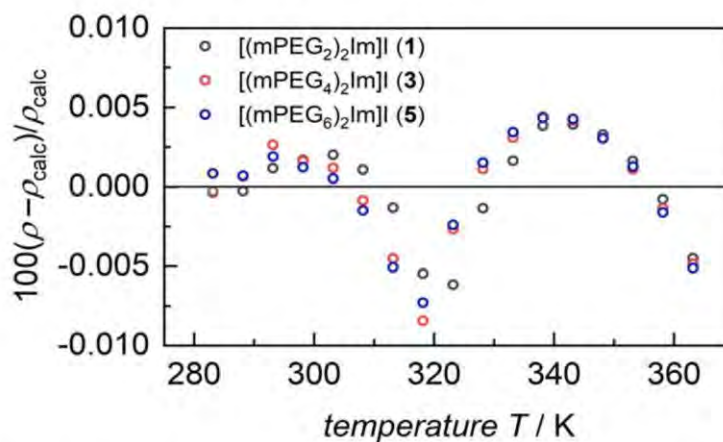


Figure S7. Relative deviations of the experimental liquid density data from the second-order polynomial fit $\rho_{\text{calc}}(T) = \rho_0 + \rho_1 T + \rho_2 T^2$.

6 Electrochemical Measurements

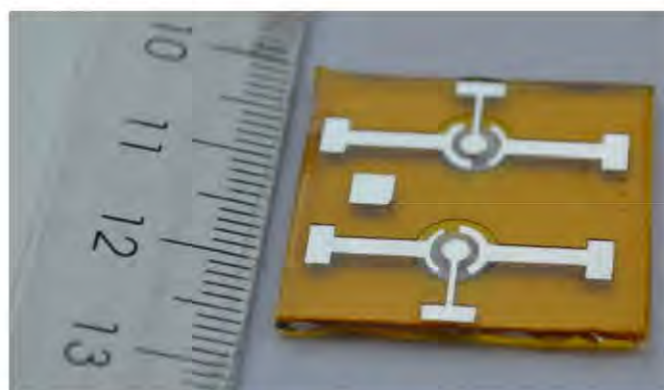


Figure S8. Home-made microelectrode system used for cyclic voltammetry, linear sweep voltammetry and electrochemical impedance spectroscopy (Pt as working and counter electrode, Ag as pseudo-reference electrode).

Table S6. Mean impedance ($|Z|$) and conductivity values (κ) of IL 1–8. Experimental uncertainties are shown in parentheses.

IL	$ Z / \text{k}\Omega$	$\kappa / \text{mS cm}^{-1}$
[(mPEG ₂) ₂ Im]I (1)	19.6	0.18 (±0.008)
[(mPEG ₃) ₂ Im]I (2)	21.6	0.17 (±0.011)
[(mPEG ₄) ₂ Im]I (3)	23.4	0.15 (±0.015)
[(mPEG ₅) ₂ Im]I (4)	30.8	0.12 (±0.010)
[(mPEG ₆) ₂ Im]I (5)	35.4	0.10 (±0.008)
[(mPEG ₄) ₂ Im][OMs] (6)	22.3	0.16 (±0.005)
[(mPEG ₄) ₂ Im][PF ₆] (7)	15.4	0.23 (±0.014)
[(mPEG ₄) ₂ Im][NTf ₂] (8)	6.0	0.59 (±0.009)

S7

SUPPORTING INFORMATION

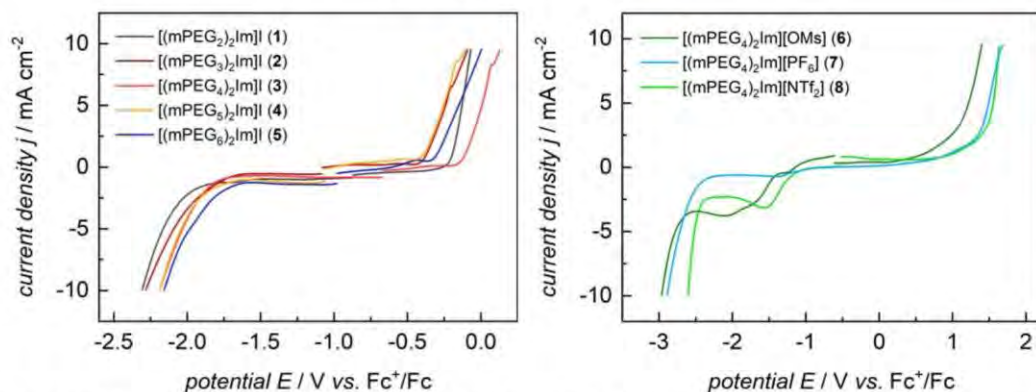


Figure S9. Linear sweep voltammetry of $[(m\text{PEG}_n)_2\text{Im}]\text{I}$ ($n = 2-6$; 1-5) (left) and $[(m\text{PEG}_4)_2\text{Im}][\text{A}]$ ($\text{A} = \text{OMs}^-$, PF_6^- , NTf_2^- ; 6-8) (right).

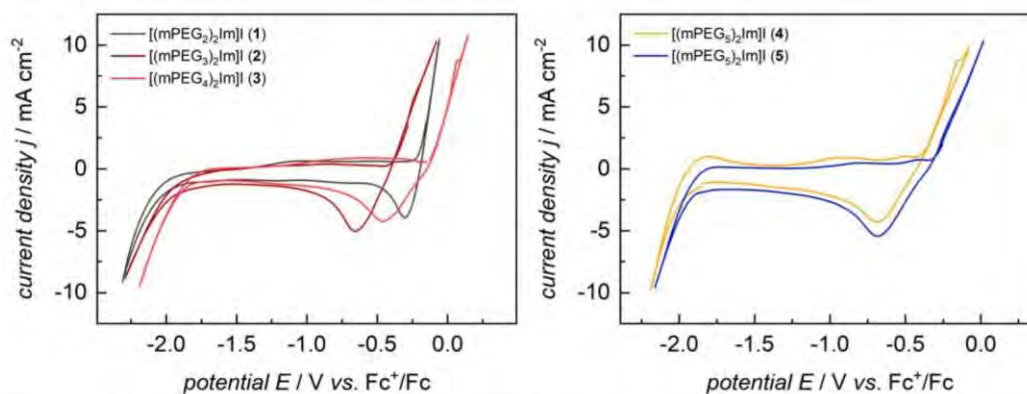


Figure S10. Cyclic voltammetry of $[(m\text{PEG}_n)_2\text{Im}]\text{I}$ ($n = 2-4$; 1-3) (left) and $[(m\text{PEG}_n)_2\text{Im}]\text{I}$ ($n = 5, 6$; 4, 5) (right).

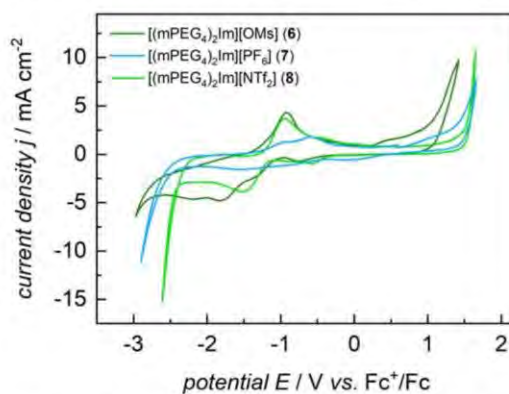


Figure S11. Cyclic voltammetry of $[(m\text{PEG}_4)_2\text{Im}][\text{A}]$ ($\text{A} = \text{OMs}^-$, PF_6^- , NTf_2^- ; 6-8).

SUPPORTING INFORMATION

7 Angle-Resolved X-ray Photoelectron Spectroscopy (ARXPS)



Figure S12. Sketch and assignment of carbon atoms exemplified for [(mPEG₂)₂Im]I.

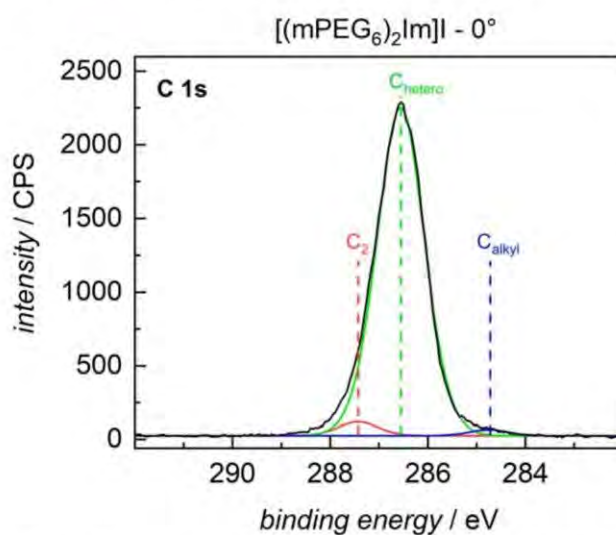


Figure S13. Peak fitting for the C 1s spectrum of [(mPEG₆)₂Im]I (5) in 0°, including C_{alkyl} from a minor (unknown) contamination.

SUPPORTING INFORMATION

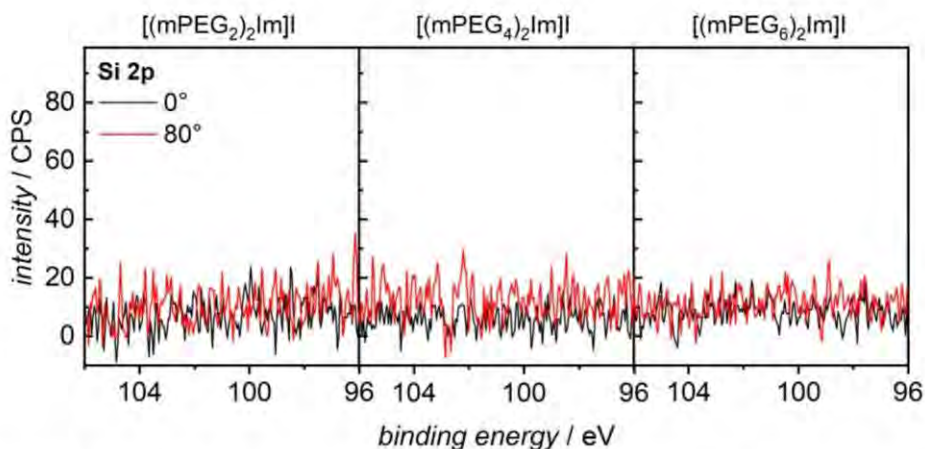


Figure S14. Si 2p region of the [(mPEG_n)₂Im]I (*n* = 2, 4, 6) (1, 3, 5) after mild sputtering.

8 Surface Tension

Table S7. Temperature-dependent surface tension (γ) of [(mPEG_n)₂Im]I (*n* = 2, 4, 6) (1, 3, 5) at argon pressure *p*.

[(mPEG ₂) ₂ Im]I (1)			[(mPEG ₄) ₂ Im]I (3)			[(mPEG ₆) ₂ Im]I (5)		
<i>T</i> / K	<i>p</i> / MPa	γ / (mN m ⁻¹)	<i>T</i> / K	<i>p</i> / MPa	γ / (mN m ⁻¹)	<i>T</i> / K	<i>p</i> / MPa	γ / (mN m ⁻¹)
303.11	0.101	45.92	303.23	0.115	43.47	303.10	0.103	42.63
318.08	0.103	44.85	318.43	0.120	42.07	318.05	0.108	41.02
333.21	0.105	43.42	333.51	0.126	40.72	332.99	0.113	39.67
348.16	0.102	42.44	348.72	0.131	39.15	347.94	0.117	38.29
363.19	0.102	41.43	363.87	0.136	37.96	362.88	0.116	37.08

^{a)} The expanded uncertainties (*k* = 2) for temperature and pressure are 0.02 K and 5 kPa, respectively. For the surface tension, the relative expanded uncertainty (*k* = 2) is 2%.

Table S8. Fit coefficients of the linear correlation $\gamma_{\text{calc}}(T) = \gamma_0 + \gamma_1 T$ for temperature-dependent surface tension data of [(mPEG_n)₂Im]I (*n* = 2, 4, 6) (1, 3, 5).

IL	γ_0 / (mN m ⁻¹)	γ_1 / (mN m ⁻¹ K ⁻¹)	R ²	AARD / % ^{a)}
[(mPEG ₂) ₂ Im]I (1)	68.87	-0.07582	0.996	0.20
[(mPEG ₄) ₂ Im]I (3)	71.40	-0.09210	0.999	0.13
[(mPEG ₆) ₂ Im]I (5)	70.55	-0.09254	0.998	0.23

^{a)} Average absolute relative deviation between experimental γ data and the linear correlation

SUPPORTING INFORMATION

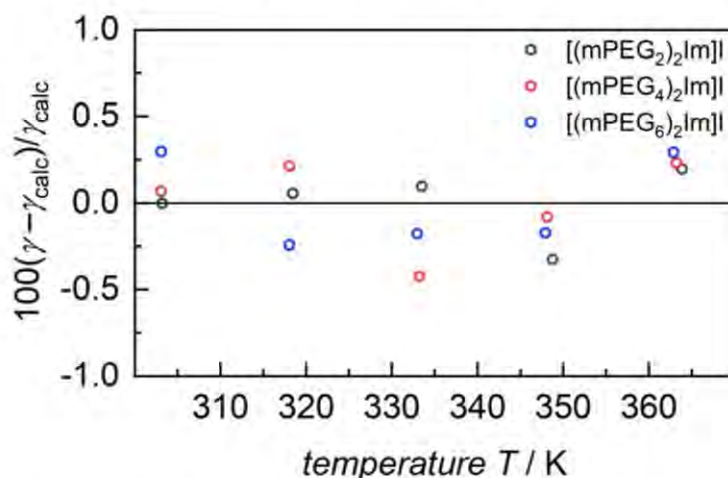


Figure S15. Relative deviations of the experimental surface tension data from the linear fit $\gamma_{\text{calc}}(T) = \gamma_0 + \gamma_1 T$.

9 Molecular Dynamics Simulations

Development of Partial Atomic Charges

Partial atomic charges were derived for $[(\text{mPEG}_n)_2\text{Im}]^+$ ($n = 2, 4$) (**1, 3**) by means of the RESP method, utilizing the RED III.5 tools.[1, 2] Input molecular geometries for charge calculations were produced by Gaussian 16[3] at the HF/6-31G(d)[4-7] level of theory,[8] using a representative set of conformations (local minima of the potential energy surface) as obtained by quantum mechanical optimization. Specifically, by exploiting the geometrical symmetries of the cation, we created and then optimized six conformers for $[(\text{mPEG}_1)_2\text{Im}]^+$ (**Figure S16**). The resulting structures were then prolonged to become $[(\text{mPEG}_2)_2\text{Im}]^+$, with each core $n = 1$ structure contributing three new conformers to $n = 2$. The latter was accomplished by first adding side-chain atoms in an all-extended-chain fashion (**Figure S17**), and then rotating the newly added, side-chain bonds to obtain two extra conformations. These new eighteen conformers were then optimized and the resulting geometries input to a multi-conformation RESP charge fitting.

An analogous procedure was repeated to extend $n = 2$ to $n = 4$ but such that for each set of three conformers inherited from $n = 2$, only the all-extended one was prolonged to $n = 4$. The new bonds were then rotated yielding thirty-six structures in total. The resulting charges are listed in **Figure S18**. It should be noted that any optimized conformation showing a strong interaction between a side-chain oxygen and the acidic hydrogen of the imidazolium ring was removed from the set to avoid polarization of the oxygen, which sensibly reduced the oxygen's charge (**Figure S19**).



Figure S16. The six optimized conformers of $[(\text{mPEG}_1)_2\text{Im}]^+$ that started the derivation of partial atomic charges for longer cations.

SUPPORTING INFORMATION

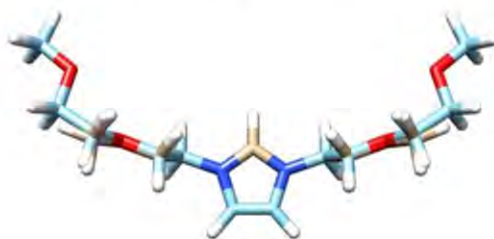


Figure S17. Prolonging a core structure of $[(m\text{PEG}_1)_2\text{Im}]^+$ to $[(m\text{PEG}_2)_2\text{Im}]^+$ by adding side chain atoms in an all-extended fashion. For visual purposes, the two structures have been superimposed by matching the imidazolium moieties.

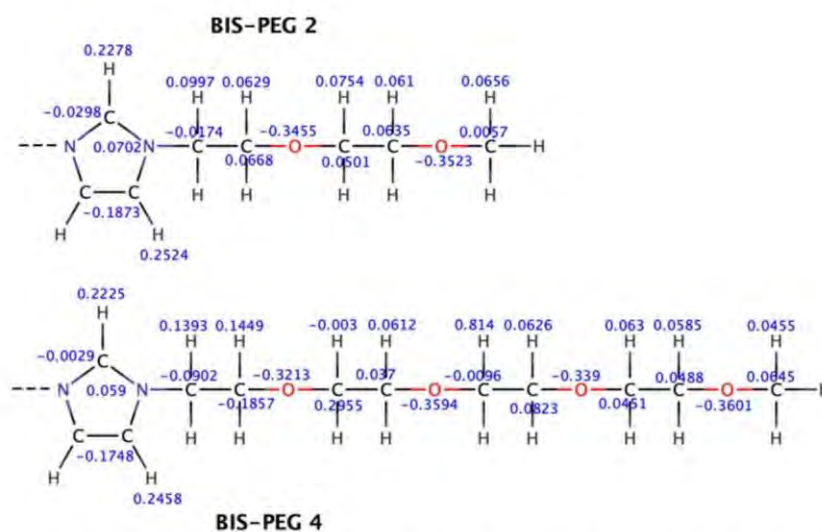


Figure S18. Partial atomic charges for $[(m\text{PEG}_n)_2\text{Im}]^+$ ($n = 2, 4$). These charges are the outcome of the multi-conformation RESP fitting procedure described in the main text. By symmetry, charges are reported only for one side chain of the cation.

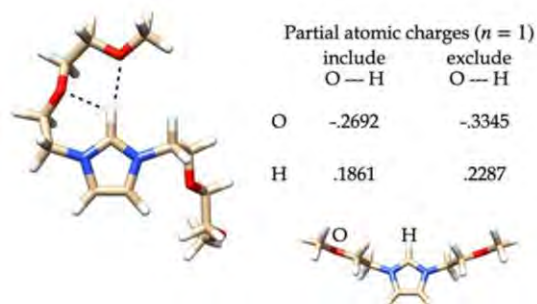


Figure S19. A conformation of $[(m\text{PEG}_2)_2\text{Im}]^+$ affected by the interaction of two side chain oxygen atoms with the acidic hydrogen of the imidazolium ring (left) and the $[(m\text{PEG}_1)_2\text{Im}]^+$ partial atomic charges of one side chain oxygen and the acidic hydrogen (right), when left-panel-like structures are both included and excluded from the pool of conformations used to derive charges. It is evident how including such interactions polarized the electron cloud from the oxygen to the hydrogen, making the former less negative and the latter less positive.

SUPPORTING INFORMATION

System Construction

Initial molecular dynamics (MD) cubic boxes were assembled using Packmol.[9] Each system consisted of 1400 [(mPEG_n)₂Im]I pairs, for $n = 2$ and $n = 4$, amounting to 63000 and 102200 atoms, with initial densities of 1.287 and 1.007 g/cm³, respectively (**Figure S20**). The AMBER tleap routine was then used to output coordinate and topology files for these systems, utilizing GAFF[8] force field parameters for the cations and iodide Lennard-Jones parameters from Migliorati *et al.*[10] Finally, conversion to GROMACS[11, 12] file formats was carried out using ACPYPE.[13]

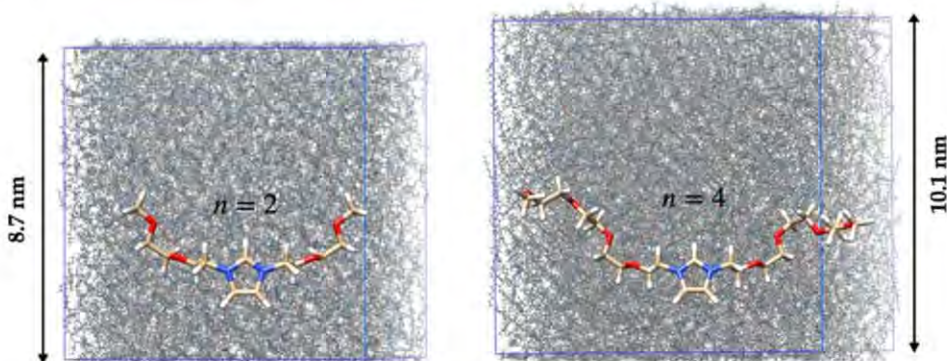


Figure S20. The initial MD cubic boxes for [(mPEG_n)₂Im]I, $n = 2,4$, as assembled by Packmol. Both the size of each box and a sample cation molecule are reported.

Simulation Methods

All simulations were conducted using GROMACS 2019.5, utilizing a Nose-Hoover thermostat (fluctuation period of 2 ps) in combination with a Parrinello-Rahman barostat (fluctuation period of 9 ps). Carbon-hydrogen bonds were constrained using the LINCS algorithm, allowing the leap-frog integrator to use a time step of 2 fs. Electrostatic interactions were calculated directly within a radius of 1.2 nm and the Particle-Mesh-Ewald method was used to calculate longer-range interactions. Periodic boundary conditions in all directions were in effect.

The equilibration was performed over several steps. Each system was minimized by steepest descent and then subject to an initial 5 ns NVT relaxation at 303 K. This was followed by an annealing protocol consisting of raising the temperature from 303 K to 700 K in 3 ns (133 K/ns), maintaining 700 K for 3 ns and finally returning to 303 K in the span of 4 ns (100 K/ns). The $n = 2$ and $n = 4$ systems were then equilibrated in the NPT ensemble at 303 K for 215 ns and 350 ns, respectively, in order to relax the volume of the box following annealing. A second round of annealing was then applied, using the same protocol as before, followed by a further NPT equilibration at 303 K for both systems; 65 ns and 80 ns, respectively, were necessary before the density reached steady state.

At this point, the GROMACS tool *gmx trjconv* was employed to remove periodic boundary conditions from the systems, which were later extended along the z axis introducing 13 nm and 15 nm vacuum slabs for $n = 2$ and $n = 4$, respectively (**Figure S21**). This effectively established two ionic-liquid-vacuum (VLV) interfaces within each system, perpendicular to the z axis.

SUPPORTING INFORMATION

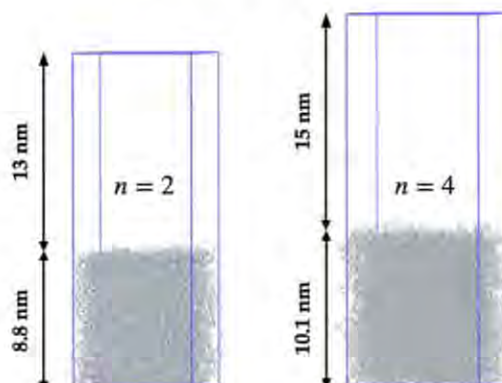


Figure S21. The MD boxes for $[(m\text{PEG}_n)_2\text{Im}]I$, ($n = 2, 4$) (1, 3) after equilibration of the bulk, fully periodic ILs and establishment of the VLV interfaces.

The newly created VLV systems were equilibrated in the NVT ensemble at 303 K for time lengths of 2400 ns and 2000 ns for $n = 2$ and $n = 4$, respectively. We then created three more simulation boxes (adopting the same annealing rate as before) at temperatures of 317, 333, and 338 K, which were relaxed in the NVT ensemble for 600 ns. Production analysis was limited to the last 300 ns in each case. For $n = 4$, however, a second annealing was necessary: this annealing protocol was identical to the one previously adopted, except that the final cooling occurred at a rate of -20 K/ns, i.e., 6.5 times slower than before. During cooling, replicas of the system were saved at 370, 350, 330, and 303 K. After NVT-equilibrating all four boxes for 600 ns, we again applied an identical second cycle of annealing and equilibration. The ensuing production run was 300 ns long.

Simulation Analysis

The GROMACS tool *gmx density* was used to extract the z-axis density profiles of both VLV systems at each temperature, averaged over the last 300 ns of trajectory (**Figure S22**). The temperature dependent bulk density was estimated from the VLV simulations by evaluating the density of the IL in the central slab, where density profiles saturate. Surface tension was calculated from pressure-pressure correlations using the GROMACS tool *gmx energy*. Because of the slow convergence of this property, 600 ns long trajectories were used for analysis.

The predicted enrichment factors comparable to ARXPS data were obtained by first determining the position of the IL interface, which was set to be at the inflection point of the vacuum-exposed part of density profile of the IL. The profiles for hetero-carbon (C_{hetero}), nitrogen (N), oxygen (O) and iodide (I) were obtained from the ratios of integrals of the number-density profiles from negative infinity to the experimental penetration depths of the ARXPS experiment, at both 0° (bulk sensitive) and 80° (surface sensitive) angles. More details on this procedure are disclosed in **Figures S23** and **S24**.

SUPPORTING INFORMATION

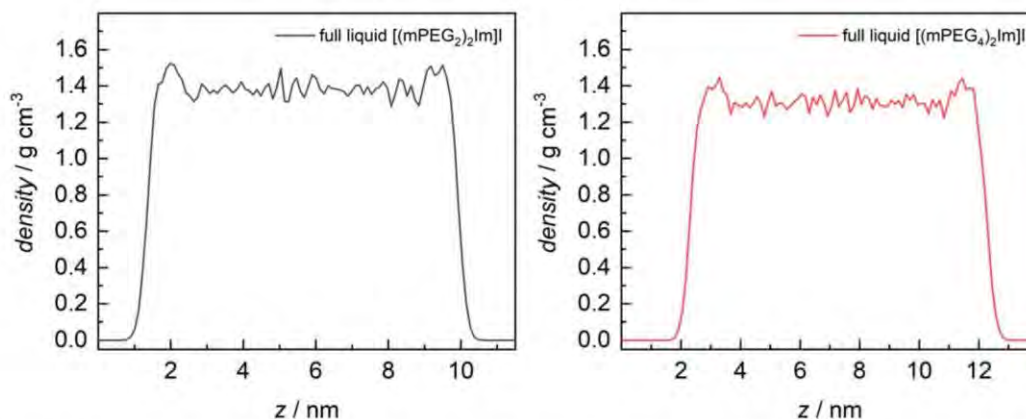


Figure S22. Z-axis mass density profiles for $[(\text{mPEG}_2)_2\text{Im}]^+$ (left) and $[(\text{mPEG}_4)_2\text{Im}]^+$ (right) at 303 K, averaged over the last 300 ns of trajectory.

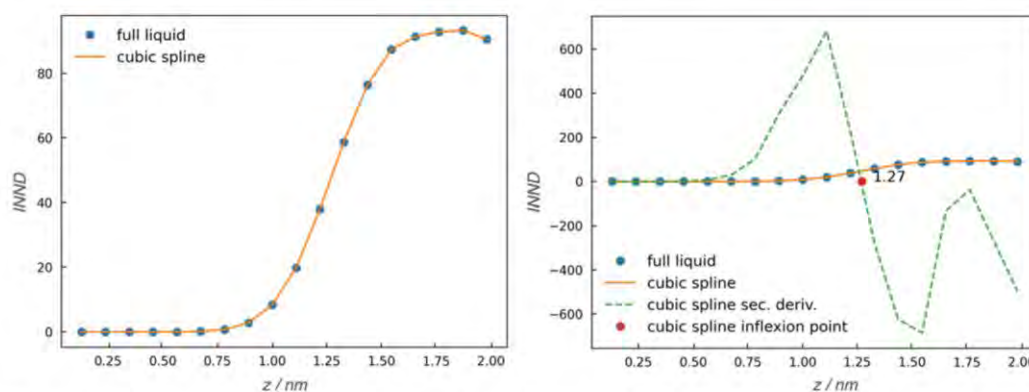


Figure S23. Z-axis number density profile for $[(\text{mPEG}_2)_2\text{Im}]^+$ at 303 K (left), time-averaged over the last 300 ns of trajectory and spatially averaged over both halves of the liquid (only a fraction of the profile in the bulk region, *i.e.* the plateau, is shown). Data points were interpolated by a third-order spline. The second derivative of the cubic spline and its root at $z_i = 1.27$ nm (right), marking the point of inflection of the full-liquid profile, are shown.

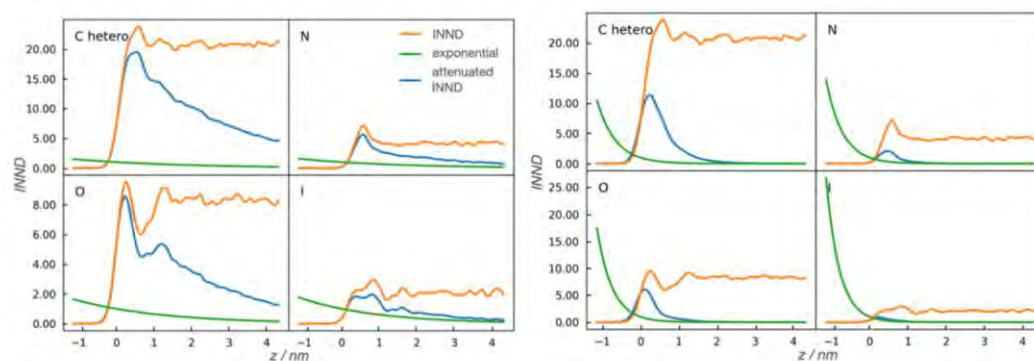


Figure S24. Z-axis number density profiles for $[(\text{mPEG}_n)_2\text{Im}]^+$, $n = 2$ at 303 K (INND: interface normal number density profile), averaged over the last 300 ns of trajectory, for the four chemical species that were experimentally investigated by ARXPS. Each profile (labeled 'INND') was multiplied by the decaying exponential function $\exp(-\frac{z}{\lambda \cos\theta})$ (labeled 'exponential'), where λ is the ARXPS mean free path of the corresponding species (C hetero: 2.8 nm; N: 2.5 nm; O: 2.3

SUPPORTING INFORMATION

nm; λ : 2.1 nm), and ϑ is the grazing angle of X-rays in ARXPS. This is supposed to mimic the experimental attenuation of the ARXPS signal as a function of penetration depth and grazing angle, given by $I(z) = I(0)\exp(-\frac{z}{\lambda \cos\vartheta})$. The resulting product function (labeled 'attenuated INND') was then integrated over the entire length of the IL slab ($\vartheta = 0^\circ$ (bulk sensitive, left); $\vartheta = 80^\circ$ (surface sensitive, right)). In order to obtain the interface-to-bulk composition ratios, these integrals were appropriately normalized (for experimental comparison) and then the $80^\circ/0^\circ$ ratios were computed for each species.

Comparison of Experiments and Simulations

We obtained very good agreement between measured and modeled temperature dependence of the IL's density (**Figure 2**), which validates our IL parametrization. The disparity does not exceed 0.03 g/cm^3 , with most experimental data points lying within the error bars of simulation results. Indeed, the agreement for $n = 4$ is excellent. Furthermore, **Figure 5** compares the surface tensions of the ILs obtained both experimentally and by simulations at four temperatures. As expected, the measured surface tension decreases nearly linearly as a function of temperature, a trend that is well recovered in simulations for $n = 4$. For $n = 2$, this trend is violated, but that is likely due to the very slow convergence of the associated integrals observed for this IL. This is caused by the IL's high viscosity and the slowness of the large wavelength fluctuations, which are not properly sampled, leading to the underestimation of surface tension, particularly at lower temperatures. Even though current errors do not exceed a few mN/m, this suggests that even longer simulations and, potentially, even larger systems would be necessary to correctly recover the surface tension.

Finally, we compare ARXPS measurements to simulations (**Figure 7**), showing that both unveil the enrichment of mPEG chains at the liquid-vacuum interface. Indeed, the $80^\circ/0^\circ$ ratios for O and C_{hetero} atoms both exceed one, with C_{hetero} being in excellent agreement with experimental data. Also, the ratios for N and I are both below one, corroborating the depletion of these two species observed by ARXPS. Such depletion is more pronounced for $n = 4$ than it is for $n = 2$, again in agreement with experiment. This conclusion is also supported by the normal number density profiles shown in **Figure S25**. For both liquids, the profile with the leftmost peak is O, indicating that mPEG_n side chains preferentially populate the interface. This is followed by a deep trough at the same location of the first N peak, signifying that imidazolium groups are enriched further down the interface than the side chains are. The same holds for I, which peaks slightly to the right of N, testifying to the iodide/imidazolium coordination that emerged experimentally. Finally, because a few imidazolium carbon atoms contribute to the C_{hetero} signal, it is no surprise that this profile attains its maximum to the right of the O peak and in the vicinity of the N maximum.

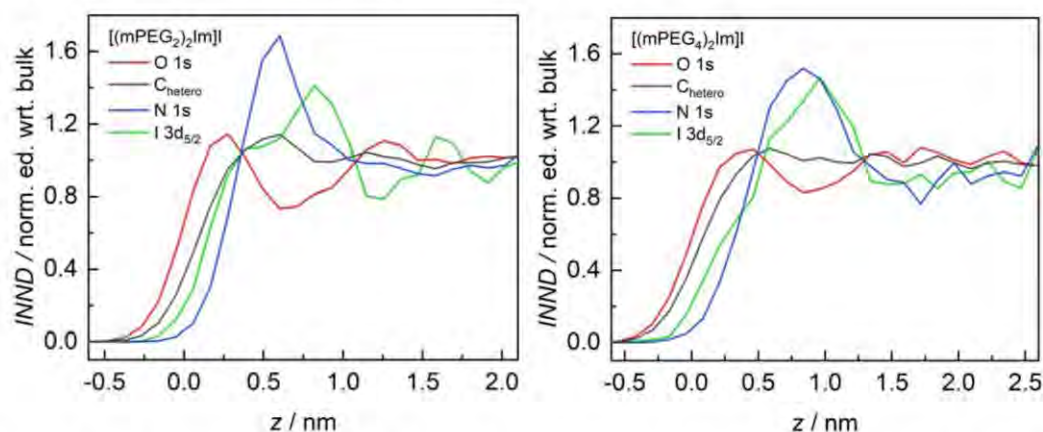


Figure S25. Interface normal number density (INND) normalized with respect to its own bulk average value, of hetero carbon, oxygen, nitrogen atoms and iodide ions, for $n = 2$ (left) and $n = 4$ (right).

SUPPORTING INFORMATION

Analysis of interface-cation conformations based on MD simulations

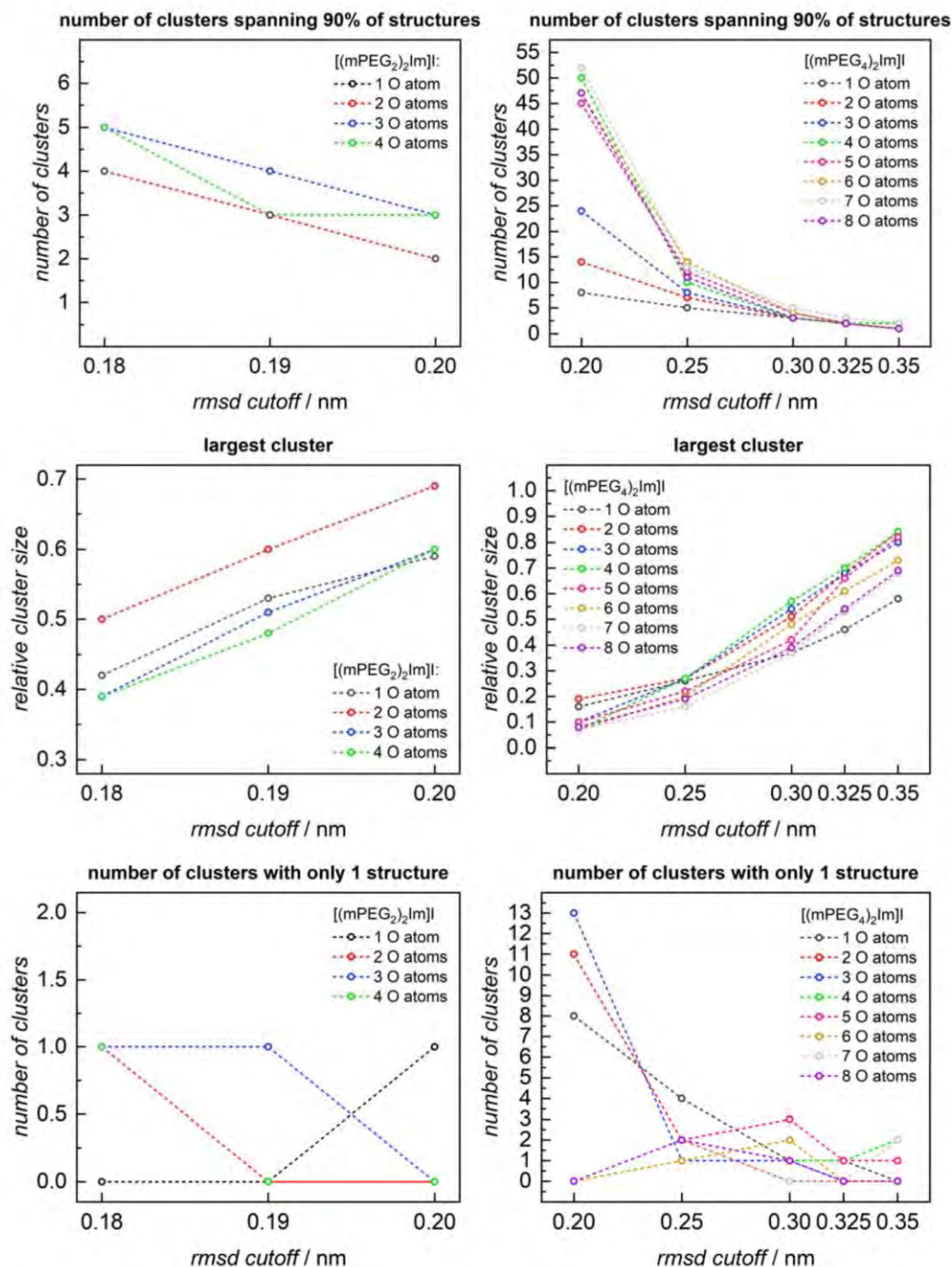


Figure S26. Investigation of multiple rmsd cutoff values for the clustering procedure described in the main text. The following properties were studied as a function of the rmsd cutoff: number of clusters spanning 90% of all conformations (top), relative size of the most populated cluster (middle), and number of clusters containing only a single structure (bottom).

SUPPORTING INFORMATION

(bottom) of [(mPEG₂)₂Im]⁺ (left) and [(mPEG₄)₂Im]⁺ (right). The chosen cutoff values were 0.2 nm for $n = 2$ and 0.325 nm for $n = 4$. In the $n = 2$ case, this was mostly to guarantee a high representativeness of the most populated cluster, close to at least 60% at all oxygen numbers. This choice also ensures that only one cluster contains a single conformation, while the number of clusters spanning nearly all structures does not exceed three, again contributing to clusters' representativeness. In the $n = 4$ case, the value 0.325 nm strikes the best balance between representativeness and specificity: between about 50% and 70% of conformations fall within the largest cluster, while the number of clusters spanning almost all structures is about five. The value 0.35 nm, for example, would reduce this number to about one, impeaching conformational specificity (*i.e.* the midpoint structure would be too generic), while the value 0.3 nm would not produce sufficient representativeness of the most populated cluster.

10 References

- [1] F.Y. Dupradeau, A. Pigache, T. Zaffran, C. Savineau, R. Lelong, N. Grivel, D. Lelong, W. Rosanski, P. Cieplak, *Phys. Chem. Chem. Phys.* 12 (2010) 7821.
- [2] A. Pigache, P. Cieplak, F. Dupradeau, *Abstracts Of Papers Of The American Chemical Society* 227 (2004) U1011.
- [3] M.J. Frisch, G.W. Trucks, H.B. Schlegel, G.E. Scuseria, M.A. Robb, J.R. Cheeseman, G. Scalmani, V. Barone, G.A. Petersson, H. Nakatsuji, X. Li, M. Caricato, A.V. Marenich, J. Bloino, B.G. Janesko, R. Gomperts, B. Mennucci, H.P. Hratchian, J.V. Ortiz, A.F. Izmaylov, J.L. Sonnenberg, D. Williams-Young, F. Ding, F. Lipparini, F. Egidi, J. Goings, B. Peng, A. Petrone, T. Henderson, D. Ranasinghe, V.G. Zakrzewski, J. Gao, N. Rega, G. Zheng, W. Liang, M. Hada, M. Ehara, K. Toyota, R. Fukuda, J. Hasegawa, M. Ishida, T. Nakajima, Y. Honda, O. Kitao, H. Nakai, T. Vreven, K. Throssell, J.A. Montgomery, Jr., J.E. Peralta, F. Ogliaro, M.J. Bearpark, J.J. Heyd, E.N. Brothers, K.N. Kudin, V.N. Staroverov, T.A. Keith, R. Kobayashi, J. Normand, K. Raghavachari, A.P. Rendell, J.C. Burant, S.S. Iyengar, J. Tomasi, M. Cossi, J.M. Millam, M. Klene, C. Adamo, R. Cammi, J.W. Ochterski, R.L. Martin, K. Morokuma, O. Farkas, J.B. Foresman, *Gaussian* 16, Revision C.01 (2016).
- [4] R. Ditchfield, W.J. Hehre, J.A. Pople, *J. Chem. Phys.* 54 (1971) 724.
- [5] W.J. Hehre, R. Ditchfield, J.A. Pople, *J. Chem. Phys.* 56 (1972) 2257.
- [6] M.M. Francl, W.J. Pietro, W.J. Hehre, *J. Chem. Phys.* 77 (1982) 3654.
- [7] V.A. Rassolov, M.A. Ratner, J.A. Pople, P.C. Redfern, L.A. Curtiss, *J. Comput. Chem.* 22 (2001) 976.
- [8] J. Wang, R.M. Wolf, J.W. Caldwell, P.A. Kollman, D.A. Case, *J. Comput. Chem.* 25 (2004) 1157.
- [9] L. Martinez, R. Andrade, E.G. Birgin, J.M. Martinez, *J. Comput. Chem.* 30 (2009) 2157.
- [10] V. Migliorati, A. Serva, G. Aquilanti, L. Olivi, S. Pascarelli, O. Mathon, P. D'Angelo, *Phys. Chem. Chem. Phys.* 17 (2015) 2464.
- [11] S. Pronk, S. Pall, R. Schulz, P. Larsson, P. Bjelkmar, R. Apostolov, M.R. Shirts, J.C. Smith, P.M. Kasson, D. van der Spoel, B. Hess, E. Lindahl, *Bioinformatics* 29 (2013) 845.
- [12] M.J. Abraham, T. Murtola, R. Schulz, S. Páll, J.C. Smith, B. Hess, E. Lindahl, *SoftwareX* 1-2 (2015) 19.
- [13] A.W.S. da Silva, W.F. Vranken, *BMC Res. Notes* 5 (2012).

8.1.2. PROBING SURFACE AND INTERFACIAL TENSION OF IONIC LIQUIDS IN VACUUM WITH THE PENDANT DROP AND SESSILE DROP METHOD^[P2]



International Journal of
Molecular Sciences



Article

Probing Surface and Interfacial Tension of Ionic Liquids in Vacuum with the Pendant Drop and Sessile Drop Method

Ulrike Paap, Bernd Kreß, Hans-Peter Steinrück and Florian Maier

Lehrstuhl für Physikalische Chemie II, Friedrich-Alexander-Universität Erlangen-Nürnberg, Egerlandstr. 3, 91058 Erlangen, Germany

* Correspondence: florian.maier@fau.de

Abstract: We report on the surface and interface tension measurements of the two ionic liquids (ILs) $[C_8C_1Im][PF_6]$ and $[m(PEG_n)_2Im]I$ ($n = 2, 4, 6$) in a surface science approach. The measurements were performed in a newly developed and unique experimental setup, which allows for surface tension (ST) measurements using the pendant drop method and for contact angle measurements using the sessile drop method under the well-defined conditions of a high vacuum (from 10^{-7} mbar). The setup also allows for in vacuum transfer to an ultrahigh vacuum system for surface preparation and analysis, such as in angle-resolved X-ray photoelectron spectroscopy. For $[C_8C_1Im][PF_6]$, we observe a linear decrease in the surface tension with increasing temperature. The ST measured under high vacuum is consistently found to be larger than under ambient conditions, which is attributed to the influence of water uptake in air by the IL. For $[m(PEG_n)_2Im]I$ ($n = 2, 4, 6$), we observe a decrease in the ST with increasing polyethylene glycol chain length in a vacuum, similar to very recent observations under 1 bar Argon. This decrease is attributed to an increasing enrichment of the PEG chains at the surface. The ST data obtained under these ultraclean conditions are essential for a fundamental understanding of the relevant parameters determining ST on the microscopic level and can serve as a benchmark for theoretical calculations, such as molecular dynamic simulations. In addition to the ST measurements, proof-of-principle data are presented for sessile drop measurements in HV, and a detailed description and characterization of the new setup is provided.

Keywords: ionic liquids (ILs); surface tension; interface tension; pendant drop; sessile drop; surface science; vacuum



Citation: Paap, U.; Kreß, B.; Steinrück, H.-P.; Maier, F. Probing Surface and Interfacial Tension of Ionic Liquids in Vacuum with the Pendant Drop and Sessile Drop Method. *Int. J. Mol. Sci.* **2022**, *23*, 13158. <https://doi.org/10.3390/ijms232113158>

Academic Editor: Qianjin Guo

Received: 4 October 2022
Accepted: 26 October 2022
Published: 29 October 2022

Publisher's Note: MDPI stays neutral with regard to jurisdictional claims in published maps and institutional affiliations.



Copyright: © 2022 by the authors. Licensee MDPI, Basel, Switzerland. This article is an open access article distributed under the terms and conditions of the Creative Commons Attribution (CC BY) license (<https://creativecommons.org/licenses/by/4.0/>).

1. Introduction

The macroscopic property surface tension (ST) γ of a liquid is the change in surface free energy per change in surface area. It plays an important role for many applications, particularly, when coating, impregnation or spraying processes are involved. In a microscopic picture, to increase the surface area, molecules in the bulk have to break the attractive interactions with their neighbours to be exposed to a different environment (vacuum, gas phase or another liquid phase). Notably, we refer to the term “surface tension” for the liquid–gas and the liquid–vacuum interface; in case of the liquid being in contact with a second dense phase, such as a solid or another liquid, we will use the term “interfacial tension” [1,2]. Despite the highly dynamic situation at the liquid surface, on average, the molecular moieties with the least attractive interactions in the bulk are preferentially exposed at this outer surface. This general behaviour was already stated by Irving Langmuir in his so-called “Langmuir principle” many decades ago, according to which the surface tension is represented by “the result of superposition over the molecule parts present at the outer surface” [3]. The more non-isotropic the molecules of the liquid, the more complicated the prediction or modelling of its surface tension is. This holds particularly true for ionic liquids (ILs), which are salts characterized by low melting points, often even liquid below room temperature, and negligible vapour pressure. They are typically made

from highly asymmetric and weakly coordinating ions, and thus their properties can be tailored over a wide range, which make them interesting for many applications [4–7]. The composition of the IL's surface layer is governed by a preferential orientation of the ions towards the gas (or vacuum) side in order to minimize the surface free energy, which is then directly reflected in the experimentally observable surface tension [8].

These considerations illustrate that the surface tension of a liquid depends on the chemical composition of the surface layer, and thus will be sensitive to contaminations or the gaseous environment. On the one hand, surface-active residual contaminations dissolved in the bulk will preferentially be located at the outer surface. On the other hand, the gas environment might contain additional gas atoms/molecules apart from the liquid's vapour, which can adsorb at the surface (e.g., volatile hydrocarbons or water from the air) or even react with surface species. Both sources for surface contamination or modification will have an impact on the measured surface tension [9,10]. In order to obtain a fundamental understanding on the intrinsic surface tension of a liquid, which can, e.g., serve as a benchmark for theoretical calculations such as molecular dynamic simulations, it is thus necessary to be able to accurately determine the intrinsic surface tension under well-defined and ultraclean conditions, that is, at best, in a high or even ultra-high vacuum (UHV). As has been shown over the last two decades, UHV-based surface science methods can be well applied to study the surface properties of ILs due to their extremely low vapour pressures [11–15]. This enables one to characterize the surface composition and the molecular arrangement of cations and anions with high accuracy, which in turn sets the stage for studying the surface tension of well-defined and well-characterized clean surfaces. The obtained correlation between surface tension and microscopic structure at the surface can then also be used to tailor surface properties for specific experiments in fundamental science, e.g., by using liquid mixtures or for targeted applications in industry.

The ST γ of a liquid can be determined with different experimental methods, such as the capillary rise, the Du Noüy ring, the Wilhelmy plate, the spinning drop, the maximum bubble pressure and the pendant drop method [16,17]. All of these methods have already been successfully applied to study the ST of ILs under non-vacuum conditions [18]. The pendant drop (PD) method is one of the most popular standard techniques and is used in various gas atmospheres and under different pressure conditions. As will be shown in this work, it is also suitable to investigate the ST of ILs under vacuum conditions, since the exact shape of a pendant IL drop at the end of a vertically mounted capillary can be recorded through a vacuum-tight window. Moreover, the pendant IL drop can be subsequently placed onto a well-defined and clean solid surface (e.g., a single metal crystal surface previously cleaned by argon sputtering and thermal annealing in UHV) to determine the intrinsic interfacial tension by recording contact angles (CA) without breaking the clean vacuum conditions. For both the PD and CA measurements, the physico-chemical background is shortly summarized in the following.

The exact determination of the shape of the pendant drop is the most important factor for the accuracy of PD surface tension measurements [16,19–21]. In 1881, Worthington had already proposed that the surface tension of a liquid can be determined from the shape of a hanging drop, which is deformed by gravity [22–24]. Shortly thereafter, in 1883, Bashford and Adams published numerical tables for the approximate solutions of the axially symmetric Young–Laplace equation [25]. The Young–Laplace equation is a nonlinear partial differential equation describing the capillary pressure difference sustained across the interface between the liquid and a gas phase (or across the interface between the liquid and another immiscible liquid phase) due to the surface (or the interfacial) tension γ . This equation is still used today to derive γ . The shape of the drop is determined by a single dimensionless quantity $\beta = \Delta\rho g R_0^2/\gamma$ as a measure of the ratio of gravitational and interfacial forces. Therein, $\Delta\rho$ is the density difference between the liquid and the second phase to account for the drop buoyancy, g the acceleration due to gravity and R_0 the radius of the drop curvature at its apex [25]. In 1947, β was defined as the 'Bond number'

by Merrington and Richardson [26]. The surface (interfacial) tension thus can be directly obtained from the density, gravitational force and drop size if the bond number can be accurately determined from the drop shape. This, however, proved to be challenging for some systems, particularly for drops strongly elongated due to a low surface tension with just R_0 as the characteristic drop shape parameter. In 1938, Andreas et al. demonstrated an improved approach to determine γ from the aspherical drop shape [27]: this approach is based on the value $S = d_s / d_e$, which is the ratio of the maximum drop diameter, d_e , and the drop diameter, d_s , measured at a distance d_e from the apex (see Figure S1 of Supporting Information, SI). This ratio S is then compared with tables calculated experimentally by Andreas et al., which correlate the bond number and interfacial tension. These tables were further improved over time by numerical integration of the Young–Laplace equation [27,28]. Today, standard programs to calculate surface tension are based on the ADSA algorithm (axisymmetric drop shape analysis) developed by Neumann et al. [19,29–33].

As already stated above, the wetting behaviour of liquids on solid surfaces is closely related to the solid–liquid interfacial tension γ^{SL} . For interface tension measurements between a liquid and a solid, the contact angle (CA) of a sessile drop is commonly measured [34]. In 1805, Young proposed a force balance equation in the thermodynamic equilibrium for the relation between the interfacial tension γ^{SL} and the contact angle: $\cos \theta = \frac{\gamma^{SG} - \gamma^{LG}}{\gamma^{SL}}$. Therein, θ is the contact angle between liquid and solid, and γ^{SG} and γ^{LG} are the solid–gas and liquid–gas surface tensions, respectively [34–36]. From this Young equation, the impact of any impurities being present at the solid or liquid surface as well as at the solid–liquid interface becomes obvious. Thus, to obtain the intrinsic interfacial tension between a well-defined solid surface and an ultraclean IL, sessile drop measurements under ultraclean vacuum conditions are also extremely helpful.

Here, we report on a novel experimental setup for high vacuum (HV) pendant drop (PD) and sessile drop (SD) measurements developed in our group. It can operate in the pressure range from 10^{-7} mbar up to approx. 1 bar. Moreover, it allows for sample transfers without breaking vacuum conditions between this setup and another UHV instrument, the so-called Dual Analyzer System for Surface Analysis, DASSA [37]. This transfer allows us, on the one hand, to prepare and characterize a solid surface in the DASSA by sputtering, annealing, low-energy electron diffraction (LEED) and angle-resolved X-ray photoelectron spectroscopy (ARXPS) for subsequent sessile drop measurements. On the other hand, the surface composition of the IL used in the pendant drop experiments can be subsequently determined by ARXPS for a direct correlation between surface composition/purity and surface tension values measured without risking additional contaminations by sample transport in air.

In the following, we first present the new PD/SD setup. After calibration with the well-known standard systems of clean water and clean benzene in air, the first temperature-dependent surface tension measurements under vacuum conditions for ILs will be shown. The studied ILs, $[C_8C_1Im][PF_6]$ and $[m(PEG)_nIm]I$ ($n = 2, 4, 6$), are characterized by very different chain substituents in the cation and different anions. The derived surface tension values will be discussed in light of the composition at the outermost surface determined by ARXPS along the Langmuir’s principle [8]. In addition, we demonstrate for $[C_8C_1Im][PF_6]$ in contact with stainless-steel the influence of impurities (as deduced by XPS) on the measured contact angle with the SD method.

2. Setup

2.1. General Setup

The new high vacuum (HV) pendant drop/sessile drop (PD/SD) apparatus operates in the pressure range from atmosphere (≈ 1 bar) to HV (10^{-7} mbar), and in a temperature range from room temperature to about 400 K (see Figure 1). The setup is mounted in a small stainless-steel vacuum six-way cubic cross as vacuum chamber, which is pumped by a turbomolecular pump (Pfeiffer, HiPace 80) combined with an oil-free scroll pump (Pfeiffer, HiScroll 6). In order to vary the pressure or introduce a certain gas atmosphere, the gate

valve to the pumping is closed, and the chamber can be either vented with or gases can be introduced by a fine dosing valve. The pressure is recorded using a multi-range pirani/cold cathode gauge (Pfeiffer, PKR 251). Heating tapes allow for uniform baking the chamber, for degassing the liquids and for temperature-dependent measurements. Optical images of the pendant or sessile drops are recorded through a CF40 window using a high-speed camera (DataPhysics, iDS, UI-3350CP-M-GL R2); the drops are illuminated from the back by a diffuse LED light screen, mounted on the opposite window for accurate imaging [16,38]. In order to reduce reflections from the metallic walls inside the cross, a cover with minimum sized rectangular opening ($10 \times 25 \text{ mm}^2$) is positioned at the illumination flange (that is, between the light source and the drop).

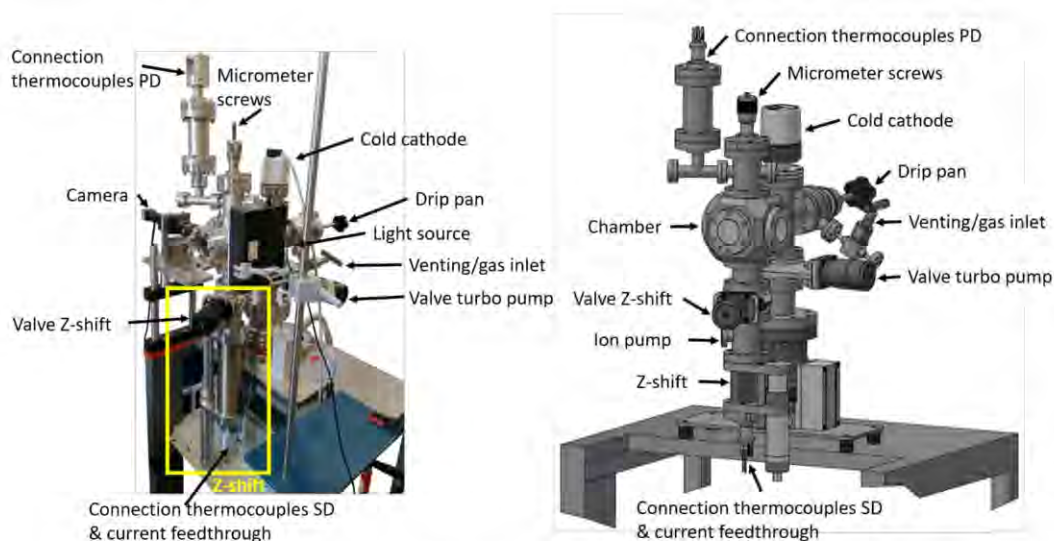


Figure 1. Photograph (left) and drawing (right) of the whole vacuum PD/SD system.

2.2. Pendant Drop

When performing pendant (and also sessile) drop measurements in vacuum, one has to consider specific boundary conditions. Most importantly, nearly all (conventional) liquids do simply evaporate at low pressures, which means they cannot withstand vacuum. Here, ILs are an exception, since most of them have a negligible vapour pressure at room temperature and thus are stable even under ultrahigh vacuum conditions. In addition, there is another very fundamental practical issue: In a standard PD/SD setup with a syringe operating under ambient pressure, the 1 bar pressure acting at the pendant drop surface allows for pushing out from or drawing back into the vertically mounted cannula by moving the syringe stamp, which enables an easy adjustment of a constant and stable drop volume. For measurements in vacuum, there is no pressure acting at the droplet surface, which implies that the liquid can only be pushed out while no negative pressure difference can be generated by pulling back the syringe stamp. The liquid droplet and the liquid inside the cannula is thus held back only by capillary forces (without capillary forces, it would simply leak from the syringe). Consequently, the cannula has to be designed such that for a drop of an appropriate size, the capillary forces are comparable to the gravitational ones (see also SI). To obtain suitable and relatively stable pendant drops for the ILs measured here, this is achieved by using a stainless-steel capillary of an outer and inner capillary diameter of 2.02 and 0.50 mm, respectively; in addition, two twisted stainless-steel wires (0.2 mm diameter) are inserted into the cannula in order to increase the contact area (and thus, the capillary forces) within the cannula (for more details, see Figure S2 of SI). When

the drop size exceeds a certain size, the excessive gravitational forces eventually lead to the separation of the drop from the cannula.

In order to be able to perform PD measurements in a high vacuum, we had to build a specific new PD syringe setup. The self-designed construction made of stainless-steel consists of a stationary reservoir with holes for degassing, a replaceable cannula and a stamp that can be moved in vertical direction using a micrometre screw-drive (see Figure 2a). The whole setup is mounted on a CF 40 flange (see Figure 2b) such that the tip of the cannula will end in the centre of the six-way cross after mounting. Liquid tightness between the stamp and the reservoir, and between the cannula and the reservoir, is achieved via viton seals mounted on the stamp and between the cannula and the reservoir (see Figure 2a). The IL under investigation is filled into the reservoir in air with retracted stamp (that is, with open degassing holes), and the setup is then attached to the HV chamber via the top CF flange and carefully pumped down. Notably, great care has to be taken during initial pumping, since any traces of gases dissolved in the IL will lead to bubble formations in vacuum and, eventually, splashing of the IL inside the vacuum chamber. As detailed in the SI, the pumping and IL degassing take place over several hours at chamber temperatures of 70 up to 100 °C to remove any volatile species from the bulk liquid.

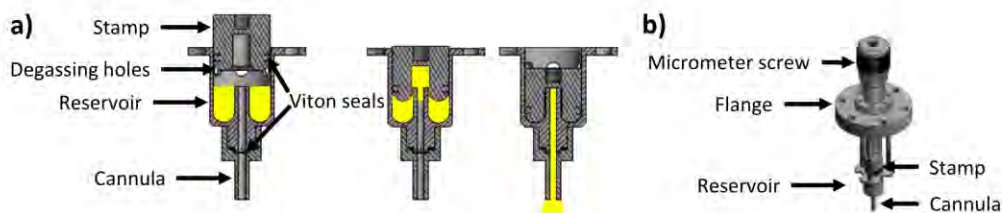


Figure 2. Concept and construction to form a drop in HV: (a) Representation of the inner part in the vacuum consisting of a stamp, reservoir with degassing holes and cannula. The stamp is pushed in the reservoir to press the liquid (in yellow) into the cannula forming a drop at its tip. (b) Full setup with the micrometre screw moving the stamp in a vertical direction.

Once the final vacuum is reached and the IL is fully degassed, the stamp is slowly moved down into the reservoir (thereby closing the degassing holes before touching the liquid surface), pushes the liquid into the cannula and, at the end of the cannula, a drop of growing size is slowly formed (see scheme of Figure 2a). Just before a targeted drop has reached its maximum size, that is, close to disconnection, the stamp must be moved back a little; otherwise, the IL is further pushed out of the reservoir into the cannula and the drop falls off very quickly. At this metastable stage, the pendant drop grows only very slowly due to gravity without significantly changing its shape. Eventually, it becomes too heavy and disconnects from the cannula and is collected in a glass vessel, which is placed under the cannula in an extra tube attached to the chamber. The challenge is to record the final shape of the drop just before it disconnects. While this is difficult when taking single photographs, it becomes easy when taking a video, where single images for PD analysis can be selected later. To illustrate the reproducibility for one single IL drop formed under these conditions, 100 ST values extracted from the final 20 s before drop disconnection (video rate: 5 frames/second) are shown in Figure S4 of the SI (for illustration of the growing drop size, four selected images are indicated; the full video is also provided in SI). Over the first 80 images, a very constant ST value of 43.47 ± 0.02 mN/m is deduced before a strong increase in the ST values starts at image 85, shortly before the drop is released. For the corresponding axisymmetric drop shape analysis (ADSA) of the drop shape and the self-consistent solution of the Young–Laplace equation, we used the SCA 22/15 software (surface and interfacial tension; pendant drop) from DataPhysics, which numerically solves the Young–Laplace equation in a self-consistent way with respect to manually set reference lines (see Figure 3).

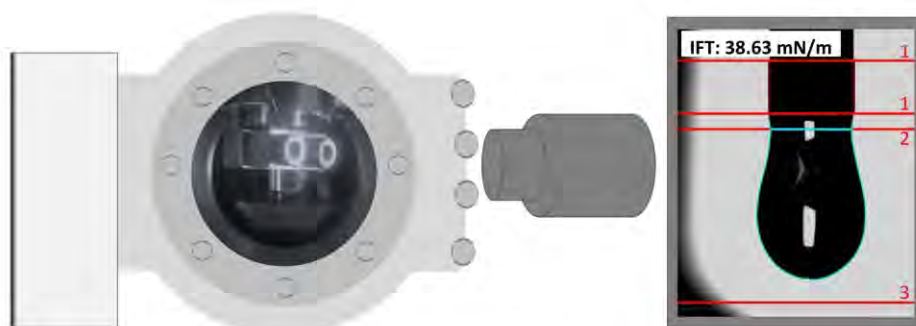


Figure 3. Left: Schematic representation of the PD setup with diffuse light source (left), chamber with drop (middle) and camera (right). Right: Drop image with manually set reference lines for surface tension evaluation (red, 1: magnification lines, 2: cannula end line, 3: boundary line for calibration) and obtained contour lines (turquoise).

As mentioned above, the whole vacuum chamber is heated with heating tapes in order to determine surface tensions at different temperatures. As the mass and thermal inertia of the stainless-steel chamber is quite large and the heat conductance of the vacuum is zero, heating and cooling of a pendant drop is very slow, and it is very difficult to target a certain absolute and constant temperature. The videos for the temperature-dependent ST-measurements are, thus, typically recorded as close as possible to the targeted temperatures with as low a thermal drift of the cannula temperature as possible (around ± 0.1 K/min) to achieve good thermal equilibration. Note that the accuracy of the temperature determination at the location of the pendant drop is, nevertheless, very precise (± 0.2 K). The homogeneity of the temperature is verified by two independent type K-thermocouples, which are mounted next to the cannula tip (see Figure 4); the maximum difference between the two thermocouples is 0.2 K. Data at specific absolute temperatures values (e.g., the standard temperature of 298.15 K or other ST values of ILs given in literature) are obtained by linear interpolating our ST values measured for temperatures below and above the targeted temperature.

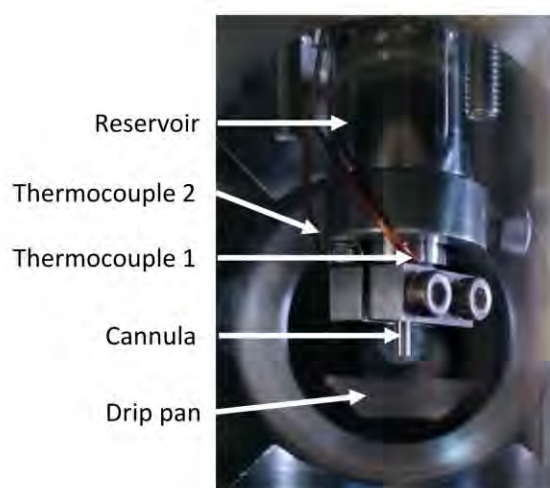


Figure 4. View into chamber for pendant drop measurements (note the two thermocouples attached to the cannula for accurate and independent temperature readings).

2.3. Sessile Drop

Our system can also be used for sessile drop measurements onto ultraclean surfaces. For these measurements, we use a cannula with a smaller outer diameter of $\varnothing_o = 1.05$ mm (inner diameter: $\varnothing_i = 0.5$ mm) in order to obtain a suitable small size of the formed droplets. According to literature [34,39–43], the volume of a sessile drop should be 0.5 to 10 μL so that the influence of the gravitational force can be neglected and reproducible data are obtained. After pumping down the chamber and degassing the liquid in the reservoir, first, a few preliminary drops are formed and disposed into a small drip pan, which can be moved under the cannula. Thereafter, the actual deposition of droplets on solid samples is performed.

The sample is mounted on a z-shift manipulator in a vacuum suitcase, which is attached to the bottom flange of the PD/SD chamber via a gate valve and is pumped by a small ion getter pump. The transport suitcase allows for the transfer of well-prepared samples (e.g., cleaning by sputtering and annealing in UHV, followed by surface analysis by XPS) via a fast entry load-lock (FEL) chamber from our UHV XPS system DASSA [37] to the PD/SD chamber without breaking the vacuum. Vice versa, it also allows for vacuum-transfer of deposited sessile drops without air contact to the DASSA for further XPS analysis with respect to IL composition and purity.

In order to deposit a drop onto the solid sample surface, the gate valve is opened and the sample is moved into the targeted position below the cannula with the z-shift (see Figures 1 and 5). After deposition of the droplet, the contact angle is determined by taking photographs with the camera and analysing the images using the software SCA 20 (contact angle measurement) from DataPhysics (see Figure 6). A pBN heater (Neyco, PCPBNP05, $\Phi = 12.7$ mm, resistance: 5–7 Ohm, maximum power: 80 W) mounted in the z-shift allows for simultaneous heating of the sample (up to 800 K) in order to perform temperature-dependent contact angle measurements.

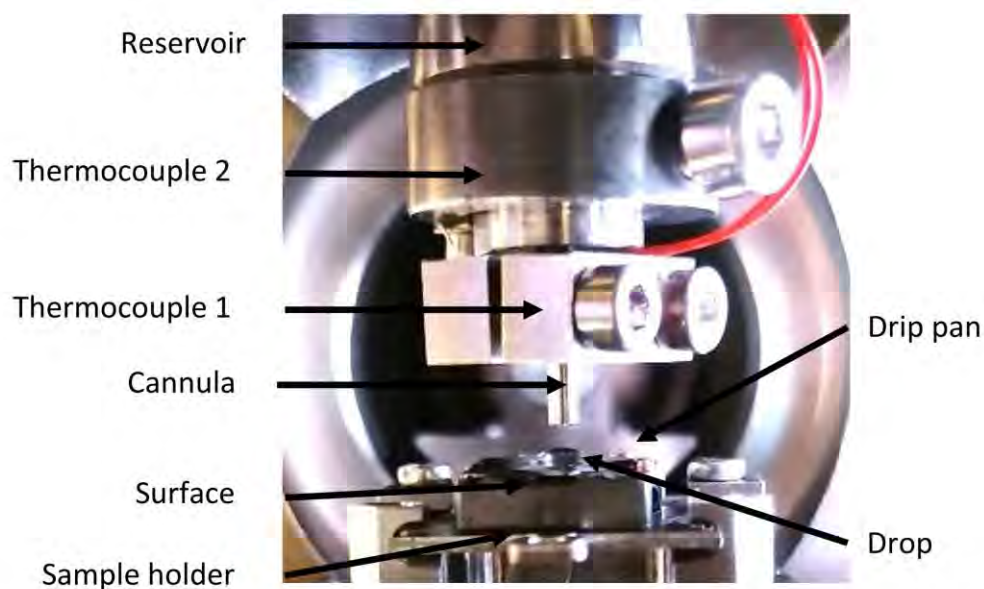


Figure 5. View into chamber for sessile drop measurements. A sample holder is positioned directly under the cannula to place a drop on a sample surface.

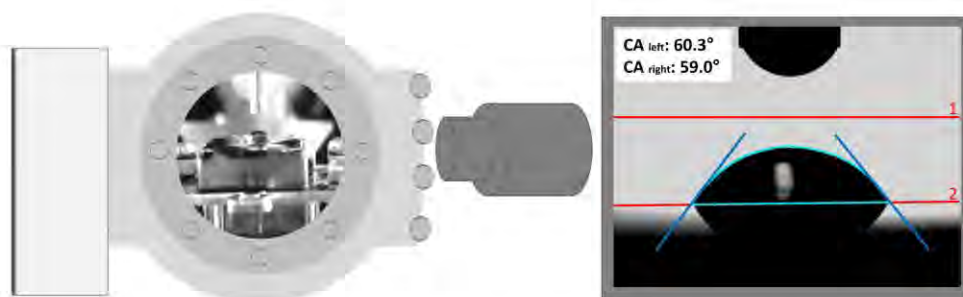


Figure 6. Left: Schematic representation of the SD configuration for interface tension measurements with the diffuse light source (left), chamber with sessile drop (middle) and camera (right). Right: Image of a sessile drop of $[\text{C}_8\text{C}_1\text{Im}][\text{PF}_6]$ placed at room temperature under vacuum conditions on carbon-contaminated stainless-steel with the manually set reference lines in red (1: boundary line, 2: base line). From the software-derived contour line (turquoise) with its tangents (blue), the values for the left and the right contact angle are deduced.

In a preliminary test in air, contact angles (CA) of a drop of the IL $[\text{C}_8\text{C}_1\text{Im}][\text{PF}_6]$ (see next section also) on two different stainless-steel samples were measured (see photographs, CA values and ex situ survey XP spectra in Figure S5 in SI). The sample surface with a larger carbon content in XPS (and an additional fluorine contamination) exhibited a considerably larger CA ($\sim 54^\circ$) and, thus, a worse IL wetting behaviour compared to the less-carbon contaminated surface, where a significantly smaller CA ($\sim 24^\circ$) was measured. These first findings are in line with our earlier studies on the change in IL wetting behaviour with surface carbon content in cases of ultrathin IL films deposited by physical vapour deposition onto various carbonaceous surfaces [44]. The proof-of-principle sessile drop experiment under vacuum is shown in Figure 6: a small drop of $[\text{C}_8\text{C}_1\text{Im}][\text{PF}_6]$ was placed under HV conditions on a stainless-steel sample holder confirming that well-defined sessile drops for reliable CA measurements in vacuum can be performed with our setup. In the future, detailed SD measurements of clean ILs in contact with well-defined single crystal surfaces are foreseen.

3. Reference Pendant Drop Measurements in Air

When introducing a new experimental apparatus, it is essential to perform calibration measurements under well-defined conditions. For this purpose, we decided to measure the surface tensions of water and benzene under ambient conditions (≈ 1 bar air). Thereafter, the first experiments on two IL systems were performed (in HV and for comparison under ambient conditions). For all PD measurements presented herein, we used a cannula with $\varnothing_0 = 2.02$ mm and $\varnothing_1 = 0.5$ mm (for the reasons for choosing this size, see above and SI).

3.1. Water

The surface tension measurements were performed with Millipore water (resistivity 18.2 $\text{M}\Omega\cdot\text{cm}$) at room temperature (295.45 K, literature value for γ at this temperature: 72.34 mN/m [45]) at 1 bar ambient pressure to find the optimum conditions/positions for the light source and the high-speed camera relative to the setup and to calibrate the whole system. Images were taken at different contrast and brightness settings in the SCA 22/15 software from DataPhysics (see Figure S3 SI) to illustrate the influence on the drop contour and, thus, on the resulting γ values using the density value for water of 0.9990 g/cm^3 [46]. With settings for contrast of 16 and brightness of 12 (and also with slightly lower or higher brightness), the obtained surface tension values of 72.40 ± 0.06 mN/m deviate with the literature value by less than 0.1% (see Table 1 and Figure S3 in the SI). Thus, these settings were also used for all PD measurements in the following.

Table 1. Surface tension reference measurements with water and benzene at room temperature and atmospheric pressure ($p \approx 1$ bar). Density and literature surface tension for water are from Refs. [45,46] and for benzene from Refs. [47,48]. The maximum error in the surface tension compared to the literature values is 0.1% for water and 0.8% for benzene.

Reference Liquid	T (K)	ρ (g/cm ³)	γ (mN/m)	γ (mN/m) Literature	Standard Deviaton $\Delta\gamma$ (mN/m)	Maximum Deviaton $\Delta\gamma = \frac{ \gamma_{min} - \gamma_{max} }{2}$ (mN/m)	Deviation from Literature Value (%)
MP-water	295.45	0.9990 [46]	72.40 ± 0.06	72.34 [45]	0.06		<0.1
Benzene	295.15	0.8767 [47]	28.85 ± 0.03	28.62 [48]	0.23	0.03	0.8

3.2. Benzene

To crosscheck our calibration, PD measurements were also carried out for benzene (C₆H₆) in air at room temperature ($p \approx 1$ bar, 295.15 K, see Table 1), using the settings deduced for water (see above). The surface tension values were determined using the density for benzene at this temperature and compared with the values from Ref. [47], obtained under equilibrium benzene vapour pressure conditions (note that we were not able to apply these conditions in our setup). Our determined surface tension of 28.85 ± 0.03 mN/m falls slightly above the literature value (28.62 mN/m at 295.15 K [48]). Note that this 0.8% deviation falls in the statistical uncertainty range of ± 2% typically observed for surface tensions values measured with the PD method [18,49]. In contrast to water, we partly attribute the slightly higher surface tension value of benzene as compared to literature to the higher benzene vapour pressure and to the non-equilibrium conditions in our setup. As can be directly observed in the videos, the formed benzene drops slowly evaporate during the image recording, which leads to a decrease in drop volume and more spherical drop shapes; thus, the prerequisite of a stable pendant drop is not fully fulfilled. Since the system is operated manually, no μ L addition to the drop can be performed to compensate for the loss due to evaporation, as is often done in literature [38,50,51]. However, since our system was designed for surface tension measurements of non-volatile liquids, this evaporation issue is not relevant for our targeted measurements on ILs. Finally, we want to emphasize again the advantage of our video recording approach, which also proved very useful for the evaluation of the surface tension for liquids with a high vapour pressure, since it allows one to record the shape of the drop in any state, particularly before it becomes too small.

4. Pendant Drop Measurements on Ionic Liquids in High Vacuum

4.1. 1-Methyl-3-Octylimidazolium Hexafluorophosphate [C₈C₁Im][PF₆] in Vacuum and Air

As the first IL system, we investigated the surface tension of the common IL [C₈C₁Im][PF₆] in a high vacuum and in air. We started with the high vacuum measurements. After inserting [C₈C₁Im][PF₆] into the PD reservoir, the chamber was slowly pumped down and then heated to ≈ 360 K for IL degassing during 12 h at this temperature. Thereafter, we measured the surface tension at a pressure of $3.3 \cdot 10^{-6}$ mbar from 360 down to 295 K. As a next step, we vented the chamber with air and measured the surface tension of the HV-degassed IL in the same temperature range at ambient pressure of ≈ 1 bar. For comparison, we also performed surface tension measurements of the initial, that is, the non-degassed [C₈C₁Im][PF₆], at a pressure of ≈ 1 bar in a similar temperature range. For all datasets, we used the temperature-dependent density of dried [C₈C₁Im][PF₆] from Ref. [52] to evaluate the surface tension; the corresponding ST data are shown in Figure 7a (individual values are provided in Table S1 of SI along their uncertainties, which are typically the size of the data points shown). In all cases, a linear temperature dependence was observed, which was fitted by the following equation:

$$\gamma_{\text{calc}} = \gamma_0 + \gamma_1 \cdot T \quad (1)$$

where γ_0 and γ_1 are the fitting coefficients and T the temperature in Kelvin. With this equation and the corresponding coefficients, the surface tension values were calculated for the specific temperature of 298.15 K (see Table 2) and plotted for the different measurement conditions (see Figure 7b). For the degassed IL at 298.15 K in air under ambient pressure, we deduced a surface tension value of 34.03 mN/m. This value agrees to within 0.24% with the one obtained in Ref. [53] with the Wilhelmy Plate method under similar conditions (33.95 mN/m for degassed $[\text{C}_8\text{C}_1\text{Im}][\text{PF}_6]$, ambient pressure, 298.13 K, see Table 2), while it deviates by approx. 2% from the value measured by Freire et al. with the Du Noüy ring method (34.87 mN/m for degassed $[\text{C}_8\text{C}_1\text{Im}][\text{PF}_6]$, ambient pressure, 298.15 K, Ref. [54]). However, deviations of several % are quite common when comparing differences in ABSOLUTE surface tensions values from different groups [18,49]. Nevertheless, much smaller RELATIVE changes in surface tension, e.g., induced by a changed water content, can be reliably detected with high accuracy when using an identical apparatus, as was done herein.

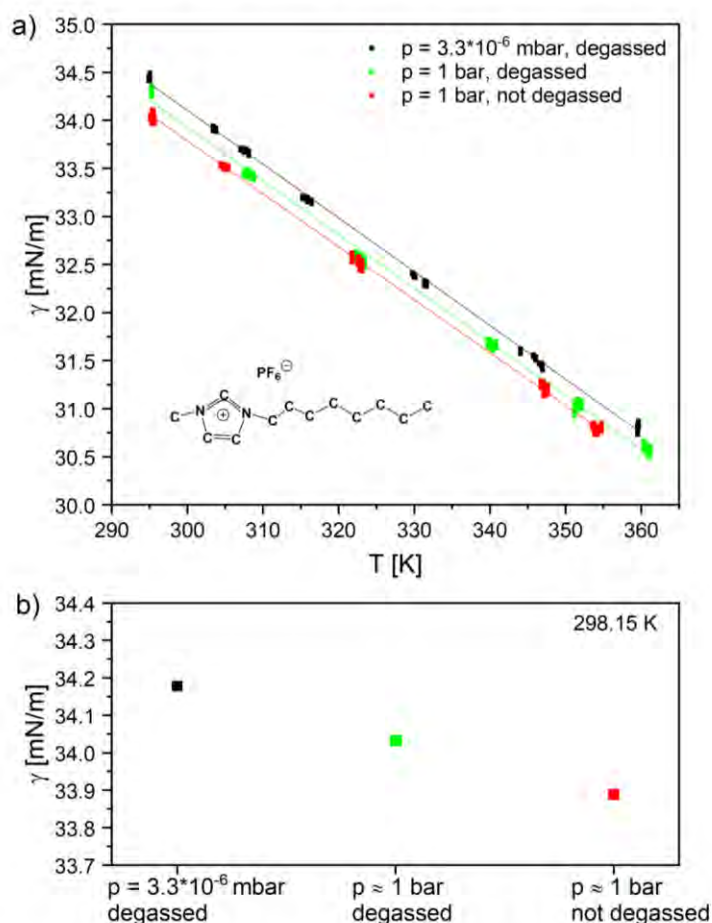


Figure 7. Surface tension of $[\text{C}_8\text{C}_1\text{Im}][\text{PF}_6]$ (see inset) in vacuum and in air ($p \approx 1$ bar) under degassed and non-degassed conditions at different temperatures (a) using the temperature-dependent density of dried $[\text{C}_8\text{C}_1\text{Im}][\text{PF}_6]$ from Ref. [52] (ST values are provided in Table S1 of SI). (b) Calculated ST values at room temperature (298.15 K) for the three different conditions (see also Table 2) based on the linear fits of (a) using Equation (1).

addition, note that drop changes due to evaporation also do not have an influence on the determined surface tension (see Figure S4 SI) as compared to the calibration measurements with benzene (see above).

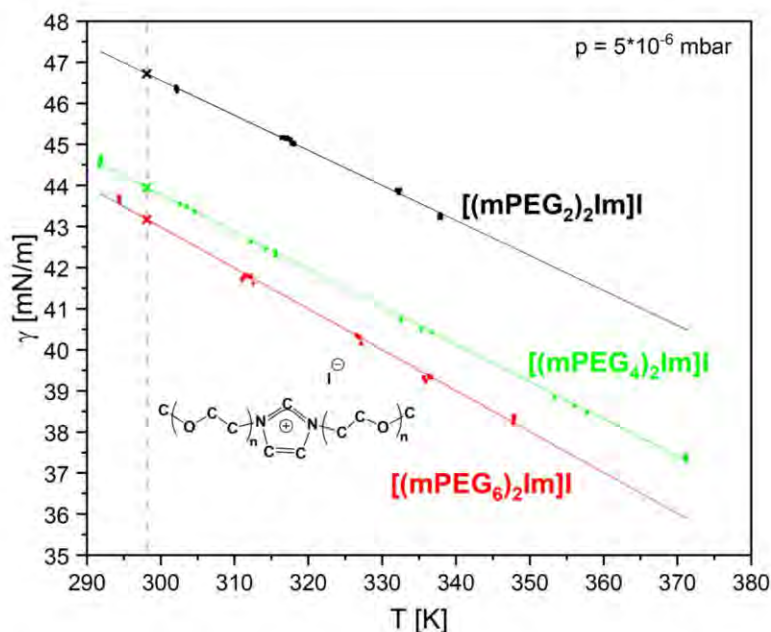


Figure 8. Surface tension values (see also Table S2 of SI) of the three degassed ILs $[(m\text{PEG}_n)_2\text{Im}]\text{I}$ (see inset) with $n = 2, 4, 6$ measured under vacuum ($p = 5 \cdot 10^{-6}$ mbar) for different temperatures; symbol heights correspond to measurement error; crosses at 298.15 K (dashed line) represent the values given in Table 3 based on the linear fits according to Equation (1).

Table 3. Surface tension values of $[(m\text{PEG}_n)_2\text{Im}]\text{I}$ with $n = 2, 4, 6$ at $T = 298.15$ K measured under vacuum in comparison to literature data measured under 1 bar Ar atmosphere [56]. Coefficients γ_0 and γ_1 of Equation (1) for the temperature-dependent surface tension are also given along the R^2 values of the linear fits.

IL	γ (mN/m) at $5 \cdot 10^{-6}$ mbar ($T = 298.15$ K)	γ (mN/m) from Ref. [56] at 1 bar Ar ($T = 298.15$ K)	γ_0 (mN/m)	γ_1 (mN/m·K ⁻¹)	R^2
$[(m\text{PEG}_2)_2\text{Im}]\text{I}$	46.72	46.26	72.17	-0.0854	0.997
$[(m\text{PEG}_4)_2\text{Im}]\text{I}$	43.95	43.94	71.05	-0.0909	0.999
$[(m\text{PEG}_6)_2\text{Im}]\text{I}$	43.17	42.96	72.87	-0.0996	0.997

With increasing temperature, we again observe a linear decrease in surface tension. When comparing the different ILs, we find that the surface tension decreases with increasing PEG_n chain length n . At 298.15 K, the surface tension decreases from 46.72 mN/m for PEG_2 to 43.95 mN/m for PEG_4 , to 43.17 mN/m for PEG_6 (see Table 3); that is, the surface tension decreases by -5.9% when increasing the PEG-chain length from 2 to 4 and only by -1.8% when increasing the PEG-chain length from 4 to 6. Our PD measurements in HV are accompanied by ARXPS measurements in UHV: the latter clearly indicate a preferential orientation of the PEG chains towards the surface and a depletion of the iodine anion, which increases with increasing chain length [56]. The pronounced decrease in ST from PEG_2 to PEG_4 and the second moderate decrease from PEG_4 to PEG_6 can be understood

in terms of a simplified Langmuir principle, which relates surface tension to composition at the outermost surface [8]. Above a certain PEG-chain length, the surface layer is more or less fully saturated with PEG-chain constituents and, thus, the surface tension levels off. A similar behaviour has also been reported for $[C_nC_1Im][Tf_2N]$ anion-based ILs with different alkyl chain lengths [8]. Here, ARXPS measurements also revealed an orientation of the alkyl chains towards the surface, which goes along with the observation that above a certain chain length, the surface tension remains more or less constant due to saturation of the alkyl chains being present at the outer surface.

5. Summary and Conclusions

We described and characterized a new experimental setup for measuring the surface tension by the pendant drop method and the interface tension by the sessile drop method (contact angle) in the pressure range from 10^{-7} mbar up to 1 bar for non-volatile liquids such as ionic liquids (ILs). Such temperature-dependent measurements on well-defined ILs, as characterized by in situ angle-resolved photoelectron spectroscopy (ARXPS) under ultraclean vacuum conditions, allow for determining intrinsic surface tension values of ILs and interface tension values of ILs in contact with solid surfaces without the influence of additional surface contaminations, which are known to be omnipresent for ILs and solids. This information is instrumental for a fundamental understanding of microscopic properties, such as composition and ion orientation at the surface/interface layer, which contribute to the macroscopic surface and interface tension. Such data also serve as a benchmark for theoretical calculations and molecular dynamic simulations. Using the pendant drop method, the surface tensions of two different IL systems were determined, and for the sessile drop method, proof-of-principle experiments were performed. The pendant drop measurements at different pressures and gas ambiances provide insights into the influence of these variables on the surface tension with very high accuracy. Compared to $[C_8C_1Im][PF_6]$ measured in vacuum, we indeed observed a significant decrease in surface tension when measured in air, which is attributed to the uptake of water in the case of this IL. The temperature-dependent surface tension values of $[m(PEG_n)_2Im]I$ ILs with different PEG chain lengths ($n = 2, 4, 6$) showed very good agreement with previously published data of these ILs measured under 1 bar Ar in a completely different setup. The reported decrease in surface tension with increasing chain length chains could be confirmed by our vacuum data and is attributed to an increasing enrichment of the PEG chains at the surface found in ARXPS.

6. Materials

Surface tension measurements were performed with Millipore water (resistivity $18.2 \text{ M}\Omega\text{-cm}$), analytically benzene (C_6H_6) (purity 99.7%) purchased from Merck, acquired from Sigma-Aldrich and 1-Methyl-3-octylimidazolium hexafluorophosphate $[C_8C_1Im][PF_6]$ (purity 99%), purchased from IoLiTec and used as delivered. The $[m(PEG_n)_2Im]I$ with ($n = 2, 4, 6$) were synthesized by V. Seidl according to Ref. [56].

Supplementary Materials: The following supporting information can be downloaded at: <https://www.mdpi.com/article/10.3390/ijms232113158/s1>. References [57–61].

Author Contributions: Conceptualization: U.P., H.-P.S. and F.M.; development, construction and evaluation of final setup and methodology: U.P. and B.K.; investigation and analysis: U.P.; validation of data: U.P., H.-P.S. and F.M.; writing: U.P., H.-P.S. and F.M.; project administration and funding acquisition: H.-P.S. All authors have read and agreed to the published version of the manuscript.

Funding: This work was supported by the DFG in the course of the Collaborative Research Center (CRC)/Sonderforschungsbereich (SFB) 1452—Project-ID 431791331.

Acknowledgments: We acknowledge V. Seidl and K. Meyer for the supply of the bis-polyethylene glycol-functionalized ILs $[m(PEG_n)_2Im]I$ and Z. Zhai and Th. Koller for fruitful collaboration and discussion concerning the surface tension measurements.

Conflicts of Interest: The authors declare no conflict of interest.

References

1. Sedev, R. Surface tension, interfacial tension and contact angles of ionic liquids. *Curr. Opin. Colloid Interface Sci.* **2011**, *16*, 310–316. [[CrossRef](#)]
2. Ahmadi, M.A.; Mahmoudi, B. Development of robust model to estimate gas–oil interfacial tension using least square support vector machine: Experimental and modeling study. *J. Supercrit. Fluids* **2016**, *107*, 122–128. [[CrossRef](#)]
3. Langmuir, I. Forces Near the Surfaces of Molecules. *Chem. Rev.* **1930**, *6*, 451–479. [[CrossRef](#)]
4. Pádua, A.A.; Costa Gomes, M.F.; Canongia Lopes, J.N. Molecular solutes in ionic liquids: A structural perspective. *Acc. Chem. Res.* **2007**, *40*, 1087–1096. [[CrossRef](#)]
5. Jiang, W.; Wang, Y.; Yan, T.; Voth, G.A. A multiscale coarse-graining study of the liquid/vacuum interface of room-temperature ionic liquids with alkyl substituents of different lengths. *J. Phys. Chem. C* **2008**, *112*, 1132–1139. [[CrossRef](#)]
6. Plechkova, N.V.; Seddon, K.R. Applications of ionic liquids in the chemical industry. *Chem. Soc. Rev.* **2008**, *37*, 123–150. [[CrossRef](#)]
7. Kaur, G.; Kumar, H.; Singla, M. Diverse applications of ionic liquids: A comprehensive review. *J. Mol. Liq.* **2022**, *351*, 118556. [[CrossRef](#)]
8. Shimizu, K.; Heller, B.S.J.; Maier, F.; Steinrück, H.-P.; Lopes, J.N.C. Probing the surface tension of ionic liquids using the langmuir principle. *Langmuir* **2018**, *34*, 4408–4416. [[CrossRef](#)]
9. Massoudi, R.; King, A.D. Effect of pressure on the surface tension of water. Adsorption of low molecular weight gases on water at 25. deg. *J. Phys. Chem.* **1974**, *78*, 2262–2266. [[CrossRef](#)]
10. Sachs, W.; Meyn, V. Pressure and temperature dependence of the surface tension in the system natural gas/water principles of investigation and the first precise experimental data for pure methane/water at 25 °C up to 46.8 MPa. *Colloids Surf. A Physicochem. Eng. Asp.* **1995**, *94*, 291–301. [[CrossRef](#)]
11. Steinrück, H.-P.; Libuda, J.; Wasserscheid, P.; Cremer, T.; Kolbeck, C.; Laurin, M.; Maier, F.; Sobota, M.; Schulz, P.S.; Stark, M. Surface science and model catalysis with ionic liquid-modified materials. *Adv. Mater.* **2011**, *23*, 2571–2587. [[CrossRef](#)] [[PubMed](#)]
12. Hashimoto, H.; Ohno, A.; Nakajima, K.; Suzuki, M.; Tsuji, H.; Kimura, K. Surface characterization of imidazolium ionic liquids by high-resolution Rutherford backscattering spectroscopy and X-ray photoelectron spectroscopy. *Surf. Sci.* **2010**, *604*, 464–469. [[CrossRef](#)]
13. Smith, E.F.; Rutten, F.J.M.; Villar-Garcia, I.J.; Briggs, D.; Licence, P. Ionic liquids in vacuo: Analysis of liquid surfaces using ultra-high-vacuum techniques. *Langmuir* **2006**, *22*, 9386–9392. [[CrossRef](#)] [[PubMed](#)]
14. Santos, C.S.; Baldelli, S. Gas–liquid interface of room-temperature ionic liquids. *Chem. Soc. Rev.* **2010**, *39*, 2136–2145. [[CrossRef](#)] [[PubMed](#)]
15. Goodman, D.W. Model studies in catalysis using surface science probes. *Chem. Rev.* **1995**, *95*, 523–536. [[CrossRef](#)]
16. Berry, J.D.; Neeson, M.J.; Dagastine, R.R.; Chan, D.Y.C.; Tabor, R.F. Measurement of surface and interfacial tension using pendant drop tensiometry. *J. Colloid Interface Sci.* **2015**, *454*, 226–237. [[CrossRef](#)]
17. Franses, E.I.; Basaran, O.A.; Chang, C.-H. Techniques to measure dynamic surface tension. *Curr. Opin. Colloid Interface Sci.* **1996**, *1*, 296–303. [[CrossRef](#)]
18. Tariq, M.; Freire, M.G.; Saramago, B.; Coutinho, J.A.; Lopes, J.N.C.; Rebelo, L.P.N. Surface tension of ionic liquids and ionic liquid solutions. *Chem. Soc. Rev.* **2012**, *41*, 829–868. [[CrossRef](#)]
19. Hoorfar, M.; Kurz, M.A.; Neumann, A.W. Evaluation of the surface tension measurement of axisymmetric drop shape analysis (ADSA) using a shape parameter. *Colloids Surf. A Physicochem. Eng. Asp.* **2005**, *260*, 277–285. [[CrossRef](#)]
20. Ferrera, C.; Montanero, J.M.; Cabezas, M.G. An analysis of the sensitivity of pendant drops and liquid bridges to measure the interfacial tension. *Meas. Sci. Technol.* **2007**, *18*, 3713–3723. [[CrossRef](#)]
21. Saad, S.M.; Policova, Z.; Acosta, E.J.; Neumann, W.A. Range of validity of drop shape techniques for surface tension measurement. *Langmuir* **2010**, *26*, 14004–14013. [[CrossRef](#)] [[PubMed](#)]
22. Worthington, A.M. II. On pendent drops. *Proc. R. Soc. Lond.* **1881**, *32*, 362–377.
23. Worthington, A.M. IV. Note on a point in the theory of pendent drops. *Lond. Edinb. Dublin Philos. Mag. J. Sci.* **1885**, *19*, 46–48. [[CrossRef](#)]
24. Ferguson, A. Photographic measurements of pendant drops. *Philos. Mag.* **1911**, *23*, 417–430. [[CrossRef](#)]
25. Bashforth, F.; Adams, J.C. *An Attempt to Test the Theories of Capillary Action by Comparing the Theoretical and Measured Forms of Drops of Fluid*; University Press: Cambridge, UK, 1883.
26. Merrington, A.C.; Richardson, E.G. The break-up of liquid jets. *Proc. Phys. Soc.* **1947**, *59*, 1–13. [[CrossRef](#)]
27. Andreas, J.M.; Hauser, E.A.; Tucker, W.B. Boundary tension by pendant drops. *J. Phys. Chem.* **1938**, *42*, 1001–1019. [[CrossRef](#)]
28. Fordham, S.; Freeth, F.A. On the calculation of surface tension from measurements of pendant drops. *Proc. R. Soc. London. Ser. A Math. Phys. Sci.* **1948**, *194*, 1–16.
29. Cheng, P.; Li, D.; Boruvka, L.; Rotenberg, Y.; Neumann, W.A. Automation of axisymmetric drop shape analysis for measurements of interfacial tensions and contact angles. *Colloids Surf.* **1990**, *43*, 151–167. [[CrossRef](#)]
30. Del Rio, O.I.; Neumann, A.W. Axisymmetric drop shape analysis: Computational methods for the measurement of interfacial properties from the shape and dimensions of pendant and sessile drops. *J. Colloid Interface Sci.* **1997**, *196*, 136–147.

31. Rotenberg, Y.; Boruvka, L.; Neumann, A.W. Determination of surface tension and contact angle from the shapes of axisymmetric fluid interfaces. *J. Colloid Interface Sci.* **1983**, *93*, 169–183. [CrossRef]
32. Hoorfar, M.; Neumann, A.W. Recent progress in axisymmetric drop shape analysis (ADSA). *Adv. Colloid Interface Sci.* **2006**, *121*, 25–49. [CrossRef] [PubMed]
33. Huh, C.; Reed, R.L. A method for estimating interfacial tensions and contact angles from sessile and pendant drop shapes. *J. Colloid Interface Sci.* **1983**, *91*, 472–484. [CrossRef]
34. Schuster, J.M.; Schvezov, C.E.; Rosenberger, M.R. Influence of experimental variables on the measure of contact angle in metals using the sessile drop method. *Procedia Mater. Sci.* **2015**, *8*, 742–751. [CrossRef]
35. Young, T. III. An essay on the cohesion of fluids. *Philos. Trans. R. Soc. Lond.* **1805**, *95*, 65–87.
36. Spelt, J.K.; Absolom, D.R.; Neumann, A.W. Solid surface tension: The interpretation of contact angles by the equation of state approach and the theory of surface tension components. *Langmuir* **1986**, *2*, 620–625. [CrossRef]
37. Niedermaier, I.; Kolbeck, C.; Steinrück, H.-P.; Maier, F. Dual analyzer system for surface analysis dedicated for angle-resolved photoelectron spectroscopy at liquid surfaces and interfaces. *Rev. Sci. Instrum.* **2016**, *87*, 045105. [CrossRef]
38. Saad, S.M.I.; Policova, Z.; Neumann, A.W. Design and accuracy of pendant drop methods for surface tension measurement. *Colloids Surf. A Physicochem. Eng. Asp.* **2011**, *384*, 442–452. [CrossRef]
39. Kaelble, D.H.; Cirlin, E.H. Dispersion and polar contributions to surface tension of poly (methylene oxide) and Na-treated polytetrafluoroethylene. *J. Polym. Sci. Part A-2 Polym. Phys.* **1971**, *9*, 363–368. [CrossRef]
40. Blythe, A.R.; Briggs, D.; Kendall, C.R.; Rance, D.G.; Zichy, V.J.I. Surface modification of polyethylene by electrical discharge treatment and the mechanism of autoadhesion. *Polymer* **1978**, *19*, 1273–1278. [CrossRef]
41. Fowkes, F.M.; McCarthy, D.C.; Mostafa, M.A. Contact angles and the equilibrium spreading pressures of liquids on hydrophobic solids. *J. Colloid Interface Sci.* **1980**, *78*, 200–206. [CrossRef]
42. Rudawska, A.; Jacniacka, E. Analysis for determining surface free energy uncertainty by the Owen–Wendt method. *Int. J. Adhes. Adhes.* **2009**, *29*, 451–457. [CrossRef]
43. Vuckovac, M.; Latikka, M.; Liu, K.; Huhtamäki, T.; Ras, R.H.A. Uncertainties in contact angle goniometry. *Soft Matter* **2019**, *15*, 7089–7096. [CrossRef] [PubMed]
44. Rietzler, F.; Nagengast, J.; Steinrück, H.P.; Maier, F. Interface of ionic liquids and carbon: Ultrathin [C1C1Im][Tf2N] films on graphite and graphene. *J. Phys. Chem. C* **2015**, *119*, 28068–28076. [CrossRef]
45. Vargaftik, N.B.; Volkov, B.N.; Voljak, L.D. International tables of the surface tension of water. *J. Phys. Chem. Ref. Data* **1983**, *12*, 817–820. [CrossRef]
46. Kell, G.S. Density, thermal expansivity, and compressibility of liquid water from 0. deg. to 150. deg. Correlations and tables for atmospheric pressure and saturation reviewed and expressed on 1968 temperature scale. *J. Chem. Eng. Data* **1975**, *20*, 97–105. [CrossRef]
47. Parkhurst, H.J., Jr.; Jonas, J. Dense liquids. II. The effect of density and temperature on viscosity of tetramethylsilane and benzene. *J. Chem. Phys.* **1975**, *63*, 2705–2709. [CrossRef]
48. Sugden, S. VI—The variation of surface tension with temperature and some related functions. *J. Chem. Soc. Trans.* **1924**, *125*, 32–41. [CrossRef]
49. Sánchez, L.G.; Espel, J.R.; Onink, F.; Meindersma, G.W.; Haan, A.B.D. Density, viscosity, and surface tension of synthesis grade imidazolium, pyridinium, and pyrrolidinium based room temperature ionic liquids. *J. Chem. Eng. Data* **2009**, *54*, 2803–2812. [CrossRef]
50. Naser, M.A.; Permadi, A.K.; Bae, W.; Ryoo, W.; Siregar, S. A laboratory investigation of the effects of saturated steam properties on the interfacial tension of heavy-oil/steam system using pendant drop method. *Energy Environ. Res.* **2015**, *5*, 94. [CrossRef]
51. Kahl, H.; Wadewitz, T.; Winkelmann, J. Surface tension of pure liquids and binary liquid mixtures. *J. Chem. Eng. Data* **2003**, *48*, 580–586. [CrossRef]
52. Gardas, R.L.; Freire, M.G.; Carvalho, P.J.; Marrucho, I.M.; Fonseca, I.M.A.; Ferreira, A.G.M.; Coutinho, J.A.P. High-pressure densities and derived thermodynamic properties of imidazolium-based ionic liquids. *J. Chem. Eng. Data* **2007**, *52*, 80–88. [CrossRef]
53. Klomfar, J.; Součková, M.; Pátek, J. Surface tension measurements for four 1-alkyl-3-methylimidazolium-based ionic liquids with hexafluorophosphate anion. *J. Chem. Eng. Data* **2009**, *54*, 1389–1394. [CrossRef]
54. Freire, M.G.; Carvalho, P.J.; Fernandes, A.M.; Marrucho, I.M.; Queimada, A.J.; Coutinho, J.A.P. Surface tensions of imidazolium based ionic liquids: Anion, cation, temperature and water effect. *J. Colloid Interface Sci.* **2007**, *314*, 621–630. [CrossRef] [PubMed]
55. Freire, M.G.; Neves, C.M.S.S.; Marrucho, I.M.; Coutinho, J.A.P.; Fernandes, A.M. Hydrolysis of tetrafluoroborate and hexafluorophosphate counter ions in imidazolium-based ionic liquids. *J. Phys. Chem. A* **2010**, *114*, 3744–3749. [CrossRef] [PubMed]
56. Seidl, V.; Bosch, M.; Paap, U.; Livraghi, M.; Zhai, Z.; Wick, C.; Koller, T.M.; Wasserscheid, P.; Maier, F.; Smith, A.-S.; et al. Bis-polyethylene glycol-functionalized imidazolium ionic liquids: A multi-method approach towards bulk and surface properties. *J. Ion. Liq.* **2022**, *2*, 100041. [CrossRef]
57. Lin, S.-Y.; Hwang, H.-F. Measurement of low interfacial tension by pendant drop digitization. *Langmuir* **1994**, *10*, 4703–4709. [CrossRef]
58. Morita, A.; Carastan, D.; Demarquette, N. Influence of drop volume on surface tension evaluated using the pendant drop method. *Colloid Polym. Sci.* **2002**, *280*, 857–864. [CrossRef]

59. Alvarez, N.J.; Walker, L.M.; Anna, S.L. A non-gradient based algorithm for the determination of surface tension from a pendant drop: Application to low Bond number drop shapes. *J. Colloid Interface Sci.* **2009**, *333*, 557–562. [[CrossRef](#)]
60. Yang, J.; Yu, K.; Zuo, Y.Y. Accuracy of Axisymmetric Drop Shape Analysis in Determining Surface and Interfacial Tensions. *Langmuir* **2017**, *33*, 8914–8923. [[CrossRef](#)]
61. Hoorfar, M.; Neumann, A.W. Axisymmetric drop shape analysis (ADSA) for the determination of surface tension and contact angle of water. *J. Adhes.* **2004**, *80*, 727–743. [[CrossRef](#)]

Supporting Information

Probing Surface and Interfacial Tension of Ionic Liquids in Vacuum with the Pendant Drop and Sessile Drop Method

Ulrike Paap¹ ORCID: 0000-0002-1442-0239, Bernd Kreß¹, Hans-Peter Steinrück¹ ORCID: 0000-0003-1347-8962,

Florian Maier^{1*} ORCID: 0000-0001-9725-8961

Optimizing cannula dimensions

In addition to the setup calibration in air using ultrapure water (see main text), PD measurements were also performed in air using the ionic liquid (IL) 1-Methyl-3-octylimidazolium hexafluorophosphate ($[\text{C}_8\text{C}_1\text{Im}][\text{PF}_6]$) at different inner and outer cannula diameters. Here, systematic changes in the surface tension were detected: the derived surface tension (ST) values are largest with smallest outer cannula diameter, slightly decreases with increasing outer diameter and starts to increase again for a very large outer cannula diameter. The reason for this behavior is attributed to the difference in drop shape for different cannula diameters [1]. Very small cannulas form very small drops with practically no deformation due to gravity and thus, the drops are rather round [2-4]. For spherical drops, the bond number is very small and the error in ST grows as the bond number decreases [5]. This leads to a greater difference in the individual ST values for each measured drop. On the other end, diameters that are very large can form droplets with a large volume, but the constriction at the neck of the droplet is also not very pronounced [6,7] as for the very small cannulas. Since the constriction at the drop neck is a decisive factor for reliable surface tension determination, we decided to use a cannula with an outer diameter of $\varnothing_o = 2.02$ mm and $\varnothing_i = 0.5$ mm made of stainless-steel (note that the inner diameter does not influence the surface tension if the wettability of the cannula is given [8]; cannula diameters of at least 1.65 mm for PD are also recommended by different manufacturers such as Krüss and DataPhysics).

Drop stability in HV

In contrast to the situation under atmospheric pressure, several difficulties occurred before stable pendant drops of an ionic liquid in vacuum could be measured. Starting with conventional PD cannula dimensions with rather large inner diameters at the beginning, the emerging drops quickly fell off due to the excess of gravitational force without the counterbalancing atmospheric pressure. The only forces that counteract gravity and keep the drop at the tip's end are capillary forces. We tested stainless-steel cannula sizes with different inner and outer diameters. The smaller the inner diameter compared to the outer diameter of the cannula, the more stable the drop was. However, 0.5 mm as inner bore was the minimum limit for practical drilling reasons, which was not sufficient to form stable IL drops. We thus increased the capillary forces by simply inserting two twisted stainless-steel wires (0.2 mm in diameter) into the 0.5 mm cannula bore to further reduce the inner diameter and increase contact surface and thereby the capillary forces. By using this approach, stable drops were successfully formed. For all HV measurements presented here, the twisted wires were always present to ensure stability of the drops even at higher temperatures (see Fig. S2).

Bubble formation in HV

Another very serious problem turned out to be gas bubble formation during the drop formation in HV. Correct degassing of the ILs was thus crucial. Otherwise, bubbles regularly appeared during drop formation, which then caused drop shape deformations and additional IL wetting problems at the outer cannula after bubble bursts accompanied by IL spilling inside the vacuum chamber (see also video SI-movie1-bubble-formation-live.mp4, SI). For the degassing of the ILs measured so far, a reservoir temperature of at least 70 °C to 100 °C was necessary depending on IL with a degassing time of about 8 to 10 hours while applying a vacuum better than 10^{-5} mbar.

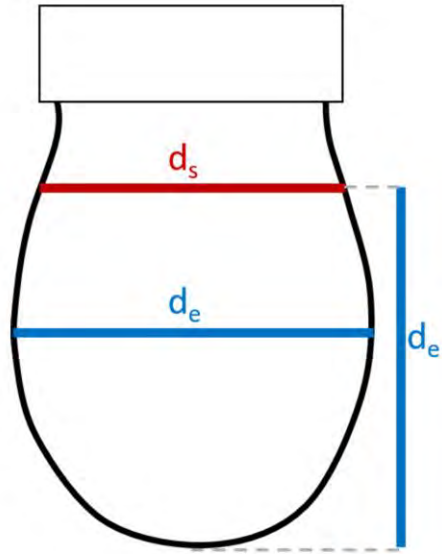


Figure S1: Representation of the “Method of selected planes” from Ref. [9] using the ratio $S = d_s/d_e$ as characteristic descriptor for the pendant drop shape, with the maximum drop diameter d_e (blue) and the drop diameter d_s (red) at the distance d_e above the apex.



Figure S2: Left: Schematic representation of the twisted wires in the cannula, middle: Photo of the twisted wires and the cannula and right: Photo of the twisted wires inserted into the cannula.

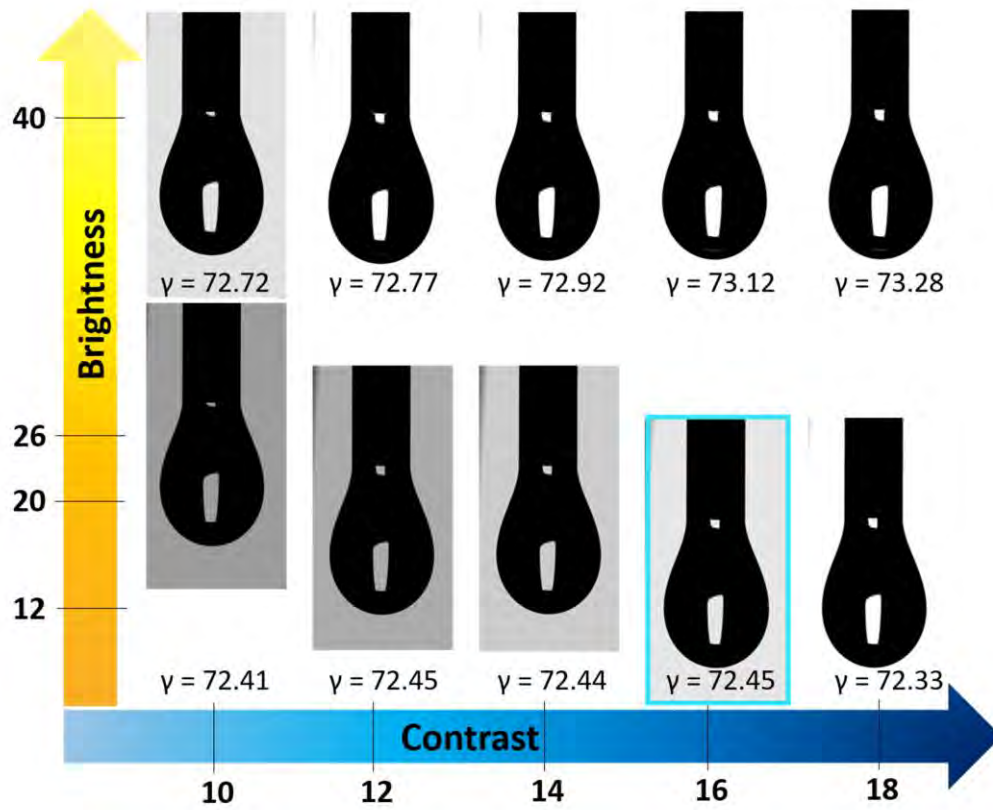


Figure S3: Photographs of Millipore water taken at different contrast and brightness settings in the software SCA 22/15. The drop with the final settings for this work (brightness 12, contrast 16) is outlined in turquoise.

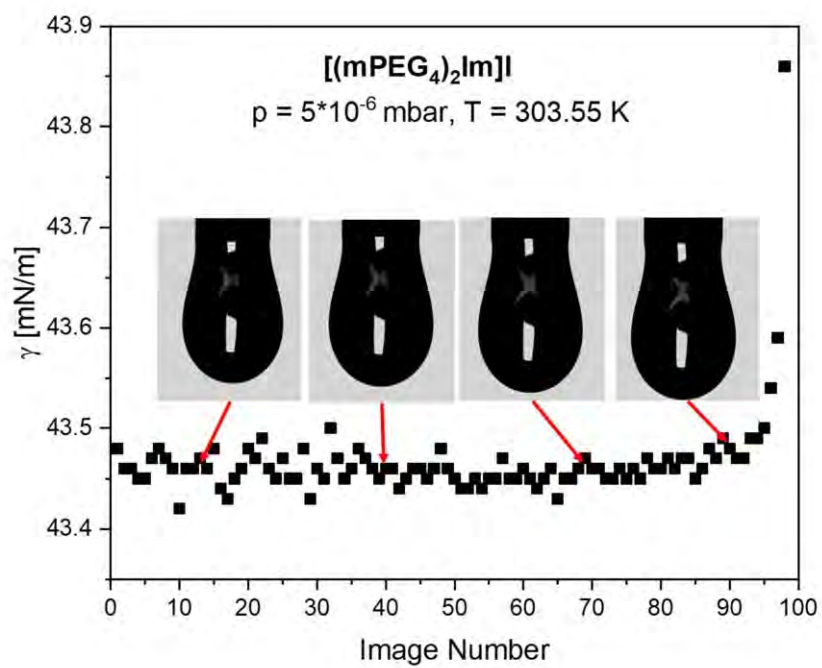


Figure S4: Surface tension of $[(mPEG_4)_2Im]I$ at $T = 303.55$ K derived from a 20 second video (rate of 5 fps); drop fell off after image 100 (see also time lapse video SI-movie2-IL-drop-FigS4-5xfaster.mp4, SI).

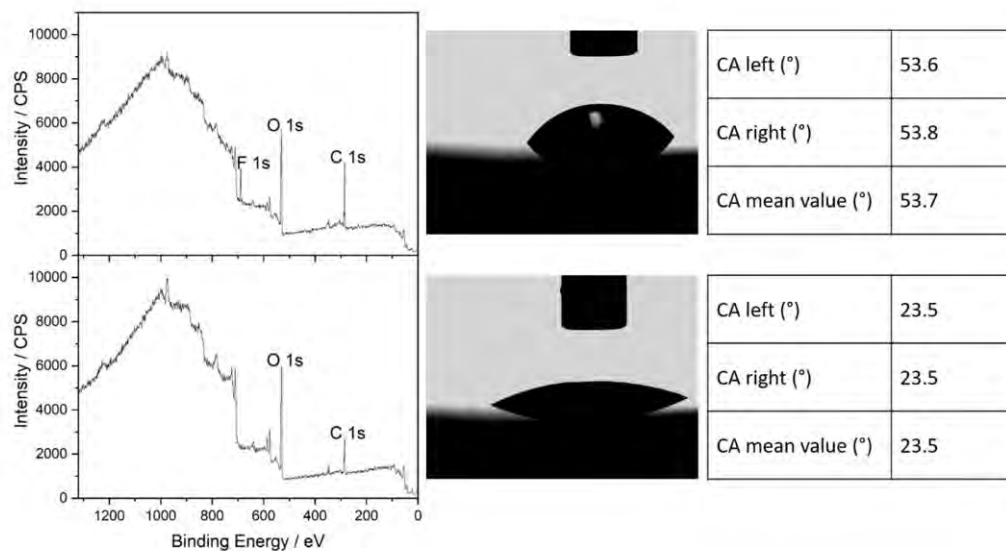


Figure S5: Comparison of room temperature contact angles and thus, wetting behavior, of $[C_8C_1Im][PF_6]$ on stainless-steel supports with different levels of carbon and fluorine contamination. Left: XPS surveys of the supports measured in 0° in UHV, middle: images of the drops on the corresponding surfaces recorded in air, right: related contact angles (CA) of the corresponding images.

Table S1: Individual surface tension values γ plotted in Fig. 7a of $[\text{C}_8\text{C}_1\text{Im}][\text{PF}_6]$ at different pressures under degassed and non-degassed conditions and at different temperatures. At a given temperature, each γ value is obtained by averaging over the ST values derived from several pictures of at least two stable pendant drops (maximum deviations $\Delta_{\text{max}}\gamma$ of the corresponding average values γ are also given).

$[\text{C}_8\text{C}_1\text{Im}][\text{PF}_6]$								
Degassed ($p = 3.3 \cdot 10^{-6}$ mbar)			Degassed ($p = 1.0 \cdot 10^3$ mbar)			Non-degassed ($p = 1.0 \cdot 10^3$ mbar)		
T [K]	γ [mN/m]	$\Delta_{\text{max}}\gamma$ [mN/m]	T [K]	γ [mN/m]	$\Delta_{\text{max}}\gamma$ [mN/m]	T [K]	γ [mN/m]	$\Delta_{\text{max}}\gamma$ [mN/m]
294.95	34.43	± 0.02	295.25	34.29	± 0.04	295.15	34.03	± 0.03
295.05	34.44	± 0.05	295.35	34.31	± 0.06	295.35	34.04	± 0.08
303.45	33.91	± 0.03	307.55	33.44	± 0.02	295.45	34.10	± 0.01
303.65	33.90	± 0.02	307.75	33.46	± 0.03	295.55	34.06	± 0.03
303.75	33.90	± 0.02	307.95	33.44	± 0.02	295.65	34.00	± 0.04
307.35	33.70	± 0.02	308.75	33.40	± 0.02	304.45	33.53	± 0.02
307.55	33.68	± 0.02	321.95	32.60	± 0.02	304.75	33.50	± 0.01
307.75	33.68	± 0.02	322.25	32.60	± 0.09	304.85	33.51	± 0.01
307.95	33.67	± 0.01	322.95	32.57	± 0.07	304.95	33.53	± 0.02
308.15	33.66	± 0.03	323.25	32.55	± 0.05	305.15	33.49	± 0.01
315.25	33.20	± 0.02	323.45	32.53	± 0.06	305.35	33.52	± 0.02
315.85	33.18	± 0.02	339.75	31.70	± 0.05	305.45	33.51	± 0.01
315.95	33.17	± 0.02	339.95	31.68	± 0.05	321.75	32.58	± 0.05
316.35	33.16	± 0.01	340.35	31.65	± 0.05	321.85	32.56	± 0.04
316.45	33.15	± 0.02	340.75	31.66	± 0.04	322.55	32.54	± 0.04
329.75	32.40	± 0.01	351.25	31.00	± 0.07	322.65	32.50	± 0.06
329.95	32.38	± 0.02	351.35	31.02	± 0.04	322.85	32.52	± 0.04
330.15	32.37	± 0.01	351.45	31.06	± 0.05	323.15	32.50	± 0.07
331.35	32.30	± 0.03	351.65	31.05	± 0.05	346.75	32.25	± 0.04
331.45	32.32	± 0.00	351.95	31.05	± 0.03	347.05	31.27	± 0.02
331.65	32.30	± 0.03	352.05	31.03	± 0.03	347.15	31.19	± 0.06
344.05	31.60	± 0.03	352.15	31.04	± 0.03	347.25	31.15	± 0.02
345.75	31.55	± 0.01	360.35	30.63	± 0.03	347.55	31.21	± 0.04
346.05	31.53	± 0.03	360.45	30.59	± 0.03	347.65	31.19	± 0.05
346.55	31.46	± 0.01	360.65	30.60	± 0.03	353.55	30.81	± 0.07
346.85	31.45	± 0.02	360.85	30.58	± 0.04	353.95	30.77	± 0.03
346.95	31.44	± 0.04	361.15	30.56	± 0.06	354.25	30.77	± 0.04
359.55	30.77	± 0.06	361.25	30.58	± 0.02	354.45	30.78	± 0.02
359.65	30.84	± 0.04				354.75	30.82	± 0.06

Table S2: Individual surface tension values γ plotted in Fig. 8 for the three degassed ILS $[m(\text{PEG}_n)_2\text{Im}]$ ($n = 2, 4, 6$) measured in vacuum ($p = 5 \cdot 10^{-6}$ mbar) at different temperatures (values obtained by averaging over several drops and pictures at a given temperature; maximum deviations $\Delta_{\text{max}}\gamma$ of the corresponding average values γ are also given).

[(mPEG ₂) ₂ Im]			[(mPEG ₄) ₂ Im]			[(mPEG ₆) ₂ Im]		
T [K]	γ [mN/m]	$\Delta_{\text{max}}\gamma$ [mN/m]	T [K]	γ [mN/m]	$\Delta_{\text{max}}\gamma$ [mN/m]	T [K]	γ [mN/m]	$\Delta_{\text{max}}\gamma$ [mN/m]
302.05	46.37	±0.03	291.75	44.52	±0.10	394.35	43.65	±0.07
302.25	46.31	±0.06	291.95	44.62	±0.06	394.45	43.63	±0.05
316.35	45.17	±0.02	302.65	44.55	±0.02	311.05	41.71	±0.02
316.75	45.16	±0.02	303.55	43.47	±0.03	311.35	41.79	±0.02
316.95	45.13	±0.01	304.65	43.37	±0.02	311.65	41.81	±0.01
317.15	45.14	±0.03	312.25	42.63	±0.01	312.05	41.78	±0.01
317.35	45.12	±0.02	314.15	42.46	±0.01	312.25	41.78	±0.02
317.65	45.10	±0.02	315.55	42.31	±0.03	312.55	41.61	±0.01
317.75	45.03	±0.02	332.55	40.72	±0.02	326.25	39.70	±0.02
317.95	45.03	±0.03	335.35	40.49	±0.01	326.55	40.36	±0.01
318.05	45.03	±0.02	336.65	40.41	±0.01	326.75	40.30	±0.02
318.15	45.01	±0.02	353.35	38.84	±0.01	327.05	40.30	±0.01
331.95	43.88	±0.01	356.05	38.63	±0.01	327.15	40.15	±0.01
332.25	43.84	±0.06	357.75	38.47	±0.01	335.65	39.32	±0.02
332.45	43.89	±0.01	371.15	37.40	±0.02	335.95	39.23	±0.01
337.25	43.22	±0.02	370.95	37.39	±0.02	336.35	39.34	±0.03
337.85	43.28	±0.02	371.25	37.37	±0.03	336.65	39.33	±0.02
337.95	43.26	±0.01				347.75	38.21	±0.01
338.05	43.23	±0.03				347.85	38.34	±0.05
						347.95	38.37	±0.02

References:

1. Lin, S.-Y.; Hwang, H.-F. Measurement of low interfacial tension by pendant drop digitization. *Langmuir* **1994**, *10*, 4703-4709, doi:10.1021/la00024a052.
2. Berry, J.D.; Neeson, M.J.; Dagastine, R.R.; Chan, D.Y.C.; Tabor, R.F. Measurement of surface and interfacial tension using pendant drop tensiometry. *J. Colloid Interface Sci.* **2015**, *454*, 226-237, doi:10.1016/j.jcis.2015.05.012.
3. Hoorfar, M.; W. Neumann, A. Recent progress in Axisymmetric Drop Shape Analysis (ADSA). *Adv. Colloid Interface Sci.* **2006**, *121*, 25-49, doi:10.1016/j.cis.2006.06.001.
4. Morita, A.; Carastan, D.; Demarquette, N. Influence of drop volume on surface tension evaluated using the pendant drop method. *Colloid Polym. Sci.* **2002**, *280*, 857-864, doi:10.1007/s00396-002-0694-z.
5. Alvarez, N.J.; Walker, L.M.; Anna, S.L. A non-gradient based algorithm for the determination of surface tension from a pendant drop: Application to low Bond number drop shapes. *J. Colloid Interface Sci.* **2009**, *333*, 557-562, doi:10.1016/j.jcis.2009.01.074.
6. Yang, J.; Yu, K.; Zuo, Y.Y. Accuracy of Axisymmetric Drop Shape Analysis in Determining Surface and Interfacial Tensions. *Langmuir* **2017**, *33*, 8914-8923, doi:10.1021/acs.langmuir.7b01778.
7. Hoorfar, M.; Neumann, A.W. Axisymmetric drop shape analysis (ADSA) for the determination of surface tension and contact angle of water. *J. Adhes.* **2004**, *80*, 727-743, doi:10.1080/00218460490477684.
8. Hoorfar, M.; Kurz, M.A.; Neumann, A.W. Evaluation of the surface tension measurement of axisymmetric drop shape analysis (ADSA) using a shape parameter. *Colloids Surf. A Physicochem. Eng. Asp.* **2005**, *260*, 277-285, doi:10.1016/j.colsurfa.2004.08.080.
9. Andreas, J.M.; Hauser, E.A.; Tucker, W.B. Boundary tension by pendant drops 1. *J. Phys. Chem.* **1938**, *42*, 1001-1019, doi:10.1021/j100903a002.

8.1.3. DIRECT CORRELATION OF SURFACE TENSION AND SURFACE COMPOSITION OF IONIC LIQUID MIXTURES – A COMBINED VACUUM PENDANT DROP AND ANGLE-RESOLVED X-RAY PHOTOELECTRON SPECTROSCOPY STUDY^[P3]



Article

Direct Correlation of Surface Tension and Surface Composition of Ionic Liquid Mixtures—A Combined Vacuum Pendant Drop and Angle-Resolved X-ray Photoelectron Spectroscopy Study

Ulrike Paap¹, Vera Seidl², Karsten Meyer², Florian Maier¹ and Hans-Peter Steinrück^{1,*}

¹ Department of Chemistry and Pharmacy, Physical Chemistry II, Friedrich-Alexander-Universität Erlangen-Nürnberg (FAU), Egerlandstr. 3, 91058 Erlangen, Germany

² Department of Chemistry and Pharmacy, Inorganic Chemistry, Friedrich-Alexander-Universität Erlangen-Nürnberg (FAU), Egerlandstr. 1, 91058 Erlangen, Germany

* Correspondence: hans-peter.steinrueck@fau.de

Abstract: We investigated the surface tension and surface composition of various mixtures of the two ionic liquids (ILs) 1-methyl-3-octyl-imidazolium hexafluorophosphate [C₈C₁Im][PF₆] and 1,3-bis(polyethylene glycol)imidazolium iodide [(mPEG)₂Im]I in the temperature range from 230 to 370 K under ultraclean vacuum conditions. The surface tension was measured using a newly developed apparatus, and the surface composition was determined by angle-resolved X-ray photoelectron spectroscopy (ARXPS). In the pure ILs, the alkyl chains of [C₈C₁Im][PF₆] and the PEG chains of [(mPEG)₂Im]I are enriched at the IL/vacuum interface. In the mixtures, a strong selective surface enrichment of the alkyl chains occurs, which is most pronounced at low [C₈C₁Im][PF₆] contents. For the surface tension, strong deviations from an ideal mixing behaviour take place. By applying a simple approach based on the surface composition of the mixtures as deduced from ARXPS, we are able to predict and reproduce the experimentally measured temperature-dependent surface tension values with astonishingly high accuracy.

Keywords: ionic liquids; angle-resolved X-ray photoelectron spectroscopy (ARXPS); surface composition; pendant drop (PD); surface tension; ultra-high vacuum (UHV)



Citation: Paap, U.; Seidl, V.; Meyer, K.; Maier, F.; Steinrück, H.-P. Direct Correlation of Surface Tension and Surface Composition of Ionic Liquid Mixtures—A Combined Vacuum Pendant Drop and Angle-Resolved X-ray Photoelectron Spectroscopy Study. *Molecules* **2022**, *27*, 8561. <https://doi.org/10.3390/molecules27238561>

Academic Editors: José C. S. Costa and Luís M. N. B. F. Santos

Received: 9 November 2022
Accepted: 1 December 2022
Published: 5 December 2022

Publisher's Note: MDPI stays neutral with regard to jurisdictional claims in published maps and institutional affiliations.



Copyright: © 2022 by the authors. Licensee MDPI, Basel, Switzerland. This article is an open access article distributed under the terms and conditions of the Creative Commons Attribution (CC BY) license (<https://creativecommons.org/licenses/by/4.0/>).

1. Introduction

Ionic liquids (ILs)—salts with melting points typically well below 100 °C—have raised great interest in research and industry over the last two decades [1–7]. Apart from other benefits, it is the sheer uncountable possibility of adapting their physicochemical properties by adequate and independent choice among many available cations and anions with specific molecular sub-units, which gained ILs the term “designer solvents” [8,9]. An extension of this design concept is to mix two (or even more) pure ILs [10–12]. While the preparation of such a new IL system by mixing known ILs is rather simple, the resulting properties of the mixture often strongly deviate from those of the individual ILs and do not follow ideal mixing rules. These deviations are related to the complex interplay of different short- and long-range interactions between the ions in the mixture [10,11]. It is known that these interactions lead to rather complex structures on the nanoscale in the bulk of pure ILs and IL mixtures [13,14]. The situation for ions at interfaces of the IL with a solid or with the gas phase is even more difficult to predict. A typical example is mixtures containing fluorinated chains, where a preferential enrichment of these moieties at the surface has been reported [15–18].

In the present study, we focus on the surfaces of IL mixtures, particularly on the resulting surface tension and its relation to the surface composition. While the surfaces and interfaces of pure ILs under the well-defined conditions of ultrahigh vacuum have been studied quite extensively by several groups, including our own [6,19–29], the investigation

on the surface composition of IL mixtures with surface science techniques is a rather new field [17,25,30–34]. One important quantity related to liquid surfaces is surface tension (ST), which is the macroscopically observable change in free energy per change in unit surface area. On the microscopic level, the ST originates from the fact that molecules in bulk and at the surface, that is, the boundary to vacuum (or a gas phase), have very different local environments and, thus, different interactions. From this point of view, the ST of ILs has been in the focus of many experimental and theoretical groups [35–38]. Moreover, the ST also is most relevant for many applications of ILs, including wetting and coating, gas adsorption and release, and multiphase catalysis phenomena occurring at the liquid-gas interface, to name a few (see also the extensive review provided by Tariq et al. and references therein [37]).

The break in symmetry at the surface of a liquid can lead to very distinct preferential orientation and segregation effects of molecules close to the liquid-gas interface, as already discussed at the beginning of the last century by Hardy [39] and Langmuir [40,41]. When studying a series of fatty acid solutions in water, Langmuir observed that at lower concentrations, the hydrocarbon chains lie flat on the water surface. As the concentration of the solution increases, the fatty acid molecules in the surface layer become more densely packed until the surface is saturated by the hydrocarbon chains arranged vertically while the ST levels off [41]. These early findings demonstrate that changes in ST often are very different from changes in bulk composition, that is, the ST cannot be derived from ideal mixing rules. In his review “Forces Near the Surfaces of Molecules”, Langmuir also reported that for all pure organic liquids comprised of molecules with long alkyl tails (such as *n*-hexane and *n*-hexanol), the surface tensions are virtually equal and, thus, independent of the hydrocarbon length. He deduced that the forces along the entire length of the alkyl part of the molecule are almost uniform. To explain the ST values of aliphatic alcohols, Langmuir split the ST into independently acting contributions of head (that is, the hydroxyl group) and tail group (hydrocarbon chain) [42]: for the long-tail liquids, the tails are predominantly covering the outer surface (and thus, very similar ST values are measured) while for liquids with shorter alkyl chains, the hydroxyl groups are also significantly exposed to the gas phase leading to changes in ST. In this simple picture, the ST of these hydrocarbons is thus ascribed as the result of independent contributions from the molecular units (Langmuir called them “parts of molecular surfaces”) that are exposed on average to the outer surface [42,43].

Following these ideas, we already employed this “Langmuir principle” successfully for a series of pure *n*-alkyl-imidazolium ILs with increasing chain length *n*. By combining structural data obtained from angle-resolved X-ray photoelectron spectroscopy (ARXPS) experiments with molecular dynamics (MD) simulations, we were able to predict the correct surface tension trend along this IL series [44]. We also performed a first study addressing mixtures of ILs with the common $[PF_6]^-$ anion and imidazolium cations carrying either short butyl or partially fluorinated butyl chains [15,45] by combining conventional ST measurements (pendant drop measurements under 1 bar argon atmosphere) and ARXPS. Very recently, a similar approach was successfully employed by the McKendrick group using reactive-atom scattering with laser-induced fluorescence (RAS-LIF) in combination with MD and ST measurements [17,18]. From their RAS-LIF signals that originate mainly from alkyl units located at the outer surface, the authors derived a quantitative analysis of the alkyl content at the surface, which allowed them to describe the observed ST values of the mixture using the Langmuir concept as described above. They studied mixtures of ILs with different alkyl chain lengths in the cation and also with partially fluorinated chains at room temperature. From the underrepresentation of the alkyl signals, the authors could indirectly deduce a preferential surface enrichment of the fluorine chains in the mixtures [17,18].

In the present work, we now extend this concept to IL mixtures with very different anions and cations. The corresponding measurements of the temperature-dependent ST were performed under ultraclean vacuum conditions with an apparatus recently developed

in our lab [46], thereby minimizing any risk of possible surface contamination affecting the ST. The surface composition was determined from temperature-dependent ARXPS in an ultra-high vacuum [26,47–49]. ARXPS allows, in particular, for verifying the purity of the ILs and the analysis of all elements (but hydrogen) present in the IL mixtures. In particular, we studied the pure ILs [(mPEG)₂Im]I and [C₈C₁Im][PF₆], and their mixtures with about 5, 10, 20, and 50 mol% [C₈C₁Im][PF₆] content at temperatures between 230 and 370 K. The two ILs have different anions (I[−] and [PF₆][−]) and imidazolium-based cations with long functionalized and non-functionalized chains (see Figure 1), allowing for very different types of interactions in the mixtures. Both ILs were also selected due to (a) their rather wide liquid temperature window, (b) the existing knowledge on surface composition and surface tension of the pure ILs [31,37,50,51], and (c) the fact that each ion contains atoms that can be unambiguously assigned in the ARXP spectra. For the mixtures, we deduce a clear preferential surface enrichment of the [C₈C₁Im]⁺ cations from the octyl chains' XPS signals and a concomitant depletion of the [(mPEG)₂Im]⁺ cations from the polyethylene glycol (PEG) chains. This non-stoichiometric surface behaviour is reflected in the measured surface tension values of the mixtures. We demonstrate that the simple Langmuir concept allows for linking surface tension and surface composition of IL mixtures in a quantitative way, even for very complex ions. Based on the surface composition and the temperature-dependent ST data of the pure ILs, we can predict the ST of IL mixtures from their surface composition as determined by ARXPS. As a reverse conclusion, the ST value measured for an IL mixture at a certain temperature under clean conditions (ruling out surface impurities) allows for deriving the composition at the surface.

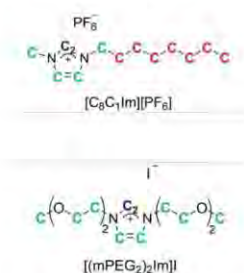


Figure 1. Structure of 1-methyl-3-octyl-imidazolium hexafluorophosphate [C₈C₁Im][PF₆] (**top**) and 1,3-bis-(polyethylene glycol)imidazolium iodide [(mPEG₂)₂Im]I (**bottom**). The different carbon atoms giving rise to the three discernible C 1s peaks are color-coded in blue (C₂ peak), in turquoise (C_{hetero}), and in pink (C_{alkyl}).

2. Results and Discussion

2.1. ARXPS

We performed temperature-dependent ARXPS measurements for the pure ILs 1-methyl-3-octyl-imidazolium hexafluorophosphate [C₈C₁Im][PF₆] and 1,3-bis-(polyethylene glycol)imidazolium iodide [(mPEG₂)₂Im]I (see Figure 1) and for different mixtures of the two ILs with 4.5, 9.6, 19.4, and 49.8 mol% [C₈C₁Im][PF₆] content under ultra-clean UHV conditions at a pressure in the range from 8×10^{-11} to 1.5×10^{-9} mbar (further details are provided in Section 4 Experimental). Figure 2 shows the O 1s and C 1s regions of these mixtures at 298 K along with the corresponding data of the pure ILs, for emission angles of 0° and 80° (the fitting deconvolution of the C 1s spectra is demonstrated in Figure S1 of the Supplementary Materials for the 49.8 mol% mixture). The spectra of all other species are provided in Figure S2.

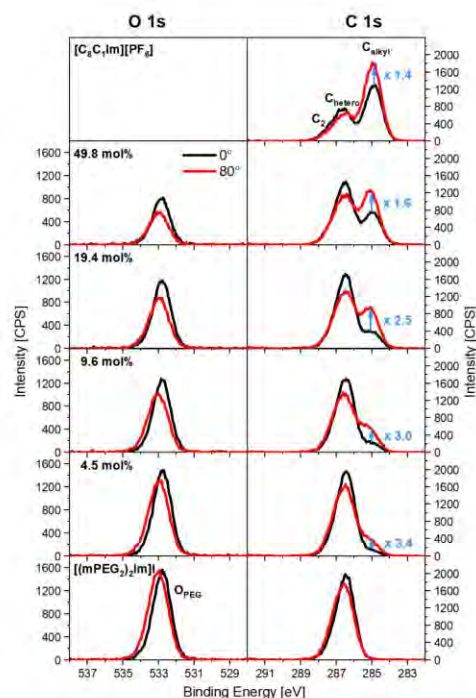


Figure 2. O 1s and C 1s spectra at 0° (black) and 80° (red) emission of pure $[C_8C_1Im][PF_6]$, pure $[(mPEG_2)_2Im]$, and of different mixtures of these ILs, collected at $T = 298$ K. The relative increase in C_{alkyl} intensity upon changing the emission angle from 0° to 80° is indicated (for details, see text).

Comparing the bulk-sensitive normal (0°) and the surface-sensitive grazing (80°) emission spectra for pure $[(mPEG_2)_2Im]$ (Figure 2, bottom), we observe a small shift to higher binding energies for the O_{PEG} peak (0.3 eV) and the C_{hetero} peak (0.2 eV) in the surface-sensitive 80° spectra, which is not present for the N and I signals (see Figure S2; for peak assignments, see also colour coding in Figure 1 and Figure S1). This shift is due to the preferential enrichment of the PEG chains at the surface and a related surface core level shift (SCLS) for these chain atoms. This SCLS stems from the different environment of chains at the outer surface as compared to chains in the bulk, as has been discussed previously for other IL mixtures [51]; the effect is less pronounced for the C_{hetero} signal since atoms from the imidazolium ring also contribute to this peak. SCLSs in the O_{PEG} peak are also observed for the mixtures, indicating the presence of PEG chains at the surface, albeit to a lower extent (see below).

The preferential surface presence of the PEG chains in the case of pure $[(mPEG_2)_2Im]$ is also evident from the ARXPS intensities: the O 1s spectra at 0° and 80° show the same height of the O_{PEG} peak but a slightly larger full-width-half-maximum (FWHM) at 80°, which yields 1.1 times larger O 1s intensity (peak area) in grazing emission as compared to normal emission. In the C 1s region, the C_{hetero} peak has a lower peak height but a larger FWHM at 80° compared to 0°, which results in similar intensities at both angles. The larger O_{PEG} and C_{hetero} peak widths at 80° are due to the fact that at this emission angle, the signals originate from the shifted contribution of oxygen or carbon atoms in the outermost layer plus unshifted contributions from underneath, whereas at 0° the signal is strongly dominated by atoms in the bulk. These observations for pure $[(mPEG_2)_2Im]$ are in line with a moderate preferential orientation of the PEG chains towards the surface, which is described in more detail in Ref. [50]. With increasing $[C_8C_1Im][PF_6]$ content in the bulk, we observe for the mixtures a clear decrease in O_{PEG} intensity at 0° in Figure 2, as expected.

In contrast to the situation of pure [(mPEG₂)₂Im]I, a very pronounced decrease in O_{PEG} intensity is found when changing the emission angle to 80°. This selective surface depletion of the PEG chains becomes more pronounced with increasing [C₈C₁Im][PF₆] content in the mixtures.

For pure [C₈C₁Im][PF₆] (Figure 2, top), the C 1s spectrum at 80° displays a lower intensity of the C₂/C_{hetero} peaks but a significantly larger intensity of the C_{alkyl} peak as compared to 0°. These findings indicate an orientation of the surface cations with the alkyl chains pointing towards the vacuum and the C₂ and C_{hetero} atoms towards the bulk, as already observed for many ILs with the [C₈C₁Im]⁺ cation [52]. For the mixtures, these enrichment and depletion effects are also present. Notably, the relative C_{alkyl} enrichment at the surface is stronger at lower [C₈C₁Im][PF₆] content (see numbers given next to the C_{alkyl} peaks in Figure 2). At the same time, the C₂ and C_{hetero} depletion is less pronounced at lower [C₈C₁Im][PF₆] content, which is attributed to the different degrees of enrichment and depletion of the C_{alkyl} and PEG chains in the different mixtures (note again that the two different cations both contribute to the C₂ and C_{hetero} signals, while C_{alkyl} solely originates from the [C₈C₁Im]⁺ cation, see Figure 1).

To obtain more detailed insight, we quantitatively analyse the O_{PEG} and C_{alkyl} signals of the pure ILs and the IL mixtures at 298 K. We concentrate on the surface-sensitive measurements at 80°, since they reflect the surface composition of the IL mixtures, which will later be correlated with the macroscopic surface tension. In Figure 3, the normalised O_{PEG} (red circles) and C_{alkyl} (grey circles) contents, that is, the atomic ratios $n(80^\circ)/n_{\text{nominal}}$, are plotted, as derived from the corresponding XP spectra at 80°. Notably, a value of 1 (dashed line) would correspond to an isotropic mixture with randomly oriented cations and anions in the bulk as well as at the surface. Figure 3 clearly shows a strong selective presence of the alkyl chains of the [C₈C₁Im]⁺ cation at the outer surface at very low [C₈C₁Im][PF₆] contents, yielding an $n(80^\circ)/n_{\text{nominal}}$ value of ~5 at 4.5 mol%. With increasing [C₈C₁Im][PF₆] content, the alkyl chain enrichment becomes less pronounced and reaches a value of 1.34 for pure [C₈C₁Im][PF₆] at 298 K. Whereas the moderate enrichment factor of 1.34 is solely due to the orientation of the [C₈C₁Im]⁺ cations in the surface layer of [C₈C₁Im][PF₆], the high values for the mixtures are mainly due to preferential surface segregation (plus chain orientation) of the [C₈C₁Im]⁺ cations. Simultaneously to the enrichment of the alkyl chains, we observe in ARXPS the depletion of the PEG chains (O_{PEG} signal) with increasing [C₈C₁Im][PF₆] content in the mixtures, from 1.18 for pure [(mPEG₂)₂Im]I to 0.71 for the 1:1 mixture with 49.8 mol% [C₈C₁Im][PF₆].

Next, we discuss the temperature dependence of surface enrichment and depletion as well as the orientation effects of the mixtures and also pure ILs. The measurements were performed from 363 K down to 238 / 233 K, with the lower temperature depending on the solidification temperature of the samples. The quantitative analysis of the C_{alkyl} and O_{PEG} data is given in Figure 4. For pure [C₈C₁Im][PF₆] (black squares), the $n(80^\circ)/n_{\text{nominal}}$ ratio for C_{alkyl} shows a weak decrease from 1.48 at 223 K to 1.32 at 363 K, which is attributed to the fact that the surface [C₈C₁Im]⁺ cations are more randomly oriented at higher temperatures. For the mixtures, however, the $n(80^\circ)/n_{\text{nominal}}$ ratio for C_{alkyl} shows a very pronounced decrease with increasing temperature. This decrease is attributed to the loss of selective surface enrichment of the alkyl chains relative to the PEG chains (see below), that is, a loss in preferential surface segregation of the [C₈C₁Im]⁺ cations at elevated temperatures. It is most pronounced for small [C₈C₁Im][PF₆] contents: e.g., for the 4.5 mol% mixture, the $n(80^\circ)/n_{\text{nominal}}$ ratio decreases from around 10 at 238 K down to 2.1 at 363 K.

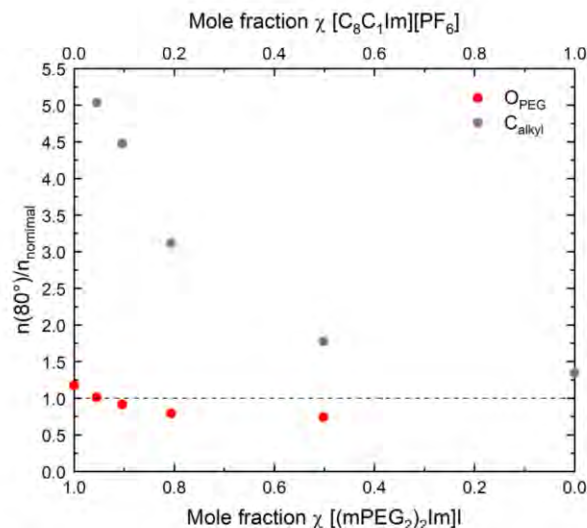


Figure 3. Normalized content $n(80^\circ)/n_{\text{nominal}}$ for O_{PEG} (red) and C_{alkyl} (grey), derived from the corresponding 80° intensities and the nominal atomic numbers of O_{PEG} and C_{alkyl} for the pure ILs and mixtures at $T = 298$ K.

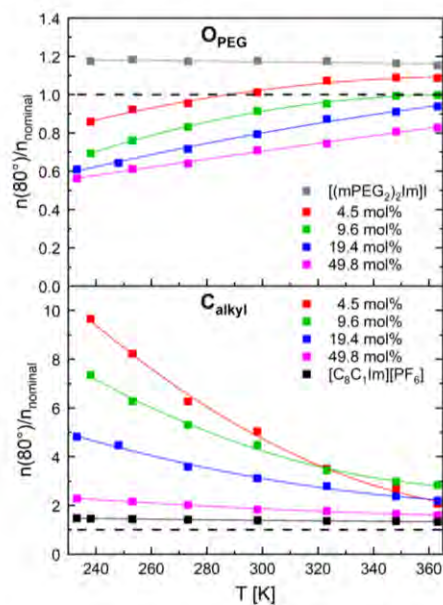


Figure 4. Normalized content $n(80^\circ)/n_{\text{nominal}}$ for O_{PEG} (top) and C_{alkyl} (bottom), derived from the corresponding 80° intensities and their nominal atomic numbers of O_{PEG} and C_{alkyl} for the pure ILs and mixtures for different temperatures (measurements started at 363 K).

With increasing temperature, in the case of pure $[(m\text{PEG}_2)_2\text{Im}]\text{I}$ the normalised O_{PEG} content (grey squares) at the surface measured at 80° shows virtually no change (see a very weak decrease from 1.17 to 1.15 in Figure 4). In contrast, the mixtures display a clear and continuous increase of the O surface content with temperature, e.g., from 0.86

at 238 K to 1.09 at 363 K for the mixture with 4.5 mol% $[\text{C}_8\text{C}_1\text{Im}][\text{PF}_6]$. This behaviour reflects the increase of the PEG chain contribution at the surface, which goes along with the above-described loss in the alkyl chain signal. As already discussed previously for pure ILs and IL mixtures [15,30], we attribute the generally observed loss in alkyl chain enrichment in ARXPS with increasing temperature to the loss in surface order as an entropic effect.

Finally, all other core level intensities of the imidazolium head groups and the anions show little changes with temperature (for the corresponding $n(80^\circ)/n_{\text{nominal}}$ values, see Figure S3 of Supplementary Materials). This is to be expected, as they are preferentially depleted from the outer surface, which is deduced from their values below one. Only the F content of the $[\text{PF}_6]^-$ anion increases with increasing temperature to values above 1 for the 4.5 mol% and 9.6 mol% mixtures, which might indicate that $[\text{PF}_6]^-$ has a higher surface affinity as compared to I^- as the other anionic species.

2.2. Pendant Drop Measurements

Temperature-dependent pendant drop measurements were performed to determine the surface tension for the above-studied pure ILs and IL mixtures under clean HV conditions at background pressures in the low 10^{-6} mbar range. As in the case of ARXPS, ST data were recorded starting with the highest temperature from 363 down to 300 K, as shown in Figure 5 for the pure ILs (open squares) and the IL mixtures (full squares). For all systems studied, we observe a linear decrease of the ST with increasing temperature, which is fitted by the following equation

$$\gamma_{\text{calc}} = \gamma_0 + \gamma_1 \cdot T \quad (1)$$

where γ_0 and γ_1 are the fitting coefficients (see Table 1) and T the temperature in Kelvin. This equation is then used to calculate the ST at the standard temperature of 298 K (Table 1). The density parameters used for ST evaluation are given in Table S1 in the Supplementary Materials.

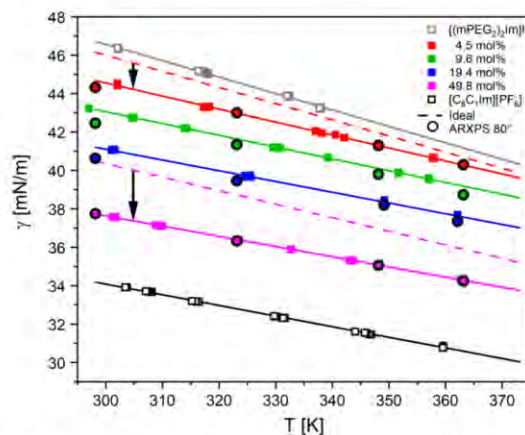


Figure 5. Surface tension values measured using the PD method are shown as open and full squares, along with their linear fits (lines) using Equation (1). The surface tension values calculated from the 80° ARXPS data using Equation (3) are shown as filled circles. Furthermore, the ideal behaviour for the surface tension of the 4.5 and 49.8 mol% mixtures as determined by Equation (2) (dashed lines) is included for comparison (a comparison for all mixtures is shown in Figure S4).

Table 1. Coefficients of the linear fits to the data according to Equation (1) for pure ILs and mixtures and ST values at 298 K.

	$[\text{C}_8\text{C}_1\text{Im}][\text{PF}_6]$	49.8 mol%	19.4 mol%	9.6 mol%	4.5 mol%	$[(\text{mPEG}_2)_2\text{Im}]\text{I}$
γ_0 [mN/m]	50.67	53.54	57.89	61.44	64.84	72.22
γ_1 [mN/m·K ⁻¹]	-0.0553	-0.0530	-0.0560	-0.0613	-0.0677	-0.0855
$\gamma_{298\text{ K}}$ [mN/m]	34.18	37.72	41.20	43.16	44.67	46.72

The ST decreases with increasing $[\text{C}_8\text{C}_1\text{Im}][\text{PF}_6]$ content. When comparing the different ST values at 298 K in Table 1 and in Figure 6a (black squares), we find the highest value of $\gamma = 46.72$ mN/m for pure $[(\text{mPEG}_2)_2\text{Im}]\text{I}$ and the lowest value of 34.18 mN/m for $[\text{C}_8\text{C}_1\text{Im}][\text{PF}_6]$, with the values for the mixtures falling in between. Notably, the change in ST is more pronounced at lower $[\text{C}_8\text{C}_1\text{Im}][\text{PF}_6]$ contents: it decreases from 46.72 for 0 mol% to 44.67 for 4.5 mol% (by -2.05 mN/m), and further to 43.16 mN/m for 9.6 mol% (by -1.51 mN/m), whereas it only decreases from 37.72 mN/m for 49.8 mol% to 34.18 mN/m for 100 mol% (by -3.56 mN/m); see also Table 1. The same behaviour is observed for all temperatures studied, as is evident from Figure 5.

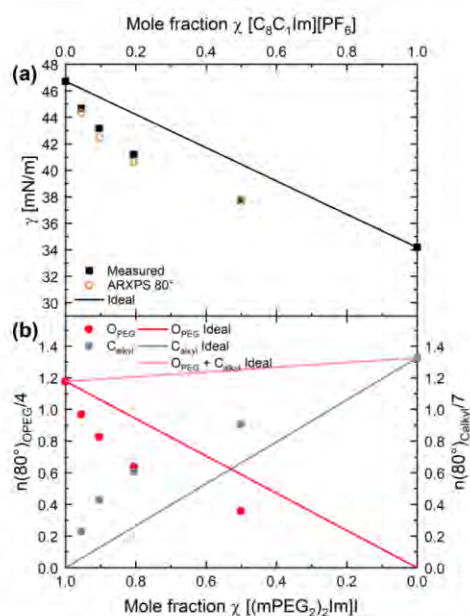


Figure 6. (a) Surface tension values of the pure ILs and the mixtures at 298 K (black squares), as determined from pendant drop measurements in Figure 5, along with the surface tension values calculated from the 80° ARXPS data according to Equation (3) (open orange circles) as a function of bulk mole fraction. For comparison, the surface tension of ideal mixtures without enrichment/depletion effects is shown as the black line. (b) Number of atoms, $n(80^\circ)$, as determined from the ARXPS data at 80°, normalised to the number of corresponding atoms in the IL for O_{PEG} (red circles) and for C_{alkyl} (grey circles) for the pure ILs and for the mixtures at $T = 298$ K. Straight lines show ideal behaviour, that is, expected changes without surface enrichment/depletion effects being present.

The ST of the mixtures thus does not follow an ideal behaviour, which would be obtained from the ST values γ_i of the pure ILs weighted with the corresponding bulk mole fractions x_i :

$$\gamma_{T,mixture}(x) = \gamma_{T,[(mPEG_2)_2Im]I} \cdot x_{[(mPEG_2)_2Im]I} + \gamma_{T,[C_8C_1Im][PF_6]} \cdot x_{[C_8C_1Im][PF_6]} \quad (2)$$

In Figure 5, the non-ideal behaviour is evident from the fact that the fits to the measured data for 4.5 mol% (solid red line) and 49.8 mol% (solid pink line) fall significantly below the ideal characteristics (dashed lines with deviations indicated by black vertical arrows, see also Figure S4 in the Supplementary Materials for all mixtures studied).

In Figure 6a, an ideal behaviour of the ST would correspond to a linear decrease with increasing $[C_8C_1Im][PF_6]$ content (solid black line). The much stronger decrease than the ideal behaviour at low $[C_8C_1Im][PF_6]$ contents and the fact that the ST values of all mixtures fall below the ideal line is attributed to the strong preferential enrichment and depletion effects occurring at the liquid-vacuum interface. The latter were deduced from the $[C_8C_1Im]^+$ and $[(mPEG_2)_2]^+$ chain signals in ARXPS (see above). This deviation between bulk and surface composition then strongly affects the ST, as will be detailed in the next section.

2.3. Comparison of ARXPS and PD Results

To obtain further insight, we directly link our ARXPS and PD results. For this purpose, we correlate the ST data for the mixtures at 298 K in Figure 6a to the corresponding atomic O_{PEG} and C_{alkyl} contents in Figure 6b, as determined from the 80° ARXP spectra; the latter are normalised to the number of corresponding atoms in the ion, that is, four O_{PEG} atoms in $[(mPEG_2)_2Im]I$, and seven C_{alkyl} atoms in $[C_8C_1Im][PF_6]$. In this presentation, the O_{PEG} signal (red circles) represents the surface concentration of the PEG chains of the $[(mPEG_2)_2Im]^+$ cation, and the C_{alkyl} signal (grey circles) the surface concentration of the alkyl chains of the $[C_8C_1Im]^+$ cation. When comparing the experimentally obtained data with the linear concentration dependences expected for ideal behaviour (red and grey solid lines for O_{PEG} and C_{alkyl} , respectively), we again observe a clear deviation: The measured O_{PEG} data clearly fall below the ideal line and the C_{alkyl} data above the ideal grey line. This reflects the preferential depletion of the PEG chains and the enrichment of the alkyl chains in the mixtures at the surface, as discussed above.

As the next step, we follow an approach, which has been put forward by us recently for pure ILs along the denoted Langmuir principle [44], which directly relates the ST value of a liquid to the superposition of independent group contributions from the molecular moieties being present right at the liquid/gas interface, that is, at the outer surface. The basic idea now is that we transfer this concept to the binary IL mixtures: the groups of $[(mPEG_2)_2Im]I$ and the $[C_8C_1Im][PF_6]$, which are predominantly present at the outer surface—and thus, mainly contribute to the ST of the pure ILs—are used to represent the effective surface mole fraction of the corresponding IL in the mixture. Since the alkyl chains (C_{alkyl} peak) and the PEG chains (O_{PEG} peak) are the dominating surface species in $[C_8C_1Im][PF_6]$ and $[(mPEG_2)_2Im]I$, respectively, we start with only these two signals measured in our most surface sensitive 80° geometry. As it will be shown, this simplification already provides very good agreement with the measured temperature-dependent ST values without further refinement needed.

Instead of Equation (2) for ideal mixing behaviour, the ST of a mixture with a certain bulk composition x at temperature T is estimated from $n_{O_{PEG},80^\circ}(x)$ and $n_{C_{alkyl},80^\circ}(x)$, that is, the number of O_{PEG} and C_{alkyl} atoms, respectively (see Table S2), as derived from the temperature-dependent 80° ARXP spectra:

$$\gamma_{T,ARXPS\ 80^\circ}(x) = \frac{\gamma_{T,[(mPEG_2)_2Im]I} \cdot \frac{n_{O_{PEG},80^\circ}(x)}{4} + \gamma_{T,[C_8C_1Im][PF_6]} \cdot \frac{n_{C_{alkyl},80^\circ}(x)}{7}}{\frac{n_{O_{PEG},80^\circ}(x)}{4} + \frac{n_{C_{alkyl},80^\circ}(x)}{7}} \quad (3)$$

with $\gamma_{T,[(mPEG)_2Im]}$ and $\gamma_{T,[C_8C_1Im][PF_6]}$ being the temperature-dependent ST values of pure $[(mPEG)_2Im]$ and $[C_8C_1Im][PF_6]$ (Table 1), respectively.

The XPS-derived ST values of the mixtures using Equation (3) are plotted for selected temperatures (circles for 298, 323, 348, 363 K) in Figure 5 as a function of $[C_8C_1Im][PF_6]$ mole fraction; see also Table 2. The agreement between the calculated and measured ST of the mixtures is extremely good (around 1% deviation with a maximum deviation of 1.7% for one data point). Note that this small deviation is even more surprising since the overall accuracy in IL surface composition determination by ARXPS is at best 5% due to our experience over many years, and thus, further improvement of our model makes little sense. Moreover, we are aware that using this simplified model with two signals only (neglecting, e.g., all other IL components that are also in part present at the outer surface) and the limited surface sensitivity of the 80° geometry [44] makes the agreement between measured and calculated ST even more surprising. Concerning the second argument, the 80° geometry apparently is sensitive enough to account for the deviations in surface mole fraction from the bulk composition. In contrast, this is not the case for the 0° spectra: As a control experiment, we also calculated the ST from the $n_{OPEG,0^\circ}(x)$ and $n_{Calkyl,0^\circ}(x)$ values derived from the 0° ARXP spectra using Equation (3) (see Tables S2 and S3). The corresponding ST values for 298 K in Figure S5 in the Supplementary Materials and also the temperature-dependent measurements in Figure S6 in the Supplementary Materials show only very small deviations from the ideal behaviour, which is to be expected since the ARXPS signals at 0° with the—around six times—larger information depth as compared to the 80° are in fact dominated by bulk with the small surface contributions only.

Table 2. Experimental ST values γ for different mixtures and temperatures (as derived from linear fits to the data according to Equation (1) with coefficients from Table 1), along with calculated ST values γ_{80° (calc) using Equation (3) and the ARXPS 80° results shown in Figure 6b (see also bottom row of Table S2).

T [K]	49.8 mol%		19.4 mol%		9.6 mol%		4.5 mol%	
	γ [mN/m]	γ_{80° (calc) [mN/m]						
363	34.28	34.24	37.56	37.35	39.17	38.72	40.27	40.29
348	35.07	35.06	38.40	38.19	40.09	39.80	41.29	41.30
323	36.40	36.32	39.80	39.45	41.63	42.34	42.98	43.00
298	37.72	37.75	41.20	40.36	43.16	42.45	44.67	44.32

At this point, we briefly want to come back to the very recent study by the McKendrick group, who addressed mixtures of ILs with different alkyl chain lengths and mixtures of non-fluorinated ILs with ILs carrying per-fluorinated alkyl chains using an overall very similar approach [17,18]. They employed reactive-atom scattering with laser-induced fluorescence (RAS-LIF) in combination with MD simulations and ST measurements with the pendant drop method under atmospheric conditions, all performed solely at room temperature. Particularly for the mixtures with fluorinated IL chains, the underrepresentation of the alkyl signals in RAS-LIF provided a quantitative measure for the preferential depletion of the alkyl chains and—indirectly—the enrichment of the fluorine chains at the outer surface [17,18]. This allowed the authors to describe the observed ST values of the mixture using the Langmuir concept reported previously [17,18]. When comparing RAS-LIF employed by the McKendrick group and our ARXPS approach, one has to state that both methods are very well suited to monitor the surface composition but have their strengths and weaknesses. RAS-LIF is most sensitive solely to the outermost hydrogenated carbon atoms at the surface, while ARXPS at 80°, as applied here, integrates over the topmost one nm. On the other hand, ARXPS is able to analyse all elements, and thus in our case, we studied the enrichment of the alkyl chains and the depletion of the PEG

chains, whereas RAS-LIF only relies on the depletion of the alkyl constituents. For the IL mixtures studied here, this would be quite challenging, as the PEG chains also contain CH_x groups in the chains that cannot be simply differentiated from the octyl chains. One other advantage of our study is that the investigation of surface composition and ST over a wide temperature range and under well-defined vacuum conditions allows for collecting very reliable data sets.

3. Conclusions

We investigated the macroscopic property surfaces tension and the microscopic surface composition of the newly synthesised and characterised IL [(mPEG₂)₂Im]I, of the well-studied IL [C₈C₁Im][PF₆], and in particular of mixtures of these two ILs under ultra-clean vacuum conditions. Mixing common and well-characterized ILs is a relatively simple way to obtain new and fine-tuned IL systems for targeted applications. In particular, for large surface-area systems, which are used, e.g., in gas separation and adsorption technologies, film coatings, and catalysis, an understanding of surface composition and the related properties plays a crucial role.

The surface tension values of the pure ILs and their mixtures were measured using a new pendant drop setup, which allowed for measuring the ST in vacuum, and, thereby, minimised possible surface-active contaminations affecting the ST. The surface compositions were determined from ARXP spectra of all elements but hydrogen in UHV. ARXPS also allowed for verifying the ultraclean nature of the studied ILs. Both PD and ARXPS measurements were performed for the pure ILs and mixtures with about 5, 10, 20, and 50 mol% [C₈C₁Im][PF₆] in the temperature range from about 300 to 360 K.

The ST of the pure ILs are found to be quite different, that is, 46.72 mN/m for pure [(mPEG₂)₂Im]I and 34.18 mN/m for [C₈C₁Im][PF₆]. The values for the mixtures fall in between but strongly deviate from simple ideal mixing rules. From ARXPS, we deduce that the alkyl chain of pure [C₈C₁Im][PF₆] and the PEG chains of pure [(mPEG₂)₂Im]I are enriched at the IL/vacuum interface. For the surface composition of the mixtures, a strong deviation from an ideal mixing behaviour also takes place with a strong selective enrichment of the alkyl chains for all mixtures, which is most pronounced at the lowest [C₈C₁Im][PF₆] content. By applying a simple Langmuir approach based on the surface composition as deduced from ARXPS, we are able to predict and to reproduce the experimentally measured surface tension with astonishingly high accuracy. The comparison of the ST values obtained by PD measurements and those obtained from ARXPS measurements based on this simple Langmuir principle shows very good agreement in the case of the IL mixtures in our proof-of-concept model study. On the one hand, the information obtained from ARXPS thus provides a microscopic explanation for the macroscopic surface tension. On the other hand, one can now go a step further and deduce information on surface enrichment effects in mixtures from the deviation of the ST data obtained by the PD method from the ideal behaviour. While this certainly cannot fully replace using very complex and costly microscopic methods such as ARXPS, PD measurements nevertheless can provide important insights. This is particularly true for conditions such as high temperatures or gas pressures (even reactive conditions) where UHV-based methods cannot be applied.

4. Experimental Section

4.1. Materials

Angle-resolved X-ray photoelectron spectroscopy (ARXPS) and surface tension (ST) measurements were performed on 1-methyl-3-octyl-imidazolium hexafluorophosphate [C₈C₁Im][PF₆] and 1,3-bis(polyethylene glycol)imidazolium iodide [(mPEG₂)₂Im]I, and mixtures thereof with 4.5, 9.6, 19.4, and 49.8 mol% [C₈C₁Im][PF₆] content. [C₈C₁Im][PF₆] (purity 99%) was purchased from IoLiTec (Heilbronn, Germany) and used as delivered, and [(mPEG₂)₂Im]I was synthesised as described in Ref. [50]. The structure of both ILs is shown in Figure 1. Mixtures were prepared in total amounts of one to three grams by

weighing $[\text{C}_8\text{C}_1\text{Im}][\text{PF}_6]$ into $[(\text{mPEG}_2)_2\text{Im}]\text{I}$, swirling, and waiting overnight; the weights are provided in Table S4 in the Supplementary Materials).

For the ARXPS measurements, each liquid sample was placed as a planar film of about 0.5 mm thickness on a molybdenum sample holder. Thereafter, sample degassing was performed in the fast entry load-lock of the vacuum chamber for at least 12 h. The ARXPS measurements were performed under ultra-high vacuum (UHV) at temperatures from 363 K down to around 240 K (and slightly below), where the onset of sample charging in ARXPS indicated solidification (see Table S4) [49]. The ST measurements were carried out under high vacuum (HV) conditions of $\sim 10^{-6}$ mbar background pressure in a separate chamber [46], where the ILs and IL mixtures were first carefully degassed at a temperature of about 373 K for 15 h and then measured also from 363 K down to room temperature.

4.2. Angle-Resolved X-ray Photoelectron Spectroscopy

ARXPS was performed using our unique DASSA (dual analyser system for surface analysis) system; for details, see Ref. [49]. The measurements were performed with a monochromatic Al K α source ($h\nu = 1486.6$ eV) at a power of 238 W. Spectra were acquired simultaneously with two ARGUS-type analysers positioned at $\vartheta = 0^\circ$ (normal emission) and $\vartheta = 80^\circ$ (grazing emission) with respect to the surface normal of the horizontally mounted sample. The information depth (ID) in 0° emission is 7 to 9 nm yielding predominantly information on the IL bulk. At 80° emission, the ID decreases by a factor of about six to 1 to 1.5 nm, yielding highly surface-sensitive information [49]. The temperature of the sample was measured directly at the IL-filled molybdenum reservoir with uncertainty in absolute temperature of ± 2 K in the applied temperature window. High-resolution spectra were recorded with a pass energy of 35 eV to ensure an energy resolution of 0.4 eV. Survey scans were recorded with a pass energy of 150 eV.

The XPS data were analysed using the CasaXPS software (version 2.3.16Dev6, Casa Software Ltd., Teignmouth, United Kingdom). For all peaks, a two-point linear background was subtracted, with the exception of the I 3d region, where a three-point linear background was set. Fitting was performed using a Gauss–Lorentzian function with a 30% Lorentzian contribution. For the quantitative analysis of the core levels, atomic sensitivity factors (ASFs) were applied [53]. For the spin-orbit split P 2p $_{1/2}$ and 2p $_{3/2}$ core levels, the intensity ratio was set to 1:2, with a peak separation of 0.9 eV and equal full width at half maximum (FWHM). For pure $[\text{C}_8\text{C}_1\text{Im}][\text{PF}_6]$, the C 1s region was fitted with three peaks for C $_2$, C $_{\text{hetero}}$, and C $_{\text{alkyl}}$. The C $_2$ and C $_{\text{hetero}}$ peaks are separated by 0.9 eV, with an intensity ratio of 1:4 and FWHMs of 1:1.1; C $_2$ and C $_{\text{alkyl}}$ have the same FWHM. For $[(\text{mPEG}_2)_2\text{Im}]\text{I}$, the C 1s region was fitted with two peaks, C $_2$ and C $_{\text{hetero}}$, with peak separation of 0.87 eV and a ratio of 1:12. The FWHM of C $_{\text{hetero}}$ was 1.19 times that of the C $_2$ peak. The C 1s region of the mixtures was fitted by considering the different peak positions, peak widths of the pure ILs, and the corresponding mixing ratios and resulting atomic ratios; since the C $_{\text{alkyl}}$ signals in the mixtures are small for low $[\text{C}_8\text{C}_1\text{Im}][\text{PF}_6]$ content, we used an additional constraint for unambiguous fitting, namely a fixed peak separation of the C $_{\text{hetero}}$ and the C $_{\text{alkyl}}$ peaks of 1.59 eV in 0° and 1.46 eV in 80° (these values were derived at 298 K from the 1:1 mixture, where the two peaks were clearly discernible, and varied by ± 0.05 eV with temperature—see Table S5 in the Supplementary Materials; an exemplary fit of the 298 K C 1s spectrum measured in 0° is shown in Figure S1 in the Supplementary Materials; the resulting binding energies and the quantitative analysis of all ARXPS data at 298 K are provided in Table S6 in the Supplementary Materials).

To allow for visualising depletion/enrichment effects through direct comparison, all 80° measurements were scaled up by a geometry factor, which is derived from the sum of the weighted intensities of all core levels obtained in 0° and 80° , following a previously established procedure [15,49]. Moreover, the energy scales of all 80° spectra were slightly shifted by -0.1 eV such that the N 1s peaks in 80° of the common imidazolium head group fall onto the N 1s peaks in 0° .

4.3. High Vacuum Pendant Drop Measurements

Surface tension measurements were performed in a high vacuum pendant drop (PD) system, which was recently developed by our group. The properties and calibration of the setup were described in a recent publication [46]. The applied stainless steel cannula has an outer diameter of 2.02 mm. Videos of the drops were recorded with a high-speed camera (4 frames per second). For the evaluation of the ST, 10 frames were used per droplet. To ensure the reproducibility of the data, 5 droplets were formed at a fixed temperature (with a maximum temperature drift of ± 1 K). The ST was determined from each droplet shape using the axisymmetric drop shape analysis—(ADSA) and the Young–Laplace equation solution—software package SCA 22/15 (version 5.0.35) from DataPhysics (V.5.0.35build5035, DataPhysics Instruments GmbH, Filderstadt, Germany); for further details on the setup and evaluation procedure, see Ref. [46].

Supplementary Materials: The following supplementary material can be downloaded at: <https://www.mdpi.com/article/10.3390/molecules27238561/s1>, Figure S1: Exemplary fitting procedure for the C 1s region of the 49.8 mol% $[\text{C}_8\text{C}_1\text{Im}][\text{PF}_6]$ content mixture in 0° at $T = 298$ K; Figure S2: F 1s, I $3d_{5/2}$, O 1s, N 1s, C 1s and P 2p spectra at 0° and 80° emission of pure $[\text{C}_8\text{C}_1\text{Im}][\text{PF}_6]$, pure $[(\text{mPEG}_2)_2\text{Im}]\text{I}$, and of different mixtures of these ILs, collected at $T = 298$ K; Figure S3: Composition ratios $n(80^\circ)/n_{\text{nominal}}$ for F 1s, O_{PEG} , I $3d_{5/2}$, N 1s, C₂, C_{hetero}, C_{alkyl} and P 2p, derived from the corresponding 80° intensities and their nominal atomic numbers for the neat ILs and mixtures for different temperatures; Figure S4: Comparison of the linear fits of the experimental data determined using the pendant drop method in vacuum with the surface tension as expected for ideal behaviour of different mixtures; Figure S5: (a) Surface tension values of the pure ILs and the mixtures at 298 K, as determined from pendant drop measurements in Figure 5, along with the surface tension values calculated from the 0° ARXPS data according to Equation (3). For comparison, the surface tension of ideal mixtures without enrichment/depletion effects is shown as black line. (b) Number of atoms, $n(0^\circ)$, as determined from the ARXPS data at 0° , normalized to the number of corresponding atoms in the IL for O_{PEG} and for C_{alkyl} for the pure ILs and for the mixtures at $T = 298$ K; Figure S6: Comparison of the experimentally determined surface tension values derived from the pendant drop measurements in vacuum with the surface tension expected for ideal behaviour of the different mixtures. Also shown are the predictions of the surface tension from the ARXPS data at 0° ; Table S1: Temperature-dependent density parameters for pure $[\text{C}_8\text{C}_1\text{Im}][\text{PF}_6]$ from Ref. [54], $[(\text{mPEG}_2)_2\text{Im}]\text{I}$ from Ref. [50] and their mixtures with 4.5, 9.6, 19.4 and 49.8 mol% $[\text{C}_8\text{C}_1\text{Im}][\text{PF}_6]$ content; the densities for the surface tension evaluation at different temperatures are obtained following $\rho = \rho_0 + \rho_1 \cdot T + \rho_2 \cdot T^2$ (temperature in K); Table S2: Number of O_{PEG} and C_{alkyl} atoms derived from the temperature-dependent 0° and 80° ARXPS spectra; Table S3: ST values γ (ideal) for different mixtures and temperatures as expected from ideal mixing behaviour using Equation (2) along calculated ST values γ_0 (calc.) using Equation (3) with the number of O_{PEG} and C_{alkyl} atoms as deduced from the 0° ARXP spectra; Table S4: Weights of $[\text{C}_8\text{C}_1\text{Im}][\text{PF}_6]$ and $[(\text{mPEG}_2)_2\text{Im}]\text{I}$ used for the 4.5, 9.6, 19.4 and 49.8 mol% mixtures; last column shows solidification temperatures of the corresponding mixtures as indicated by the onset of sample charging in ARXPS; Table S5: Binding energy (BE) differences of the C_{hetero} and C_{alkyl} peaks for both angles as a function of temperature of the 49.8 mol% mixture. These ΔBE values were used as constraints to fit the C 1s spectra of all other mixtures; Table S6: Quantitative analysis of the 0° and 80° ARXPS spectra for pure $[\text{C}_8\text{C}_1\text{Im}][\text{PF}_6]$, $[(\text{mPEG}_2)_2\text{Im}]\text{I}$ and their mixtures with 4.5, 9.6, 19.4 and 49.8 mol% $[\text{C}_8\text{C}_1\text{Im}][\text{PF}_6]$ content at 298 K. Reference [54] are cited in the Supplementary Materials.

Author Contributions: Conceptualization, F.M. and H.-P.S.; Data curation, U.P.; Funding acquisition, H.-P.S.; Investigation, U.P. and F.M.; Methodology, U.P., V.S., K.M., F.M. and H.-P.S.; Project administration, F.M. and H.-P.S.; Resources, H.-P.S.; Supervision, K.M., F.M. and H.-P.S.; Validation, F.M.; Visualization, U.P. and V.S.; Writing—original draft, U.P.; Writing—review & editing, F.M. and H.-P.S. All authors have read and agreed to the published version of the manuscript.

Funding: This research was funded by the DFG in the course of the Collaborative Research Center (CRC)/Sonderforschungsbereich (SFB) 1452—Project-ID 431791331.

Institutional Review Board Statement: Not applicable.

Informed Consent Statement: Not applicable.

Data Availability Statement: The data presented in this study are available on request from the corresponding author.

Acknowledgments: We acknowledge Z. Zhai and Th. Koller for fruitful collaboration and discussion concerning the surface tension measurements.

Conflicts of Interest: The authors declare no conflict of interest.

Sample Availability: Samples of the compounds are not available from the authors.

References

1. Zhao, D.; Wu, M.; Kou, Y.; Min, E. Ionic liquids: Applications in catalysis. *Catal. Today* **2002**, *74*, 157–189. [[CrossRef](#)]
2. Welton, T. Ionic liquids in catalysis. *Coord. Chem. Rev.* **2004**, *248*, 2459–2477. [[CrossRef](#)]
3. Plechkova, N.V.; Seddon, K.R. Applications of ionic liquids in the chemical industry. *Chem. Soc. Rev.* **2008**, *37*, 123–150. [[CrossRef](#)] [[PubMed](#)]
4. Olivier-Bourbigou, H.; Magna, L.; Morvan, D. Ionic liquids and catalysis: Recent progress from knowledge to applications. *Appl. Catal. A Gen.* **2010**, *373*, 1–56. [[CrossRef](#)]
5. MacFarlane, D.R.; Tachikawa, N.; Forsyth, M.; Pringle, J.M.; Howlett, P.C.; Elliott, G.D.; Davis, J.H.; Watanabe, M.; Simon, P.; Angell, C.A. Energy applications of ionic liquids. *Energy Environ. Sci.* **2014**, *7*, 232–250. [[CrossRef](#)]
6. Steinrück, H.-P.; Wasserscheid, P. Ionic Liquids in Catalysis. *Catal. Lett.* **2015**, *145*, 380–397. [[CrossRef](#)]
7. Singh, S.K.; Savoy, A.W. Ionic liquids synthesis and applications: An overview. *J. Mol. Liq.* **2020**, *297*, 112038. [[CrossRef](#)]
8. Freemantle, M. Designer solvents—Ionic liquids may boost clean technology development. *Chem. Eng. News Arch.* **1998**, *76*, 32–37. [[CrossRef](#)]
9. Newington, I.; Perez-Arlandis, J.M.; Welton, T. Ionic liquids as designer solvents for nucleophilic aromatic substitutions. *Org. Lett.* **2007**, *9*, 5247–5250. [[CrossRef](#)]
10. Niedermeyer, H.; Hallett, J.P.; Villar-Garcia, I.J.; Hunt, P.A.; Welton, T. Mixtures of ionic liquids. *Chem. Soc. Rev.* **2012**, *41*, 7780–7802. [[CrossRef](#)]
11. Chatel, G.; Pereira, J.F.B.; Debbeti, V.; Wang, H.; Rogers, R.D. Mixing ionic liquids—“simple mixtures” or “double salts”? *Green Chem.* **2014**, *16*, 2051–2083. [[CrossRef](#)]
12. Clough, M.T.; Crick, C.R.; Gräsvik, J.; Hunt, P.A.; Niedermeyer, H.; Welton, T.; Whitaker, O.P. A physicochemical investigation of ionic liquid mixtures. *Chem. Sci.* **2015**, *6*, 1101–1114. [[CrossRef](#)] [[PubMed](#)]
13. Hayes, R.; Warr, G.G.; Atkin, R. Structure and Nanostructure in Ionic Liquids. *Chem. Rev.* **2015**, *115*, 6357–6426. [[CrossRef](#)] [[PubMed](#)]
14. Wang, Y.-L.; Li, B.; Sarman, S.; Mocci, F.; Lu, Z.-Y.; Yuan, J.; Laaksonen, A.; Fayer, M.D. Microstructural and Dynamical Heterogeneities in Ionic Liquids. *Chem. Rev.* **2020**, *120*, 5798–5877. [[CrossRef](#)] [[PubMed](#)]
15. Heller, B.S.J.; Lexow, M.; Greco, F.; Shin, S.; Partl, G.; Maier, F.; Steinrück, H.-P. Temperature-Dependent Surface Enrichment Effects in Binary Mixtures of Fluorinated and Non-Fluorinated Ionic Liquids. *Chem.—A Eur. J.* **2020**, *26*, 1117–1126. [[CrossRef](#)] [[PubMed](#)]
16. Heller, B.S.J.; Paap, U.; Maier, F.; Steinrück, H.-P. Pronounced surface enrichment of fluorinated ionic liquids in binary mixtures with methoxy-functionalized ionic liquids. *J. Mol. Liq.* **2020**, *305*, 112783. [[CrossRef](#)]
17. Smoll, E.J.; Tesa-Serrate, M.A.; Purcell, S.M.; D’Andrea, L.; Bruce, D.W.; Slattey, J.M.; Costen, M.L.; Minton, T.K.; McKendrick, K.G. Determining the composition of the vacuum–liquid interface in ionic-liquid mixtures. *Faraday Discuss.* **2018**, *206*, 497–522. [[CrossRef](#)]
18. Purcell, S.M.; Lane, P.D.; D’Andrea, L.; Elstone, N.S.; Bruce, D.W.; Slattey, J.M.; Smoll, E.J.; Greaves, S.J.; Costen, M.L.; Minton, T.K.; et al. Surface Structure of Alkyl/Fluoroalkylimidazolium Ionic-Liquid Mixtures. *J. Phys. Chem. B* **2022**, *126*, 1962–1979. [[CrossRef](#)]
19. Steinrück, H.-P.; Libuda, J.; Wasserscheid, P.; Cremer, T.; Kolbeck, C.; Laurin, M.; Maier, F.; Sobota, M.; Schulz, P.S.; Stark, M. Surface Science and Model Catalysis with Ionic Liquid-Modified Materials. *Adv. Mater.* **2011**, *23*, 2571–2587. [[CrossRef](#)]
20. Hashimoto, H.; Ohno, A.; Nakajima, K.; Suzuki, M.; Tsuji, H.; Kimura, K. Surface characterization of imidazolium ionic liquids by high-resolution Rutherford backscattering spectroscopy and X-ray photoelectron spectroscopy. *Surf. Sci.* **2010**, *604*, 464–469. [[CrossRef](#)]
21. Smith, E.F.; Rutten, F.J.M.; Villar-Garcia, I.J.; Briggs, D.; Licence, P. Ionic Liquids in Vacuo: Analysis of Liquid Surfaces Using Ultra-High-Vacuum Techniques. *Langmuir* **2006**, *22*, 9386–9392. [[CrossRef](#)] [[PubMed](#)]
22. Santos, C.S.; Baldelli, S. Gas–liquid interface of room-temperature ionic liquids. *Chem. Soc. Rev.* **2010**, *39*, 2136–2145. [[CrossRef](#)] [[PubMed](#)]
23. Iwahashi, T.; Nishi, T.; Yamane, H.; Miyamae, T.; Kanai, K.; Seki, K.; Kim, D.; Ouchi, Y. Surface Structural Study on Ionic Liquids Using Metastable Atom Electron Spectroscopy. *J. Phys. Chem. C* **2009**, *113*, 19237–19243. [[CrossRef](#)]
24. Lovelock, K.R.J.; Villar-Garcia, I.J.; Maier, F.; Steinrück, H.-P.; Licence, P. Photoelectron Spectroscopy of Ionic Liquid-Based Interfaces. *Chem. Rev.* **2010**, *110*, 5158–5190. [[CrossRef](#)]

25. Chen, L.G.; Lerum, R.V.; Aranda-Espinoza, H.; Bermudez, H. Surfactant-Mediated Ion Exchange and Charge Reversal at Ionic Liquid Interfaces. *J. Phys. Chem. B* **2010**, *114*, 11502–11508. [CrossRef]
26. Steinrück, H.-P. Recent developments in the study of ionic liquid interfaces using X-ray photoelectron spectroscopy and potential future directions. *Phys. Chem. Chem. Phys.* **2012**, *14*, 5010–5029. [CrossRef]
27. Villar-Garcia, I.J.; Fearn, S.; De Gregorio, G.F.; Ismail, N.L.; Gschwend, F.J.V.; McIntosh, A.J.S.; Lovelock, K.R.J. The ionic liquid–vacuum outer atomic surface: A low-energy ion scattering study. *Chem. Sci.* **2014**, *5*, 4404–4418. [CrossRef]
28. Lexow, M.; Maier, F.; Steinrück, H.-P. Ultrathin ionic liquid films on metal surfaces: Adsorption, growth, stability and exchange phenomena. *Adv. Phys. X* **2020**, *5*, 1761266. [CrossRef]
29. Nakajima, K.; Lisal, M.; Kimura, K. Surfaces of Ionic Liquids. In *Surface and Interface Science*; Wandelt, K., Ed.; Wiley-VCH Verlag GmbH & Co.KGaA: Weinheim, Germany, 2020; pp. 351–389. [CrossRef]
30. Kolbeck, C.; Deyko, A.; Matsuda, T.; Kohler, F.T.U.; Wasserscheid, P.; Maier, F.; Steinrück, H.-P. Temperature-Dependent Surface-Enrichment Effects of Imidazolium-Based Ionic Liquids. *ChemPhysChem* **2013**, *14*, 3726–3730. [CrossRef]
31. Souda, R. Surface segregation in binary mixtures of imidazolium-based ionic liquids. *Surf. Sci.* **2010**, *604*, 1694–1697. [CrossRef]
32. Nakajima, K.; Miyashita, M.; Suzuki, M.; Kimura, K. Surface structures of binary mixtures of imidazolium-based ionic liquids using high-resolution Rutherford backscattering spectroscopy and time of flight secondary ion mass spectroscopy. *J. Chem. Phys.* **2013**, *139*, 224701. [CrossRef] [PubMed]
33. Nakajima, K.; Nakanishi, S.; Lisal, M.; Kimura, K. Surface structures of binary mixture of ionic liquids. *J. Mol. Liq.* **2017**, *230*, 542–549. [CrossRef]
34. Oz, E.; Sahin, O.; Okur, H.I.; Suzer, S. Surface Propensity of Anions in a Binary Ionic-Liquid Mixture Assessed by Full-Range Angle-Resolved X-ray Photoelectron Spectroscopy and Surface-Tension Measurements. *ChemPhysChem* **2020**, *21*, 2397–2401. [CrossRef] [PubMed]
35. Freire, M.G.; Carvalho, P.J.; Fernandes, A.M.; Marrucho, I.M.; Queimada, A.J.; Coutinho, J.A.P. Surface tensions of imidazolium based ionic liquids: Anion, cation, temperature and water effect. *J. Colloid Interface Sci.* **2007**, *314*, 621–630. [CrossRef]
36. Gardas, R.L.; Coutinho, J.A.P. Applying a QSPR correlation to the prediction of surface tensions of ionic liquids. *Fluid Phase Equilibria* **2008**, *265*, 57–65. [CrossRef]
37. Tariq, M.; Freire, M.G.; Saramago, B.; Coutinho, J.A.; Lopes, J.N.C.; Rebelo, L.P.N. Surface tension of ionic liquids and ionic liquid solutions. *Chem. Soc. Rev.* **2012**, *41*, 829–868. [CrossRef]
38. Luís, A.; Shimizu, K.; Araújo, J.M.M.; Carvalho, P.J.; Lopes-da-Silva, J.A.; Canongia Lopes, J.N.; Rebelo, L.P.N.; Coutinho, J.A.P.; Freire, M.G.; Pereira, A.B. Influence of Nanosegregation on the Surface Tension of Fluorinated Ionic Liquids. *Langmuir* **2016**, *32*, 6130–6139. [CrossRef]
39. Hardy, W.B. The tension of composite fluid surfaces and the mechanical stability of films of fluid. *Proc. R. Soc. Lond. Ser. A Contain. Pap. Math. Phys. Character* **1912**, *86*, 610–635.
40. Langmuir, I. The constitution and fundamental properties of solids and liquids. Part I. Solids. *J. Am. Chem. Soc.* **1916**, *38*, 2221–2295. [CrossRef]
41. Langmuir, I. The constitution and fundamental properties of solids and liquids. II. Liquids. *J. Am. Chem. Soc.* **1917**, *39*, 1848–1906. [CrossRef]
42. Langmuir, I. Forces Near the Surfaces of Molecules. *Chem. Rev.* **1930**, *6*, 451–479. [CrossRef]
43. Langmuir, I. Nobel Lecture. NobelPrize.org. Available online: <https://www.nobelprize.org/prizes/chemistry/1932/langmuir/lecture/> (accessed on 20 October 2022).
44. Shimizu, K.; Heller, B.S.J.; Maier, F.; Steinrück, H.-P.; Lopes, J.N.C. Probing the Surface Tension of Ionic Liquids Using the Langmuir Principle. *Langmuir* **2018**, *34*, 4408–4416. [CrossRef] [PubMed]
45. Koller, T.M.; Lenahan, F.D.; Schmidt, P.S.; Klein, T.; Mehler, J.; Maier, F.; Rausch, M.H.; Wasserscheid, P.; Steinrück, H.-P.; Fröba, A.P. Surface Tension and Viscosity of Binary Mixtures of the Fluorinated and Non-fluorinated Ionic Liquids [PFBMIm][PF6] and [C4C1Im][PF6] by the Pendant Drop Method and Surface Light Scattering. *Int. J. Thermophys.* **2020**, *41*, 144. [CrossRef]
46. Paap, U.; Krefß, B.; Steinrück, H.P.; Maier, F. Probing Surface and Interfacial Tension of Ionic Liquids in Vacuum with the Pendant Drop and Sessile Drop Method. *Int. J. Mol. Sci.* **2022**, *23*, 13158. [CrossRef] [PubMed]
47. Lockett, V.; Rossen, S.; Bassell, C.; Ralston, J. Angle-resolved X-ray photoelectron spectroscopy of the surface of imidazolium ionic liquids. *Phys. Chem. Chem. Phys.* **2008**, *10*, 1330–1335. [CrossRef] [PubMed]
48. Maier, F.; Cremer, T.; Kolbeck, C.; Lovelock, K.R.J.; Paape, N.; Schulz, P.S.; Wasserscheid, P.; Steinrück, H.-P. Insights into the surface composition and enrichment effects of ionic liquids and ionic liquid mixtures. *Phys. Chem. Chem. Phys.* **2010**, *12*, 1905–1915. [CrossRef]
49. Niedermaier, I.; Kolbeck, C.; Steinrück, H.-P.; Maier, F. Dual analyzer system for surface analysis dedicated for angle-resolved photoelectron spectroscopy at liquid surfaces and interfaces. *Rev. Sci. Instrum.* **2016**, *87*, 045105. [CrossRef]
50. Seidl, V.; Bosch, M.; Paap, U.; Livraghi, M.; Zhai, Z.; Wick, C.R.; Koller, T.M.; Wasserscheid, P.; Maier, F.; Smith, A.-S.; et al. Bis-polyethylene glycol-functionalized imidazolium ionic liquids: A multi-method approach towards bulk and surface properties. *J. Ion. Liq.* **2022**, *2*, 100041. [CrossRef]
51. Heller, B.S.J.; Kolbeck, C.; Niedermaier, I.; Dommer, S.; Schatz, J.; Hunt, P.; Maier, F.; Steinrück, H.-P. Surface Enrichment in Equimolar Mixtures of Non-Functionalized and Functionalized Imidazolium-Based Ionic Liquids. *ChemPhysChem* **2018**, *19*, 1733–1745. [CrossRef]

52. Kolbeck, C.; Cremer, T.; Lovelock, K.R.J.; Paape, N.; Schulz, P.S.; Wasserscheid, P.; Maier, F.; Steinrück, H.-P. Influence of Different Anions on the Surface Composition of Ionic Liquids Studied Using ARXPS. *J. Phys. Chem. B* **2009**, *113*, 8682–8688. [[CrossRef](#)]
53. Wagner, C.D.; Davis, L.E.; Zeller, M.V.; Taylor, J.A.; Raymond, R.H.; Gale, L.H. Empirical Atomic Sensitivity Factors for Quantitative Analysis by Electron Spectroscopy for Chemical Analysis. *Surf. Interface Anal.* **1981**, *3*, 211–225. [[CrossRef](#)]
54. Gardas, R.L.; Freire, M.G.; Carvalho, P.J.; Marrucho, I.M.; Fonseca, I.M.A.; Ferreira, A.G.M.; Coutinho, J.A.P. High-Pressure Densities and Derived Thermodynamic Properties of Imidazolium-Based Ionic Liquids. *J. Chem. Eng. Data* **2006**, *52*, 80–88. [[CrossRef](#)]

Supplementary Materials

Direct Correlation of Surface Tension and Surface Composition of Ionic Liquid Mixtures – A Combined Vacuum Pendant Drop and Angle-Resolved X-Ray Photoelectron Spectroscopy Study

Ulrike Paap *ORCID: 0000-0002-1442-0239 [a]*, Vera Seidl *ORCID: 0000-0003-3310-700X [b]*,
Karsten Meyer *ORCID: 0000-0002-7844-2998 [b]*, Florian Maier *ORCID: 0000-0001-9725-8961 [a]*,
and Hans-Peter Steinrück* *ORCID: 0000-0003-1347-8962 [a]*

^[a] Department of Chemistry and Pharmacy, Physical Chemistry II, Friedrich-Alexander-Universität
Erlangen-Nürnberg (FAU), Egerlandstr. 3, 91058 Erlangen

^[b] Department of Chemistry and Pharmacy, Inorganic Chemistry, Friedrich-Alexander-Universität
Erlangen-Nürnberg (FAU), Egerlandstr. 1, 91058 Erlangen

(* hans-peter.steinrueck@fau.de)

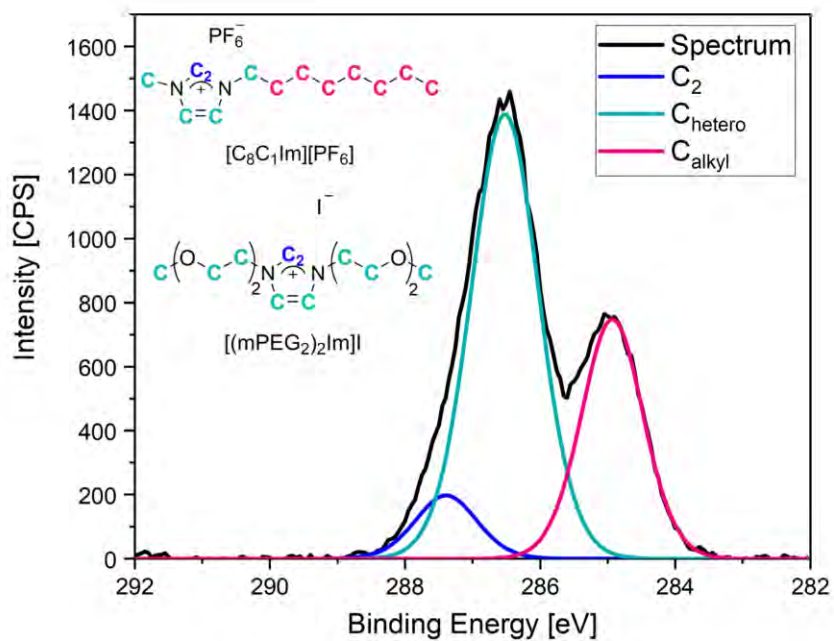


Figure S1: Exemplary fitting procedure for the C 1s region of the 49.8 mol% [C₈C₁Im][PF₆] content mixture in 0° at T = 298 K. The spectrum (black) is fitted with peaks for C₂ (blue), C_{hetero} (turquoise) and C_{alkyl} (pink) carbon atoms (see inset).

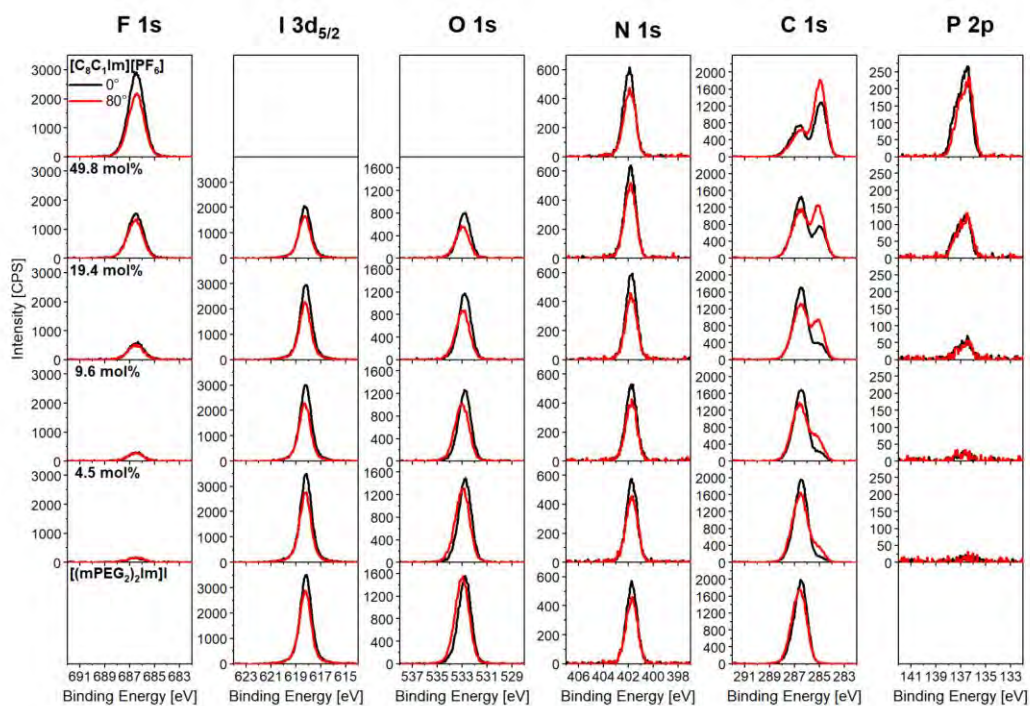


Figure S2: F 1s, I 3d_{5/2}, O 1s, N 1s, C 1s and P 2p spectra at 0° (black) and 80° (red) emission of pure [C₈C₁Im][PF₆] (top row), pure [(mPEG₂)₂Im]I (bottom row), and of different mixtures of these ILs, collected at T = 298 K.

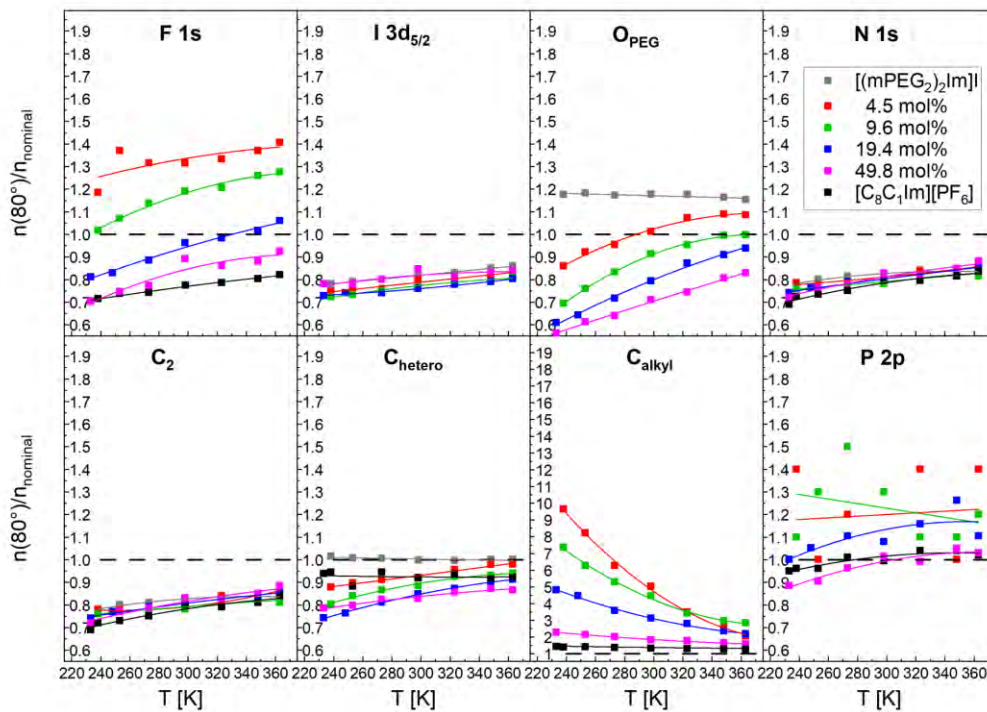


Figure S3: Composition ratios $n(80^\circ)/n_{\text{nominal}}$ for F 1s, O_{PEG} , I 3d_{5/2}, N 1s, C₂, C_{hetero}, C_{alkyl} and P 2p, derived from the corresponding 80° intensities and their nominal atomic numbers for the neat ILs and mixtures for different temperatures (note the different scaling for the C_{alkyl} signal).

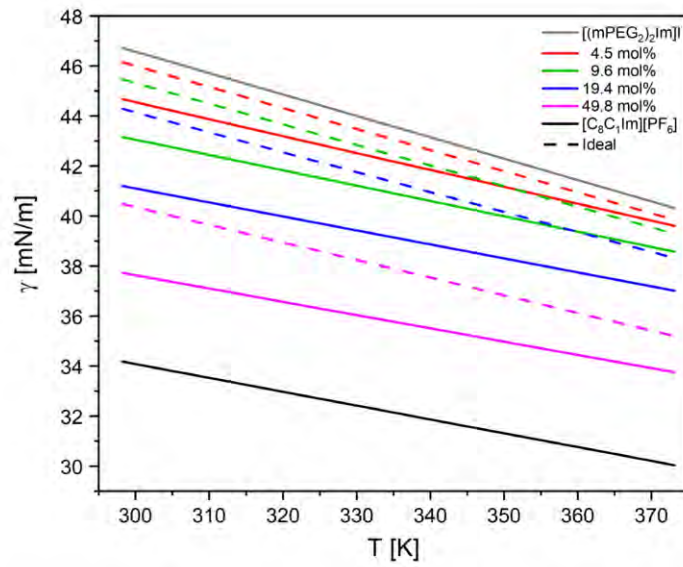


Figure S4: Comparison of the linear fits (solid lines) of the experimental data determined using the pendant drop method in vacuum (Figure 5 and equation (1) in the manuscript) with the surface tension as expected for ideal behaviour of different mixtures (dashed lines). Clearly, the measured surface tension of all mixtures and temperatures strongly deviates from the ideal mixing rules.

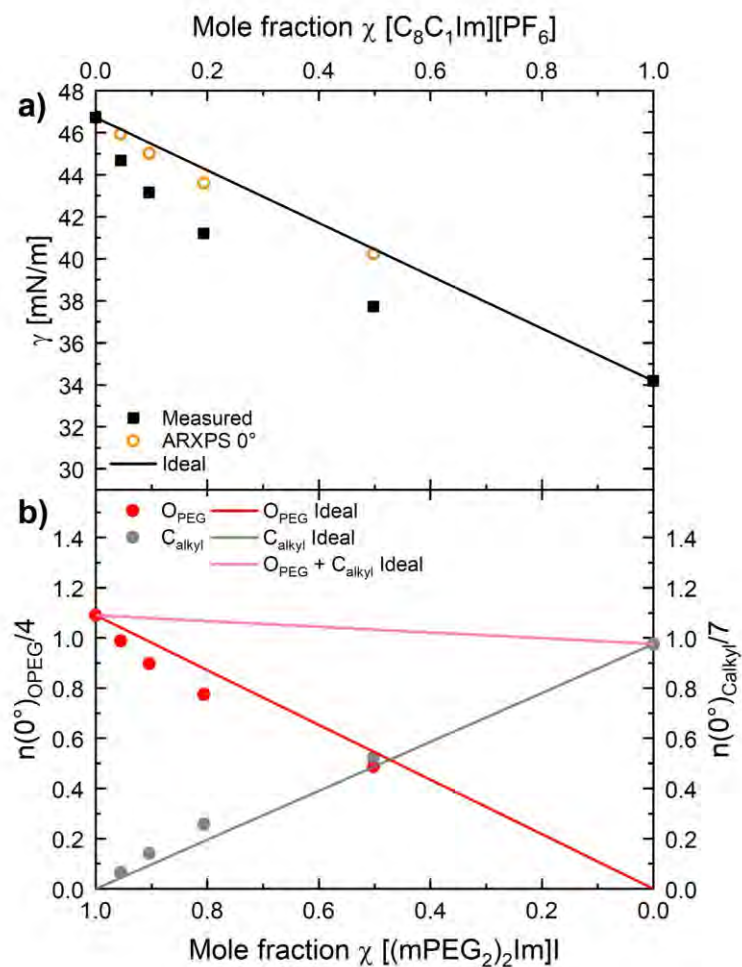


Figure S5: a) Surface tension values of the pure ILs and the mixtures at 298 K (black squares), as determined from pendant drop measurements in Figure 5, along with the surface tension values calculated from the 0° ARXPS data according to equation (3) (open orange circles). For comparison, the surface tension of ideal mixtures without enrichment/depletion effects is shown as black line. b) Number of atoms, $n(0^\circ)$, as determined from the ARXPS data at 0°, normalized to the number of corresponding atoms in the IL for O_{PEG} (red circles) and for C_{alkyl} (grey circles) for the pure ILs and for the mixtures at $T = 298$ K. Lines represent the ideal bulk mixing behaviour without enrichment/depletion effects at the surface. In contrast to the 80° ARXPS data that reproduce the measured surface tension values (see Figure 6a), the 0° data follow the ideal behaviour as expected due to their reduced surface sensitivity.

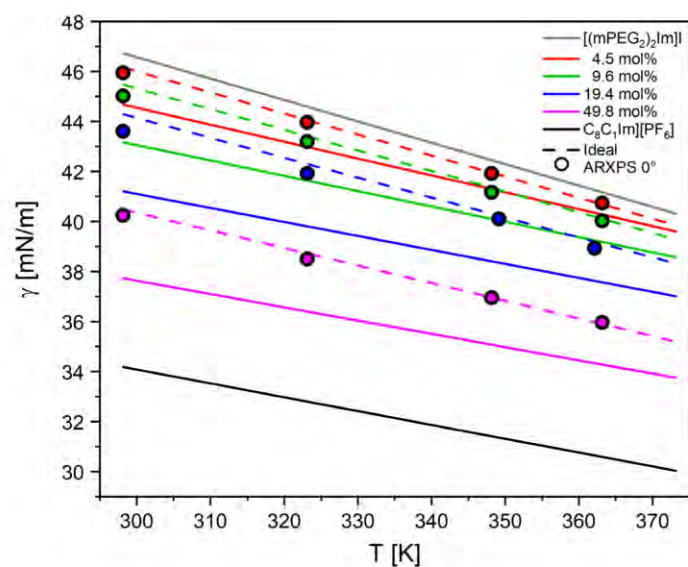


Figure S6: Comparison of the experimentally determined surface tension values derived from the pendant drop measurements in vacuum (solid lines as linear fits to the experimental data, see Figure 5 and equation (1) in the manuscript) with the surface tension expected for ideal behaviour of the different mixtures (dashed lines). Also shown are the predictions of the surface tension from the ARXPS data at 0° (filled circles, for details, see text). For each mixture, the surface tension values predicted from ARXPS at 0° strongly deviate from the pendant drop results (solid lines), but follow the expected ideal behaviour (dashed lines, see equation (2)).

Table S1: Temperature-dependent density parameters for pure $[C_8C_1Im][PF_6]$ from Ref. [1], $[(mPEG)_2Im]I$ from Ref. [2] and their mixtures with 4.5, 9.6, 19.4 and 49.8 mol% $[C_8C_1Im][PF_6]$ content; the densities for the surface tension evaluation at different temperatures are obtained following $\rho = \rho_0 + \rho_1 \cdot T + \rho_2 \cdot T^2$ (temperature in K).

	ρ_0 [g/cm ³]	ρ_1 [g/cm ³ ·K]	ρ_2 [g/cm ³ ·K ²]
$[C_8C_1Im][PF_6]$	1.61	-1.59·10 ⁻³	1.21·10 ⁻⁶
49.8 mol%	1.65	-1.30·10 ⁻³	7.39·10 ⁻⁷
19.4 mol%	1.69	-1.29·10 ⁻³	6.40·10 ⁻⁷
9.6 mol%	1.71	-1.22·10 ⁻³	6.07·10 ⁻⁷
4.5 mol%	1.72	-1.21·10 ⁻³	5.91·10 ⁻⁷
$[(mPEG)_2Im]I$	1.72	-1.20·10 ⁻³	5.70·10 ⁻⁷

Table S2: Number of O_{PEG} and C_{alkyl} atoms derived from the temperature-dependent 0° and 80° ARXPS spectra.

0°								
	49.8 mol%		19.4 mol%		9.6 mol%		4.5 mol%	
T [K]	$n_{OPEG,0^\circ}(x)$	$n_{Calkyl,0^\circ}(x)$	$n_{OPEG,0^\circ}(x)$	$n_{Calkyl,0^\circ}(x)$	$n_{OPEG,0^\circ}(x)$	$n_{Calkyl,0^\circ}(x)$	$n_{OPEG,0^\circ}(x)$	$n_{Calkyl,0^\circ}(x)$
363	2.04	3.46	3.22	1.51	3.71	0.79	4.09	0.31
348	2.01	3.50	3.20	1.52	3.69	0.85	40.5	0.36
323	1.95	3.65	3.18	1.63	3.65	0.86	4.04	0.40
298	1.95	3.67	3.10	1.80	3.59	0.99	3.95	0.46
80°								
	49.8 mol%		19.4 mol%		9.6 mol%		4.5 mol%	
T [K]	$n_{OPEG,80^\circ}(x)$	$n_{Calkyl,80^\circ}(x)$	$n_{OPEG,80^\circ}(x)$	$n_{Calkyl,80^\circ}(x)$	$n_{OPEG,80^\circ}(x)$	$n_{Calkyl,80^\circ}(x)$	$n_{OPEG,80^\circ}(x)$	$n_{Calkyl,80^\circ}(x)$
363	1.67	5.53	3.02	2.98	3.61	1.90	4.15	0.66
348	1.62	5.75	2.93	3.22	3.60	1.99	4.16	0.85
323	1.50	6.18	2.81	3.80	3.45	2.30	4.10	1.12
298	1.43	6.34	2.55	4.23	3.31	3.00	3.87	1.61

Table S3: ST values γ (ideal) for different mixtures and temperatures as expected from ideal mixing behaviour using equation (2) along calculated ST values γ_0 (calc.) using equation (3) with the number of O_{PEG} and C_{alkyl} atoms as deduced from the 0° ARXP spectra (top row of Table S5).

	49.8 mol%		19.4 mol%		9.6 mol%		4.5 mol%	
T [K]	γ (ideal) [mN/m]	γ_0 (calc.) [mN/m]						
363	35.90	35.96	39.11	38.93	40.11	40.02	40.68	40.73
348	36.96	36.95	40.30	40.10	41.34	41.17	41.95	41.92
323	38.72	38.50	42.30	41.92	43.41	43.19	44.05	43.96
298	40.48	40.24	44.29	43.60	45.47	45.02	46.15	45.94

Table S4: Weights of $[C_8C_{12}Im][PF_6]$ and $[(mPEG)_2Im]I$ used for the 4.5, 9.6, 19.4 and 49.8 mol% mixtures; last column shows solidification temperatures of the corresponding mixtures as indicated by the onset of sample charging in ARXPS.

	$[C_8C_{12}Im][PF_6]$ [g]	$[(mPEG)_2Im]I$ [g]	Solidification Temperature [K]
4.5 mol%	0.0424	1.0486	237
9.6 mol%	0.2476	2.7352	235
19.4 mol%	0.1624	0.7992	231
49.8 mol%	1.0257	1.2193	230

Table S5: Binding energy (BE) differences of the C_{hetero} and C_{alkyl} peaks for both angles as a function of temperature of the 49.8 mol% mixture. These ΔBE values were used as constraints to fit the C 1s spectra of all other mixtures (for details, see text).

T [K]	$\Delta BE(0^\circ)$ [eV]	$\Delta BE(80^\circ)$ [eV]
363	1.62	1.49
348	1.61	1.48
323	1.61	1.47
298	1.59	1.46
273	1.57	1.42
253/248	1.54	1.40
238/233	1.53	1.39

Table S6: Quantitative analysis of the 0° and 80° ARXPS spectra for pure [C₈C₁Im][PF₆], [(mPEG₂)₂Im]I and their mixtures with 4.5, 9.6, 19.4 and 49.8 mol% [C₈C₁Im][PF₆] content at 298 K.

	F 1s	I 3d _{5/2}	O 1s	N 1s	C ₂	C _{hetero}	C _{alkyl}	P 2p
ASF	1.00	6.17	0.67	0.46	0.3	0.3	0.3	0.46
[C₈C₁Im][PF₆]								
0° BE/eV	686.5			401.9	287.5	286.6	284.9	137.4
80° BE/eV	686.7			402.1	287.6	286.7	285.1	137.4
Nominal	6			2	1	4	7	1
n(0°)	6.11			1.99	1.00	3.97	6.84	1.09
n(80°)	4.62			1.60	0.80	3.61	9.38	0.99
49.8 mol%								
0° BE/eV	868.6	618.3	532.9	401.9	287.4	286.5	284.9	137.5
80° BE/eV	868.7	618.4	533.1	402.0	287.5	286.6	285.2	137.5
Nominal	2.99	0.50	2.01	2.00	1.00	8.02	3.48	0.50
n(0°)	3.14	0.53	1.96	1.99	0.99	7.61	3.75	0.52
n(80°)	2.70	0.44	1.48	1.69	0.85	6.68	6.15	0.52
19.4 mol%								
0° BE/eV	686.5	618.2	532.8	401.8	287.3	286.5	284.9	137.4
80° BE/eV	686.6	618.4	533.1	401.9	287.5	286.6	285.1	137.4
Nominal	1.17	0.81	3.22	2.00	1.00	10.5	1.36	0.19
n(0°)	1.30	0.82	3.12	1.98	0.99	9.89	1.85	0.25
n(80°)	1.12	0.62	2.56	1.56	0.78	8.80	4.54	0.21
9.6 mol%								
0° BE/eV	686.5	618.2	532.8	401.8	287.3	286.5	284.9	137.5
80° BE/eV	686.7	618.4	533.2	401.9	287.6	286.7	285.2	137.6
Nominal	0.58	0.90	3.62	2.00	1.00	11.2	0.67	0.10
n(0°)	0.70	0.90	3.59	1.95	0.98	10.9	0.99	0.11
n(80°)	0.69	0.69	3.31	1.56	0.78	9.93	3.00	0.13
4.5 mol%								
0° BE/eV	868.6	618.2	532.8	401.7	287.3	286.5	284.9	137.1
80° BE/eV	686.7	618.4	533.1	401.8	287.5	286.6	285.2	137.3
Nominal	0.27	0.95	3.82	2.00	1.00	11.6	0.32	0.05
n(0°)	0.33	0.96	3.96	1.91	0.96	11.4	0.48	0.08
n(80°)	0.40	0.76	3.94	1.64	0.82	10.8	1.63	
[(mPEG₂)₂Im]I								
0° BE/eV		618.2	532.8	401.7	287.3	286.5		
80° BE/eV		618.4	533.2	401.9	287.6	286.7		
Nominal		1	4	2	1	12		
n(0°)		1.00	4.34	1.94	0.97	11.7		
n(80°)		0.84	4.74	1.66	0.83	11.9		

References:

1. Gardas, R.L.; Freire, M.G.; Carvalho, P.J.; Marrucho, I.M.; Fonseca, I.M.A.; Ferreira, A.G.M.; Coutinho, J.A.P. High-Pressure Densities and Derived Thermodynamic Properties of Imidazolium-Based Ionic Liquids. *Journal of Chemical & Engineering Data* **2007**, *52*, 80-88, doi:10.1021/je060247x.
2. Seidl, V.; Bosch, M.; Paap, U.; Livraghi, M.; Zhai, Z.; Wick, C.R.; Koller, T.M.; Wasserscheid, P.; Maier, F.; Smith, A.-S.; et al. Bis-polyethylene glycol-functionalized imidazolium ionic liquids: A multi-method approach towards bulk and surface properties. *Journal of Ionic Liquids* **2022**, *2*, 100041, doi:10.1016/j.jil.2022.100041.

8.1.4. B/N-DOPED CARBON SHEETS FROM A NEW IONIC LIQUID WITH EXCELLENT SORPTION PROPERTIES FOR METHYLENE BLUE^[P4]

Journal of Ionic Liquids 1 (2021) 100004



Contents lists available at ScienceDirect

Journal of Ionic Liquids

journal homepage: www.elsevier.com/locate/jil



B/N-doped carbon sheets from a new ionic liquid with excellent sorption properties for methylene blue

Julian Mehler^a, Matthias Ermer^b, Ulrike Paap^c, Bettina S.J. Heller^c, Florian Maier^c, Hans-Peter Steinrück^c, Martin Hartmann^b, Carsten Korte^d, Peter S. Schulz^{a,*}, Peter Wasserscheid^{a,e}

^a Institute of Chemical Reaction Engineering, Friedrich-Alexander University Erlangen-Nürnberg, 91058 Erlangen, Germany

^b Erlangen Center for Interface Research and Catalysis (ECRC), Friedrich-Alexander University Erlangen-Nürnberg, 91058, Erlangen, Germany

^c Chair of Physical Chemistry II, Friedrich-Alexander-University Erlangen-Nürnberg, 91058 Erlangen, Germany

^d Forschungszentrum Jülich, Institute of Energy and Climate Research - Fuel Cells (IEK-14), 52425 Jülich, Germany

^e Forschungszentrum Jülich, Helmholtz-Institute Erlangen-Nürnberg for Renewable Energy (IEK 11), 91058 Erlangen, Germany

ARTICLE INFO

Keywords:

Material synthesis
Ionic liquid precursor
B/N doped carbon nanosheets
Adsorption

ABSTRACT

The pyrolytic treatment of the novel ionic liquid 1-ethyl-3-methyl-imidazolium tetrakis-(1-imidazolyl)borate ([EMIM][BIm₄]) allowed the preparation of B/N-doped carbonaceous materials with an exceptional performance in the adsorptive removal of the cationic dye methylene blue (MB) from wastewater. [EMIM][BIm₄] was prepared via an easy and scalable synthesis protocol in very good yield. The carbon materials obtained after salt templated pyrolysis of the IL displayed high degrees of heteroatom doping (up to 22 wt% N, 3 wt% B) and high surface areas of up to 1860 m² g⁻¹. The materials were tested for their performance in the adsorptive removal of MB from contaminated water. Adsorption equilibrium experiments revealed an adsorption capacity exceeding

500 mg g⁻¹, which is, to the best of our knowledge, the highest value reported so far. Time-resolved adsorption experiments showed that the materials not only exhibit high capacity but also very fast adsorption kinetics. Complete decolorization of MB solutions in only 5 min at high MB concentrations of 100 mg L⁻¹ was observed. These results demonstrate that [EMIM][BIm₄] is an excellent precursor for the preparation of IL-derived B/N-doped carbon sorbents.

1. Introduction

Due to their tunability, high surface area and stability, heteroatom-doped porous carbons have become a very interesting material class. In addition to their adsorptive properties, they have shown great potential in catalysis, energy conversion, energy storage, and sensing technologies. (Titirici et al., 2015, Su et al., 2013, Zhao et al., 2019, Jariwala et al., 2013, Liang et al., 2008) In most cases, their preparation is carried out via chemical vapor deposition (CVD) or via pyrolysis of an organic precursor. A wide choice of precursors has been found suitable, ranging from simple organic molecules like acetonitrile or melamine (Pacula et al., 2016, Mombeshora et al., 2017, Yao et al., 2015), to polymers (Paraknowitsch et al., 2011), mixtures of organic salts (Luo et al., 2020), bio-based heterocycles (Yang et al., 2015), human hair (Chaudhari et al., 2014) or chicken feathers (Gao et al., 2014). Chemists have pyrolysed virtually everything in the search for new doped carbon materials!

A very popular class of pyrolysis precursors are ionic liquids (ILs). Their thermal stability and low volatility provide high yield during carbonization. Furthermore, the wide variety of possible cation-anion combinations allows for control over the amount and nature of doped heteroatoms in the product. (Paraknowitsch and Thomas, 2012, Zhang et al., 2015) For the preparation of heteroatom-doped carbon materials from ILs, there are two general *modi operandi*, as the pyrolysis of neat, non-functionalized ILs still leads to decomposition and evaporation of the decomposition products.

In the first approach, the nano-confinement or templating approach, the ionic liquid is entrapped inside a porous support like silica. Mixing the IL with an inorganic salt prior to pyrolysis allows for the preparation of carbonaceous materials from ILs that would normally just decompose and evaporate under pyrolysis conditions, such as [BMIM][NTf₂] or [EMIM]Br. (Wang and Dai, 2010, Chen et al., 2013, Zhang et al., 2017) Generally, after pyrolysis, a carbon material that is a structural 'negative' of the inorganic template is obtained. This allows for a more

* Corresponding author.

E-mail address: peter.schulz@fau.de (P.S. Schulz).

<https://doi.org/10.1016/j.jil.2021.100004>

Received 2 July 2021; Received in revised form 11 August 2021; Accepted 11 August 2021

2772-4220/© 2021 The Authors. Published by Elsevier B.V. This is an open access article under the CC BY license (<http://creativecommons.org/licenses/by/4.0/>)

targeted approach towards the final product, as pore and structure engineering is possible through selection of the inorganic template.

The second pathway from ILs to doped carbon materials is pre-functionalization. The incorporation of cross-linkable nitrile groups at the IL cation or anion allows for the preparation of highly nitrogen-enriched, porous carbons *via* pyrolysis of the neat IL. It is generally understood that these functionalities undergo polymerization and condensation reactions at elevated temperatures, resulting in a thermally stable resin that carbonizes with minimal loss of small, volatile organic molecules. (Fellinger et al., 2012) (Lee et al., 2009) Cations with nitrile functionalities can be prepared *via* quaternization reactions of imidazole with chloroacetonitrile or chlorobutyronitrile, whereas suitable nitrile-bearing anions are dicyanamide [DCA] or tricyanomethanide [TCM]. (Precht et al., 2009, Drab et al., 2012, Kuzmina et al., 2017, Zhu et al., 2012) Thus with the structural variation of cation and anion of the IL, the composition of the carbon materials and their heteroatom content can be controlled. Nitrogen as a dopant is relatively straightforward to achieve, as, for example, the nitrogen content of the popular 1-ethyl-2-methylimidazolium cation ([EMIM]⁺), is already approximately 25 wt%. This cation paired with a [DCA]⁻ ion gives almost 40 wt% of N in the precursor IL, which allows for the preparation of highly N-doped carbon materials. Antonietti et al. reported that the material obtained after SBA-15 templated pyrolysis of [EMIM][DCA] at 1000°C still contained 10.4 wt% of nitrogen. (Paraknowitsch et al., 2010) If not only N but also S is desired in the product, the bistriflimide ([NTf₂]⁻) anion can be used instead of [DCA]⁻. Leung et al. used [BMIM][NTf₂] as an IL-precursor in a graphite-templated pyrolysis at 900°C. The product not only had high nitrogen content (up to 13 at%), but also incorporated sulphur (up to 0.5 at%) in the final product. (She et al., 2015) The pyrolysis of neat mixtures of [DCA]⁻ and [NTf₂]⁻-ILs was investigated by Kim et al. [EMIM][DCA] was chosen as the carbonization agent, trapping the bulky [NTf₂]⁻ ions inside the polymerized carbon matrix. Subsequent thermal decomposition of [NTf₂]⁻ then led to pore formation without the use of any additional inorganic template. A high N content (16.1 at%), as well as S (0.6 at%) and F (0.3 at%) doping, paired with a high specific surface area of 625 m² g⁻¹ was obtained after pyrolysis at 900°C. (Jeong et al., 2017) Mixing [DCA]⁻-ILs with phosphonium ILs and subsequent pyrolysis opens the pathway to N and P co-doped materials, as shown by Thomas et al. (Paraknowitsch et al., 2013) Dissolving tetrabutylphosphonium bromide in 1-butyl-3-methylpyridinium [DCA] yielded carbon materials with up to 5.7 wt% of P and 4.1 wt% of N after pyrolysis at 1000°C.

Another popular dopant for carbon materials is boron. When paired with nitrogen, B- and N-doped carbons (BNCs) are formed that offer most interesting materials properties for applications in electrocatalysis, sensing and adsorption. (Panchakarla et al., 2009, Inagaki et al., 2018, Abbas et al., 2019, Gouse Peera et al., 2020, Han et al., 2020) Interestingly, among the ions commonly used in the field of IL chemistry, there are only two containing boron, tetrafluoroborate [BF₄] and tetracyano-borate [TCB]. Although [BF₄]⁻ has been used in the preparation of B-doped carbons, its use as a precursor is hampered by the formation of gaseous HF during pyrolysis. (Chen et al., 2016) (Ohtani et al., 2008) Despite the formation of HCN during pyrolysis, [TCB]⁻-ILs proved the more popular choice as a precursor IL, most likely due to the nitrile functionality in the anion, that allows for fast network formation under thermal treatment and leads to a very effective formation of BNCs. (Paraknowitsch and Thomas, 2017, Fulvio et al., 2011, Aijaz et al., 2014, Ranjbar Sahraie et al., 2014) A drawback of using [TCB]⁻-ILs, however, is their very limited commercial availability nowadays. (SciFinder®, 2014) The synthesis of [TCB]⁻-ILs relies on the rather unpleasant preparation of K[TCB] which uses an excess of molten KCN and gives relatively low yields after tedious work-up procedures. (Bernhardt et al., 2003) Here, we want to introduce an alternative anion that, to the best of our knowledge, has not yet been explored in the context of ILs, tetrakis(1-imidazolyl)borate ([BIm₄]⁻). So far, [BIm₄]⁻ was mostly used by the metal-organic-frameworks community as a linker for the prepara-

tion of lightweight porous materials. (Zhang et al., 2010, Galvelis et al., 2012, Zheng et al., 2010) With the central boron atom and four imidazolyl wings, [BIm₄]⁻ strongly resembles [TCB]⁻ and can be used as an alternative in the pyrolytic preparation of BNCs. In this manuscript we present a synthesis protocol for the preparation of Na[BIm₄] in larger scale (up to 200 g per batch), and starting from this salt, the detailed synthesis of the new IL [EMIM][BIm₄] is reported. After the purity of the IL was confirmed, the salt was applied as a precursor in the preparation of B- and N-doped carbon materials, resulting in high degrees of heteroatom doping (up to 22 wt% N, 3 wt% B) and high surface area materials (up to 1860 m² g⁻¹ internal surface). After materials characterization by elemental analysis, ICP-OES, gas sorption, IR spectroscopy, RAMAN spectroscopy, X-ray induced photoelectron spectroscopy, XRD and microscopy, the materials were tested in the adsorptive removal of the pollutant methylene blue (MB). Excellent performance, with an uptake of 0.25 g of MB per gram of BNC in 5 min and a maximum capacity of over 500 mg g⁻¹ was found. This is, to the best of our knowledge, the highest value for this class of materials reported so far. Our study provides not only an alternative to TCB⁻-ILs for the preparation of BNCs but also shows the potential of the new [BIm₄]⁻-ILs as versatile precursor in the field of material synthesis.

2. Experimental details

2.1. Chemicals

All regular solvents and chemicals were purchased from commercial suppliers and were of reagent grade. Unless otherwise stated, all chemicals were used as received. Sodium borohydride (≥ 98 %, granular form) was purchased from Merck. Imidazole (99 %) was purchased from Alfa Aesar. 1-Ethyl-3-methylimidazolium chloride ([EMIM]Cl, >98 %) was purchased from Iolitec and recrystallized from ethyl acetate/acetonitrile 7:1 v/v, dried *in vacuo* and stored under argon, prior to the reaction.

2.2. Synthetic procedures

2.2.1. Synthesis of sodium tetrakis-(1-imidazolyl)borate

Na[BIm₄] was synthesized *via* an up-scaled synthesis procedure, originally published by Hamilton et al. and

Chao et al. (Chao and Moore, 1978; Hamilton et al., 2003) Under a constant flow of argon, a 1 l glass reactor (for a detailed flowchart see Fig. S1) was charged with imidazole (360 g, 5.287 mol, 8 eq.). The reaction temperature was set to 110°C and imidazole was molten under slow stirring (300 rpm), over the course of 30 min. As soon as the imidazole liquefied, the reaction temperature was slowly raised to 225°C and simultaneously Na[BH₄] (25 g, 0.661 mol, 1 eq) was added in small portions *via* a lab-scale snail extruder. Vigorous evolution of H₂ was observed, as the Na[BH₄] granules reacted with the molten imidazole.† Upon complete addition, the reaction mixture was stirred at 225°C for an additional 3 h, to guarantee full conversion of Na[BH₄]. The heating mantle was removed and the reaction mixture was cooled down using a water bath. 800 mL of acetone were added slowly, during which an off-white crude-product precipitated. After filtration, the residue was washed with two portions of acetone (500 mL each), then with one portion of cold ethanol (250 mL). Drying *in vacuo* gave the product as a white powder (187 g, 0.619 mol, 93.64 %). Purity was confirmed *via* NMR spectroscopy and elemental analysis (EA, see ESI for details).

2.2.2. Synthesis of 1-ethyl-3-methylimidazolium tetrakis-(1-imidazolyl)-borate

[EMIM][BIm₄] was synthesized *via* a simple salt metathesis reaction, starting from [EMIM]Cl and Na[BIm₄]. A 500 mL two-necked flask, equipped with a magnetic stirring bar and a reflux condenser, was charged with Na[BIm₄] (15.1 g, 50 mmol, 1 eq.) and 350 mL of ethanol as a solvent. The reaction mixture was heated to reflux under constant stirring (500 rpm) until Na[BIm₄] dissolved completely. A clear solution

of [EMIM]Cl (7.33 g, 50 mmol, 1 eq) in 50 mL of ethanol was added in one portion. A white precipitate formed immediately and stirring was continued under reflux for 60 min. The reaction mixture was cooled down to room temperature, filtered and the residue was washed with three portions of cold ethanol (25 mL each). The solvent was removed under reduced pressure to give a solid, yellow crude-product. To remove residual traces of NaCl in the IL, the crude-product was taken up in hot 1-butanol (250 mL) and the solution was filtered again. After removal of 1-BuOH and drying *in vacuo*, [EMIM][BIm₄] was obtained as a hygroscopic yellow solid (17.17 g, 44 mmol, 88 %, *M* = 390.26 g mol⁻¹). Purity was confirmed *via* NMR spectroscopy and elemental analysis. The melting point (57°C) was determined *via* differential scanning calorimetry. Due to the m.p., no viscosity measurements were performed. The decomposition temperature (*T*_{onset}: 213°C) was determined *via* thermogravimetric analysis. Details can be found in the ESI. Until further processing, the product was stored under argon.

2.3. Preparation and characterization of BNC materials

The BNC materials were synthesized from [EMIM][BIm₄] using a salt-templating method, adapted from Fechler et al. (Fechler et al., 2013) In a 100 mL beaker, 16 g of [EMIM][BIm₄] were combined with 48 g of a eutectic mixture of ZnCl₂ and NaCl (36.63 g and 11.37 g, respectively) that served as a porogen during pyrolysis. The IL/salt mixture was slowly heated to 80°C under gentle stirring to give a slightly yellow, homogenous paste. This precursor was transferred into porcelain crucibles and pyrolyzed at up to 1000°C in a Carbolite CWF 1100 chamber oven under a constant stream of argon for 2 h and with a heating rate of 10 K min⁻¹. The samples were allowed to cool down to room temperature, combined, ground in a mortar and washed with 200 mL of HCl (10 wt%) and NaOH (0.1 M), respectively, in two consecutive steps, for 1 h each. After filtration, the samples were washed with H₂O until a neutral pH was achieved and dried in an oven at 100°C over night. The three samples prepared were denoted as BNC-800, BNC-900 and BNC-1000, with the number representing the respective pyrolysis temperature.

To determine the bulk elemental composition of BNC materials, elemental analysis (UNICUBE®, elemental) and ICP-OES (CIROS-CCD, SPECTRO) were used. For surface analysis and evaluation of chemical bonding, X-ray photoelectron spectroscopy (DASSA (Niedermaier et al., 2016), Omicron NanoTechnology, monochromated Al K_α X-ray source, 1486.6 eV, 238 W, detection angle of 0° to the surface normal of the sample) and FTIR (FT/IR-4600, Jasco, KBr pellet) were used. The morphology was studied by SEM (ULTRA 55 SEM, Carl Zeiss) and TEM (CM 30, Philips). The specific surface area (*S*_{BET}) was calculated by applying the Brunauer-Emmett-Teller (BET) model to N₂ adsorption isotherm data points (ASAP 2000, Micromeritics). The pore size distribution was calculated using the NLDFT equilibrium model method for carbon slit pores. Powder X-ray diffraction patterns were collected on a Philips X'Pert Pro MPD diffractometer in Bragg-Brentano geometry equipped with a pixel (Zhao et al., 2019)^D line detector. The copper X-ray tube providing CuK_{α1} (λ = 1.5406 Å) radiation was operated at 40 kV and 40 mA. For Raman spectroscopy, an AvaRaman-532HERO-EVO (Avantes) system with an AvaRaman-PRB-532 (Avantes) probe was used. The Raman solution consisted of a 532 nm (green) solid state laser (Cobolt) and an AvaSpec-HERO (Avantes) spectrometer with a grating set of 1200 lines mm⁻¹ (HSC1200-0.75). The spectrometer was equipped with a 50 μm slit and the detected wavelength range was 534-696 nm. The Raman spectra were collected in 10 repetitions at 50 mW laser power with an exposure time of 10 s.

2.4. Adsorption kinetics of MB

In a typical time-resolved adsorption experiment, a 50 mL Schott bottle was charged with 20 mg of BNC adsorbent and 50 mL of MB solution (*c*₀ = 20 mg L⁻¹ or 100 mg L⁻¹) were added under vigorous stirring

(800 rpm), to guarantee a homogeneous suspension. The recording time was started immediately upon addition of the solution and samples of 2.5 mL were withdrawn either every minute (for BNC-800 at *c*₀ = 100 mg L⁻¹), or every 30 s (for BNC-900 and BNC-1000). After filtration using a 0.45 μm PTFE syringe filter, the remaining concentration of MB in solution (*c*_t) was measured using a UV/Vis spectrometer (Specord 205, Analytic Jena), calibrated at 663 nm. From *c*_t the amount of adsorbed MB at time-interval *t* (*q*_t) could then be calculated using:

$$q_t = \frac{V(c_0 - c_t)}{m} \quad (1)$$

where *V* (l) is the volume of the MB solution, *c*₀ (mg L⁻¹) is the initial concentration of MB and *m* (g) is the mass of the BNC adsorbent.

2.5. Adsorption capacity and isotherms

Stock solutions of MB (50 mg L⁻¹ up to 400 mg L⁻¹) were prepared by dissolving the respective amount of MB in 1 L of deionized H₂O and used without further pH correction. In a typical equilibration experiment, 10 mg of BNC adsorbent were mixed with 25 mL of MB stock solution and vigorously stirred for 24 h at room temperature. A sample of 3 mL was withdrawn and filtered using a 0.45 μm PTFE syringe filter. The remaining concentration of MB at equilibrium (*c*_e) was then measured using a UV/Vis spectrometer (Specord 205, Analytic Jena), calibrated at 663 nm. With *c*_e, the adsorption capacity (*q*_e) could then be calculated using the following equation:

$$q_e = \frac{V(c_0 - c_e)}{m} \quad (2)$$

where *q*_e (mg g⁻¹) is the adsorption capacity at equilibrium, *V* (l) is the volume of the MB solution, *c*₀ and *c*_e

(mg L⁻¹) are the initial and equilibrium concentration of MB, respectively and *m* (g) is the mass of the BNC adsorbent. To fit the values of *q*_e at different *c*_e, three adsorption isotherm models were used in this study. The Langmuir isotherm model is based on a monolayer sorption without interaction between sorbed molecules on the homogeneous surface. (Langmuir, 1918) The *q*_e value is determined by Equation 3.

$$q_e = \frac{q_{max} K_L c_e}{1 + K_L c_e} \quad (3)$$

with *q*_e (mg g⁻¹) and *c*_e (mg L⁻¹) being the adsorption capacity and concentration of adsorbate at equilibrium, respectively, *q*_{max} (mg g⁻¹) is the theoretical maximum adsorption capacity with monolayer coverage and *K*_L

(L mg⁻¹) is the Langmuir isotherm constant, related to the favorability of adsorption. The Freundlich equation describes multilayer sorption on a heterogeneous surface (Equation 4). (Freundlich, 1907)

$$q_e = K_F \cdot c_e^{1/n} \quad (4)$$

*K*_F and 1/*n* are constants related to adsorption capacity and intensity, respectively. The Brouers-Sotolongo isotherm model is based on statistical analysis of complex sorption processes and considers physical and chemical heterogeneities of the adsorbent and of the adsorbent/adsorbate system. (Brouers et al., 2005, Neibi et al., 2008, Altendor et al., 2009) The Brouers-Sotolongo isotherm (BSI) is calculated according to Equation 5.

$$q_e = q_{max} \left(1 - e^{(-K_W c_e^\alpha)} \right) \quad (5)$$

with *K*_W = *K*_F/*q*_{max}, where *K*_F is the Freundlich constant at low *c*_e and *α* is a measure of the energy heterogeneity of the sorbent surface.

2.6. Influence of pH on adsorption capacity

HCl (10 wt%) and NaOH (0.1 M) were used to prepare five solutions with a pH value of 2, 4, 6, 8 and 10. To these solutions, an appropriate amount of MB was added, to give an initial concentration of MB of 100 mg L⁻¹. To determine the adsorption capacity of BNC-1000 at varying

pH value, 10 mg of adsorbent were mixed with 50 mL of previously prepared stock solutions and vigorously stirred for 24 h. A sample of 3 mL was withdrawn and filtered using a 0.45 μm PTFE syringe filter. Using UV/Vis, c_e was measured and q_e was calculated (*vide supra*).

3. Results and discussion

3.1. Material synthesis

Due to the need for larger quantities of Na[BIm₄] in this study, an up-scaled synthesis protocol was developed that produces almost 200 g of Na[BIm₄] in high purity in one batch. The procedures reported in literature so far, (Chao and Moore, 1978; Hamilton et al., 2003) describe charging a flask with Na[BH₄] and an excess of imidazole, then heating the reaction mixture until H₂ evolution ceases. This formation of gaseous co-product raises severe safety concerns in larger batches, as per gram of Na[BH₄], over 2 L of flammable hydrogen gas are produced. To allow for better reaction control, in this study a fed-batch operation mode was employed, where small portions of Na[BH₄] are continuously fed into molten imidazole at elevated temperatures. As opening the reactor and manual addition of borohydride leads to loss of imidazole, a lab-scale snail extruder was used instead, which guarantees continuous addition of reagent in a closed environment. After purification, the product Na[BIm₄] is obtained in high purity and almost quantitative yield.

For the preparation of the IL [EMIM][BIm₄], a common salt-metathesis with Na[BIm₄] and [EMIM]Cl in EtOH was used (precipitation of NaCl). As with most ILs prepared *via* this method, a residual NaCl impurity was detected in the elemental analysis after this step. For further purification, the crude product was dissolved in hot 1-BuOH and insoluble NaCl was removed *via* filtration. Interestingly, the use of *n*-butanol proved crucial in this step, as more polar solvents, like isopropanol, do not lead to the precipitation of NaCl. Less polar solvents, like acetonitrile, on the other hand, also precipitate traces of Na[BIm₄] and this leads to an excess of [EMIM]Cl in solution. After drying [EMIM][BIm₄] *in vacuo*, the absence of NaCl was confirmed by elemental analysis. Furthermore, ¹H-NMR spectroscopy showed an [EMIM] to [BIm₄] ratio of 1:1 and confirmed the absence of organic impurities.

For the preparation of the porous BNC adsorbent materials from [EMIM][BIm₄], a salt-templating method, originally published by Fechler et al. (Fechler et al., 2013; Fechler et al., 2014) was used. An eutectic mixture of NaCl and ZnCl₂ served as the porogen. This approach was necessary as pyrolysis of pure [EMIM][BIm₄] only yielded non-porous materials. This result is not surprising, as literature suggests a need for polymerizable nitrile functionalities on either the IL cation or the IL anion for self-templating processes towards porous pyrolysis products. (Paraknowitsch and Thomas, 2012; Zhang et al., 2015) [EMIM][BIm₄] obviously lacks those functionalities and therefore the IL requires external templating.

In a first step, the IL was simply mixed with the salts in a beaker under elevated temperatures until a homogeneous paste was obtained. This IL/template mixture was transferred to porcelain crucibles and pyrolyzed under inert gas. During pyrolysis, the eutectic mixture of inorganic salts melts and forms an inorganic matrix. This matrix mixes with the organic IL to give heteroatom-doped carbons under pyrolysis conditions. After carbonization, the template was removed with dilute HCl, NaOH and H₂O. All materials were obtained as shiny black powders in mass yields of approximately 35%.

3.2. Material characterization

The bulk elemental analyses (EA & ICP) of BNCs are summarized in Table 1. Interestingly, EA also detected hydrogen and oxygen. Because these values closely match the stoichiometry of water and only insignificant amounts of oxygen bonds were found by other analytic methods

Table 1
Bulk elemental composition in wt% and sum formula of BNC materials prepared in this study.

Sample	C (wt%)	N (wt%)	B (wt%)	Sum formula ^a	H, O (wt%) ^b
BNC-800	53.4	21.7	2.8	C ₁₇ N ₆ B	2.6, 19.5
BNC-900	68.3	12.0	1.6	C ₃₈ N ₂ B	2.0, 16.1
BNC-1000	74.7	8.2	2.1	C ₃₂ N ₃ B	1.7, 13.3

^a calculated from bulk elemental analysis, rounded to full integers and normalized to boron ^b attributed to adsorbed water, included for completeness.

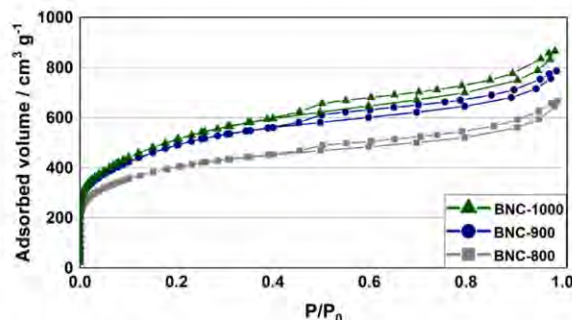


Fig. 1. N₂ sorption isotherms of BNCs pyrolyzed at different temperatures.

(*vide infra*), these amounts were mainly attributed to adsorbed water on the surface of the porous samples.

Generally, all samples show a high degree of N and B doping, with a decrease in doping with higher pyrolysis temperatures. With an increase of temperature, only a small change in absolute boron content can be observed, whereas nitrogen drastically decreases and carbon increases. This result is in accordance with investigations on the pyrolysis of tetracyanoborate-ILs by Fellingner et al. (Fellingner et al., 2012) At temperatures close to 1000 °C, the thermodynamically stable B-N bond stabilizes nitrogen bonded to boron, while imidazole units undergo rearrangements and cross-linking reactions towards carbonaceous materials. Nitrogen bonded exclusively to carbon can be lost as HCN or alkylcyanides during this process and this reduces N doping in the final material. Remarkably, even BNC-1000 still contains more than 10 wt% of heteroatoms in its structure, which is one of the highest degrees of doping for a B/N-doped porous carbon material reported so far (see Castro-Muñiz et al. (Castro-Muñiz et al., 2017), and references therein). Furthermore, as [BIm₄]⁺ inherently provides only B-N bonds, no boron bound to carbon is expected in our BNC materials.

Nitrogen sorption/desorption experiment were conducted to investigate the porous structure of BNCs and these are depicted in Fig. 1. The specific surface areas are generally very high and materials pyrolyzed at higher temperatures show a higher S_{BET} (BNC-800, 1470 m² g⁻¹, BNC-900, 1788 m² g⁻¹). It is worth noting that BNC-1000 (1860 m² g⁻¹) approaches the maximum theoretical S_{BET} of single-layer graphene sheets (2000 m² g⁻¹). (Rao et al., 2009) As can be seen, all three materials show type I(b) isotherms, typical for materials with a wide pore size distribution in the micropore and narrow mesopore region. (Thommes et al., 2015) The observed hysteresis can be attributed to interparticle condensation. Specifically the sharp uptake in the low pressure region implies numerous micropores, which is confirmed by the pore size distributions (see Fig. S2). All BNCs display a porous network of small mesopores (< 4 nm) and micropores. Interestingly, although BNC-1000 has the highest S_{BET} , it has the lowest relative amount of micropores < 1 nm, which indicates continuous burn-off during pyrolysis, resulting in an increasing amount of micro and small mesopores, as well as an increase in specific surface area.

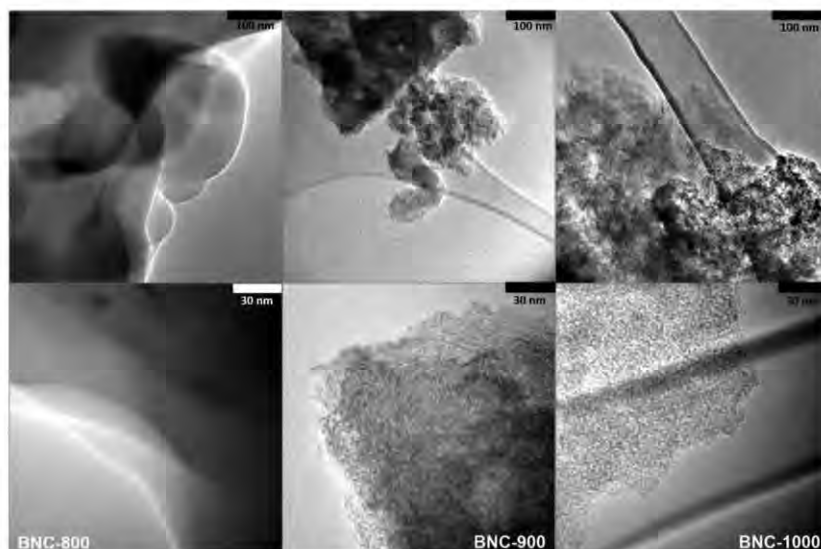


Fig. 2. TEM pictures of BNC-800 (left column), BNC-900 (middle column) and BNC-1000 (right column).

This burn-off is also observed in electron microscopy. Although the materials looked relatively similar in SEM pictures (see Fig. S3), the TEM pictures revealed significant differences in morphology, as depicted in Fig. 2. Where BNC-800 shows a 2D structure of smooth, overlapping nanosheets, BNC-900 and BNC-1000 display increasing roughness on their surface with a porous texture clearly visible. This increasing amount of defects (or holes in the sheet) originates from the evaporation of ZnCl_2 and volatile organic molecules at elevated temperatures and is most likely the reason for the higher specific surface areas of BNC-900 and BNC-1000, when compared to BNC-800.

To investigate crystallinity of BNCs, Raman spectra were recorded (see Fig. S4). Two dominant bands can be observed. The relatively broad D band at approx. 1355 cm^{-1} is assigned to asymmetric B-N domains and defective graphite. The G-band at approximately 1590 cm^{-1} is assigned to sp^2 -hybridised graphite-like structures. (Lazzarini et al., 2016, Tuinstra and Koenig, 1970, Ferrari and Robertson, 2000) Integration using a Lorentzian line shape of both bands allows for a comparison of disordered and ordered (*ergo* crystalline) domains in the material by dividing the D-band area by the G-band area (I_D/I_G). Following this, a perfect graphene sheet would have a I_D/I_G ratio of 0, as no D-band would be measurable. BNC-1000 shows the lowest I_D/I_G ratio with 1.14, which is a sign for higher degree of graphitization and crystallinity than in BNC-900 ($I_D/I_G = 1.27$) and BNC-800 ($I_D/I_G = 1.41$). This implies that higher pyrolysis temperatures (close to 1000°C) favor the burn-off of rather volatile, amorphous structures and promote the formation of sp^2 -hybridized, aromatic architectures. This observation was confirmed with XRD measurements (see Fig. S5). All three materials show two broad diffractions at 25° , corresponding to the graphite (002) plane, and at 44° , corresponding to the graphite (100) plane. Interestingly, the diffraction pattern at 25° broadens with increasing pyrolysis temperature, indicating a decrease in stacking order of BNC-sheets. In contrast, the diffraction pattern at 44° becomes more pronounced and narrow at higher temperatures. Hence, while vertical order decreases, an increase in lateral, in-plane order is observed. This shows that, although the stacking of BNC-sheets is more turbostratic at higher pyrolysis temperatures, the sheets *per se* have a more crystalline character.

To investigate chemical bonding in the bulk material, FTIR spectra were recorded (see Fig. 3). The sharp peak at 1380 cm^{-1} is assigned to in-plane vibrations of sp^2 -bonded boron nitride. The relatively broad band at

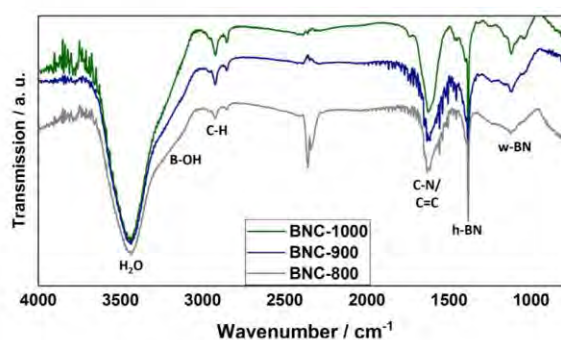


Fig. 3. FTIR spectra of BNC materials pyrolyzed at different temperatures.

1620 cm^{-1} can be ascribed to C=C and C-N stretching vibrations of the graphitic domains, nitrogen-doped in the graphitic phase and the frontier from graphitic to boron nitride domains, respectively. Both signals show that BNCs consist of a graphitic architecture, doped with single nitrogen atoms and hexagonal boron nitride (h-BN) domains. The additional bands around 2900 cm^{-1} and the shoulder around 3400 cm^{-1} can be ascribed to C-H and B-OH stretching vibrations, respectively, most likely resulting from the edges and defects of the BNC sheets. The broad band at 3400 cm^{-1} is assigned to the O-H stretching vibrations of H_2O , adsorbed on the surface of the highly porous materials. Two additional observations can be made in the FTIR spectra of BNCs. First, the characteristic B-C stretching vibration at 1020 cm^{-1} is absent. Therefore, no rearrangement at the nitrogen-bonded boron-core of $[\text{BIm}_4]^+$ takes place during pyrolysis. Second, the broad band at 1125 cm^{-1} , with additional shoulders at 1250 cm^{-1} and 1085 cm^{-1} , is characteristic for the sp^3 -bonded wurtzite structure of boron nitride (w-BN). This phase is formed under high pressure and high temperature from either hexagonal or cubic boron nitride and is still not much investigated. Interestingly, with increasing pyrolysis temperature, the w-BN band becomes more pronounced, whereas the h-BN band decreases in intensity. Therefore, a phase transformation of h-BN to w-BN during material preparation can not be excluded. (Romanos et al., 2013, Portehault et al., 2010, Chrenko, 1974, Zhang and Meng, 2019)

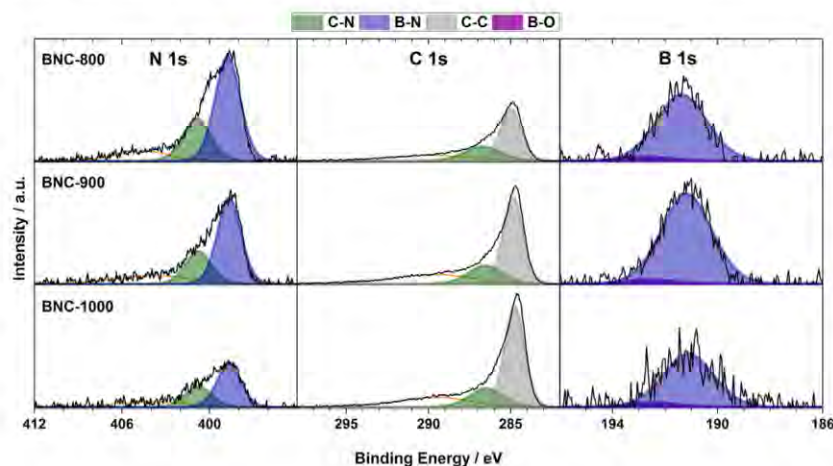


Fig. 4. XP N 1s (left), C 1s (mid) and B 1s (right) spectra of BNC-800 (first row), BNC-900 (second row), BNC-1000 (third row); intensity scales within one column are identical. Dominant signals related to C-N, B-N, and C-C species are marked in green, blue and grey, respectively, along with a small boron-oxide contribution (magenta); broad peaks (orange) at the high binding energy side of the N 1s and C 1s regions are due to satellite features of N and C atoms in an aromatic configuration. Close-ups of the respective spectra can be found in the ESI.

Table 2

Composition (relative to boron) of BNC-800, BNC-900 and BNC-1000, obtained via elemental analysis (EA) or via XPS measurements; The right column shows the atomic B:N ratio of the B-N related XPS signals (blue peaks in Fig. 4).

Sample	EA composition ^a (total sample)	XPS composition ^{b,c} (near-surface)	B: N ratio of B-N signals ^c
BNC-800	C ₁₇ N ₅ B	C ₁₇ N ₅ B	1: 3.5
BNC-900	C ₃₈ N ₇ B	C ₁₈ N ₃ B	1: 2.1
BNC-1000	C ₃₂ N ₃ B	C ₃₃ N ₃ B	1: 1.8

^a normalized to boron ^b XPS information depth of 7–9 nm ^c pure h-BN would have a B: N ratio of 1: 1, higher ratios arise from N bound to C in BNCs.

The composition and bonding configuration within the near-surface region of BNCs was investigated with X-ray photoelectron spectroscopy (XPS, information depth 7–9 nm). The XP spectra (see Fig. 4) essentially reveal the same bonding situation as FTIR according to literature binding energy (BE) values. (Hao et al., 2019) Species related to B-N (B 1s 191.2 eV, N 1s 398.7 eV), C-N (C 1s 286.6 eV, N 1s 400.8 eV) and C-C (C 1s 284.7 eV) bonds are present confirming our FTIR results that the BNC materials consist of carbon domains with boron and nitrogen incorporated. C-B bonds could be excluded, due to missing characteristic signals in C 1s (expected at 284.1 eV) and B 1s (expected at 190.4 eV). Only a very small amount of oxidized boron (192.6 eV, around 5–8 % B-O intensity relative to B-N) is visible at the high BE side of the B-N signal for the three BNC materials in XPS (see also Table S1). Note that boron-oxygen bonds have been reported in other BNC materials prepared via pyrolysis and are a result of the oxophile nature of unsaturated boron in defects. (Portehault et al., 2010) In addition, in the here investigated samples, all N 1s and C 1s spectra reveal a broad peak shifted to higher BE (orange signal in Fig. 4) that is attributed to satellites from aromatically bound carbon and nitrogen. In comparison to the overall bulk composition as given by EA, the more surface sensitive XPS analysis (integrated signal of all peaks in Fig. 4) reveals a quite good agreement of the relative C-N-B content for BNC-800 and BNC-1000 (see Table 2), in XPS, only BNC-900 shows a higher boron content relative to carbon and nitrogen determined in EA. The last column in Table 2 shows the B: N ratio of the B-N related XPS signals (blue peaks) in Fig. 4. Due to the lack of B bound to C and due to the B: N = 1: 3.5 ratio of B-N signals, we propose that in BNC-800, mainly BN₃ sites, and N at C-N sites (green peaks in Fig. 4; see also ESI Table S1) are incorporated in the carbon domains. At 900 °C, nitrogen mainly from C-N sites (and to some extent also from BN₃ sites) starts to burn off, converting carbon into C-C carbon as shown in the C-C peak increase (see grey peaks in Fig. 4), while the boron content remains more or less constant (see ESI Table S1). 1000 °C pyrolysis releases even more nitrogen but, in compar-

ison to 900 °C, also boron as shown by the drastic decreases in N 1s and B 1s intensities, again accompanied by an increased conversion into C-C carbon. The smaller B: N = 1.8 ratio of B-N signals is an indication that boron nitride configurations close to the surface are formed for BNC-1000.

3.3. Dye-removal using BNCs

With these BNC material features at hand, namely a high degree of heteroatom doping, a rough nanostructure paired with high porosity, the materials prepared in this study were tested for adsorption applications. As a model pollutant, methylene blue (MB) was chosen. This compound is a representative of the widely used, and partially carcinogenic, cationic dyes. (Tan et al., 2015) The BNC materials were investigated with regards to their adsorption kinetics, *i. e.* how fast they can adsorb a pollutant. Furthermore, their adsorption capacity, *i. e.* how much pollutant can actually be taken up, was studied. Both aspects are key performance indicators for a potential application as a sorbent material.

3.3.1. Adsorption kinetics

A fast uptake of pollutants by the adsorbent is highly desired. Therefore, all BNCs prepared in this study were tested in time-resolved adsorption experiments. Two different concentrations of MB were investigated, a moderate c_0 of 20 mg L⁻¹ and a relatively high c_0 of 100 mg L⁻¹. Samples were taken every 30 seconds (except for BNC-800 at $c_0 = 100$ mg L⁻¹ where time intervals of 1 min were used instead) and subsequently analyzed via UV/Vis. The results are depicted in Fig. 5. The first observation was that a MB concentration of 20 mg L⁻¹ was too low for these experiments, as complete decolorization occurred in less than one minute. At a higher c_0 of 100 mg L⁻¹, all three materials still showed very fast adsorption and saturation time was after approximately 5 min. The uptake curves can be divided in three phases, best

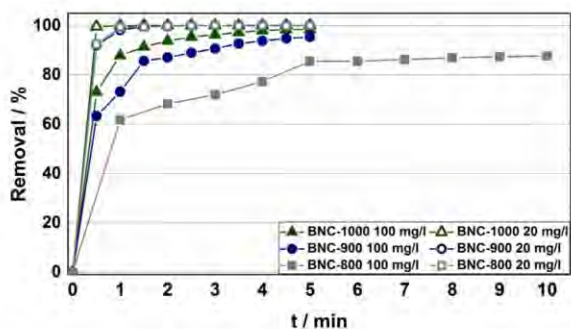


Fig. 5. Time resolved adsorption of MB on BNCs. 20 mg adsorbent, 50 mL MB solution, $c_0 = 100 \text{ mg L}^{-1}$ (full symbols), $c_0 = 20 \text{ mg L}^{-1}$ (hollow symbols), 800 rpm. Lines between data points are guidance to the eye and do not represent experimental data.

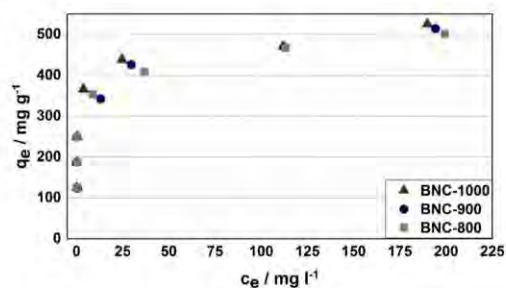
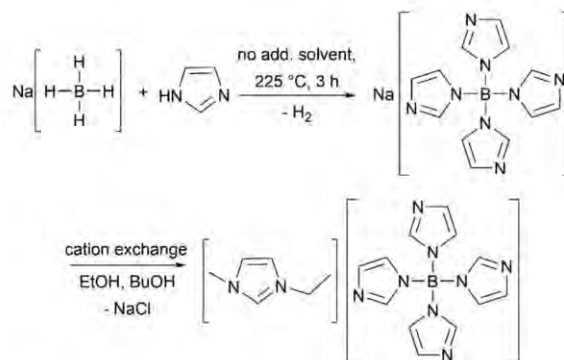


Fig. 6. Adsorption isotherms of MB on BNCs. 10 mg adsorbent, 25 mL of MB solution, 24 h. c_e measured with UV/Vis, calibrated at 663 nm. c_0 ranging from 50 mg L^{-1} up to 400 mg L^{-1} . Experiments reproduced two times and results averaged.

seen with BNC-800. In the first phase, more than 50 % of MB is adsorbed within a few seconds, due to adsorption on the outer surface of the BNC particles. In the second phase, a linear increase in adsorption occurs, due to intra-particle transport and adsorption in the pores. In the final third phase, an adsorption-desorption equilibrium establishes. BNC-1000 displays the fastest kinetics, followed by BNC-900, and the slightly slower BNC-800. This can be explained by the rough outer surface of BNC-1000, as observed in TEM, as well as its wider micropores and higher number of mesopores, allowing for easier diffusion of MB to the adsorption sites in the particle. It is important to note that complete removal of MB (>99 % adsorbed) was achieved with our BNC-1000 material, which equals a MB take-up of 0.25 g per gram of adsorbent in only 5 min.

3.3.2. Adsorption capacity

The equilibrium adsorption capacity (q_e) is a measure for the amount of adsorbate an adsorbent can remove from solution in equilibrium, given in mg (pollutant) per g (adsorbent). In this study, q_e was determined in batch sorption experiments. The prepared BNCs were mixed with stock solutions of MB of varying concentration c_0 . After 24 h of vigorous stirring, a sample was taken, analyzed via UV/Vis spectroscopy and the c_e value was calculated. The isotherm values for q_e over c_e are depicted in Fig. 6. At low concentrations of MB, q_e increases sharply for all three materials under investigation, as virtually complete decolorization of the stock solution was observed. Increasing the concentration of MB leads to the saturation of more and more adsorption sites and an adsorption-desorption equilibrium is established. The maximum adsorption capacity (q_{max}) was measured with a c_0 of 400 mg L^{-1} and exceeded 500 mg g^{-1} for all three BNC-materials (See ESI for a plot of q_e over c_0).



Scheme 1. Synthesis of [EMIM][BIm₄].

To the best of our knowledge, this is the highest adsorption capacity reported for MB on boron nitride or boron nitride-doped carbon-materials (see Table 3). It is an interesting fact that only small differences in q_{max} can be observed for all three BNCs under investigation, with BNC-1000 showing approximately 10 mg g^{-1} and 25 mg g^{-1} higher capacity than BNC-900 and BNC-800, respectively. It is known from literature, that three factors mainly determine the adsorptive properties of nanomaterials. (El-Mahdy et al., 2020, Smith and Rodrigues, 2015, Li et al., 2018) First, a high specific surface area, because a higher surface also implies a higher number of adsorption sites. As all materials prepared in this study show very high, but slightly different specific surface areas, this factor could explain the higher q_{max} of BNC-1000. Second, sufficient pore-size, as obviously, pores smaller than the adsorbate molecule can not serve as host for the adsorption process. A higher level architecture of meso- or macropores allows for easier transport of sorbent molecules to active adsorption sites. Most pores of the BNC materials reported here are larger than the length and width of MB (14.2 \AA and 5.4 \AA , respectively), therefore, the pore-size of BNCs seems not to be a restricting factor. The third and most interesting factor influencing adsorptive properties is the surface functionalization of the adsorbent. MB is an organic molecule with a large aromatic ring structure, therefore π - π interactions are highly relevant for adsorption. Boron nitride, as well as graphitic domains, both present in the materials studied here, provide an extensive aromatic system for π - π stacking with MB, explaining the high capacity of the BNCs materials.

3.3.3. Adsorption isotherm fitting

To investigate possible adsorption mechanisms and a theoretical maximum adsorption capacity, the equilibrium capacity data were non-linearly fitted with three different isotherm models, the Langmuir, the Freundlich and the Brouers-Sotolongo isotherm model (see Section 2.5 for details). To quantify the fit quality of a given model, the R^2 value was calculated and compared (see Table 4). Detailed graphs of the respective fits are depicted in Fig. S6a-c. According to the calculated correlation coefficient, the Langmuir isotherm model is the least suitable to describe adsorption of MB on BNCs with R^2 values of approximately 0.62 up to 0.92. Additionally, the q_{max} predicted by this model lies below the experimental value for all three materials, implying multi-layer adsorption of MB.

The Freundlich and Brouers-Sotolongo isotherm models both show higher values for R^2 , ranging from approximately 0.89 to 0.93 and 0.87 to 0.96, respectively. Both models describe complex multilayer sorption on heterogeneous surfaces and both appear to accurately predict the adsorption of MB on BNCs. Interestingly, the constant α in the Brouers-Sotolongo isotherm model, *i. e.* the measure for the energy heterogeneity of the surface, increases from BNC-800 over BNC-900 to BNC-1000. An increase in α is caused by two factors. (Selmi et al., 2018) First,

Table 3
Maximum adsorption capacity for MB on boron nitride based nanomaterials reported in literature.

Adsorbent	q_{\max} for MB / mg g^{-1}	Refs.
BNC-800	501	this study
BNC-900	514	this study
BNC-1000	525	this study
Norit® CN 1 decolorizing charcoal	285 ^a	(FisherScientific 2020)
Boron nitride nanosheets (BNNS)	333	(Bangari and Sinha, 2020)
Porous BNNS	313	(Lei et al., 2013)
h-BN	54	(Guo et al., 2019)
h-BN	392	(Li et al., 2015)
Porous BNNS	413 ^b	(Li et al., 2018)
BN nanocarbons	272 ^b	(Zhang et al., 2012)

^a commercial decolorizing charcoal, purchased from Acros, Lot: A0390150;

^b values obtained from the Langmuir adsorption isotherm, no experimental values for q_{\max} were reported in the original publications.

Table 4
Langmuir, Freundlich and Brouers-Sotolongo isotherm model parameters for MB adsorption on BNCs (25°C, 10 mg BNC, 25 mL MB solution). Data points nonlinearly fitted with Origin 2019.

Sample	Langmuir			Freundlich			Brouers-Sotolongo			
	q_{\max} (mg g^{-1})	K_L (L mg^{-1})	R (Su et al., 2013)	K_F	n	R (Su et al., 2013)	q_{\max} (mg g^{-1})	K_W	α	R (Su et al., 2013)
BNC-800	440	2.6	0.83	236.6	6.9	0.92	618	0.49	0.23	0.93
BNC-900	435	2.2	0.62	231.8	6.5	0.89	528	0.59	0.27	0.87
BNC-1000	463	3.5	0.92	261.0	7.3	0.93	508	0.79	0.32	0.96

an increase in specific surface area and widening of pores, which could already be observed in N_2 -sorption experiments with the BNCs under investigation. Second, α increases as the surface functionality decreases. As seen in XPS analysis, BNC-800 shows the highest and BNC-1000 shows the lowest degree of B and N doping in its surface. An increase in α in the adsorption experiments, therefore, agrees with the results from material characterization.

3.3.4. Influence of pH on adsorption

A change in the pH value of an adsorbate solution also changes the surface charge of a suspended adsorbent. As electrostatic interactions are one of the main driving forces for adsorption, the pH value is one of the key factors to tune the adsorption properties of a material. (Yu et al., 2018) BNC-1000 shows a very high capacity for MB at neutral pH, so we were interested, if at a certain pH value this property would change. A pH range from 2 to 10 with a c_0 of 100 mg L^{-1} was investigated and the results are depicted in Figure S8. Note, that for these experiments a lower adsorbent loading than for the adsorption isotherm experiments was chosen, so generally, a higher q_e can be expected.

Starting from acidic conditions, pH 2 to pH 6, BNC-1000 already shows very high capacity with 400 mg g^{-1} . In neutral to basic conditions, up to pH 10, the capacity slightly increases to 416 mg g^{-1} . An increase in pH beyond this point of zero charge leads to a negatively charged surface. An increase in adsorption capacity for the cationic dye MB at higher pH is therefore not surprising. Remarkably, no displacement of MB by H^+ occurs at low pH values, so ion-exchange and electrostatic interactions seem to play only a minor role in the adsorption on BNCs, which makes π - π stacking on the aromatic surface very likely the dominant mode of interaction. Thus, BNCs have high capacity for contaminants over a very wide range of pH. This means that effective adsorption is possible independent of the acidity or basicity of the solution.

4. Conclusions

The new ionic liquid [EMIM][Bim₄] was synthesized and used for the preparation of heteroatom-doped 2D carbon sheets via salt-templated pyrolysis. An increase in pyrolysis temperature led to burn-off of amor-

phous domains and gave more crystalline but turbostratic materials with high specific surface areas of up to $1860 \text{ m}^2 \text{ g}^{-1}$. Chemical analyses showed a high degree of heteroatom-doping with isolated nitrogen atoms and boron nitride domains incorporated into the graphitic material structure. With the prepared nanomaterials the adsorption of the industrial dye methylene blue from wastewater was investigated. Decolorization of even concentrated stock solutions was observed in less than 5 minutes, and with over 500 mg g^{-1} , the highest adsorption capacity reported so far for this class of materials was observed. Our results reveal that BNC sheets prepared from new [Bim₄]⁺ ionic liquids are highly promising candidates for applications in technical adsorption. Moreover, we anticipate that their structural properties will also make them very interesting for the use as catalysts or catalyst supports.

Conflicts of interest

There are no conflicts to declare.

Notes and references

† Powdered $\text{Na}[\text{BH}_4]$, as opposed to the granular form used here, leads to a sudden and violent formation of large volumes of the gaseous by-product H_2 and should therefore be avoided.

Acknowledgements

The authors like to acknowledge support by the Deutsche Forschungsgemeinschaft (DFG, German Research Foundation) in the frame of the SPP 1708 (Project-ID 237028221) and SFB 1452 (Project-ID 431791331).

Supplementary materials

Supplementary material associated with this article can be found, in the online version, at doi:10.1016/j.jil.2021.100004.

References

Titirici, M.-M., White, R.J., Brun, N., Budarin, V.L., Su, D.S., del Monte, F., Clark, J.H., MacLachlan, M.J., 2015. Chem. Soc. Rev. 44, 250–290.

- Su, D.S., Perathoner, S., Centi, G., 2013. *Chem. Rev.* 113, 5782–5816.
- Zhao, S., Wang, D.-W., Amal, R., Dai, L., 2019. *Adv. Mater.* 31, 1801526.
- Jariwala, D., Sangwan, V.K., Lauhon, L.J., Marks, T.J., Hersam, M.C., 2013. *Chem. Soc. Rev.* 42, 2824–2860.
- Liang, C., Li, Z., Dai, S., 2008. *Angew. Chem. Int. Ed.* 47, 3696–3717.
- Pacula, A., Uosaki, K., Socha, R.P., Bielańska, E., Pietrzyk, P., Zimowska, M., 2016. *Electrochim. Acta* 212, 47–58.
- Mombeshora, E.T., Jarvis, A.L.L., Ndungu, P.G., Doyle, B.P., Carleschi, E., Nyamori, V.O., 2017. *Mater. Chem. Phys.* 199, 435–453.
- Yao, Y., Zhang, B., Shi, J., Yang, Q., 2015. *ACS Appl. Mater. Interfaces* 7, 7413–7420.
- Paraknowitsch, J.P., Thomas, A., Schmidt, J., 2011. *Chem. Commun.* 47, 8283–8285.
- Luo, Y., Yang, Z., Guo, W., Chen, H., Wang, T., Liu, Y., Lyu, Y., Luo, H., Dai, S., 2020. *J. Mater. Chem. A* 8, 4740–4746.
- Yang, S.J., Rothe, R., Kirchhecker, S., Esposito, D., Antonietti, M., Gojzewski, H., Fehler, N., 2015. *Carbon* 94, 641–645.
- Chaudhari, K.N., Song, M.Y., Yu, J.-S., 2014. *Small* 10, 2625–2636.
- Gao, L., Li, R., Sui, X., Li, R., Chen, C., Chen, Q., 2014. *Environ. Sci. Technol.* 48, 10191–10197.
- Paraknowitsch, J.P., Thomas, A., 2012. *Macromol. Chem. Phys.* 213, 1132–1145.
- Zhang, S., Dokko, K., Watanabe, M., 2015. *Mater. Horiz.* 2, 168–197.
- Wang, X., Dai, S., 2010. *Angew. Chem. Int. Ed.* 49, 6664–6668.
- Chen, A., Yu, Y., Lv, H., Wang, Y., Shen, S., Hu, Y., Li, B., Zhang, Y., Zhang, J., 2013. *J. Mater. Chem. A* 1, 1045–1047.
- Zhang, S., Zhang, J., Zhang, Y., Deng, Y., 2017. *Chem. Rev.* 117, 6755–6833.
- Fellinger, T.-P., Su, D.S., Engenhorst, M., Gautam, D., Schlögl, R., Antonietti, M., 2012. *J. Mater. Chem.* 22, 23996–24005.
- Lee, J.S., Wang, X., Luo, H., Baker, G.A., Dai, S., 2009. *J. Am. Chem. Soc.* 131, 4596–4597.
- Precht, M.H.G., Scholten, J.D., Dupont, J., 2009. *J. Mol. Catal. A Chem.* 313, 74–78.
- Drab, D.M., Kelley, S.P., Shamshina, J.L., Smiglak, M., Cococar, O.A., Gurau, G., Rogers, R.D., 2012. *Sci. China Chem.* 55, 1683–1687.
- Kuzmina, O., Hassan, N.H., Patel, L., Ashworth, C., Bakis, E., White, A.J.P., Hunt, P.A., Welton, T., 2017. *Dalton Trans.* 46, 12185–12200.
- Zhu, X., Hillesheim, P.C., Mahurin, S.M., Wang, C., Tian, C., Brown, S., Luo, H., Veith, G.M., Han, K.S., Hagaman, E.W., Liu, H., Dai, S., 2012. *ChemSusChem* 5, 1912–1917.
- Paraknowitsch, J.P., Zhang, J., Su, D., Thomas, A., Antonietti, M., 2010. *Adv. Mater.* 22, 87–92.
- She, Y., Lu, Z., Ni, M., Li, L., Leung, M.K.H., 2015. *ACS Appl. Mater. Interfaces* 7, 7214–7221.
- Jeong, J.H., Lee, J.S., Roh, K.C., Kim, K.-B., 2017. *Nanoscale* 9, 14672–14681.
- Paraknowitsch, J.P., Zhang, Y., Wienert, B., Thomas, A., 2013. *Chem. Commun.* 49, 1208–1210.
- Panchakarla, L.S., Subrahmanyam, K.S., Saha, S.K., Govindaraj, A., Krishnamurthy, H.R., Waghmare, U.V., Rao, C.N.R., 2009. *Adv. Mater.* 21, 4726–4730.
- Inagaki, M., Toyoda, M., Soneda, Y., Morishita, T., 2018. *Carbon* 132, 104–140.
- Abbas, Q., Raza, R., Shabbir, L., Olabi, A.G., 2019. *J. Sci.: Adv. Mater. Devices* 4, 341–352.
- Gouse Peera, S., Kwon, H.-J., Lee, T.G., Hussain, A.M., 2020. *Ionics* 26, 1563–1589.
- Han, R., Liu, F., Wang, X., Huang, M., Li, W., Yamauchi, Y., Sun, X., Huang, Z., 2020. *J. Mater. Chem. A* 8, 14384–14399.
- Chen, Y., Fu, L., Liu, Z., Wang, Y., 2016. *ChemCatChem* 8, 1782–1787.
- Ohtani, H., Ishimura, S., Kumai, M., 2008. *Anal. Sci.* 24, 1335–1340.
- Paraknowitsch, J.P., Thomas, A., 2017. *Chem. Synth. Appl. Graphene Carbon Mater.* 21–42. doi:10.1002/9783527648160.ch2.
- Fulvio, P.F., Lee, J.S., Mayes, R.T., Wang, X., Mahurin, S.M., Dai, S., 2011. *PCCP* 13, 13486–13491.
- Aijaz, A., Akita, T., Yang, H., Xu, Q., 2014. *Chem. Commun.* 50, 6498–6501.
- Ranjbar Sahraie, N., Paraknowitsch, J.P., Göbel, C., Thomas, A., Strasser, P., 2014. *J. Am. Chem. Soc.* 136, 14486–14497.
- SciFinder®. The choice for chemistry research™. <https://scifinder.cas.org> 2021
- Bernhardt, E., Finze, M., Willner, H., 2003. *Zeitschrift für anorganische und allgemeine Chemie* 629, 1229–1234.
- Zhang, J., Wu, T., Feng, P., Bu, X., 2010. *Dalton Trans.* 39, 1702–1704.
- Galvelis, R., Slater, B., Cheetham, A.K., Mellot-Drazniak, C., 2012. *CrystEngComm* 14, 374–378.
- Zheng, S., Wu, T., Zhang, J., Chow, M., Nieto, R.A., Feng, P., Bu, X., 2010. *Angew. Chem. Int. Ed.* 49, 5362–5366.
- Chao, S., Moore, C.E., 1978. *Anal. Chim. Acta* 100, 457–467.
- Hamilton, B.H., Kelly, K.A., Malasi, W., Ziegler, C.J., 2003. *Inorg. Chem.* 42, 3067–3073.
- Fechler, N., Fellingner, T.-P., Antonietti, M., 2013. *Adv. Mater.* 25, 75–79.
- Niedermaier, I., Kolbeck, C., Steinrück, H.-P., Maier, F., 2016. *Rev. Sci. Instrum.* 87, 045105.
- Langmuir, I., 1918. *J. Am. Chem. Soc.* 40, 1361–1403.
- Freundlich, H., 1907. *Zeitschrift für Physikalische Chemie* 57U, 385–470.
- Brouers, F., Sotolongo, O., Marquez, F., Pirard, J.P., 2005. *Physica A* 349, 271–282.
- Ncibi, M.C., Altener, S., Seffen, M., Brouers, F., Gaspard, S., 2008. *Chem. Eng. J.* 145, 196–202.
- Altener, S., Carene, B., Emmanuel, E., Lambert, J., Ehrhardt, J.-J., Gaspard, S., 2009. *J. Hazard. Mater.* 165, 1029–1039.
- Fechler, N., Tiruye, G.A., Marcilla, R., Antonietti, M., 2014. *RSC Adv.* 4, 26981–26989.
- Castro-Muñiz, A., Nishihara, H., Hirota, T., Ohwada, M., Li, L.-X., Tsuda, T., Kuwabata, S., Maruyama, J., Kyotani, T., 2017. *Chem. Commun.* 53, 13348–13351.
- Rao, C.N.R., Sood, A.K., Subrahmanyam, K.S., Govindaraj, A., 2009. *Angew. Chem. Int. Ed.* 48, 7752–7777.
- Thommes, M., Kaneko, K., Neimark, A.V., Olivier, J.P., Rodriguez-Reinoso, F., Rouquerol, J., Sing, K.S.W., 2015. *Pure Appl. Chem.* 87, 1051–1069.
- Lazzarini, A., Piovano, A., Pellegrini, R., Agostini, G., Rudic, S., Lamberti, C., Groppo, E., 2016. *Physics Procedia* 85, 20–26.
- Tuinstra, F., Koenig, J.L., 1970. *J. Chem. Phys.* 53, 1126–1130.
- Ferrari, A.C., Robertson, J., 2000. *Phys. Rev. B* 61, 14095–14107.
- Romanos, J., Beckner, M., Stalla, D., Tekeci, A., Suppes, G., Jalisatgi, S., Lee, M., Hawthorne, F., Robertson, J.D., Firle, L., Kuchta, B., Wexler, C., Yu, P., Pfeifer, P., 2013. *Carbon* 54, 208–214.
- Portehault, D., Giordano, C., Gervais, C., Senkova, I., Kaskel, S., Sanchez, C., Antonietti, M., 2010. *Adv. Funct. Mater.* 20, 1827–1833.
- Chrenko, R.M., 1974. *Solid State Commun.* 14, 511–515.
- Zhang, X., Meng, J., 2019. *Ultra-Wide Bandgap Semiconductor Materials*. Elsevier, pp. 347–419. doi:10.1016/B978-0-12-815468-7.00004-4 eds. M. Liao, B. Shen and Z. Wang.
- Hao, Q., Song, Y., Mo, Z., Mishra, S., Pang, J., Liu, Y., Lian, J., Wu, J., Yuan, S., Xu, H., Li, H., 2019. *ACS Sustainable Chem. Eng.* 7, 3234–3242.
- Tan, K.B., Vakili, M., Horri, B.A., Poh, P.E., Abdullah, A.Z., Salamatinia, B., 2015. *Sep. Purif. Technol.* 150, 229–242.
- El-Mahdy, A.F.M., Zakaria, M.B., Wang, H.-X., Chen, T., 2020. *Y. Yamauchi and S.-W. Kuo. J. Mater. Chem. A* doi:10.1039/D0TA07281H.
- Smith, S.C., Rodrigues, D.F., 2015. *Carbon* 91, 122–143.
- Li, L., Sun, F., Gao, J., Wang, L., Pi, X., Zhao, G., 2018. *RSC Adv.* 8, 14488–14499.
- FisherScientific, <https://www.fishersci.com/shop/products/carbon-activated-norit-cn-1-acros-organics-2/AC404042500>, accessed November 2020.
- Bangari, R.S., Sinha, N., 2020. *J. Nanosci. Nanotechnol.* 20, 6222–6234.
- Lei, W., Portehault, D., Liu, D., Qin, S., Chen, Y., 2013. *Nat. Commun.* 4, 1777.
- Guo, Y., Wang, R., Wang, P., Rao, L., Wang, C., 2019. *ACS Sustainable Chem. Eng.* 7, 5727–5741.
- Li, J., Huang, Y., Liu, Z., Zhang, J., Liu, X., Luo, H., Ma, Y., Xu, X., Lu, Y., Lin, J., Zou, J., Tang, C., 2015. *J. Mater. Chem. A* 3, 8185–8193.
- Li, J., He, S., Li, R., Dai, W., Tao, J., Wang, C., Liu, J., Wu, T., Tang, C., 2018. *RSC Adv.* 8, 32886–32892.
- Zhang, X., Lian, G., Zhang, S., Cui, D., Wang, Q., 2012. *CrystEngComm* 14, 4670–4676.
- Selmi, T., Seffen, M., Sammouda, H., Mathieu, S., Jagiello, J., Celzard, A., Fierro, V., 2018. *Adsorption* 24, 11–27.
- Yu, S., Wang, X., Pang, H., Zhang, R., Song, W., Fu, D., Hayat, T., Wang, X., 2018. *Chem. Eng. J.* 333, 343–360.

Electronic Supplementary Information (ESI)

B/N doped carbon sheets from a new ionic liquid with excellent sorption properties for methylene blue

Julian Mehler,^a Matthias Ermer,^b Ulrike Paap,^c Bettina S. J. Heller,^c Florian Maier,^c Hans-Peter Steinrück,^c Martin Hartmann,^b Carsten Korte,^d Peter S. Schulz*^a and Peter Wasserscheid^{a,e}

^aInstitute of Chemical Reaction Engineering, Friedrich-Alexander University Erlangen-Nürnberg, 91058 Erlangen, Germany. E-mail: peter.schulz@fau.de

^bErlangen Center for Interface Research and Catalysis (ECRC), Friedrich-Alexander University Erlangen-Nürnberg, 91058, Erlangen, Germany.

^cChair of Physical Chemistry II, Friedrich-Alexander-University Erlangen-Nürnberg, 91058 Erlangen, Germany.

^dForschungszentrum Jülich, Institute of Energy and Climate Research – Fuel Cells (IEK-14), 52425 Jülich, Germany.

^eForschungszentrum Jülich, Helmholtz-Institute Erlangen-Nürnberg for Renewable Energy (IEK 11), 91058 Erlangen, Germany

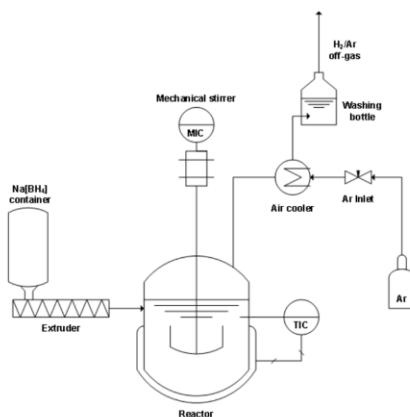


Figure S1: Flowsheet of a glass reactor for the up-scaled synthesis of Na[Blm₄]

Chemical analyses and confirmation of purity:

NMR:

All qualitative NMR spectra were recorded on a JEOL ECX 400 MHz instrument. Chemical shifts are reported relative to the peak of SiMe₄, using ¹H-(residual) chemical shifts of the solvent as a secondary standard and are reported in ppm. Sample temperature was approximately 20 °C. ¹H-NMR scans were conducted with an excitation frequency of 399.72 MHz and 8 scans. ¹¹B-NMR spectra were recorded with an excitation frequency of 128.23 MHz and 32 scans. ¹³C-NMR spectra were recorded with an excitation frequency of 100.51 MHz and 250 scans.

EA:

The bulk carbon, hydrogen, nitrogen, sulfur and oxygen contents of [EMIM][Blm₄] and carbonaceous materials were determined *via* elemental analysis in an elemental UNICUBE®. For C/H/N/S measurements, the samples were combusted at 1150 °C in an oxygen 5.0 atmosphere. Subsequent reduction of NO_x gases to N₂ was performed at 850 °C on a Cu contact. For analysis, a TCD (C/H/N) and IR-detector (S) were used. To determine the O content, the samples were reduced to CO with a large excess of graphite at 1150 °C and subsequently analyzed in a TCD. For all measurements, helium was used as a carrier gas.

DSC:

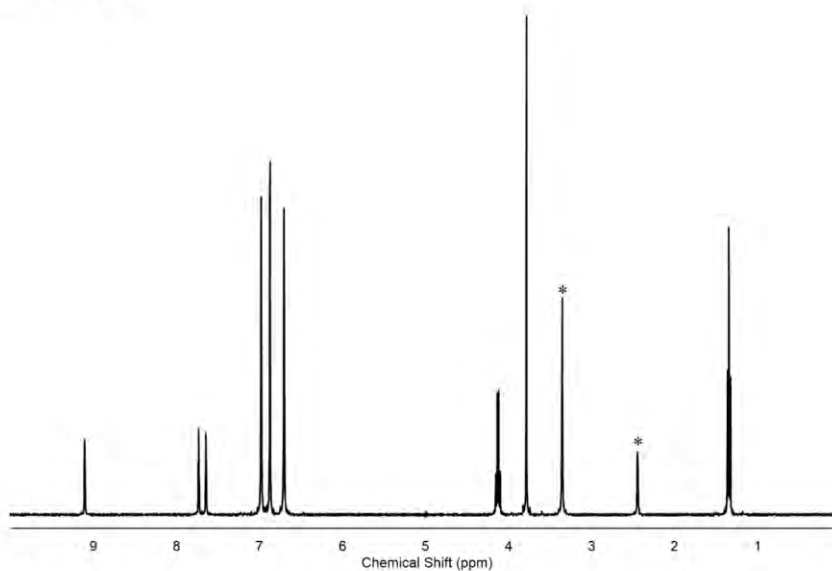
The DSC measurements were performed with a computer-controlled Phoenix DSC 204 F1 thermal analyzer from Netzsch. A small amount of sample was placed into an aluminium crucible and sealed. The samples were then heated to 100 °C with a heating ramp of 5 K min⁻¹. The melting point was determined from the heating process to avoid supercooling phenomena during cool-down. An empty sample pan with a small hole in the lid served as the reference. To avoid condensation of water, the instrument was purged with dry nitrogen.

TGA:

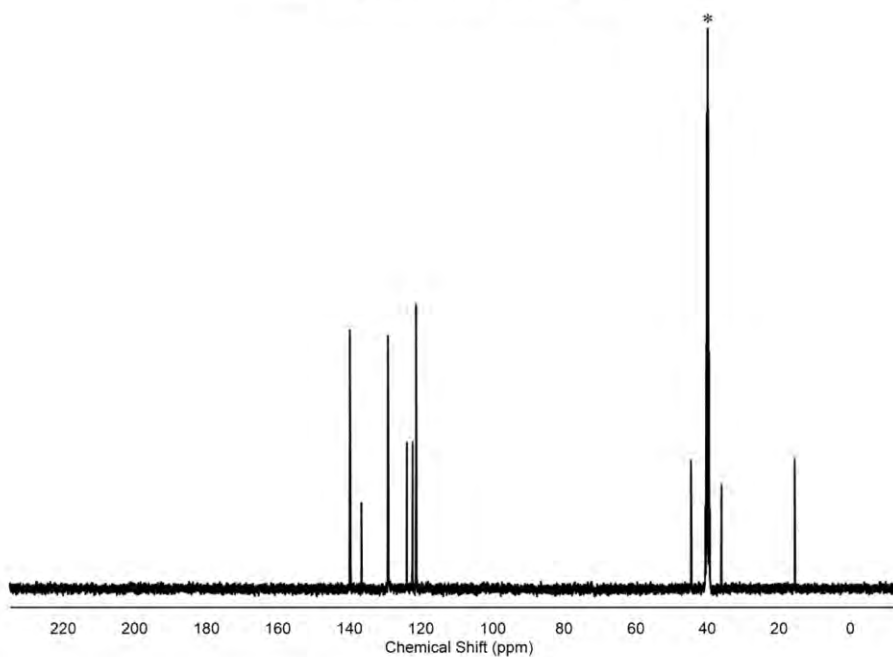
To determine the thermal stability of [EMIM][Blm₄], a Setsys Evolution from Setaram was used. Approximately 25 mg of sample were placed in a Quartz crucible and heated to 400 °C under a nitrogen

atmosphere with a flowrate of 50 mL min⁻¹. The heating ramp was 2 K min⁻¹. The initial decomposition temperature was then determined via the Onset-method.

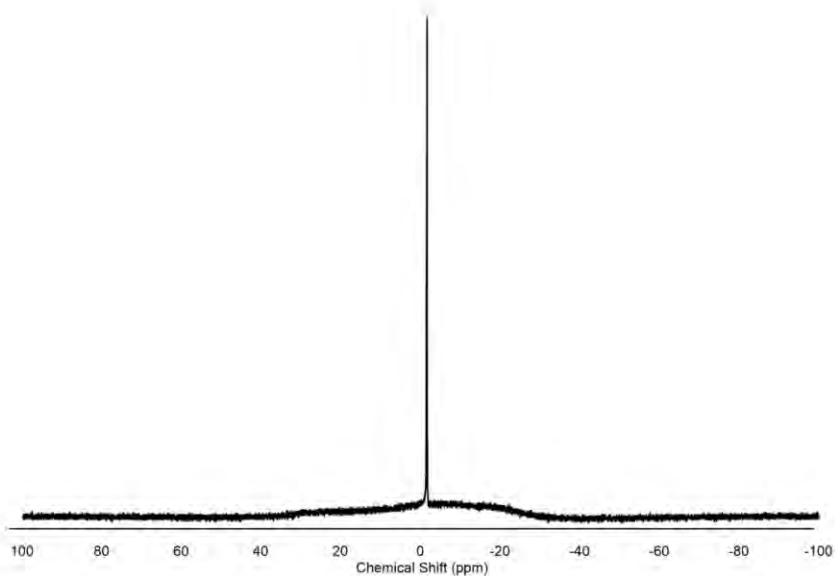
[EMIM][BIm₄]:



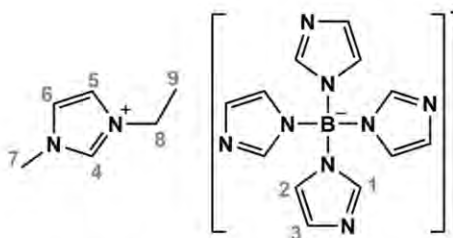
¹H-NMR of [EMIM][BIm₄], DMSO-d₆ as solvent.



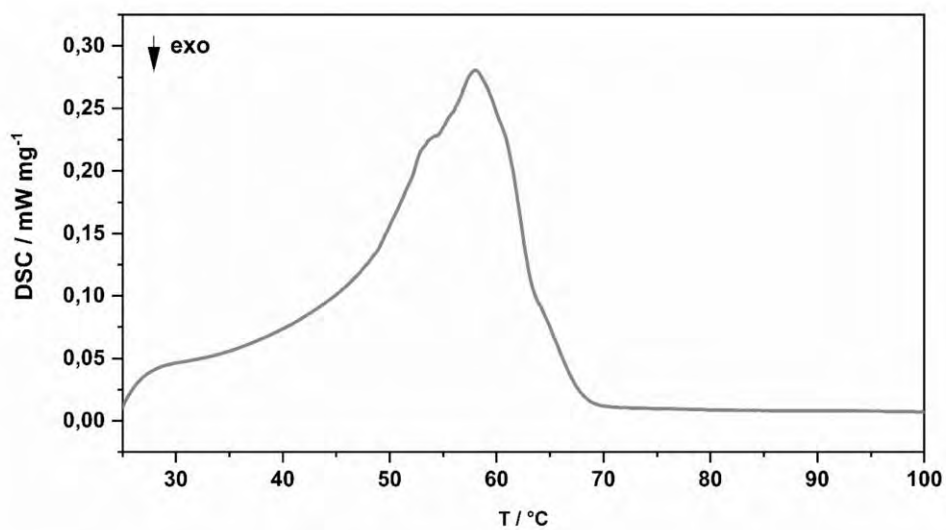
¹³C-NMR of [EMIM][BIm₄], DMSO-d₆ as solvent.



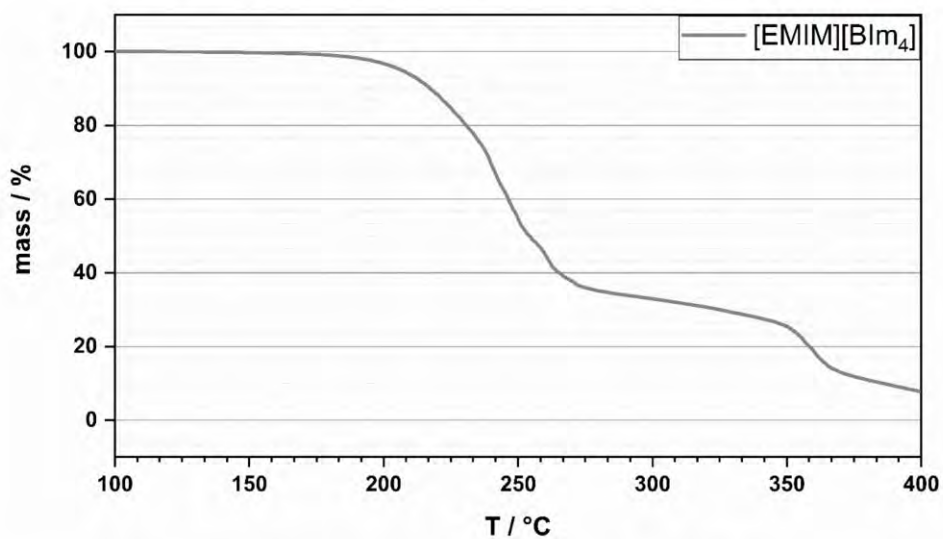
¹¹B-NMR of [EMIM][BIm₄], DMSO-d₆ as solvent. Please note that the wide, underlying signal arises from B in the borosilicate glass NMR tube.



¹ H-NMR	(400 MHz, DMSO-d ₆ , ppm): δ = 9.11 (s, 1H, 4), 7.74 (s, 1H, 5), 7.64 (s, 1H, 6), 6.99 (s, 4H, 1), 6.88 (s, 4H, 2), 6.71 (s, 4H, 3), 4.15 (q, 2H, 8), 3.79 (s, 3H, 7), 1.35 (t, 3H, 9).
¹³ C-NMR	(100 MHz, DMSO-d ₆ , ppm): δ = 139.94 (4C, 1), 136.78 (1C, 4), 129.37 (4C, 2), 124.09 (1C, 6), 122.50 (1C, 5), 121.51 (4C, 3), 44.64 (1C, 8), 36.22 (1C, 7), 15.63 (1C, 9).
¹¹ B-NMR	(128 MHz, DMSO-d ₆ , ppm) δ = -1.59 (1B).
EA:	calculated wt%: C: 55.40, H: 5.94, N: 35.89. found wt%: C: 55.35, H: 5.93, N: 35.81.
KF:	H ₂ O-content wt%: < 0.1 wt%.
TG:	T _{onset} °C: 213 °C.
m.p.:	57 °C.

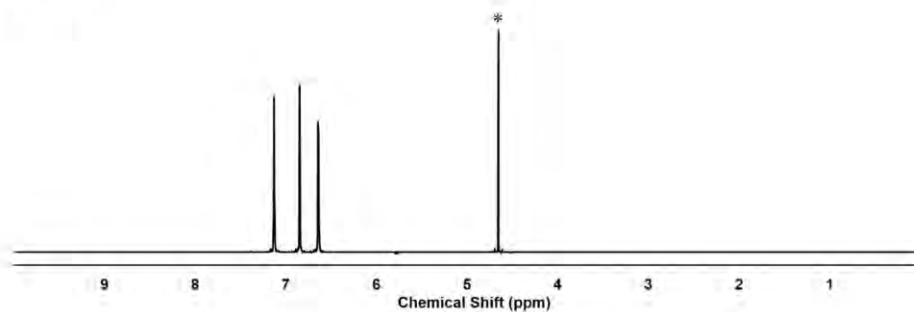


DSC thermogram of [EMIM][BIm₄] during heating from room temperature to 100 °C at 5 K min⁻¹.

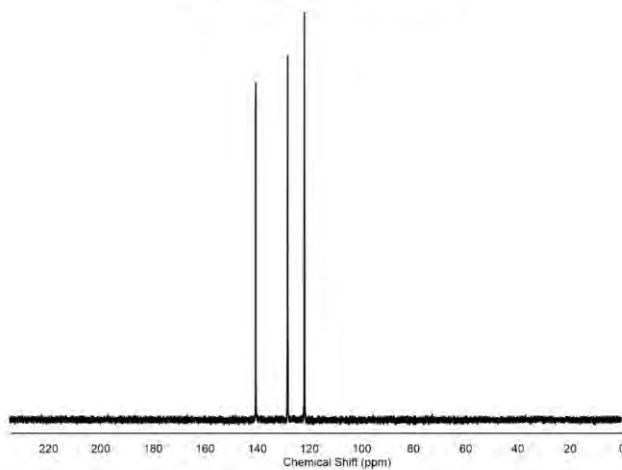


Ramped temperature TGA (2 K min⁻¹, quartz crucible) of [EMIM][BIm₄].

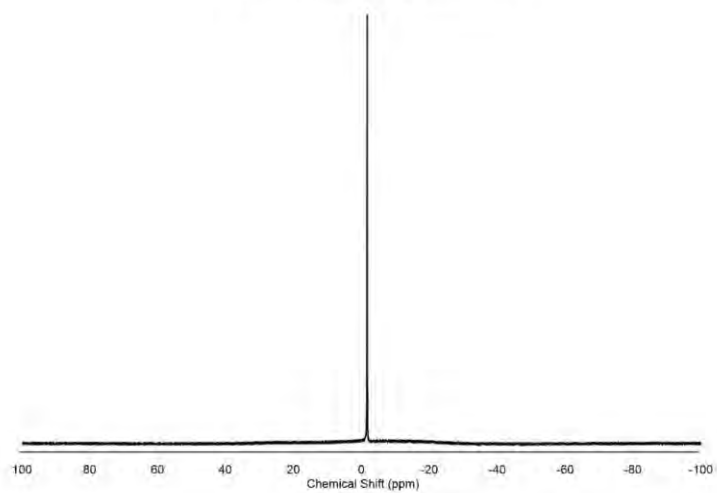
Na[BIm₄]:



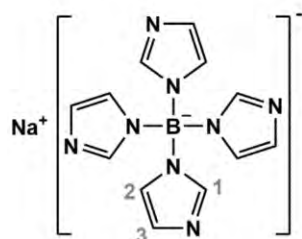
¹H-NMR of Na[BIm₄], D₂O as solvent.



¹³C-NMR of Na[BIm₄], D₂O as solvent.



¹¹B-NMR of Na[BIm₄], D₂O as solvent.



¹H-NMR (400 MHz, D₂O, ppm): δ= 7.13 (s, 4H, **1**), 6.85 (s, 4H, **2**), 6.65 (s, 4H, **3**).

¹³C-NMR (100 MHz, D₂O, ppm): δ= 140.70 (4C, **1**), 128.43 (4C, **2**), 122.04 (4C, **3**).

¹¹B-NMR (128 MHz, D₂O, ppm) δ= -1.61 (1B).

EA: calculated wt%: C: 47.71; H: 4.11; N: 37.09.
found wt%: C: 47.53; H: 4.11; N: 37.18.

Pore-size distribution:

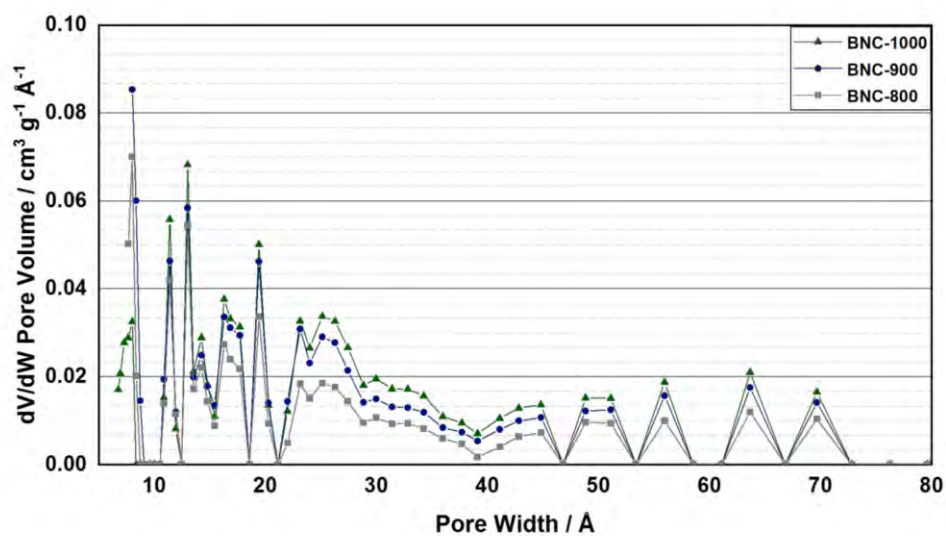


Figure S2: Pore size distribution of BNCs pyrolyzed at different temperatures.

SEM pictures:

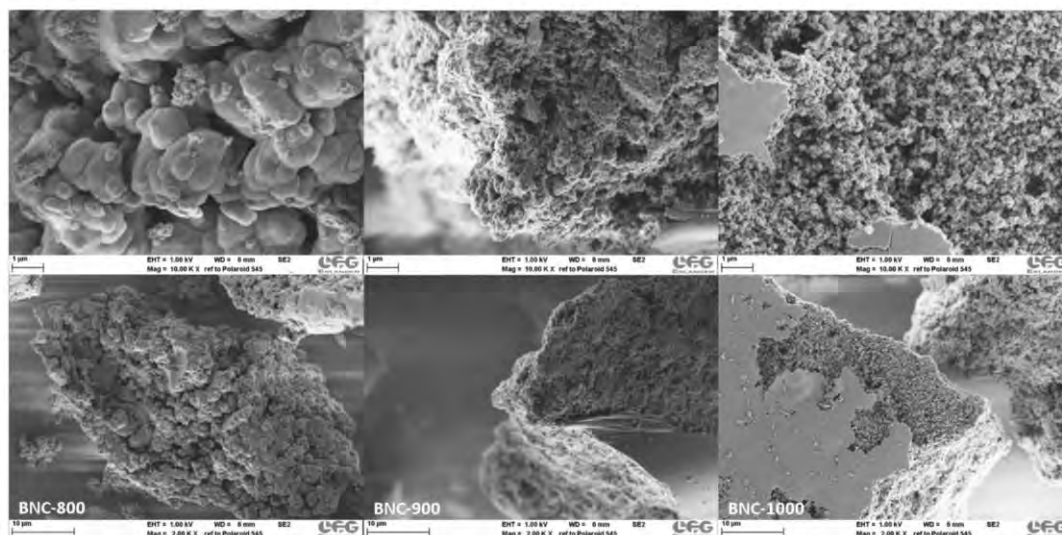


Figure S3: Scanning electron microscopy pictures of BNC-800 (left column), BNC-900 (middle column) and BNC-1000 (right column).

Raman spectra:

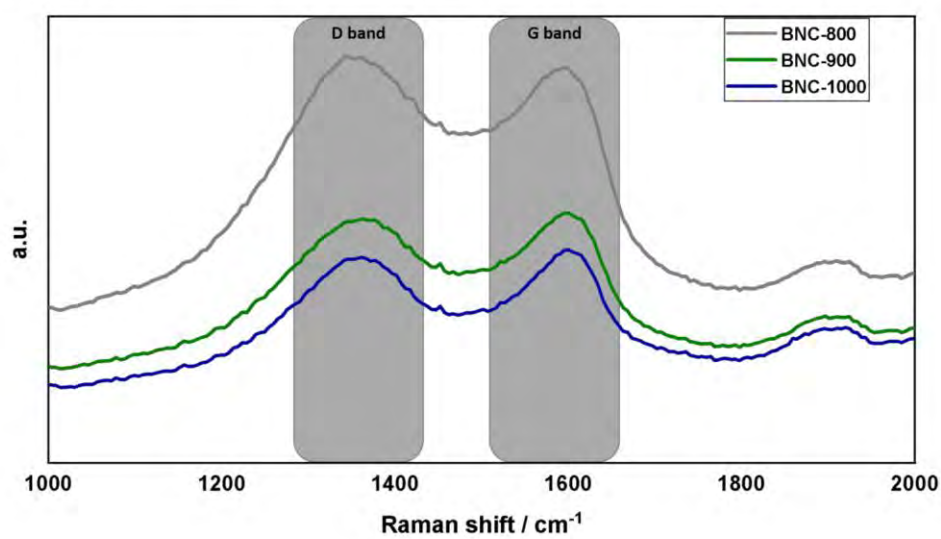


Figure S4: Raman spectra of BNC materials.

X-ray diffraction:

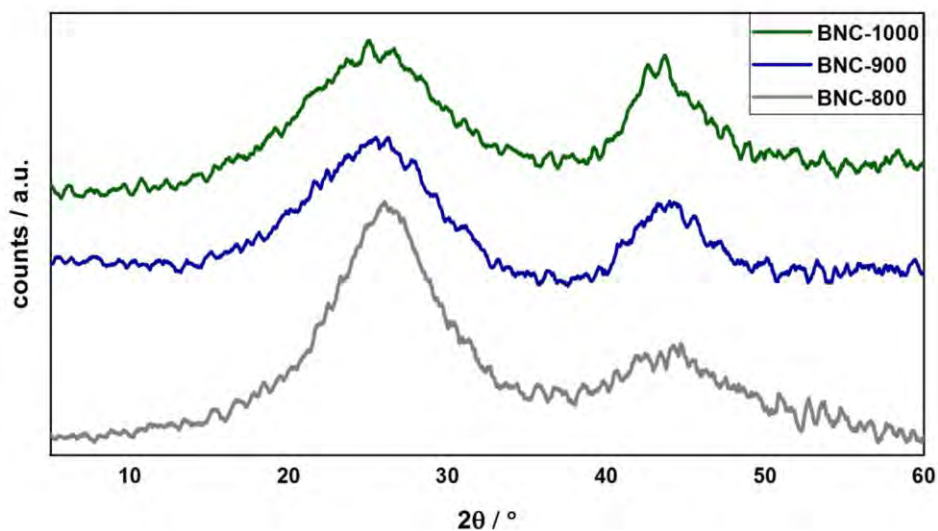


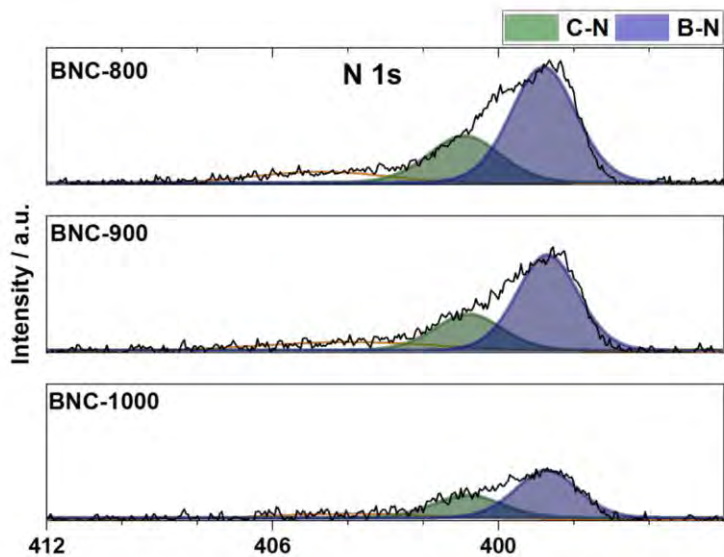
Figure S5: X-ray diffraction patterns of BNC materials.

XPS

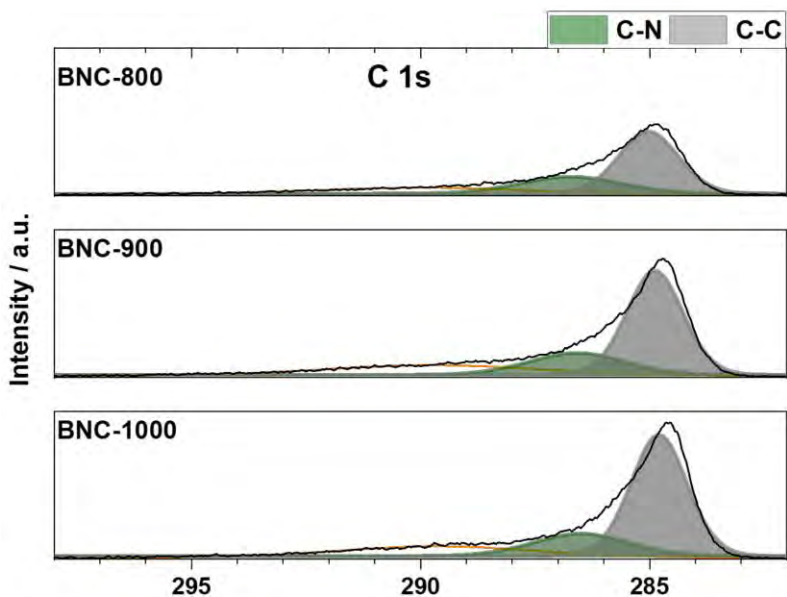
Table S1: Measured atomic composition of BNC materials in XPS.

		N(C-N)	N(B-N)	C(C-N)	C(C-C)	B(B-N)	B(B-O)
BNC-800	at-%	6.9	15.5	23.1	49.8	4.4	0.3
	at-%	22.4		72.9		4.4	0.3
	N:C:B	5.1		16.5		1.0	0.1
BNC-900	at-%	4.0	9.5	21.6	60.2	4.5	0.2
	at-%	13.5		81.8		4.5	0.2
	N:C:B	3.0		18.2		1.0	0.0
BNC-1000	at-%	2.6	4.9	21.4	68.2	2.7	0.2
	at-%	7.5		89.6		2.7	0.2
	N:C:B	2.8		33.3		1.0	0.1

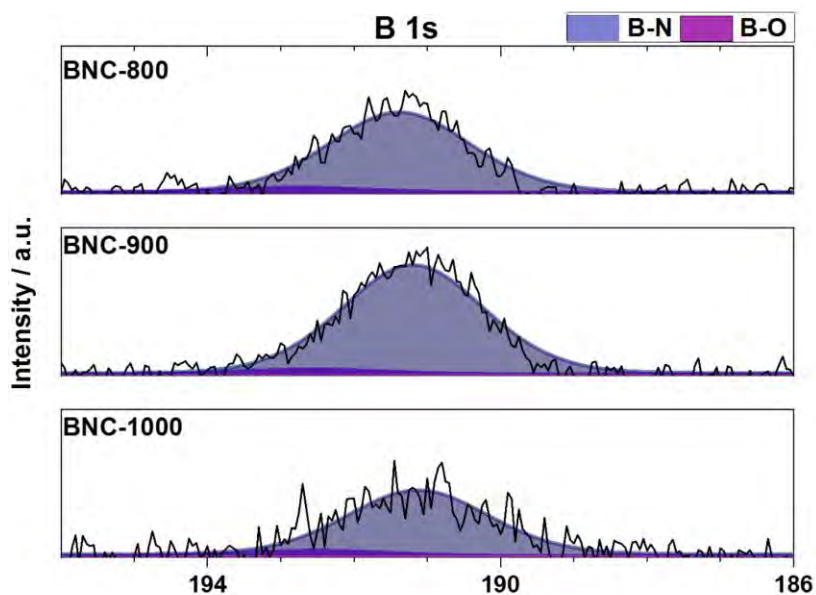
Close-Ups of Figure 4:



XP N 1s spectra of BNC-800 (first row), BNC-900 (second row), BNC-1000 (third row); intensity scales within one column are identical. Dominant signals related to C-N and B-N species are marked in green and blue, respectively; broad peaks (orange) at the high binding energy side are due to satellite features of N and C atoms in an aromatic configuration.



XP C 1s spectra of BNC-800 (first row), BNC-900 (second row), BNC-1000 (third row); intensity scales within one column are identical. Dominant signals related to C-N and C-C species are marked in green and grey, respectively; broad peaks (orange) at the high binding energy side are due to satellite features of N and C atoms in an aromatic configuration.

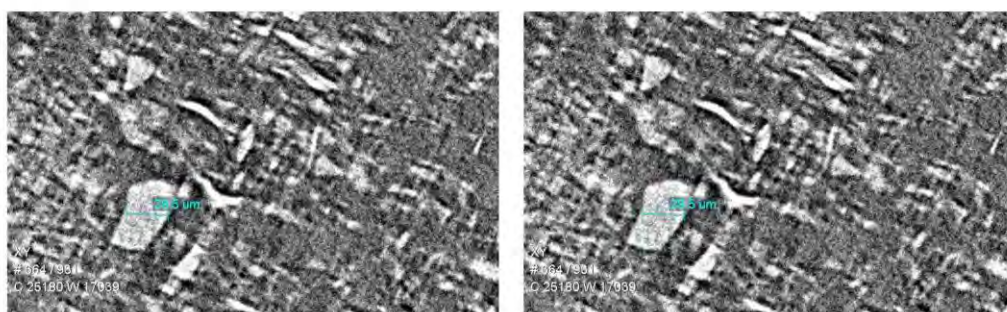


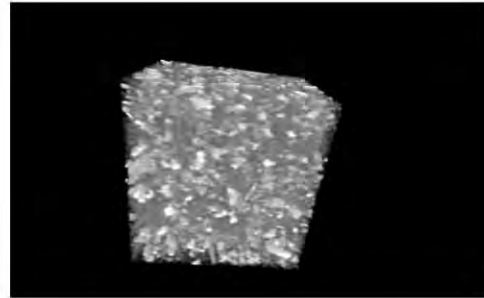
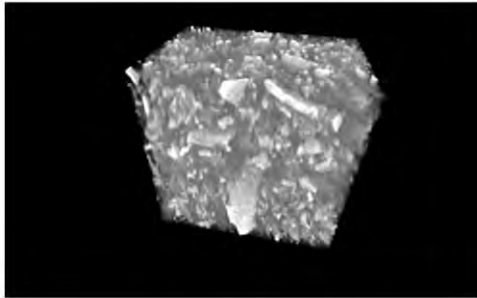
XP B 1s spectra of BNC-800 (first row), BNC-900 (second row), BNC-1000 (third row); intensity scales within one column are identical. Dominant signals related to B-N are marked in blue along with a small boron-oxide contribution (magenta).

C-nanotomography

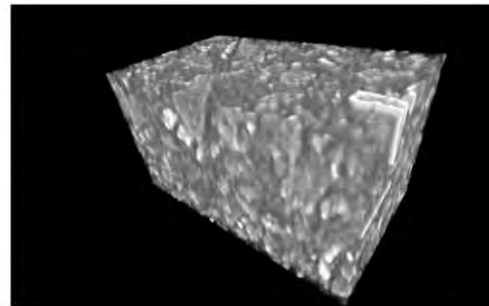
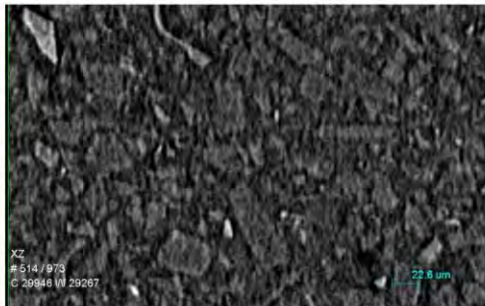
BNCs were investigated using a Bruker 410 Versa. An x-ray tube with a Mo anode was used and the acceleration voltage was adjusted to 140 kV (10 W). The fluorescence screen intermediate image is optically magnified by a x40 lens. 3001 projections were taken to perform the 3-D reconstruction, each with a exposure time of 15 s, respectively.

BNC-800:

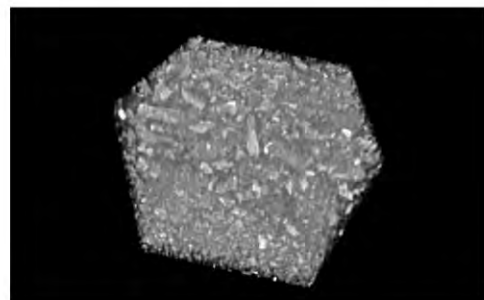
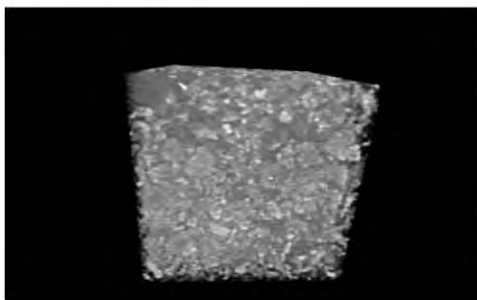
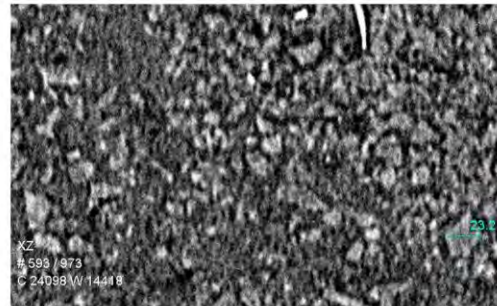
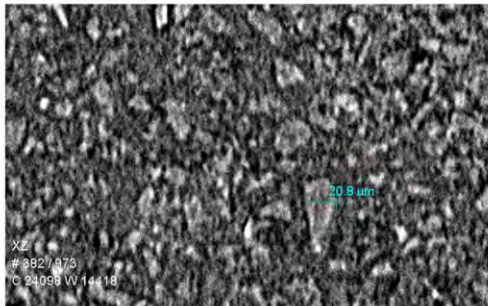




BNC-900



BNC-1000



Adsorption Isotherm Fits:

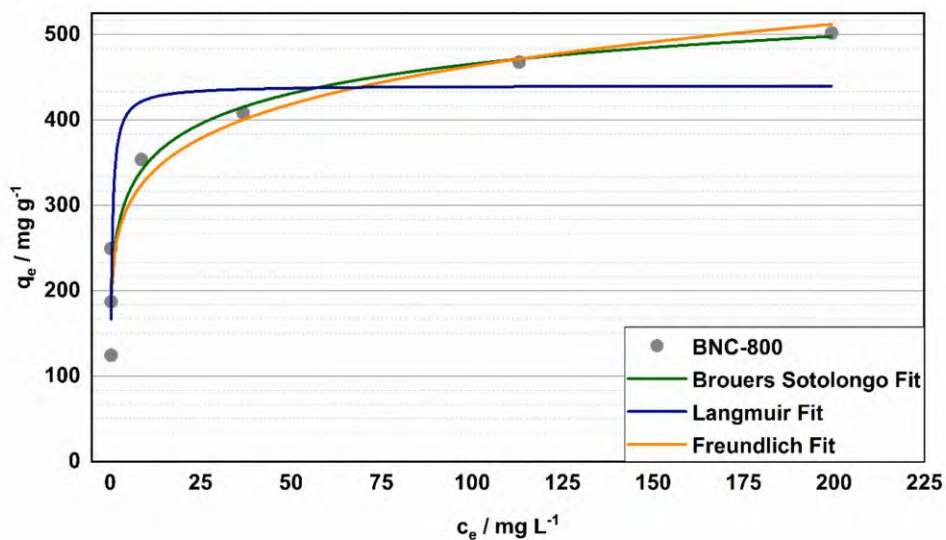


Figure S6a: Adsorption Isotherm Fits of BNC-800.

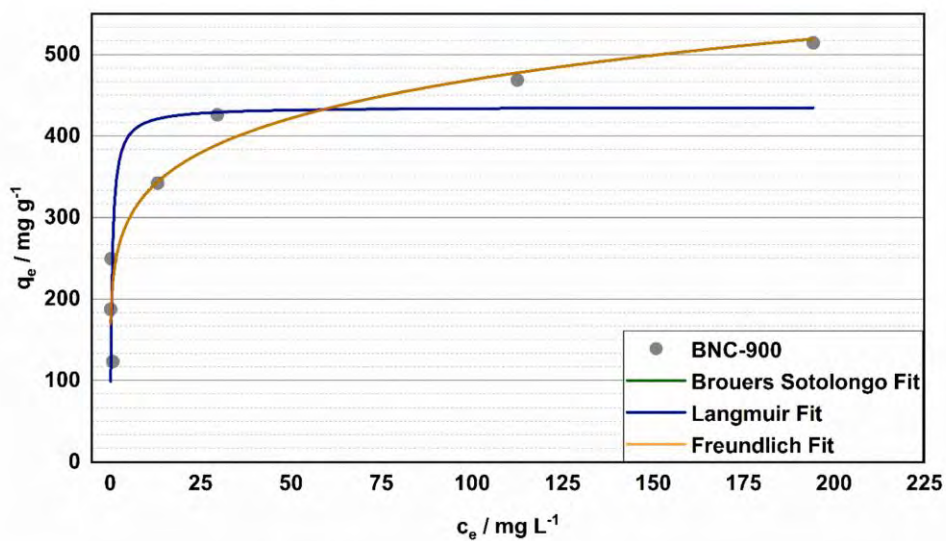


Figure S6b: Adsorption Isotherm Fits of BNC-900.

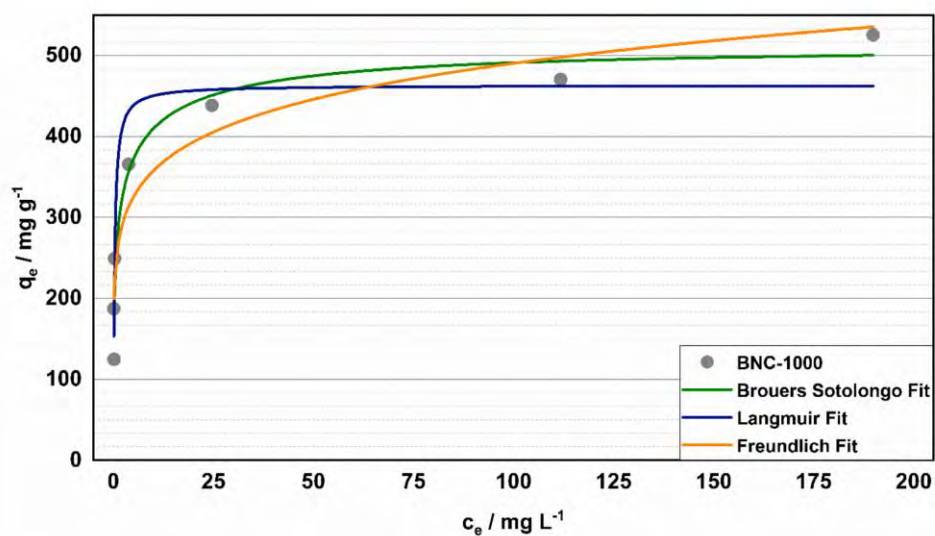


Figure S6c: Adsorption Isotherm Fits of BNC-1000.

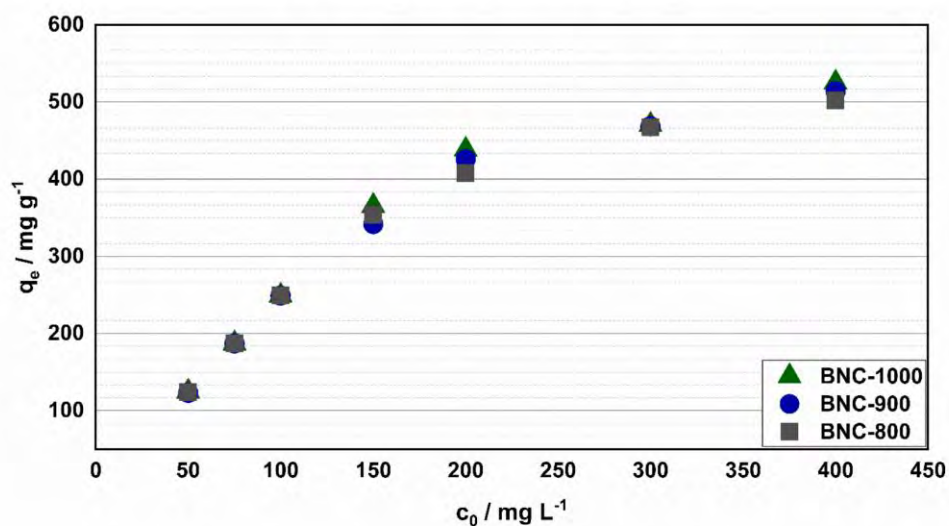


Figure S7: Values calculated for q_e at varying c_0 of MB. 10 mg adsorbent, 25 mL of MB solution, 24 h. c_e measured with UV/Vis, calibrated at 663 nm. Experiments reproduced two times and results averaged.

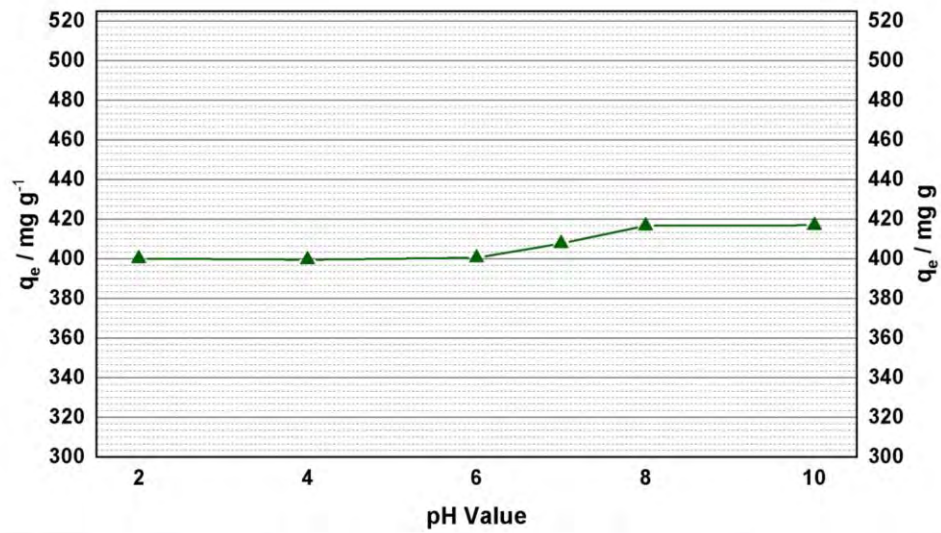


Figure S8: Adsorption capacity of BNC-1000 at varying pH value of solution. 10 mg adsorbent, 50 mL of MB solution, $c_0 = 100 \text{ mg L}^{-1}$, 24 h. Lines between data points are guidance to the eye and do not represent experimental data.

8.2. DENSITY CALCULATIONS OF MIXTURES

In [P3], as well as in this thesis (see Table 2, Chapter 3.2.2), the ideal densities of the $[\text{C}_8\text{C}_1\text{Im}][\text{PF}_6] / [(\text{mPEG}_2)_2\text{Im}]\text{I}$ mixtures with 4.5, 9.6, 19.4, and 49.8 mol% $[\text{C}_8\text{C}_1\text{Im}][\text{PF}_6]$ content were calculated according to the following simplified relation:^[131]

$$\rho_{mix}(T) = \rho_1(T) \cdot \chi_1 + \rho_2(T) \cdot (1 - \chi_1) \quad (\text{A1})$$

Here, $\rho_1(T)$ and $\rho_2(T)$ correspond to the temperature-dependent densities of the individual pure ILs and χ_1 is the respective mole fraction belonging to the density $\rho_1(T)$.

Equation A1 is the most simple approach, but yields correct values only for an ideal mixture if the two components have the same (or very similar) mole volumes, which is a good approximation for $[\text{C}_8\text{C}_1\text{Im}][\text{PF}_6] / [(\text{mPEG}_2)_2\text{Im}]\text{I}$ mixtures (see also Table A2).

A generally valid equation for any ideal homogeneous two-component mixture can be formulated based on the used weights m_i of the individual components i and their known density values $\rho_i(T)$:^[131,132]

$$\rho_{mix}(T) = \frac{m_1 + m_2}{V_1 + V_2} = \frac{m_1 + m_2}{\frac{m_1}{\rho_1(T)} + \frac{m_2}{\rho_2(T)}} \quad (\text{A2})$$

To demonstrate that the use of Equation A1 is justified and leads to correct results for the here studied systems, a direct comparison of the mixture densities derived either by Equation A1 or by A2 is shown in Table A2 (weight values are provided in Table A1). Indeed, the deviations are only noticeable in the third to fourth decimal place, and thus, the use of Equation A1 has no significant impact on the resulting mixture densities as well as on the derived surface tension values over the entire temperature range. Note that the surface tension resulting from the PD analysis scales proportionally with the used mass density, see Appendix 8.3.

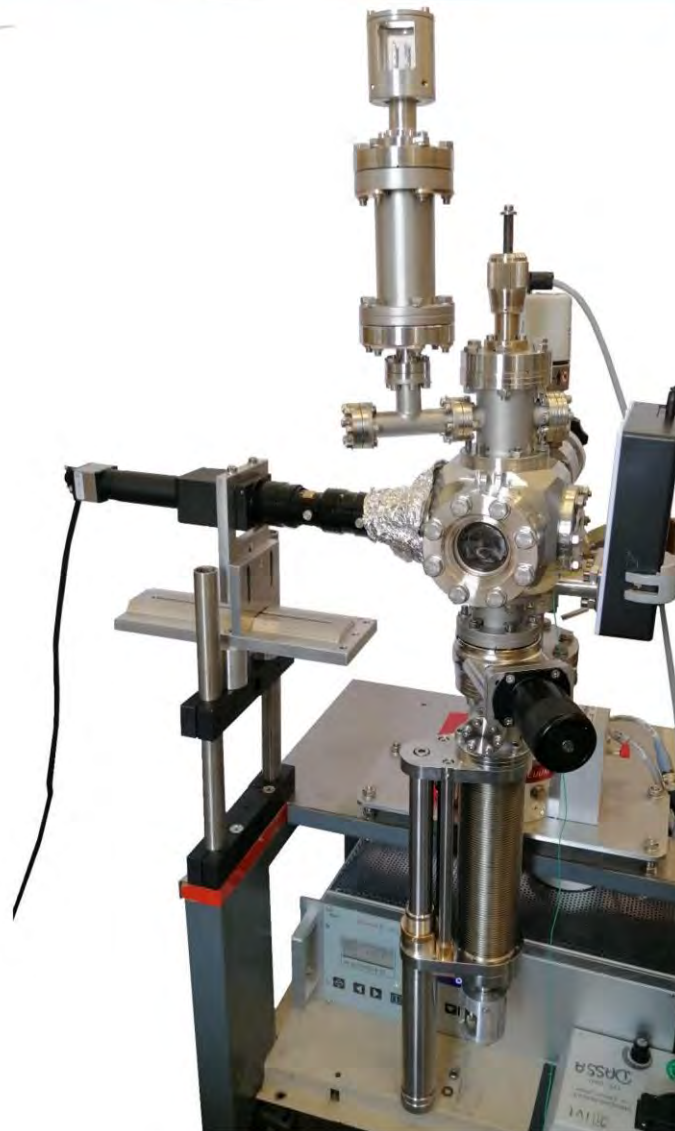
Table A1: Weights of $[C_8C_1Im][PF_6]$ (molar mass: 340.2 g/mol) and $[(mPEG_2)_2Im]I$ (403.1 g/mol) used for the 4.5, 9.6, 19.4 and 49.8 mol% mixtures. The last column shows the solidification temperatures of the corresponding mixtures as indicated by the onset of sample charging in ARXPS. Adapted from [P3] under license CC BY 4.0.

	$[C_8C_1Im][PF_6]$ [g]	$[(mPEG_2)_2Im]I$ [g]	Solidification Temperature [K]
4.5 mol%	0.0424	1.0486	237
9.6 mol%	0.2476	2.7352	235
19.4 mol%	0.1624	0.7992	231
49.8 mol%	1.0257	1.2193	230

Table A2: Temperature-dependent density parameters for pure $[C_8C_1Im][PF_6]$ and $[(mPEG_2)_2Im]I$ with references. Mixtures densities containing 4.5, 9.6, 19.4 and 49.8 mol% $[C_8C_1Im][PF_6]$ are calculated according to Equations A1 or A2. The densities at different temperatures are determined as $\rho(T) = \rho_0 + \rho_1 \cdot T + \rho_2 \cdot T^2$. In addition, the room temperature density values are also provided for a direct comparison (corresponding mole volume at room temperature $V_m(298\text{ K}) = M/\rho(298\text{ K})$ of pure $[C_8C_1Im][PF_6]$ is $340.3\text{ g}\cdot\text{mol}^{-1}/1.239\text{ g}\cdot\text{l}^{-1} = 275\text{ l/mol}$ and $400.3\text{ g}\cdot\text{mol}^{-1}/1.414\text{ g}\cdot\text{l}^{-1} = 283\text{ l/mol}$ of pure $[(mPEG_2)_2Im]I$). Adapted from [P3] under license CC BY-NC 4.0.

	Equa- tion	ρ_0 [g/cm ³]	ρ_1 [g/cm ³ ·K]	ρ_2 [g/cm ³ ·K ²]	$\rho_{298\text{ K}}$ [g/cm ³]	Devia- tion %
$[C_8C_1Im][PF_6]$ ^[101]		1.61	-1.59·10 ⁻³	1.21·10 ⁻⁶	1.2392	
49.8 mol%	A1	1.65	-1.30·10 ⁻³	7.39·10 ⁻⁷	1.3271	0.102
	A2	1.64	-1.31·10 ⁻³	7.79·10 ⁻⁷	1.3284	
19.4 mol%	A1	1.69	-1.24·10 ⁻³	6.40·10 ⁻⁷	1.3801	0.058
	A2	1.70	-1.25·10 ⁻³	6.46·10 ⁻⁷	1.3809	
9.6 mol%	A1	1.71	-1.22·10 ⁻³	6.07·10 ⁻⁷	1.3973	0.032
	A2	1.71	-1.23·10 ⁻³	6.11·10 ⁻⁷	1.3978	
4.5 mol%	A1	1.72	-1.21·10 ⁻³	5.91·10 ⁻⁷	1.4062	0.017
	A2	1.72	-1.22·10 ⁻³	5.93·10 ⁻⁷	1.4064	
$[(mPEG_2)_2Im]I$ ^[P1]		1.72	-1.20·10 ⁻³	5.70·10 ⁻⁷	1.4141	

8.3. MANUAL



Manual
High Vacuum
PENDANT DROP and SESSILE DROP

from
Bernd Krefß & Ulrike Paap

Table of contents

1.	Theory and Basics.....	2
1.1	Surface Free Energy.....	2
1.2	Young-Laplace Equation.....	3
1.3	Axisymmetric Drop Shape Analysis (ADSA).....	5
1.4	Young Equation.....	8
2.	Overview Chamber.....	9
3.	Pendant Drop (PD).....	10
3.1	Setup.....	10
3.2	Mounting Pendant Drop.....	11
3.3	Image Recording and Data Evaluation.....	12
4.	Sessile Drop (SD).....	17
4.1	Setup.....	17
4.2	Imaging Recording and Data Evaluation.....	18
5.	Z-shift Connection to DASSA.....	20
6.	Calibration and First Results.....	22
6.1	Image Acquisition.....	22
6.2	Calibration.....	22
6.3	First Results.....	24
7.	Problems and Solutions.....	25
7.1	Wires in Cannula.....	25
7.2	Water Problem.....	25
7.3	Bubble Formation and Degassing.....	25
7.4	Viton Seal.....	26
7.5	Cannula Size.....	27
8.	Bibliography.....	28
9.	Drawings and Data Sheets.....	30
9.1	Chamber Setup.....	30
9.2	Reservoir, Stamp, Cannula.....	34
9.3	Sessile Drop.....	41
9.3.1	Sample Holder.....	44
9.3.2	Data Sheet pBN Heater.....	51

Operating video and software user video can be found with the manual on the external PD/SD hard disk.

1. Theory and Basics

1.1 Surface Free Energy

Surface tension (ST) can be represented as the difference between the energies of molecules (or atoms) placed at the surface and in the bulk.^[1-4] The interactions in the bulk phase (type A) can be described in terms of a pair interaction energy W_{AA} . When a pure liquid or solid is in equilibrium with its vapor and the interaction energies are assumed to be pairwise additive, the energy $E_{A,b}$ per molecule in the bulk phase can be described as

$$E_{A,b} = \frac{Z_b}{2} W_{AA} \quad (1)$$

where Z_b is the number of nearest neighbors in the bulk phase. Correspondingly, molecules at the surface

$$E_{A,s} = \frac{Z_s}{2} W_{AA} \quad (2)$$

with Z_s being the number of nearest neighbors of a surface molecule. The movement of a molecule from the bulk to a newly created surface increases the internal energy, because W_{AA} is negative and $Z_b > Z_s$. This means that non-volumetric work must be done to create a new surface. Consequently, the energy E_s necessary for the creation of an area A is^[1]

$$\frac{E_s}{A} = \frac{E_{A,s} - E_{A,b}}{a_0} = \frac{W_{AA}(Z_s - Z_b)}{2a_0} \quad (3)$$

where a_0 corresponds to the area per molecule at the surface. In addition to the interaction energies with neighbors, an entropy contribution must also be taken into account for the surface free energy (or ST), which results, for instance, from the preferential orientation of the surface molecules and from capillary waves at the surface.^[1] However, the derived energy contribution of Equation 3 is typically the dominating one. Equation 3 implies that work W must be performed to create a new surface, which is proportional to the number of molecules transported to the surface and thus creating the area of the new surface. This work W can be expressed as^[1-4]

$$\gamma = \frac{dW}{dA} = \frac{F}{2l} = \frac{dG}{dA} \quad (4)$$

with the proportional constant γ , which is called surface tension, surface free energy, or as free energy per unit area. A typical experiment to determine the ST as shown in Figure 1 illustrates Equation 4. The apparatus consists of a wire loop and a movable slide wire. Assuming that this apparatus behaves like an idealized frictionless device, a wire loop is immersed in the liquid and a liquid film is formed. The surface pulls the sliding wire in the direction of the decreasing film area. This can be prevented by applying an opposing force $F = -(F_s + F_g)$, with F_s being the force of ST and F_g being the gravitational force. This force F has a characteristic value for each liquid, acts along the entire edge of the film and varies linearly with the length l of the slide wire. At constant temperature and pressure, the work required to increase the area

contributes to the differential Gibbs free energy dG . Therefore, Equation 4 can be expressed in terms of thermodynamic quantities describing surface tension as an increase in Gibbs free energy per unit area.^[2-4]

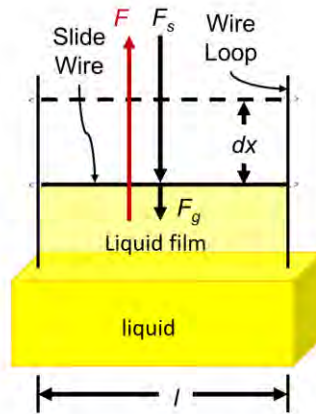


Fig. 1: Wire loop with a slide wire of a length l in a liquid. A liquid film can be formed with the slide wire and stretched by an applied force F .

1.2 Young-Laplace Equation

In order to understand the pendant drop method for surface tension determination of a droplet, one must take into account that there is a pressure difference at a curved surface/interface.^[2,4] The pressure is higher on the concave side and thus the pressure difference must be related to the curvature of the surface.

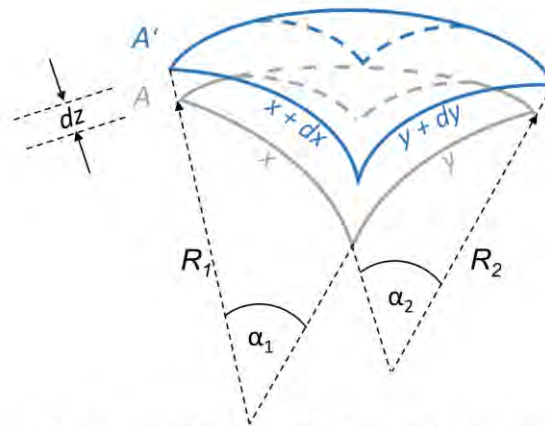


Fig. 2: Representation of the displacement of a curved surface A by dz with respect to the curved surface A' , according to Ref. [2,4].

Figure 2 illustrates a curved surface A with radii of curvature R_1 and R_2 , as well as their intersecting arcs x and y , and their displacement by dz with respect to surface A' along the extensions of the diverging radial lines. This displacement therefore increases the arc lengths to $x + dx$ and $y + dy$. Consequently, the area of the surface A' must also increase. The increase of the area during the displacement of the surface is

associated with an increase in free energy. The work required to increase the surface area must be provided by a pressure difference dp across the element of the surface area. Taking the absolute amount of the usual volumetric work $-pdV$, $dG = dpdV$, and neglecting the second order differential quantities, Equation 4 can be written as

$$\gamma = \frac{dG}{dA} = \frac{dG}{d(x \cdot y)} = \frac{dpdV}{xdy + ydx} \quad (5)$$

The arc lengths are related to the radian angles α_1 and α_2 in plane geometry thus $x = R_1\alpha_1$ and $(x + dx) = (R_1 + dz)\alpha_1$, as well as $y = R_2\alpha_2$ and $(y + dy) = (R_2 + dz)\alpha_2$. This leads to^[2,4]

$$\frac{x + dx}{R_1 + dz} = \frac{x}{R_1} \rightarrow \frac{dx}{xdz} = \frac{1}{R_1} \quad (6)$$

$$\frac{y + dy}{R_2 + dz} = \frac{y}{R_2} \rightarrow \frac{dy}{ydz} = \frac{1}{R_2} \quad (7)$$

By substituting Equations 6 and 7 into Equation 5, the Young-Laplace equation

$$dp = \gamma \left(\frac{1}{R_1} + \frac{1}{R_2} \right) \quad (8)$$

Follows, which was derived by Young^[5] and Laplace^[6] in 1805 and 1806. At equilibrium, dp is also equal to the hydrostatic pressure drop in the liquid column in a capillary and it follows

$$dp = d\rho gh = dp_0 + d\rho gz \quad (9)$$

Here $h = \frac{2\gamma \cos \theta}{\rho g r}$ is the meniscus level in a capillary (see Figure 3), $d\rho$ is the density difference between the liquid and the second phase to consider the buoyancy of the drop and g is the acceleration due to gravity.^[1-4] Equation 9 also describes the pressure difference dp_0 at a reference plane, where z is the vertical coordinate of the drop measured from the reference plane. For more details, see Ref. [1-4,7].

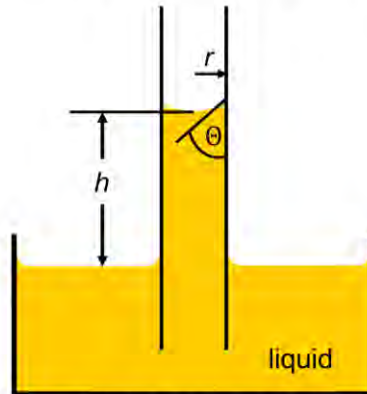


Fig. 3: Liquid rising in a capillary, where h is the meniscus height, r is the capillary radius, and θ is the wetting angle.

1.3 Axisymmetric Drop Shape Analysis (ADSA)

The most important part for accurate PD ST/IFT measurements is the exact determination of the shape of a hanging (=pendant) drop (PD).^[8-11] In 1881, Worthington suggested that the ST of a liquid can be determined from the shape of a hanging drop, which is deformed by gravity.^[12-14] Bashford and Adams published 1883 numerical tables for the approximate solutions of the axially symmetric Young-Laplace equation.^[15] There, the drop shape is defined by a single dimensionless quantity representing the ratio of gravitational and interfacial forces and is specified by

$$\beta = d\rho g \frac{R_0^2}{\gamma} \quad (10)$$

Note that R_0 is the curvature radius of the drop at its apex, $d\rho$ the difference in density of liquid and surrounding medium, g the local acceleration of gravity and γ the corresponding interfacial tension.”^[15] In 1947, Merrington and Richardson defined β as ‘Bond number’.^[16] When the bond number can be accurately determined from the drop shape, the ST or interfacial tension (IFT) can be directly obtained from the density, gravitational force and drop size. However, this proved to be challenging for some systems, especially for drops strongly elongated due to a low surface tension with only R_0 as characteristic drop shape parameter.

In 1938, Andreas et al. demonstrated an improved approach to determine γ from the aspherical drop shape based on the value $S = d_s / d_e$, which is the ratio of the maximum drop diameter d_e , and the drop diameter d_s , measured at a distance d_e from the apex.^[17] This method is named the “Method of selected planes” and is illustrated in Figure 5. The ratio S is then compared with tables calculated experimentally by Andreas et al., which correlate the bond number and interfacial tension. These tables were further improved over time by numerical integration of the Young-Laplace equation.^[17,18]

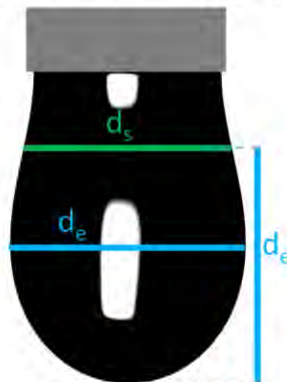


Fig. 4: Illustration of the “Method of selected planes” from Ref. [17] using the ratio $S = d_s/d_e$ as characteristic descriptor for the pendant drop shape. The maximum drop diameter d_e (blue) and the drop diameter d_s (green) at the distance d_e above the apex are shown.

Today, standard programs for calculating surface tension are based on the ADSA algorithm (axisymmetric drop shape analysis) developed by Neumann et al.^[8,19-23] The software for this algorithm uses an image-processing technique that automatically detects the edge of the drop, consisting of four steps as demonstrated in Figure 5.^[24]

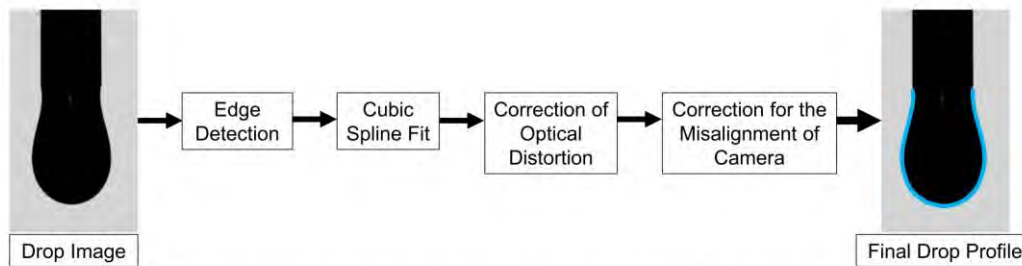


Fig. 5: Illustration of the four steps of the image analysis portion of ADSA, according to Ref. [24].

First, the Sobel edge operator is used to obtain the edge of the drop, as its value is high at the pixels where the gray levels change rapidly, i.e. at the edge. Here, the edge is a discrete curve.^[19,24-26] The minimum distance between two adjacent points is identical to the size of a pixel. To obtain higher accuracy, the edge is smoothed using a cubic spline technique to obtain subpixel resolution. Then, to eliminate the effects of optical distortion caused by the microscope lens system, the edge is corrected by means of a calibration grid. Finally, the misalignment of the camera is corrected by means of an appropriate transformation matrix.^[24]

Subsequently, the surface tension/interfacial tension is calculated from the final drop profile using a numerical method.^[22,24] The numerical scheme of ADSA is based on an optimization process. In this process, a set of Laplacian curves (theoretical curves) are fitted to the experimental profile. Before the fitting process, theoretical curves are generated by integrating the Young-Laplace equation (Equation 8) for the given values of surface tension and curvature at the apex of the drop. Figure 6 shows a coordinate system with a Laplacian curve to describe such a system.^[22]

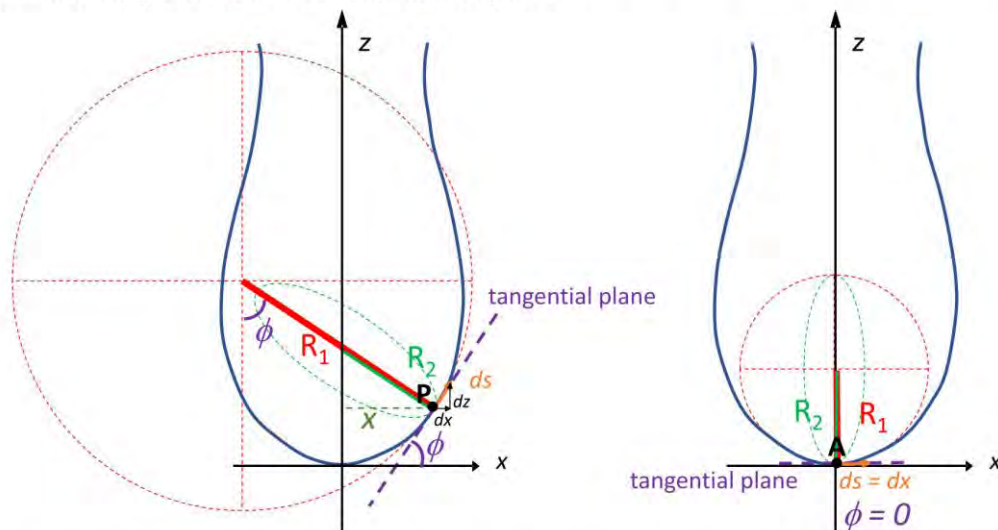


Fig. 6: Definition of the coordinate system (origin at apex) and the Laplace curve for a rotation-symmetric pendant drop according to Ref. [22]. (Left) At an arbitrary point P, the angle of the tangential plane with the x-axis is ϕ . The arc length s follows the drop contour in P by $ds = R_1 \cdot d\phi$. The two principal radii of curvature at P are R_1 and R_2 , with R_1 rotating with ϕ in the paper plane (red circle) and R_2 rotating in the corresponding perpendicular plane (green circle). (Right) At the apex A, R_1 and R_2 are identical.

Neglecting all forces except gravity, the pressure difference is a linear function of height, as already demonstrated in Equation 9. Assuming a symmetrical surface/interface around the z-axis, the main radius of curvature R_1 with the arc length s and the angle of inclination of the surface/interface to the horizontal ϕ is

$$\frac{1}{R_1} = \frac{d\phi}{ds} \quad (11)$$

The second radius is given by

$$\frac{1}{R_2} = \frac{\sin \phi}{x} \quad (12)$$

As a result of the axial symmetry of the surface/interface, the curvature at the apex is constant in all directions and the two principal radii of curvature are equal denoted as R_0 , the curvature at the origin is denoted by b :

$$\frac{1}{R_1} = \frac{1}{R_2} = \frac{1}{R_0} = b \quad (13)$$

The pressure difference at the origin at $s = 0$ is obtained from Equation 8 by

$$dp_0 = 2b\gamma \quad (14)$$

Substitution of Equations 11, 12 and 14 into Equation 8 and definition of the capillary constant c , results in

$$\frac{d\phi}{ds} = 2b + cz - \frac{\sin \phi}{x} \quad (15)$$

$$c = \frac{d\rho g}{\gamma} \quad (16)$$

The capillary constant has negative values for pendant drop (PD) and positive values for sessile drop (SD). A set of first order differential equations for x , z and ϕ are given by Equation 15 and the geometrical relations

$$\frac{dx}{ds} = \cos \phi \quad (17)$$

$$\frac{dz}{ds} = \sin \phi \quad (18)$$

as a function of the arc length s . The boundary conditions are

$$x(0) = z(0) = \phi(0) = 0 \quad (19)$$

and at $s = 0$, one obtains

$$\frac{d\phi}{ds} = b \quad (20)$$

The complete shape of the axisymmetric Laplacian curve obtained by simultaneous integration of Equations 15, 17, and 18 for specific values of b and c . After the theoretical curve is generated, the experimental profile's deviation from the Laplacian profile is determined.^[20,22] To fit the Laplacian profile to the experimental profile, an iterative solution procedure based on numerical solvers, such as the Levenberg-Marquardt or Newton-Raphson method, is necessary.^[22] As the results of the numerical solvers, the optimization parameters are obtained which give the best fit between the measured profile and a Laplacian curve. The ST is calculated based on the value of c , $d\rho$ and g . Note from Equation 15 that the solutions depend on the capillary constant c , that is, the ratio of $d\rho/\gamma$ (Equation 16); any changes in mass density difference $d\rho$ proportionally change γ . It should be also mentioned that other surface/interface properties such as drop volume, surface area and contact angle are determined from the selected Laplacian curve.^[20,22]

1.4 Young Equation

To determine the wetting of a liquid on a solid, the SD method is used as a standard method. A droplet is placed on a solid surface and the interaction of the droplet with the solid surface and the resulting wetting behavior can be determined. The droplet shape of a liquid L on a solid surface S in a gas phase G (SD) can be described by the Young equation

$$\gamma_{SG} = \gamma_{SL} + \gamma_{LG} \cos \Theta \quad (21)$$

This equation is based on the force balance at the three-phase contact line in the direction parallel to the surface, which is illustrated in Figure 7. In this equation, γ_{SG} is the surface free energy of the solid, γ_{SL} the interfacial tension between liquid and solid, $\gamma_{LG} = \gamma$ the surface tension of the liquid and $\cos \Theta$ wetting/contact angle,^[1-4,7] where $\gamma_{SG} - \gamma_{SL}$ is also termed "wetting tension".^[3] For more details see Ref. [1-4,7].

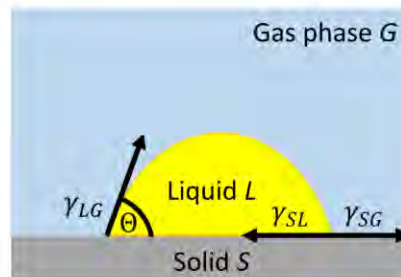


Fig. 7: Contact angle of a liquid on a solid surface.

2. Overview Chamber

Pumps (roughening pump, turbo pump), cold cathode, thermocouple, camera, light source, venting and gas inlet, fine dosing valve, heating tape, focus lens

The new high vacuum (HV) Pendant Drop (PD)/Sessile Drop (SD) system (see Fig. 8) can measure in the pressure range from atmosphere (≈ 1000 mbar) to HV (10^{-7} mbar). To realize this, a scroll pump (oil-free rough pump (Pfeiffer, Mod: HiScroll 6, main connections: 100 – 127/200 – 240 V AC ($\pm 10\%$), 50/60 Hz)) and a turbo pump (Pfeiffer, Mod: HiPace 80, M-No: PM P03 941 A) are connected to a stainless steel vacuum six-way cubic cross. In order to vary the pressure range or the gas atmosphere, a venting and gas inlet, as well as a fine dosing valve are mounted. A cold cathode transmitter (Pfeiffer, Mod: PKR 251) is installed for pressure read out. The gate valve between chamber and turbo pump must be closed, when the chamber is vented with air/liquid N_2 (venting/gas inlet) or gas is introduced by the fine dosing valve (see Fig. 1b). A high-speed camera (iDS, UI-3350CP-M-GL R2) and a light source (kwmobile, M-No: 41044), located on opposite sides, are attached to record videos/photographs of the pendant/sessile drops (see Fig. 1).^[27] At the beginning, an accessory lens (0.75x (ATL 075-P)) was needed to increase the working distance. After final assembly of the chamber, the accessory lens is no longer required. To reduce reflections from the metallic walls inside the six-way cubic cross, a paper with a rectangular opening (10 mm x 25 mm) is fixed between the light source and the illumination flange (window between light source and drop). A heating tape is attached to bake out the chamber, to degas the liquid and to allow for measurements at different temperatures. The temperatures of the liquid in the reservoir is read via thermocouples, which are attached to the cannula at two points (see Chapter 3.2).^[27] Drawings of the Chamber are given in Chapter 9.1. In the chamber, it is also possible to perform sessile droplet investigations of liquids on solids and to determine their contact angles. The z-shift (see Fig. 8) can be connected to the fast-entry load-lock (FEL) chamber of the DASSA.^[28] For more details on the setup of the PD, as well as the SD, please refer to Chapters 3 (PD), 4 (SD) and 5 (DASSA connection).

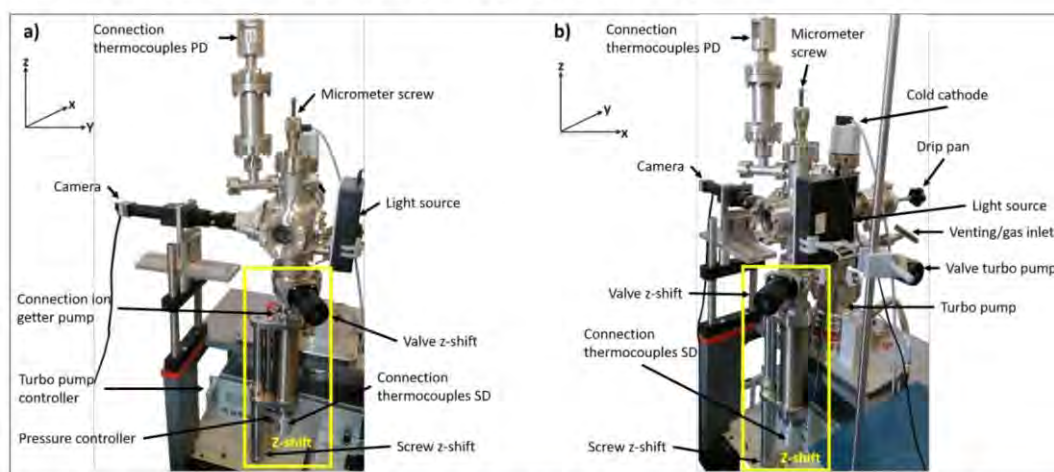


Fig. 8: a) Front view and b) side view of the PD/SD system with installed z-shift and mounted micrometer screw.

3. Pendant Drop (PD)

Setup: Reservoir, stamp (micrometer screw), cannula, collecting vessel for liquids and idea; software

3.1 Setup

The setup for forming a drop consists of a reservoir, a stamp and a

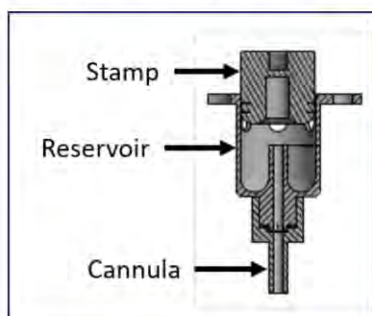


Fig. 9: Cross section of the bottom part of the Pendant Drop setup.

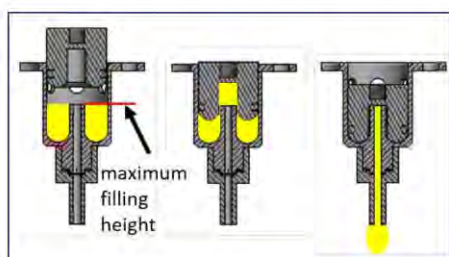


Fig. 11: Cross section of the setup with idea of drop formation. Liquid is shown in yellow.

replaceable cannula (see Fig. 9). Holes in the reservoir allow degassing of the liquid sample. Viton seals are located between the reservoir and the stamp and between the reservoir and the cannula (see Fig. 10) to achieve liquid tightness.^[27] Cannulas with different inner and outer diameters have been designed (see Table 1).

A drop can be formed when the liquid is pressed into the cannula (see Fig. 11). This is possible by connecting the stamp to a micrometer screw that can be operated from outside the chamber (see Fig. 11 and Fig. 12). To form a stable drop, it is necessary to insert twisted wires into the cannula (see Chapter 7.1).^[27] After forming a drop, videos are recorded and photographs (from the video) of the drop are evaluated. For this, the SCA 22/15 (surface and interfacial tension; pendant drop) and SCA 20 (contact angle measurement) software from DataPhysics are used. When the drop detaches from the cannula, the liquid is collected in a glass vessel, which is placed in an extra tube connected to the bottom part of the six-way cross, on the opposite side of the cannula. To change the temperature of the liquid, the chamber is heated with a heating tape wrapped around the outside of the chamber. The temperature is determined via two thermocouples attached directly to the cannula at two positions, to increase the reproducibility of the data and to keep the measurement error of the temperature as low as possible (see Fig. 14).^[27]

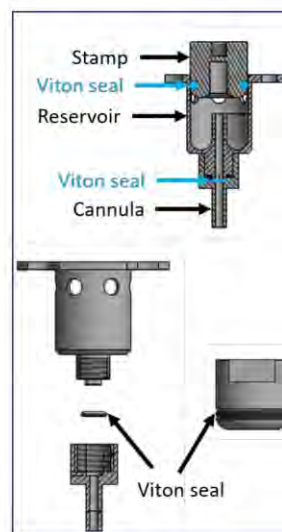


Fig. 10: Cross section of the bottom part of the Pendant Drop setup with viton seals.

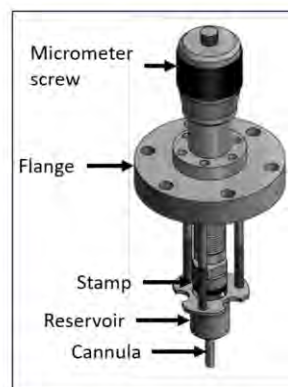


Fig. 12: Connection of the stamp to the micrometer screw.

For the **15.8 mm** outer diameter stamp use the **12x2 mm** viton seal and for the **15.04 mm** and **15.06 mm** outer diameter stamp use the **11.6x2.4 mm** viton seal. Our standard cannula size for pendant drop is $\varnothing_o = 2.02$ mm.

Table 1: Different inner and outer diameters of the changeable cannulas.

Outer diameter \varnothing_o (mm):	Inner diameter \varnothing_i (mm):
4.04	2.0
4.02	1.0
2.02	0.5
1.54	0.5
1.05	0.5

3.2 Mounting Pendant Drop

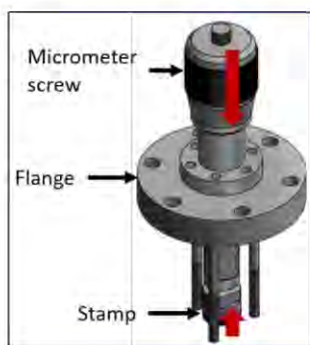


Fig. 13: Micrometer screw and stamp movement.

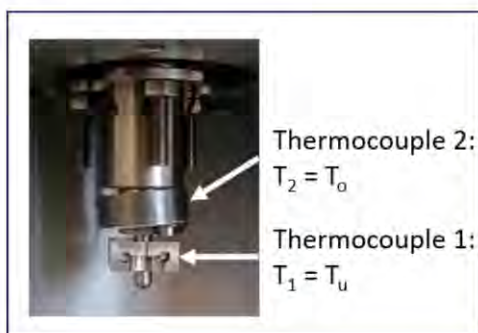


Fig. 14: Thermocouple connection to the cannula.

Before mounting the viton seals on the stamp and between the reservoir and the cannula (see Fig. 10), they must be cleaned. Isopropanol is used as standard for this purpose. For calibration measurements and more detailed information, see Chapter 7.4. The cannula is connected to the reservoir and the twisted wires should be inserted into the cannula. The wires should not be longer than the maximum filling height (see Fig. 31, Chapter 7.1). After that, the stamp is attached to the micrometer screw. The micrometer screw must be turned down so that the stamp is at the top and the reservoir can be attached (see Fig. 13). Then check that the stamp and reservoir fit together and close tightly. This is described in more detail in Chapter 7.4. When everything fits together, the liquid can be filled into the reservoir. The reservoir has a maximum filling level of 1.5 ml (see Fig. 11).

Ensure that the degassing holes are open and no liquid is therein. When filling the reservoir, the liquid should not reach the degassing holes and under no circumstances flow into the cannula. The degassing holes and in particular the cannula is then blocked and proper degassing of the liquid is no longer possible. Bubbles then form during HV measurements (see Chapter 7.3). After filling the reservoir, it must be fixed with screws to the three threaded rods around the stamp. **The position of the counter screws on the threaded rods should never be modified!** These counter screws ensure that the reservoir and thus the cannula are straight during the subsequent image

acquisition or video recording. Now move the stamp down slightly (about one turn of the micrometer screw). Afterwards, the two thermocouples can be attached to the cannula as shown in Fig. 14. Subsequently mount the complete setup from Fig. 15 to the six-wax cross. Check whether the

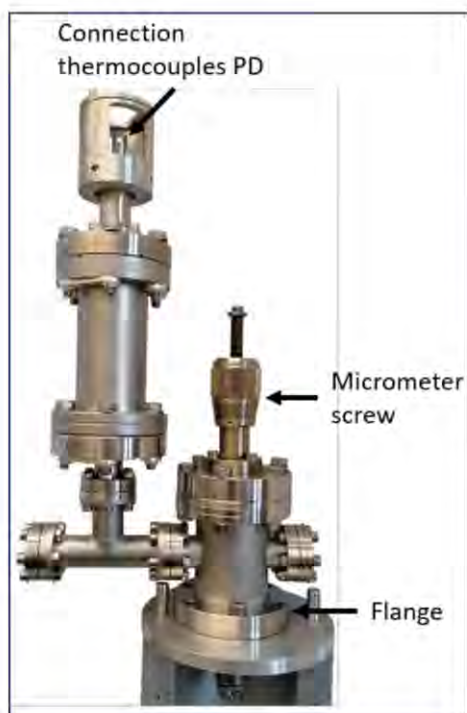


Fig. 15: External pendant drop setup of the flange with micrometer screw and thermocouple connection.

temperatures of the thermocouples can be read. Use the live window of the software to check that the cannula is straight and the paper is in the correct position to reduce light reflections (see Chapter 2). Attach the glass vessel in the extra tube to the lower part of the chamber (see Fig. 8, the tube is attached at the position of the z-shift). When pumping the chamber, wait until the pressure from the scroll pump is in the low mbar range (below 10 mbar) before starting the turbo pump. When the turbo pump has reached its full speed, the current should be a maximum of 0.3 to 0.4 A. The heating cable must then be placed around the chamber and the complete chamber covered with aluminum foil. The window to the light source and the micrometer screw should be covered separately with an extra piece of aluminum foil. This can then be removed separately when starting the measurement. The bake-out of the chamber and the degassing of the IL can finally be started. For more information on degassing time and temperature, see Chapter 7.3. For detailed drawings with dimensions of the components, see Chapter 9.2.

3.3 Image Recording and Data Evaluation

The measurement can be started, as soon as the degassing of the liquid is finished. For details on brightness and contrast, image acquisition settings, reference measurements, and error reduction, see Chapter 6 and 7. To obtain good and reproducible results, two to three drops should be formed and dropped off after degassing and before the first drop recordings. Connect the camera to the measuring computer before starting the software "SCA 22/15" (pendant drop) from DataPhysics. After starting the

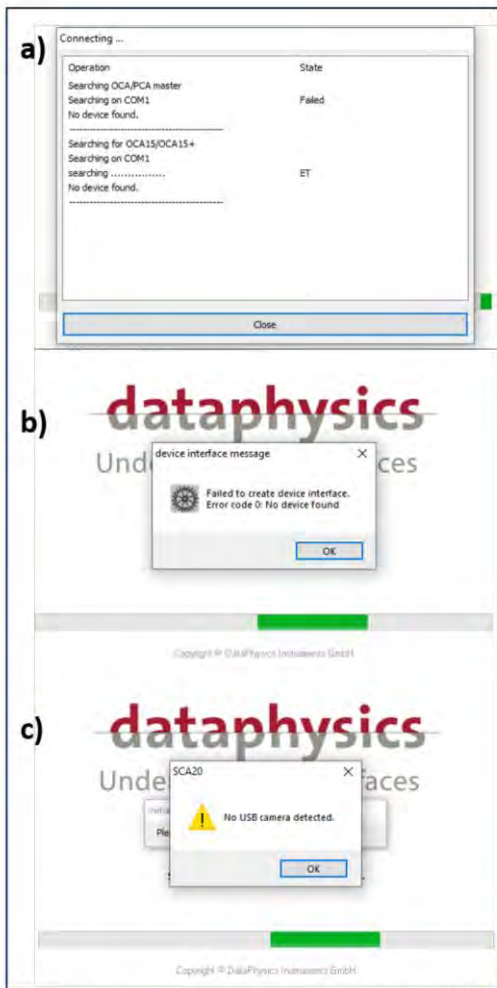


Fig. 16: Software start SCA 15/22 (SD/PD) from dataphysics.

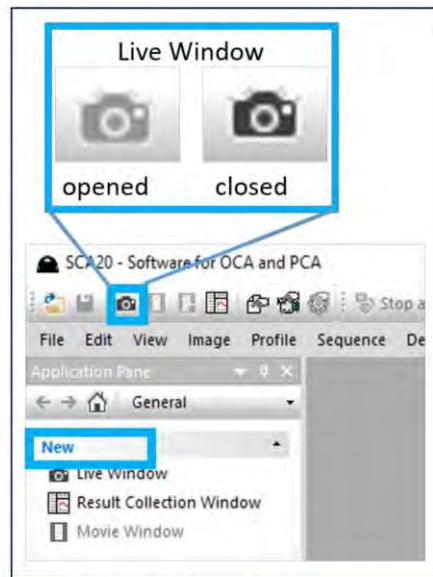


Fig. 17: Open live window.

software, a "Connecting" window appears. Press the "close" button (see Fig. 16a). After that, the window "device interface message" opens. Press the "OK" button (see Fig. 16b). When no camera is connected, a third window with "SCA20" appears: "No USB camera detected" (see Fig. 16c). In this case, press the "OK" button. Close the software and check the USB connection. Try to start the software again. When the camera is connected, a "live window" appears after opening the software (the window shown in Fig. 16c will not appear). When the "live window" is closed, it can be opened via the camera button in the top line or on the left, under "New" of the "Application Pane" window (see Fig 17).

line or on the left, under "New" of the "Application Pane" window (see Fig 17).



Fig. 18: Camera setup with rotation, magnification and focus screws.

The camera button is dark grey if a new “live window” can be opened and light grey if a “live window” is already open (see Fig. 17). For pendant drop recordings, the camera must be rotated so that the drop is completely visible on the screen. Use focus and magnification on the camera (see Fig. 18) to focus the image and record the drop sharp and large enough. The drop size should be about **1/2 to 2/3** of the screen (see Chapter 6.1).

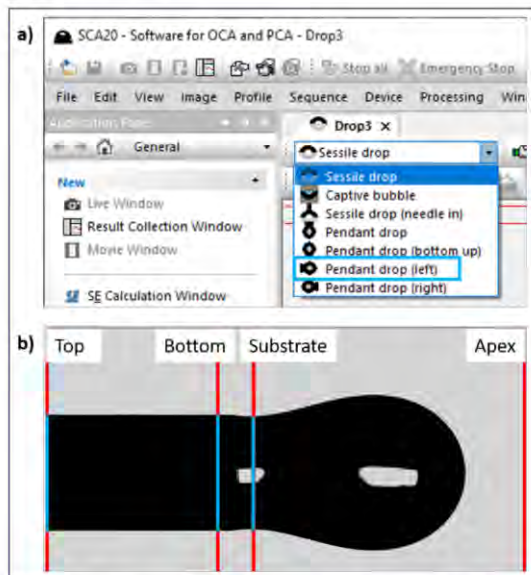


Fig. 19: a) Recording type and b) line setting for PD measurements.

A list of possible recording types can be opened in the “live window”. Select "Pendant drop (left)" to obtain the correct line setting (see Fig. 19a). Four lines are displayed that must be set correctly (see Fig. 19b). The "Top" and "Bottom" lines (reference lines) must be placed at the beginning and end of the cannula. These are necessary for the reference (cannula diameter) and thus for the correct calculation of the surface/interfacial tension. The reference line on the cannula can be used to determine whether the cannula is vertical. When the reference line contains steps, the cannula is not straight or the camera has not been positioned (rotated) correctly. This affects the calculation of the surface/interfacial tension. The calculated value will be incorrect, as it is calculated based on the number of pixels. The line "Substrate" should be placed in the constriction of the drop to obtain a correct and complete determination of the drop contour.

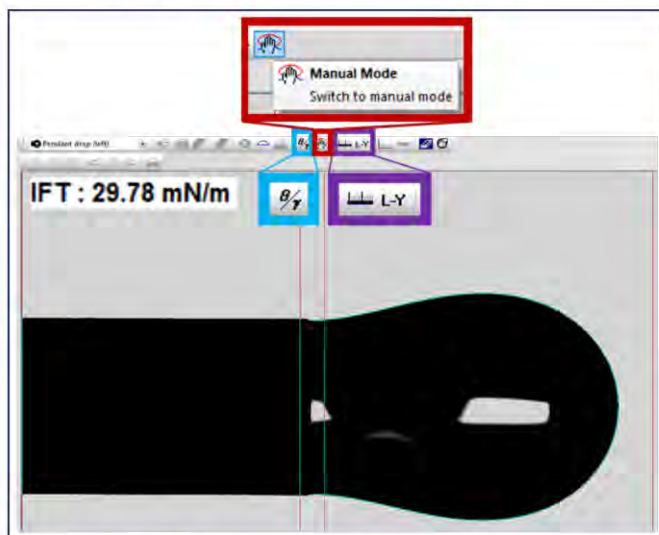


Fig. 20: Buttons for manual mode and surface tension data evaluation.

The line "Apex" must be placed at the end of the drop. It defines the area in which the drop contour can be determined. The lines can be hidden and shown again via the "Manual Mode" button (see Fig. 20). To calculate the surface/interfacial tension, press either the " β/γ " button or first the "scale" button and then the "L-Y" button. The calculated surface/interfacial tension can then be found at the top left next to the "IFT" (Interfacial Tension) label (see Fig. 20).

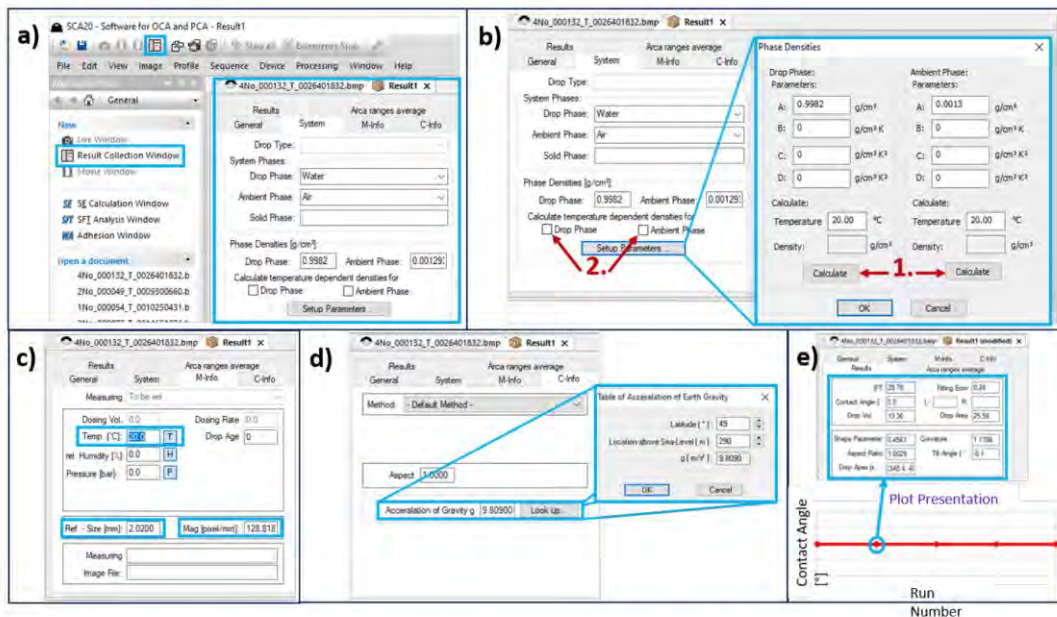


Fig. 21: Result window for surface tension measurements. a) "System" window, b) density parameters, c) "M-Info" window for temperature and cannula size parameters, d) "C-Info" window for gravitational acceleration parameters and e) "Results" window for calculated surface tension data.

To get a correct value for the surface/interfacial tension, press the button "Result Collection Window". A "Result" window opens. In the item "System", the drop phase and the ambient phase can be specified (see Fig. 21a). In the item "Phase Densities", the drop density and the ambient density are given. These can be calculated as a function of the temperature. To do this, press the "Setup Parameters..." button (see Fig. 21b). A window opens in which the temperature-dependent density coefficients for drop and ambient phase can be entered. The density coefficient **A** is the density at 0 °C or 0 K (depending on the calculation → when entering, check whether the values for coefficients A, for 0 °C or 0 K were calculated. Accordingly, the temperature must be entered in °C or in K.). Coefficients **B** to **D** are the first to third order coefficients. These define the linear and polynomial density difference per Kelvin.

$$\rho(T) = A + B \cdot (T - T_0) + C \cdot (T - T_0)^2 + D \cdot (T - T_0)^3$$

Press the "Calculate" button and the temperature-dependent density $\rho(T)$ for the entered temperature (see "Temperature" field) is calculated in the "Density" field. To accept the values, press the "OK" button. Afterwards, tick the "Drop Phase" and "Ambient Phase" boxes under "Calculate temperature dependent densities for" (see Fig. 21b). The temperature at which the image is recorded can be entered under the item "M-Info" (see Fig. 21c). As mentioned before, the temperature must be entered here in °C or K, depending on the calculated density coefficient A. In the "Ref. - Size [mm]" field, the cannula diameter is entered in mm (see Fig. 21c). Depending on whether the liquid wets the cannula or not, the outer or inner diameter must be entered (see Chapter 7.5). The "Mag [pixel/mm]" field specifies the resolution of the acquired image. Under the item "C-Info" in the box "Method" the evaluation method for SD can be selected (see Fig. 21d and Chapter 3.3). In the case of the surface tension, it is automatically the Laplace-

Young Equation. In addition, the "Acceleration of Gravity g " can be calculated for each location. To do this, press the "Look up..." button. A new window opens in which the "Latitude [°]" and the "Location above Sea-Level [m]" can be entered. This can then be accepted in the software via the "OK" button (see Fig. 21d). After calculating the surface/interfacial tension, the drop volume and the drop area as well as the fitting error can be displayed under "Results". To do this, press the corresponding red dot of the evaluated image in "Plot Presentation" (see Fig. 21e).

Further details can be found in the "Operating manual OCA 25" from DataPhysics.

Operating video and software user video can be found with the manual on the external PD/SD hard disk.

4. Sessile Drop (SD)

Setup: z-shift, sample holder, valve, ion getter pump, pBN heater, drip pan; software

4.1 Setup

To form a sessile drop, the stamp and reservoir from the PD system and a cannula ($\varnothing_0 = 1.05 \text{ mm}$) are used and mounted according to Chapters 3.1 and 3.2. Instead of the collecting vessel for the pendant drop system, a z-shift with sample holder is attached to the chamber (see Fig. 22). The z-shift is mounted to the chamber as shown in Fig. 22 middle. A valve is attached to the z-shift to transfer sputtered sample holders in the HV from the DASSA to the PD/SD chamber and sessile drops in the HV to the DASSA, without air contact (see chapter 5). To ensure that the vacuum in the z-shift is maintained, an ion getter pump can be connected to the z-shift.

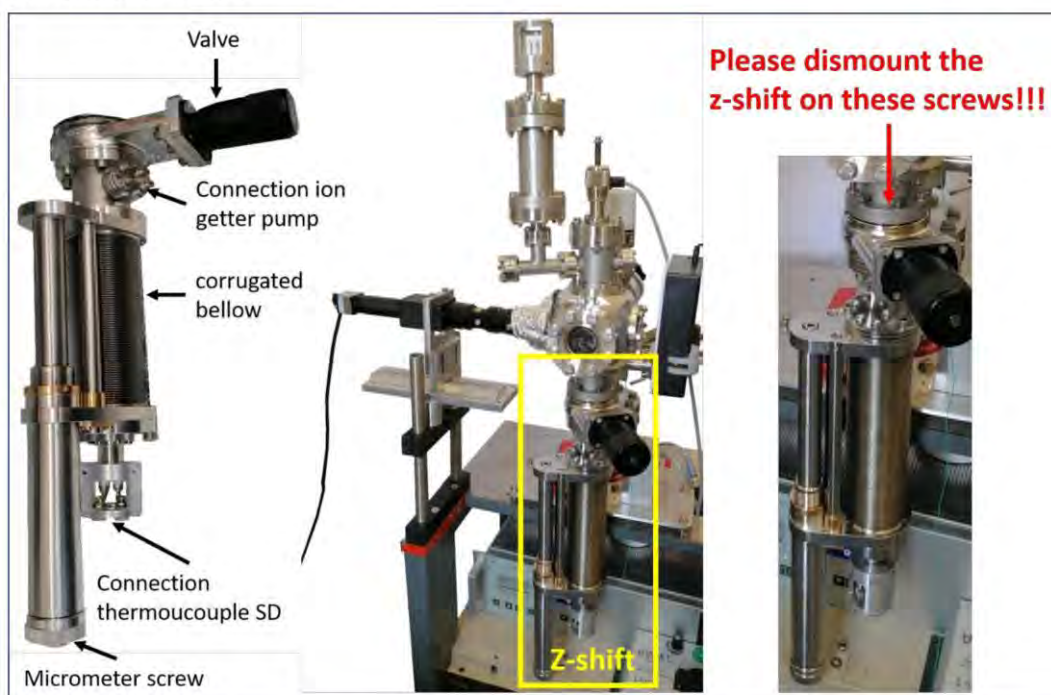


Fig. 22: Left: z-shift, Middle: Sessile Drop setup, Right: Dismounting of the z-shift of the PD/SD chamber.

For degassing, aluminum foil must be wrapped between the corrugated bellow and the heating cable.

After degassing (for further details, see Chapter 5 and 7.3), the liquid must have reached room temperature.

Before the drop can be placed on a sample, a few drops must be dropped off. For this purpose, a small drip pan is installed in the x-direction (see Chapter 9.3). It can be moved under the cannula and some drops can be collected in this drip pan after the chamber is pumped down and the liquid in the reservoir is degassed. In order to deposit the drop onto the sample holder, a z-shift is necessary to move the sample holder upwards to the cannula. A new design of the sample holder is essential for the determination of

the contact angle (see Chapter 9.3.1). Before the sample holder can be moved upwards to the cannula, the valve of the z-shift must be opened.

In this chamber, wetting and the associated contact angle can be determined at different sample temperatures (up to 800 K). For this purpose, a pBN heater is installed in the z-shift below the sample holder. The pBN heater (PCBPN05) has a diameter of 12.7 mm, a resistance of 5-7 Ohm and a maximum power of 80 W (maximum: $U = 15\text{ V}$, $I = 8\text{ A}$) (see Chapter 9.3.2). The SCA 15 (contact angle measurement) software from DataPhysics is used to evaluate the contact angle.^[27]

4.2 Imaging Recording and Data Evaluation

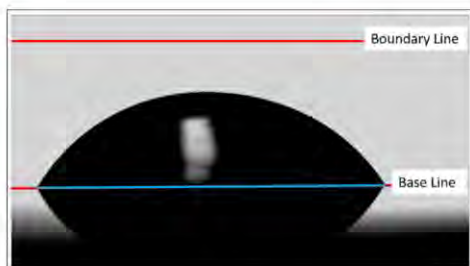


Fig. 23: "Base Line" and "Boundary Line" setting sessile drop.

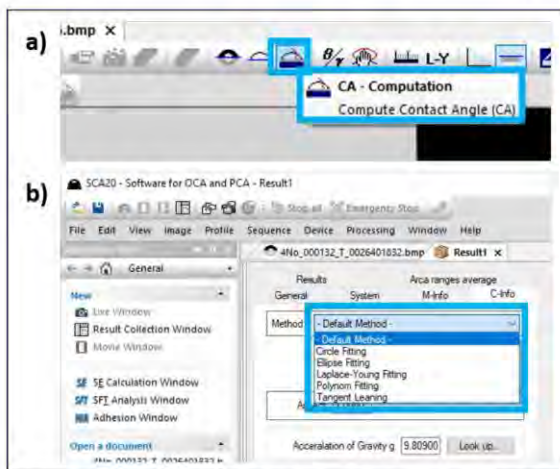


Fig. 24: a) Evaluation methods and b) automatic fitting procedure for sessile drop.

it is possible to choose between "Set Baseline", "Circle Baseline" and "Elliptic Baseline". A certain number of points must be defined for the respective baseline. For "Set Baseline", two points are sufficient. However, at least three points must be set for "Circle Baseline" and five points for "Elliptic Baseline". To set the contour line of the drop, you can then select "Straight Line", "Circle" or "Ellipse". Accordingly, points must be set again. While two points are sufficient for "Straight Line", three are required for "Circle" and at least five for "Ellipse" (see Fig 25b and c).

More details on brightness and contrast, image acquisition settings, reference measurements, and error reduction, see Chapter 6 and 7. For images of sessile drops, the camera must be rotated by 90° compared to recordings of pendant drops (see Fig. 18). To obtain high quality images, the drop should be **2/3** of the width of the screen and the light source and camera should be adjusted to obtain a good surface reflection (see Chapter 6.1).

The data evaluation for sessile drop is similar to that of pendant drop. All data evaluation procedures in the

"Result" window are initially the same as for the pendant drop. One difference is the setting of the lines (see Fig. 23). There are only two lines, the "Boundary Line" and the "Base Line". The "Boundary Line" is placed between the cannula and the drop, the "Base Line" is set exactly through the corner points of the drop and its reflections.

When evaluating the contact angles, note whether the automatic "CA - Computation" (see Fig. 24a) mode or the "Manual Mode" (see Fig. 25) is used. In case you decide to use the automatic mode, you have to select the fitting method in "Method" in the "C-Info" item of the "Result" window (see Fig. 24b).

When the manual mode (see Fig. 25a) is selected for evaluation of the contact angles,

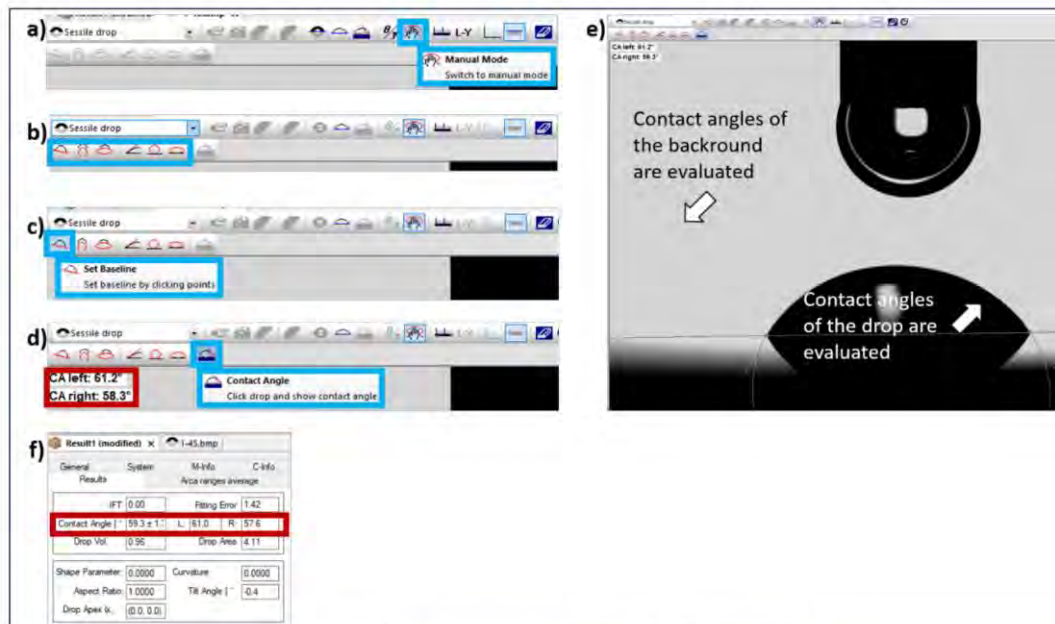


Fig. 25: Step by step presentation of the data evaluation with the manual mode.

To display the contact angles (left and right), you must press the "Contact Angle" button (see Fig. 25d). Then you must click in the drop, directly below the set fitting line. The contact angles of the drop are displayed. When you click on the background, the contact angle of the background is displayed (see Fig. 25e). In the "Result" window, the information about the contact angles "L" on the left, "R" on the right and the average value of the two contact angles and their deviation are entered. The fitting error, the drop volume and the drop area are only displayed for evaluations in the automatic mode "CA – Computation" (see Fig. 25f).

First contact angle evaluations and their results show a smaller difference of the contact angle when evaluating the images in manual mode. This is due to the fact that in automatic mode the corners of the contact angle are cut off on one side.

Further details can be found in the "Operating manual OCA 25" from DataPhysics.

5. Z-shift Connection to DASSA

As mentioned above (see Chapter 4.1), a vacuum transfer of the sample holder from the PD/SD chamber to the DASSA^[28] is possible and vice versa. To transfer the sample holder with the sessile drop into the DASSA, the z-shift from Chapter 4.1 has to be connected to the DASSA. For this purpose, the transfer cross

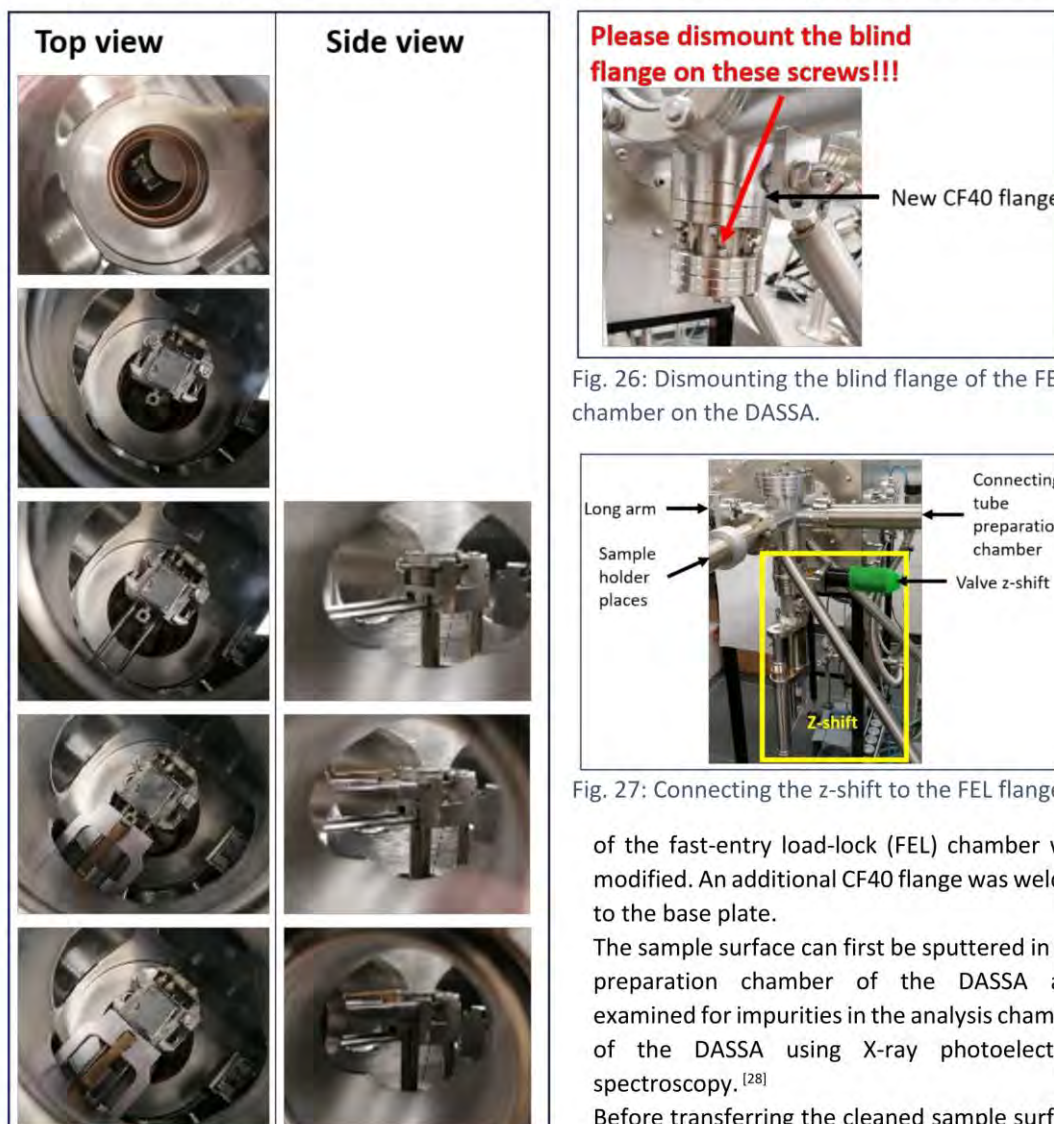


Fig. 28: Top and side view of the sample holder transfer from the z-shift to the FEL chamber of the DASSA.



Fig. 26: Dismounting the blind flange of the FEL chamber on the DASSA.

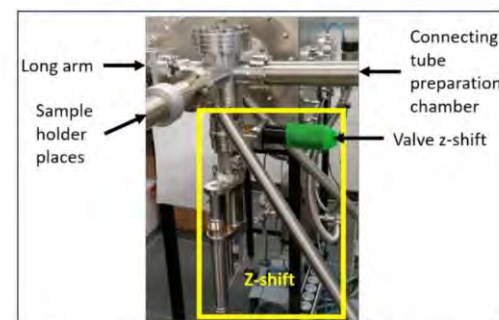


Fig. 27: Connecting the z-shift to the FEL flange.

of the fast-entry load-lock (FEL) chamber was modified. An additional CF40 flange was welded to the base plate.

The sample surface can first be sputtered in the preparation chamber of the DASSA and examined for impurities in the analysis chamber of the DASSA using X-ray photoelectron spectroscopy.^[28]

Before transferring the cleaned sample surface in HV, the FEL chamber must be vented and the z-shift, which keeps the sample in HV, must be attached to the transfer cross of the FEL chamber of the DASSA.

For this purpose, the lower blind flange of the FEL cross is removed after venting the FEL chamber (see Fig. 26). The z-shift is mounted such that the handle of the z-shift valve is parallel to the connecting tube

towards the preparation chamber (see Fig. 27). Only when the z-shift is mounted in this orientation, the sample can be picked up by the long arm of the FEL chamber or placed into the sample position of the z-shift. After mounting the z-shift to the FEL cross, the FEL chamber must be pumped down. When the z-shift is under vacuum, the valve connected to the z-shift should be closed. This valve must be kept open, when the z-shift is not under vacuum to ensure pumping of the z-shift via the FEL chamber (no valve movements with different pressure conditions on both sides!). To improve background pressure, the z-shift should be baked anytime when left with contact to air for a longer period of time. After the correct pressure has been reached in the FEL chamber, the sample holder can be transferred from the preparation chamber to the sample holder position of the z-shift. To do this, the valve on the z-shift must be opened and the sample holder stage fully extended. After completion of the sample holder transfer, the sample holder stage has to be moved completely in the z-shift and the valve has to be closed. The FEL chamber must be vented again. Then the z-shift is disassembled from the FEL cross, the blind flange is reassembled and the z-shift is attached to the PD/SD chamber (described in Chapter 4.1). The PD/SD chamber must be than pumped down and the sample in the reservoir degassed. Pre-degassing with the liquid to be tested in the PD/SD chamber can be carried out before the z-shift is attached. For this purpose, the PD assembly with the SD cannula ($\Phi_0 = 1.05$ mm) and the corresponding liquid is installed in the PD/SD chamber. A blank flange is attached instead of the z-shift. The chamber is pumped into the HV and heated, as already described in Chapter 3.2 and 7.3. After the bake-out, the PD/SD chamber is vented, the z-shift is attached and the chamber is pumped down again. Only a short cold degassing (about 1 - 2 hours, depending on pressure) of the liquid is necessary. The z-shift valve remains closed when it is attached to the PD/SD chamber and the short bake-out (around 2 hours after reaching the corresponding pre-degassing temperature) for post-degassing is started. In this case, it is sufficient to bake the chamber without baking the z-shift. Subsequently, one proceeds as described in Chapter 4.1. After the sample has been examined, the sample holder with the sessile drop can be attached to the DASSA and transferred in HV in the reverse manner as described above.

Image sections of the sample transfer from the z-displacement across the long arm of the FEL chamber at the DASSA are shown in Fig. 28.

6. Calibration and First Results

Brightness and contrast results with water (reference measurements), [C₈C₁Im][Tf₂N], [C₈C₁Im][PF₆], focus lens (no longer in use, see Chapter 2)

6.1 Image Acquisition

After inserting the cannula into the chamber, check that the cannula is vertical in the image. A tilted cannula results in a significant error in the magnification factor and therefore, in a considerable error in surface tension values. In addition, uniform background illumination is advantageous. A non-diffuse background illumination can result in overexposure or underexposure of the drop, resulting in an incorrectly determined drop contour.

During image acquisition for pendant drop, make sure that the cannula occupies at least 10 % of the total image width and 1/2 to 2/3 of the field of view. For sessile drop, the drop should occupy at least 2/3 of the image width. The magnification screw on the camera (zoom) (see Chapter 3.3, Fig. 18) is used for this purpose. A too small image of the cannula and the drop deteriorates the required resolution for reliable surface tension evaluations.

The contour of the cannula and the drop should be focused and clearly visible before the image is acquired. The image can be focused using the focus screw (see Chapter 3.3, Fig. 18). The two reference lines for determining the scale of the cannula for PD measurements should be set at least 20 pixels apart (see Chapter 3.3 and Fig. 19a ("top" and "bottom" line)). You can use these reference lines to test whether the settings, such as the vertical cannula and the sharpness behavior of the image acquisition, fit. No step edge must be visible in the displayed lines, when you press the "scale" button (see Chapter 3.3, Fig. 20) to determine the cannula width.

6.2 Calibration

Before starting the reference measurement with Millipore water, the stamp with viton seal, the reservoir and cannula are cleaned with Millipore water.

Millipore water (18.2 MΩ·cm) was used to calibrate the light source and the high-speed camera with each other. Images were acquired at different contrast and brightness settings and compared with literature values. In the previous image acquisitions in this chamber, all images were subsequently recorded with a **contrast of 16** and a **brightness of 12**.^[27]

This setting should be maintained and checked from time to time with reference measurements using Millipore water, for example when the chamber is modified or the position of the light source or camera is changed. With these settings, the water values are on the literature values even with slightly lower or higher brightness (see Fig. 29). This can reduce deviations in the measurements and the measurement error.

After the reference measurements, the water collection vessel must be removed before the chamber is pumped into vacuum (see chapter 7.2)!

For more details, see the video on image acquisition (settings can be found in the software in "Framegrabber").

Millipore water

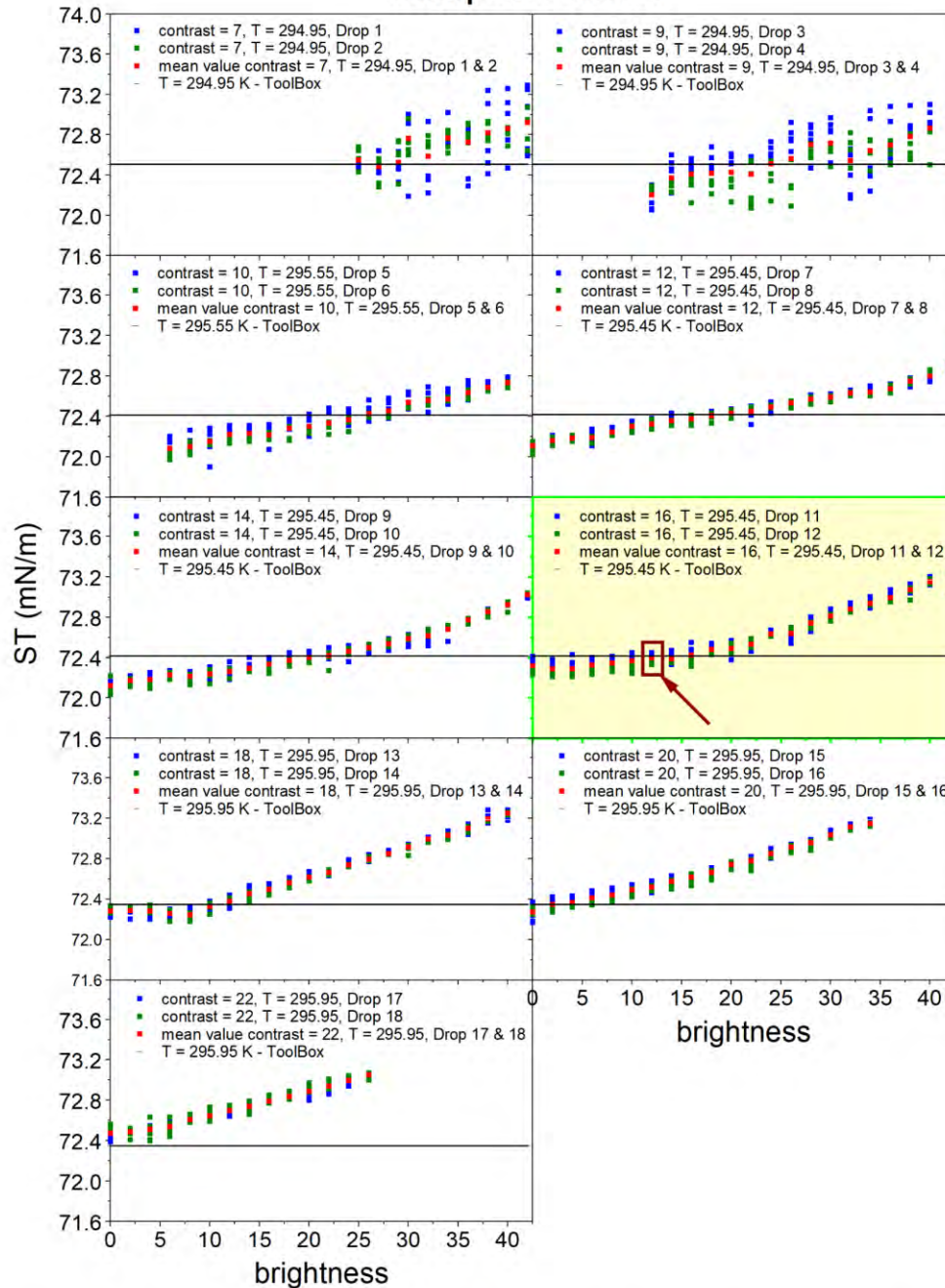


Fig. 29: Different contrast and brightness settings of the PD reference measurements. The yellow box shows selected contrast of 16, the red rectangle the selected brightness of 12. The black line shows the value of the water literature.^[29]

6.3 First Results

Videos of the surface tension of the degassed ionic liquids (ILs), $[\text{C}_8\text{C}_1\text{Im}][\text{PF}_6]$ ^[27] and $[\text{C}_8\text{C}_1\text{Im}][\text{Tf}_2\text{N}]$, in HV were recorded. The images recorded from the videos were used to evaluate the surface tension (see Fig. 30 and Table 2).

These values can be used as reference values for surface tension measurements in HV.

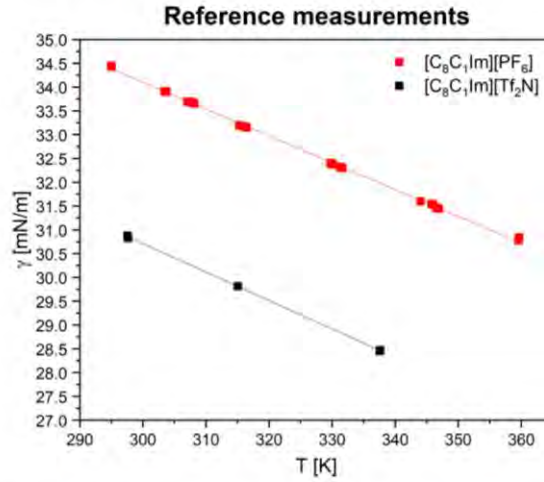


Fig. 30: Surface Tension reference measurements of $[\text{C}_8\text{C}_1\text{Im}][\text{PF}_6]$ and $[\text{C}_8\text{C}_1\text{Im}][\text{Tf}_2\text{N}]$ in high vacuum with a pressure in the lower 10^{-6} mbar range at different temperatures.

Table 2: Surface tension mean values of $[\text{C}_8\text{C}_1\text{Im}][\text{PF}_6]$ ^[27] and $[\text{C}_8\text{C}_1\text{Im}][\text{Tf}_2\text{N}]$ measured in HV with a pressure in the lower 10^{-6} mbar at different temperatures. Linear fit of the data according to the following equation: $\gamma = \gamma_0 + \gamma_1 \cdot T$.

$[\text{C}_8\text{C}_1\text{Im}][\text{PF}_6]$ ^[27]		$[\text{C}_8\text{C}_1\text{Im}][\text{Tf}_2\text{N}]$	
T [K]	γ [mN/m]	T [K]	γ [mN/m]
359.65	30.84	337.65	28.47
346.55	31.46	337.55	28.45
331.35	32.30	315.05	29.81
316.35	33.16	297.65	30.82
295.05	34.44	297.55	30.88
<i>Linear fit</i> ^[27]		<i>Linear fit</i>	
γ_0 [mN/m]	γ_1 [mN/m·K ⁻¹]	γ_0 [mN/m]	γ_1 [mN/m·K ⁻¹]
50.88	-0.0559	48.6293	-0.0597

7. Problems and Solutions

7.1 Wires in Cannula

Comparing the formation of a pendant drop at atmospheric pressure in air with that of a pendant drop in high vacuum reveals considerable differences in terms of stability and drop formation. For problems with drop formation, see Chapter 7.3. Different forces in the respective environments (high vacuum/atmospheric pressure) are decisive for the stability of the drop.

Atmospheric pressure and the gravitational force are the decisive factors for the formation of drops in air. For example, a syringe can be filled with an appropriate liquid. By inserting the syringe and pulling the syringe plunger into the liquid, a negative pressure is created in the syringe (between the syringe jacket and the syringe plunger). The pendant drop at the end of the syringe cannula is stable due to the force of the ambient pressure pressing on each element of the drop and the pressure difference inside and outside the syringe. Gravity pulls the drop lengthwise and deforms it.

Drops at the end of a cannula in the high vacuum are not stable because gravity pulls the drop down and there is no pressure difference in the cannula and the environment. The only counterforce that acts and can be influenced is the capillary force. The smaller the inner diameter compared to the outer diameter of the cannula, the more stable the drop remains. For more details on capillary forces, see Chapter 1.2, Equation 9 and Fig. 3.

A thin inner bore diameter of a cannula is only possible up to a certain length in our workshop and this is not necessarily sufficient to form a stable drop, so the capillary force have to be increased in another way. Twisted wires in the cannula reduce the inner diameter and increase the capillary force (see Fig. 31). By using **twisted stainless-steel wires in the cannula, a stable drop can be formed in a high vacuum.**^[27]

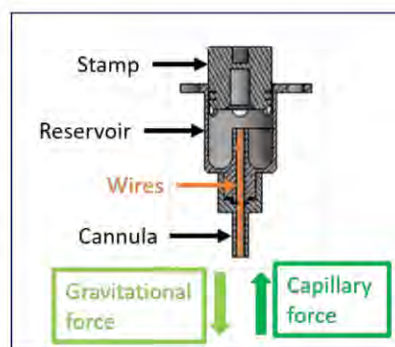


Fig. 31: Pendant drop setup with twisted wires (orange) in the cannula.

7.2 Water Problem

Atmospheric water from air easily condenses at the stainless steel chamber walls. During the first reference measurements, heating experiments have also been carried out with saturated water vapor leading to a large increase of adsorbed water causing some problems during initial pumping such as pressure fluctuations in the mbar range. For a safe pumping procedure, pumping solely with the roughening pump (including gas ballast) should be done for ≈ 30 mins. Before starting the turbo pump, check the chamber pressure (it should be in the low mbar range and no longer show any pressure fluctuations) and close the gas ballast valve.

7.3 Bubble Formation and Degassing

In order to form a drop in high vacuum, correct degassing of the liquid/IL is required. In the case that the degassing temperature of the investigated liquid is too low, bubbles will form during drop formation in vacuum (see Fig. 32).^[27] Due to the influence of the bubbles on the drop shape and the possibility of

wetting the cannula after the bubbles burst, good measurement results cannot be obtained. One should be aware that after extensive bubbling, the liquid is often splashed at the chamber walls and windows requiring extensive additional cleaning and baking procedures.

For the degassing of the ILs investigated so far, a reservoir temperature of at least **70 to 80 °C** was required. The degassing temperature depends on the liquid to be examined. **Before measuring different liquids/ILs, check the decomposition temperature of the respective liquids/ILs!** After reaching the required degassing temperature, a degassing time of at least **8 - 10 hours** should be assured. Whether the liquid/IL is well degassed can be read from the displayed pressure (should be in the lower 10^{-6} mbar range and have no pressure fluctuations).^[27]

Before starting image/video recordings at high temperatures, there should not be a large pressure fluctuation. When the stamp is moved down in the reservoir, thus closing the degassing holes, the pressure fluctuations should also be minimal. In case the pressure fluctuations are large, this is an indication that the liquid/IL is not degassed well.



Fig. 32: Surface tension measurements of $[\text{C}_8\text{C}_{11}\text{Im}][\text{PF}_6]$ in high vacuum with a pressure in the lower 10^{-6} mbar after degassing with $\approx 65^\circ\text{C}$. Degassing temperature was too low.

7.4 Viton Seal

Viton seals on the stamp, and between the reservoir and the cannula, ensure a tight seal between the stamp and the reservoir, and between the reservoir and the cannula. This allows the liquid to be pressed into the cannula without flowing past the stamp into the degassing holes or flowing out between the reservoir and the cannula.^[27]

Before fixing the viton seals to the stamp and the cannula, the exact dimension of the stamp and the viton seal should be checked (see Chapter 3.1) and the viton seal must be cleaned. As a standard for high vacuum measurements, it should be **cleaned with isopropanol**. Isopropanol is not vacuum stable and does not influence the surface tension of high vacuum stable liquids/ILs. **Acetone should never be used** as it damage the viton seal!

For Millipore water reference measurements, all parts have to be cleaned with Millipore water! The influence of isopropanol on Millipore water can be clearly seen in the surface tension. The surface tension of Millipore water is then below the literature value when the viton seals were in contact with isopropanol.

Before filling the liquid into the reservoir, check that the reservoir and the stamp fit together. In case the reservoir can be easily mounted on the stamp, the seal between the reservoir and the stamp is incorrect. Liquid flows past the stamp into the degassing holes. When the reservoir is very hard to slide over the stamp with the viton seal, the connection should be tight.

Depending on the manufacturer, viton seals have different temperature stabilities. Therefore, pay attention to the temperature at the reservoir when bake-out the chamber and degassing the liquid/IL. All viton seals must be replaced when changing the liquid, due to the fact that viton absorbs e.g. ILs.

7.5 Cannula Size

The evaluated surface tension depends on the size of the cannula. Depending on the wetting behaviour, the inner or outer diameter must be taken into account when calculating the surface tension. The outer diameter is crucial, when the horizontal cannula area is wetted by the liquid. The inner diameter of the cannula is decisive, in the case that there is no wetting behavior on the horizontal area of the cannula.

A cannula diameter that is too small or too large can lead to an incorrect result of the surface tension.

When the diameter of a cannula is too small, the volume of the formed drop is too small and the gravitational force does not have much influence on the drop shape. The longitudinal deformation of this drop is too small. For a cannula that is too large, the surface tension results may also be incorrect because the volume of the drop is too large. The drop becomes too heavy and falls off before reaching the perfect drop shape.

In both cases, the constriction of the drop just before falling is too small and the calculation of the surface tension is incorrect. Cannulas with an outer diameter of about $\varnothing_o = 2 \text{ mm}$ should be used for **pendant drop** measurements (see Fig. 33). For

sessile drop measurements, a small drop is required which, according to the literature has a volume of 0.5 to 10 μL , in order to neglect the influence of the gravity on the drop shape and to obtain reproducible data^[30-35]. Therefore, cannulas with an outer diameter of $\varnothing_o = 1 \text{ mm}$ or smaller should be used for **sessile drop** measurements.

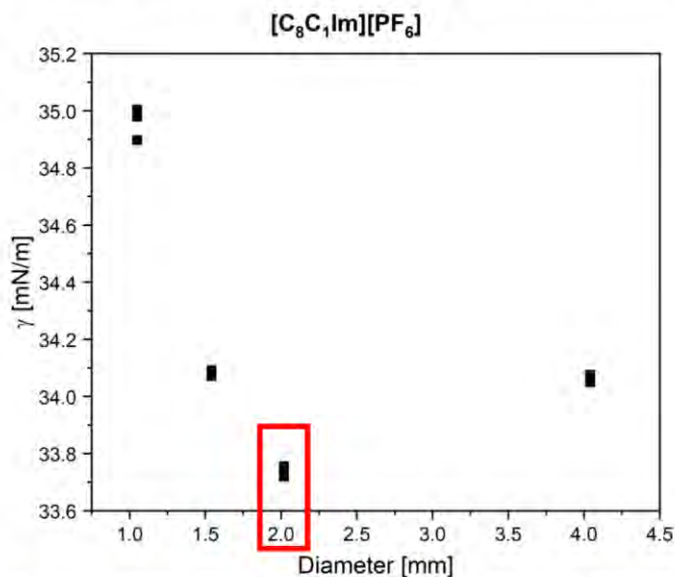
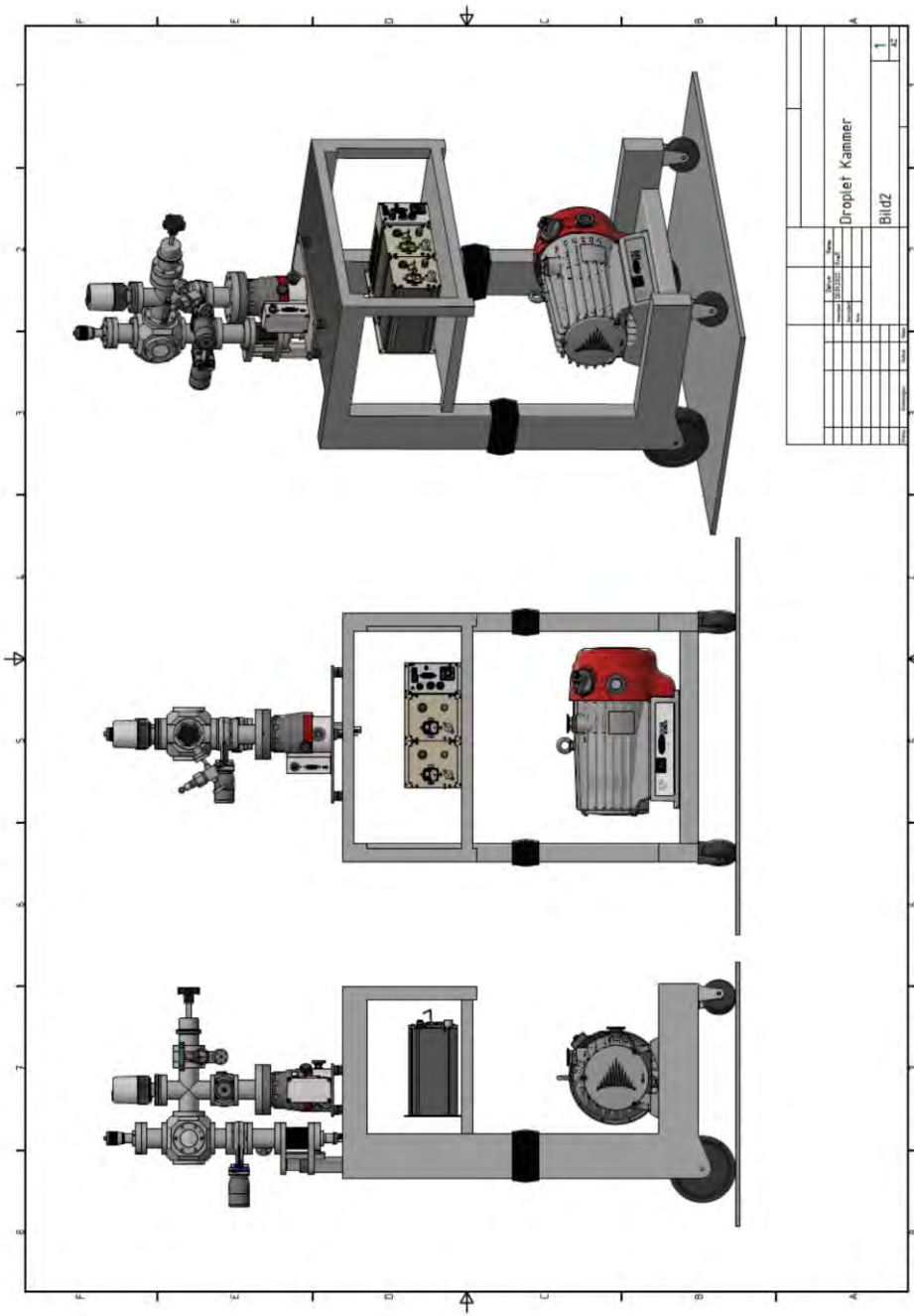


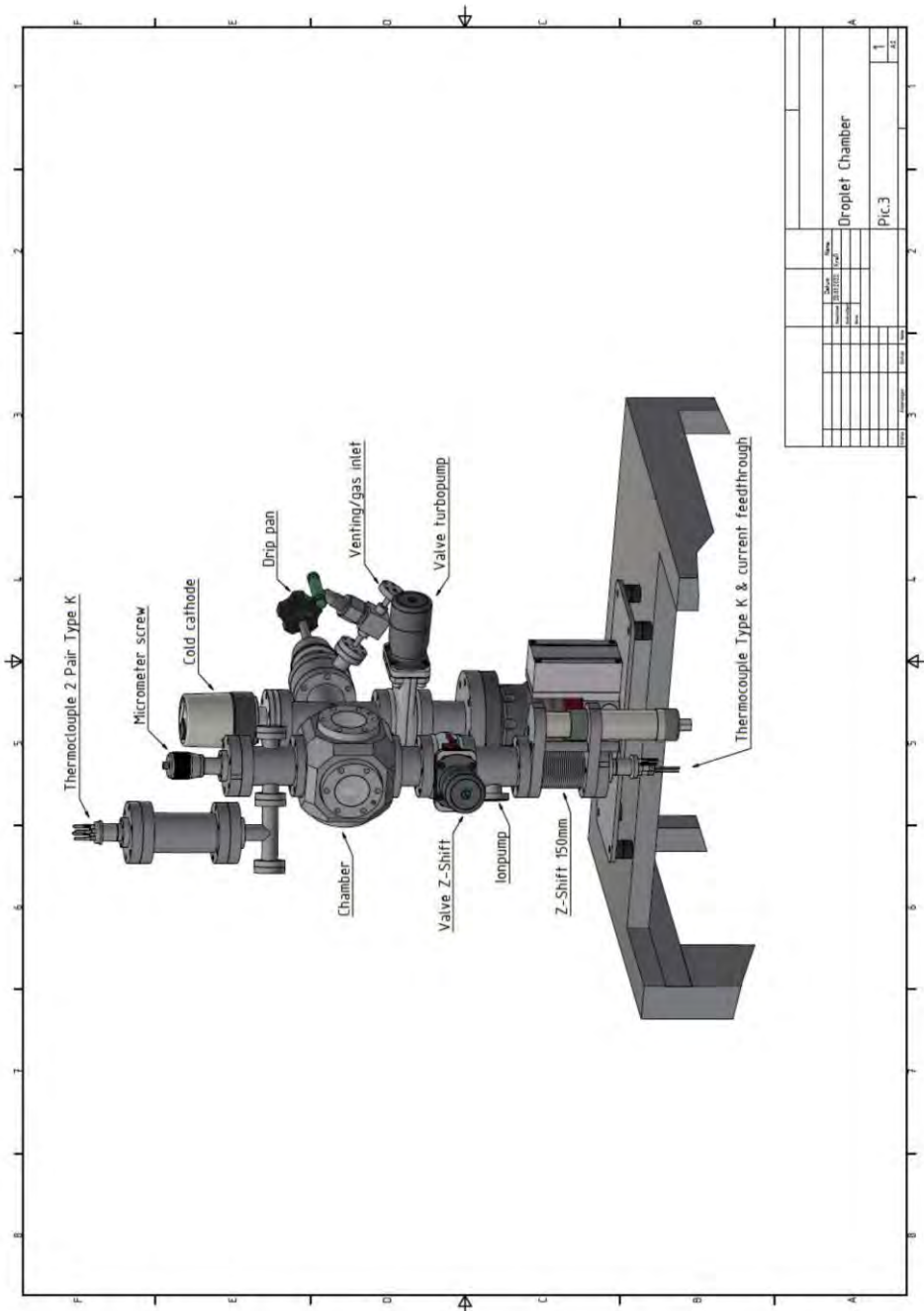
Fig. 33: Surface tension measurements of non-degassed $[\text{C}_8\text{C}_1\text{Im}][\text{PF}_6]$ with different cannula outer diameters at atmospheric pressure at room temperature. Red rectangle shows the cannula diameter we use for pendant drop measurements.

8. Bibliography

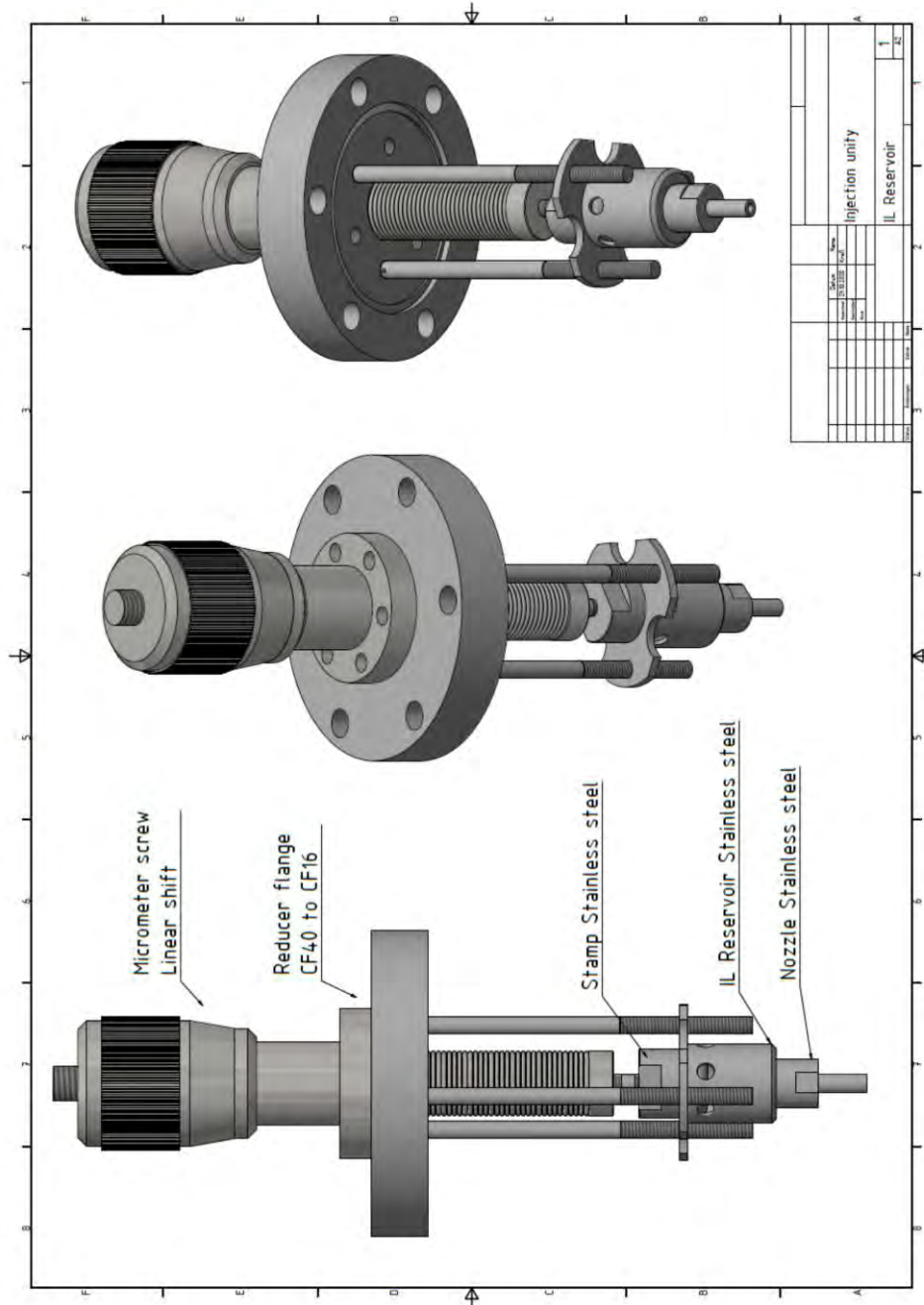
1. Evans, D.F.; Wennerström, H. *The colloidal domain: where physics, chemistry, biology, and technology meet*; Wiley-VCH, USA: 1999; Volume 2.
2. Erbil, H.Y. *Surface Chemistry*; Blackwell Publishing Ltd: 2006; Volume 1.
3. Robert J. Good, R.R.S. *Surface and Colloid Science*; Plenum Press, New York: 1979; Volume 11.
4. Paul C. Hiemenz; Rajagopalan, R. *Principle of Colloid and Surface Chemistry*; CRC Press: 1997; Volume 3.
5. Young, T. III. An essay on the cohesion of fluids. *Philosophical Transactions of the Royal Society of London* **1805**, *95*, 65-87, doi:10.1098/rstl.1805.0005.
6. Laplace, P.S., Marquis De. *Traité De Mécanique Céleste*. **1806**, *10*.
7. Holmberg, K. *Handbook of Applied Surface and Colloid Chemistry*; Wiley&Sons,England: 2002; Volume 1,2.
8. Hoorfar, M.; Kurz, M.A.; Neumann, A.W. Evaluation of the surface tension measurement of axisymmetric drop shape analysis (ADSA) using a shape parameter. *Colloids and Surfaces A: Physicochemical and Engineering Aspects* **2005**, *260*, 277-285, doi:10.1016/j.colsurfa.2004.08.080.
9. Ferrera, C.; Montanero, J.M.; Cabezas, M.G. An analysis of the sensitivity of pendant drops and liquid bridges to measure the interfacial tension. *Measurement Science and Technology* **2007**, *18*, 3713-3723.
10. Saad, S.M.; Policova, Z.; Acosta, E.J.; Neumann, A.W. Range of validity of drop shape techniques for surface tension measurement. *Langmuir* **2010**, *26*, 14004-14013, doi:10.1021/la1020675.
11. Berry, J.D.; Neeson, M.J.; Dagastine, R.R.; Chan, D.Y.C.; Tabor, R.F. Measurement of surface and interfacial tension using pendant drop tensiometry. *Journal of Colloid and Interface Science* **2015**, *454*, 226-237, doi:10.1016/j.jcis.2015.05.012.
12. Worthington, A.M. On pendent drops. *Proceedings of the Royal Society of London* **1881**, *32*, 362-377.
13. Worthington, A.M. IV. Note on a point in the theory of pendent drops. *The London, Edinburgh, and Dublin Philosophical Magazine and Journal of Science* **1885**, *19*, 46-48, doi:10.1080/14786448508627638.
14. Ferguson, A. Photographic measurements of pendant drops. *Philos. Mag.* **1911**, *23*, 417-430.
15. Bashforth, F.; Adams, J.C. *An attempt to test the theories of capillary action by comparing the theoretical and measured forms of drops of fluid*; University Press: 1883.
16. Merrington, A.C.; Richardson, E.G. The break-up of liquid jets. *Proceedings of the Physical Society* **1947**, *59*, 1-13, doi:10.1088/0959-5309/59/1/302.
17. Andreas, J.M.; Hauser, E.A.; Tucker, W.B. Boundary tension by pendant drops. *The Journal of Physical Chemistry* **1938**, *42*, 1001-1019, doi:10.1021/j100903a002.
18. Fordham, S.; Freeth, F.A. On the calculation of surface tension from measurements of pendant drops. *Proceedings of the Royal Society of London. Series A. Mathematical and Physical Sciences* **1948**, *194*, 1-16, doi:doi:10.1098/rspa.1948.0063.
19. Cheng, P.; Li, D.; Boruvka, L.; Rotenberg, Y.; Neumann, A.W. Automation of axisymmetric drop shape analysis for measurements of interfacial tensions and contact angles. *Colloids and Surfaces* **1990**, *43*, 151-167, doi:10.1016/0166-6622(90)80286-D.
20. Río, O.I.d.; Neumann, A.W. Axisymmetric Drop Shape Analysis: Computational Methods for the Measurement of Interfacial Properties from the Shape and Dimensions of Pendant and Sessile Drops. *Journal of Colloid and Interface Science* **1997**, *196*, 136-147, doi:10.1006/jcis.1997.5214.

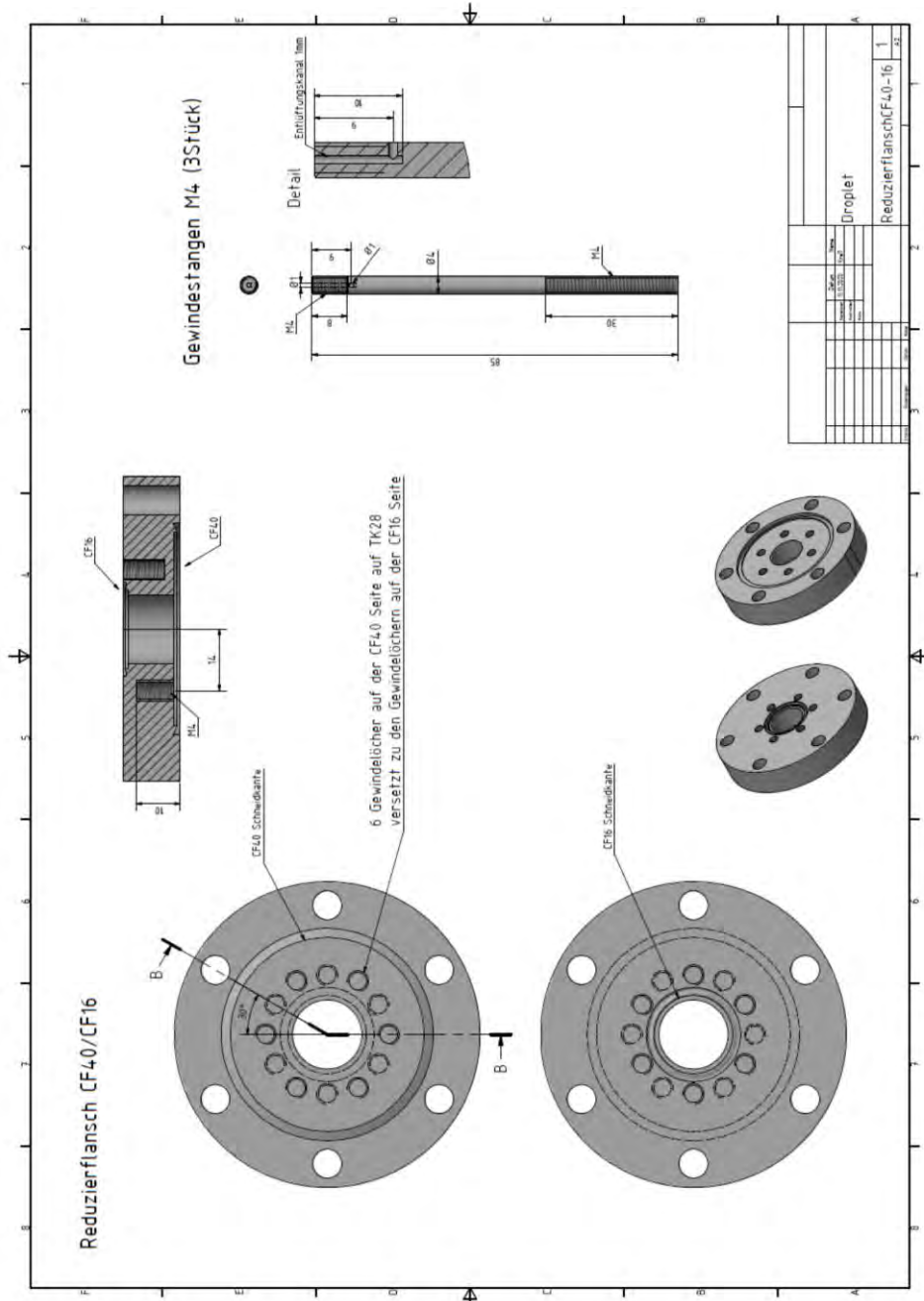
21. Rotenberg, Y.; Boruvka, L.; Neumann, A.W. Determination of surface tension and contact angle from the shapes of axisymmetric fluid interfaces. *Journal of Colloid and Interface Science* **1983**, *93*, 169-183, doi:10.1016/0021-9797(83)90396-X.
22. Hoorfar, M.; Neumann, A. Recent progress in Axisymmetric Drop Shape Analysis (ADSA). *Advances in Colloid and Interface Science* **2006**, *121*, 25-49, doi:10.1016/j.cis.2006.06.001.
23. Huh, C.; Reed, R.L. A method for estimating interfacial tensions and contact angles from sessile and pendant drop shapes. *Journal of Colloid and Interface Science* **1983**, *91*, 472-484, doi:10.1016/0021-9797(83)90361-2.
24. Hoorfar, M.; Neumann, A.W. Axisymmetric drop shape analysis (ADSA) for the determination of surface tension and contact angle. *The Journal of Adhesion* **2004**, *80*, 727-743, doi:10.1080/00218460490477684.
25. Davis, L.S. A survey of edge detection techniques. *Computer Graphics and Image Processing* **1975**, *4*, 248-270, doi:10.1016/0146-664X(75)90012-X.
26. Pratt, W.K. *Digital Image Processing*; Wiley-Interscience, New York: 1978; Volume 3.
27. Paap, U.; Kreß, B.; Steinrück, H.P.; Maier, F. Probing Surface and Interfacial Tension of Ionic Liquids in Vacuum with the Pendant Drop and Sessile Drop Method. *International Journal of Molecular Sciences* **2022**, *23*, 13158, doi:10.3390/ijms232113158.
28. Niedermaier, I.; Kolbeck, C.; Steinrück, H.-P.; Maier, F. Dual analyzer system for surface analysis dedicated for angle-resolved photoelectron spectroscopy at liquid surfaces and interfaces *Review of Scientific Instruments* **2016**, *87*, doi:10.1063/1.4942943.
29. Vargaftik, N.B.; Volkov, B.N.; Voljak, L.D. International Tables of the Surface Tension of Water. *Journal of Physical and Chemical Reference Data* **1983**, *12*, 817-820, doi:10.1063/1.555688.
30. Kaelble, D.H.; Cirlin, E.H. Dispersion and polar contributions to surface tension of poly(methylene oxide) and Na-treated polytetrafluoroethylene. *Journal of Polymer Science Part A-2: Polymer Physics* **1971**, *9*, 363-368, doi:10.1002/pol.1971.160090210.
31. Blythe, A.R.; Briggs, D.; Kendall, C.R.; Rance, D.G.; Zichy, V.J.I. Surface modification of polyethylene by electrical discharge treatment and the mechanism of autoadhesion. *Polymer* **1978**, *19*, 1273-1278, doi:10.1016/0032-3861(78)90304-X.
32. Fowkes, F.M.; McCarthy, D.C.; Mostafa, M.A. Contact angles and the equilibrium spreading pressures of liquids on hydrophobic solids. *Journal of Colloid and Interface Science* **1980**, *78*, 200-206, doi:10.1016/0021-9797(80)90508-1.
33. Rudawska, A.; Jacniacka, E. Analysis for determining surface free energy uncertainty by the Owen-Wendt method. *International Journal of Adhesion and Adhesives - INT J ADHES ADHES* **2009**, *29*, 451-457, doi:10.1016/j.ijadhadh.2008.09.008.
34. Vuckovac, M.; Latikka, M.; Liu, K.; Huhtamäki, T.; Ras, R.H.A. Uncertainties in contact angle goniometry. *Soft Matter* **2019**, *15*, 7089-7096, doi:10.1039/C9SM01221D.
35. Schuster, J.M.; Schvezov, C.E.; Rosenberger, M.R. Influence of Experimental Variables on the Measure of Contact Angle in Metals Using the Sessile Drop Method. *Procedia Materials Science* **2015**, *8*, 742-751, doi:10.1016/j.mspro.2015.04.131.

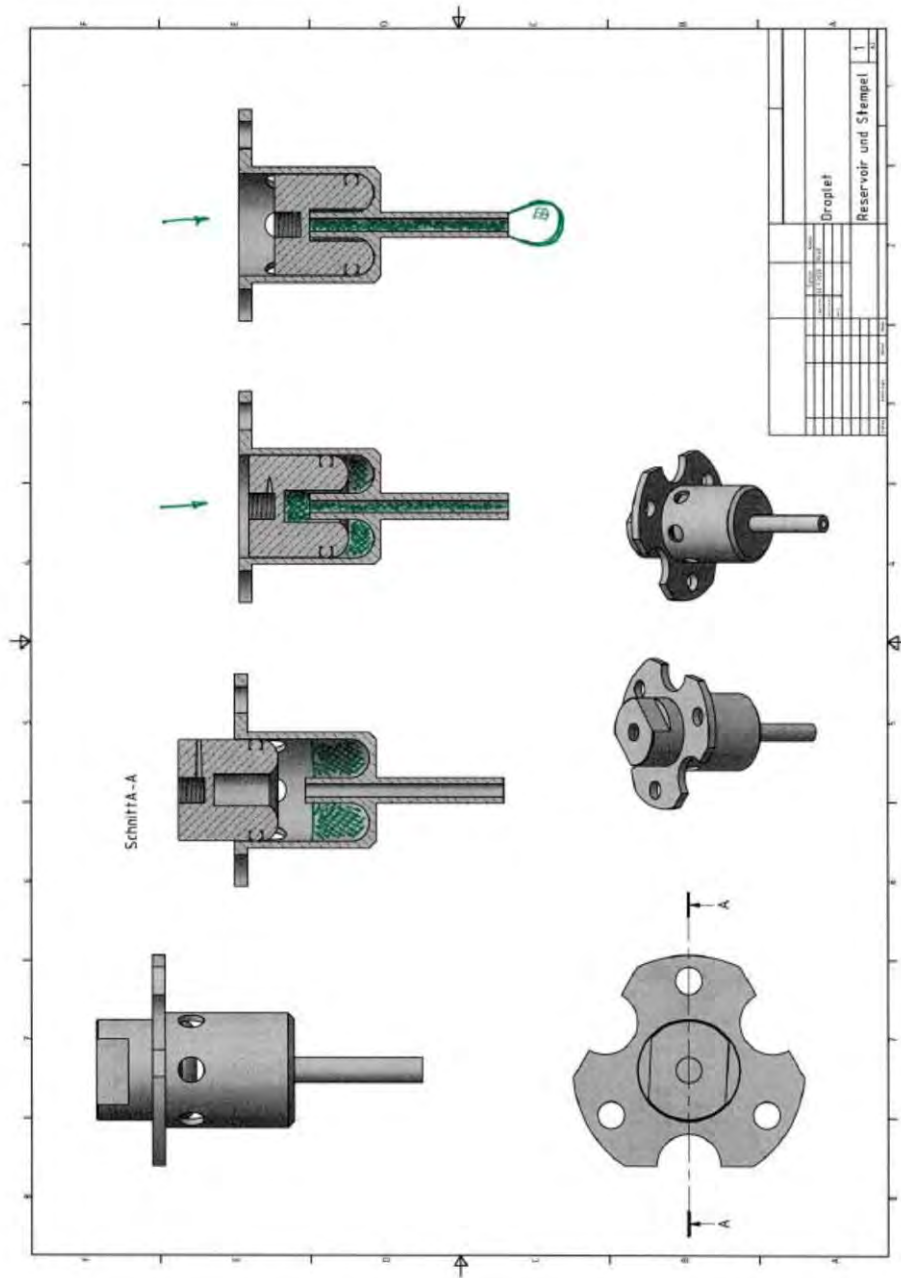


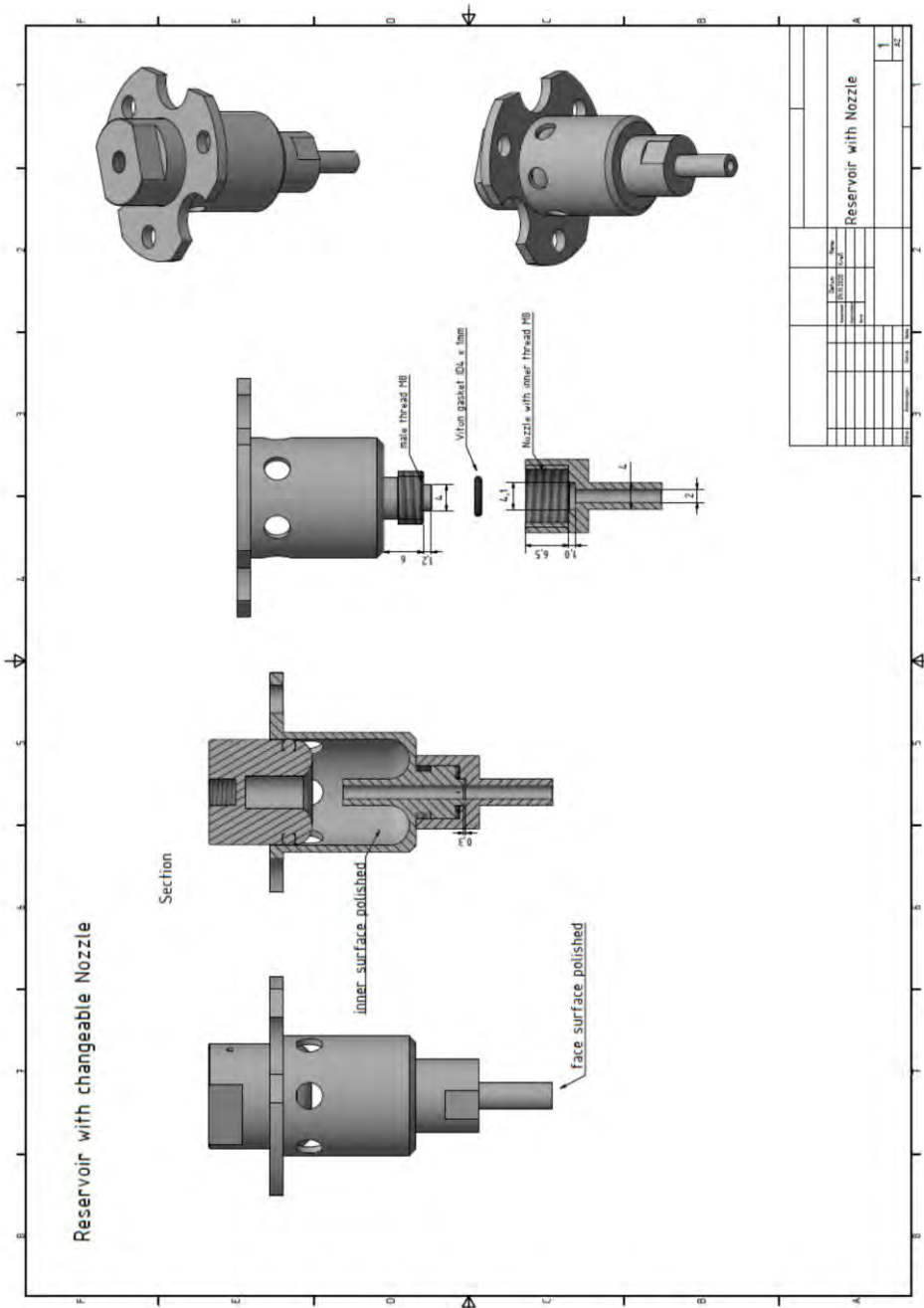


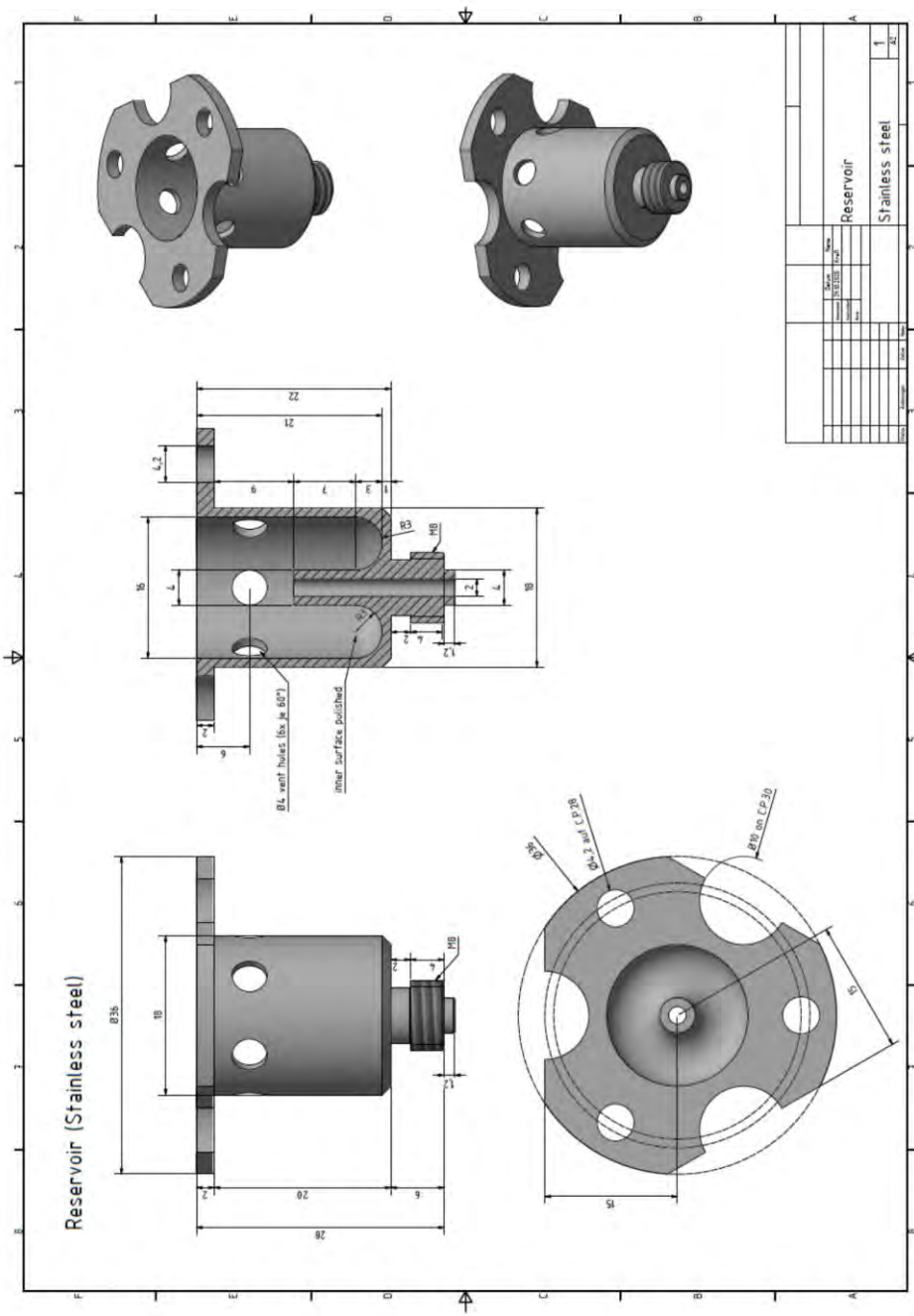
9.2 Reservoir, Stamp, Cannula

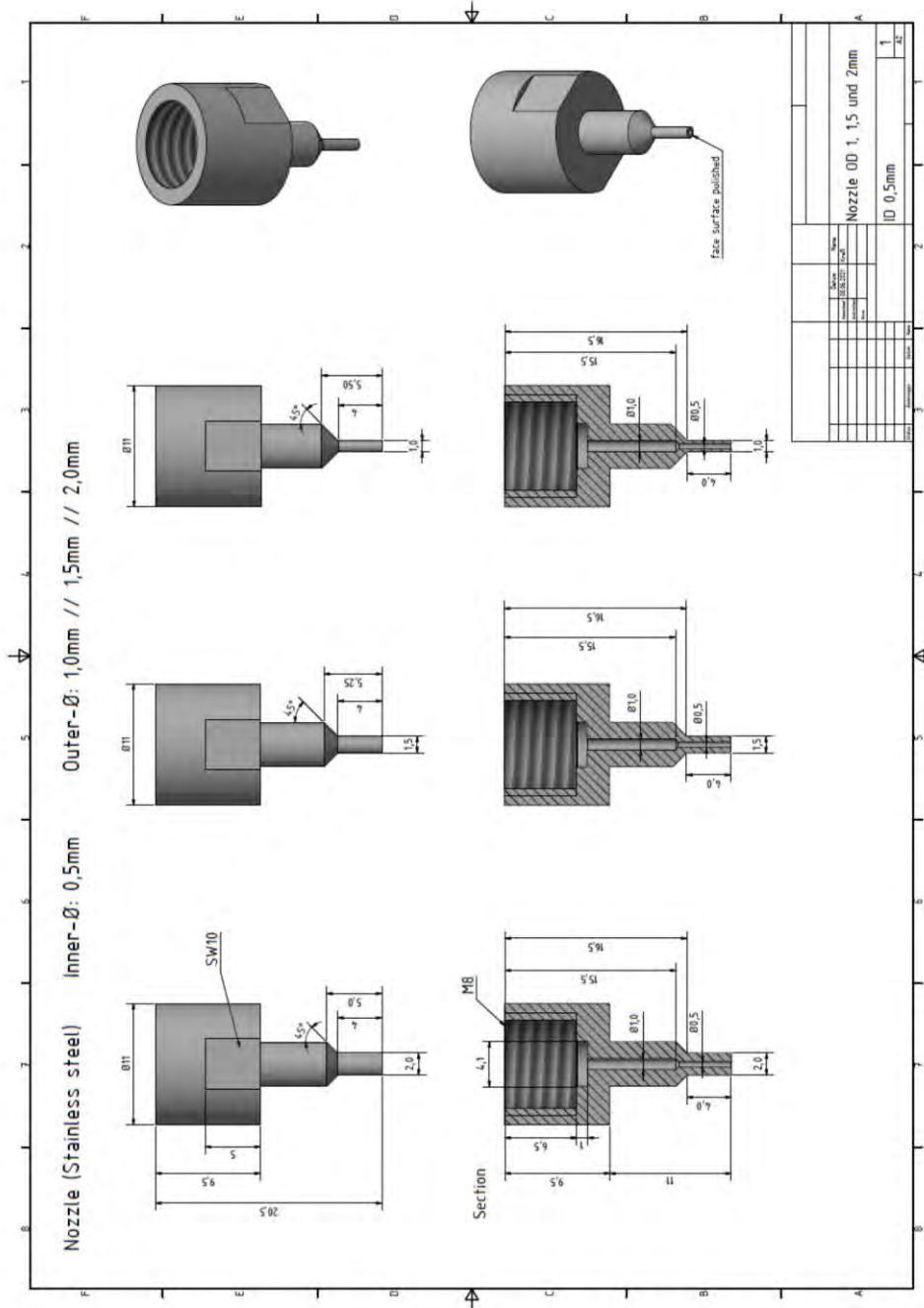












9.3 Sessile Drop

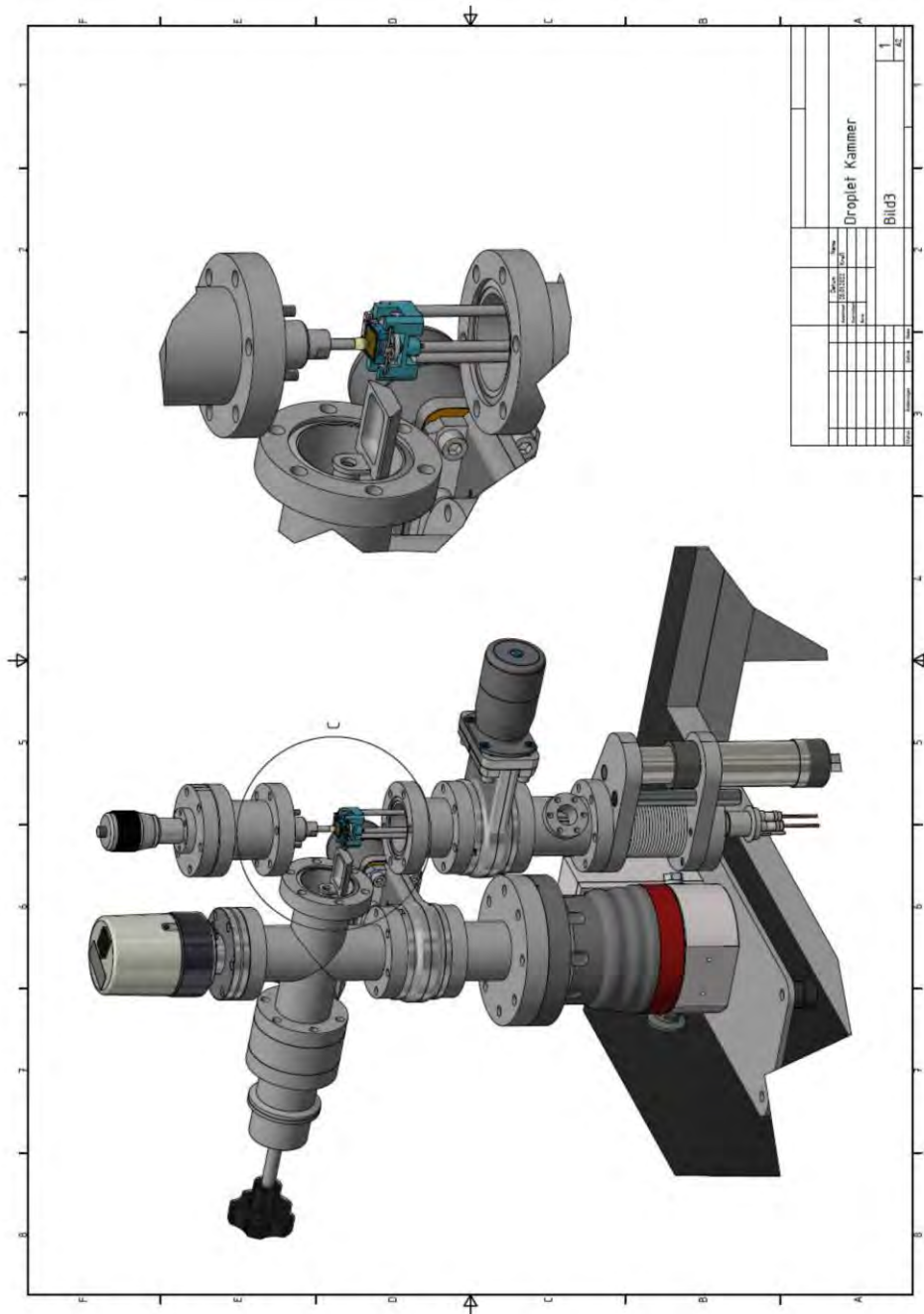




Abbildung ähnlich

DS 040 A, Elastomergedichtete Dreh-/Schiebedurchführung, DN 40 ISO-KF

Bestellnummer: PF 244 011 -T

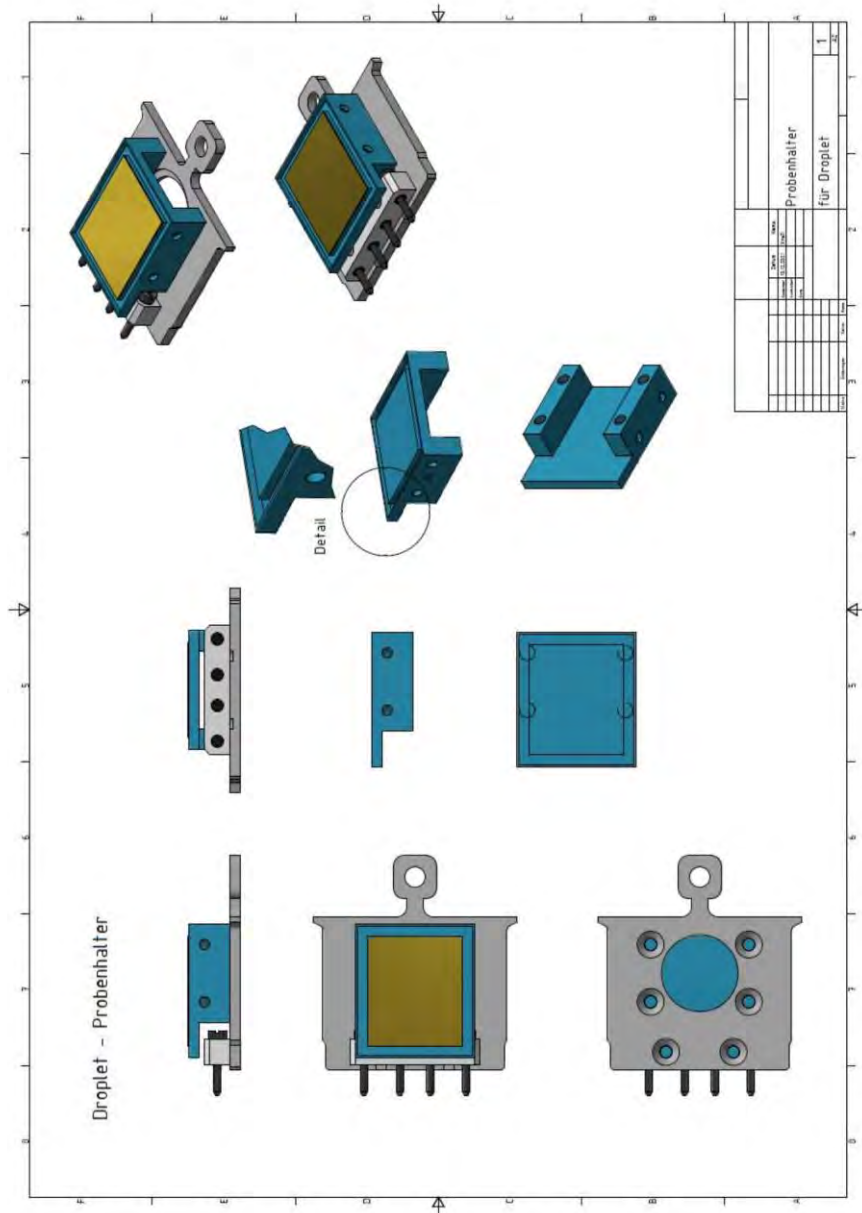
- Direkte Kraftübertragung durch elastomergedichtete Welle
- Frei drehbar und verschiebbar
- Einstellbare Hubbegrenzungen

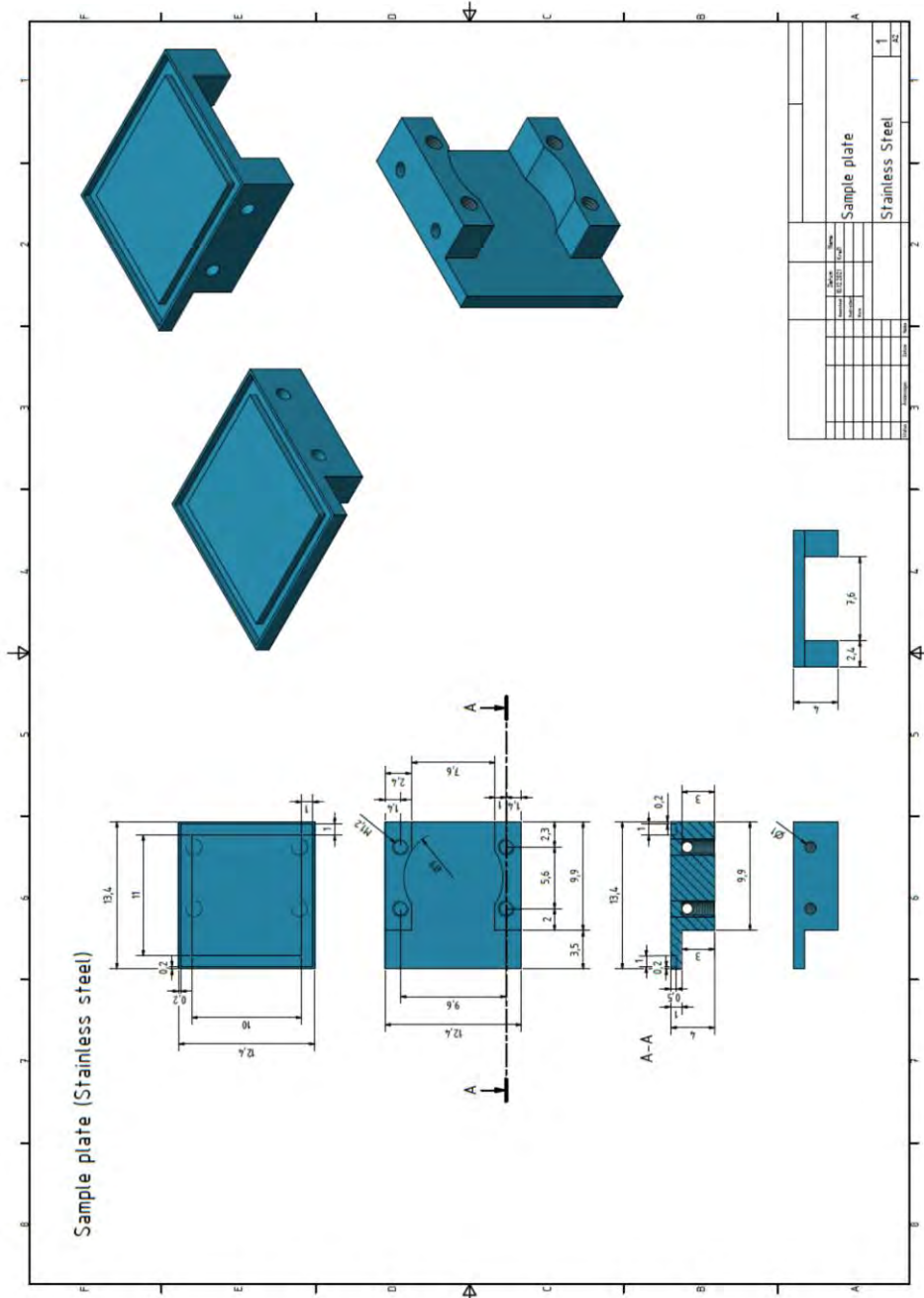
Produkt anfragen

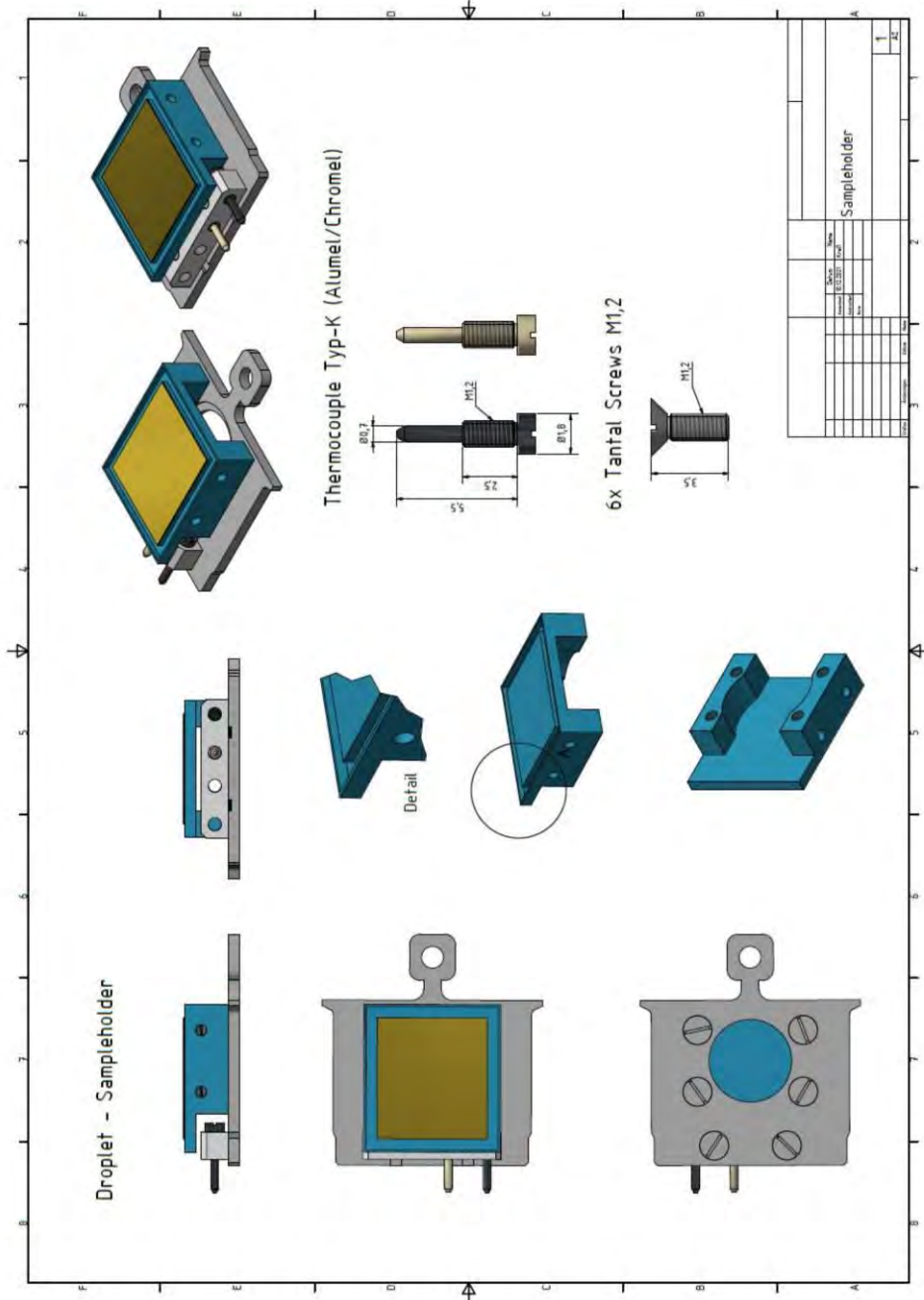
Produkt vergleichen

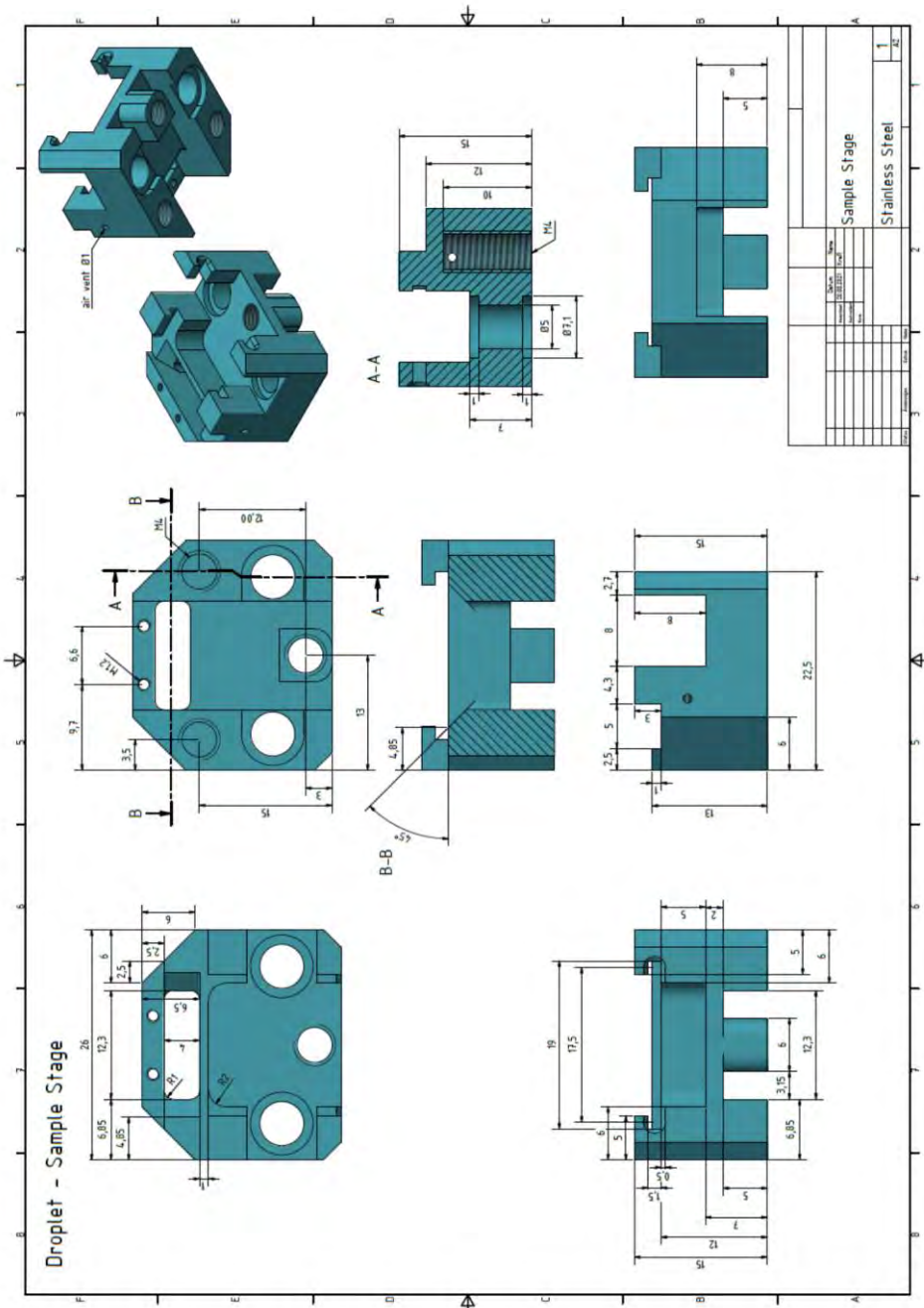
Produkt merken

9.3.1 Sample Holder









Werkstoffdatenblatt
1.4301 / X5CrNi18-10
 Nichtrostender Stahl, austenitisch



HSM®
 Hochleistungswerkstoffe
 Stahl & Metall

Beschreibung:

Bei dem Werkstoff 1.4301 handelt es sich um den häufigsten Vertreter der austenitischen Chrom-Nickel-Stähle. Wegen der guten Verarbeitungseigenschaften und des attraktiven Aussehens findet diese Güte in zahlreichen Gebieten Anwendung.

Eigenschaften:

sehr gute Schweißbarkeit, gute Korrosionsbeständigkeit, gute Zerspanbarkeit, für Tieftemperaturen geeignet

Chemische Zusammensetzung (Massenanteil in % nach DIN EN 10088-3)

	C	Si	Mn	P	S	Cr	Ni	N
min.	-	-	-	-	-	17,5	8,0	-
max	0,07	1,0	2,0	0,045	0,03	19,5	10,5	0,11

Normen und Bezeichnungen

DIN EN 10088-3	1.4301 X5CrNi18-10
AISI	304
UNS	S30400
B.S.	304S31
JIS	SUS304
AFNOR	Z7CN18-09
SS	1333
GOST	08Ch18N10
UNE	F.3504

Anwendungsgebiete

- Lebensmitteltechnik
- Automobilindustrie
- Chemie, Petrochemie
- Armaturenbau
- Appartate- und Behälterbau
- Bauindustrie
- Sanitärtechnik
- Architektur und Dekoration

[Jetzt anfragen >>](#)

HSM Stahl- und Metallhandel GmbH
 www.hsm-stahl.de
 E-Mail: hsm@hsm-stahl.de
 Tel.: +49 9172 69 00 0
 Fax: +49 9172 69 00 - 20

Wichtiger Hinweis:

Die Angaben über die Beschaffenheit oder Verwendbarkeit von Materialien bzw. Erzeugnissen dienen ausschließlich der Information und stellen keine vertragliche Verpflichtung dar. Die Angaben entsprechen lediglich den Erfahrungen der Hersteller und HSM®. Alle Angaben sind ohne Gewähr. Druckfehler, Irrtümer und Änderungen vorbehalten.

Seite 1 von 2

Werkstoffdatenblatt
1.4301 / X5CrNi18-10
 Nichtrostender Stahl, austenitisch



HSM®
 Hochleistungswerkstoffe
 Stahl & Metall

Mechanische Eigenschaften bei 20° C (Zustand lösungsgeglüht)

Härte HB 30	Dehngrenze Rp0,2%	Zugfestigkeit Rm	Dehnung A5,65	Elastizitätsmodul
≤ 215 HB	≥ 190 N / mm ²	500-700 N / mm ²	≥ 45%	200 kN / mm ²

Physikalische Eigenschaften bei 20° C

Dichte	Spezifische Wärme	Wärmeleitfähigkeit	Elektrischer Widerstand	Magnetisierbarkeit
7,90 kg/dm ³	500 J/kg K	15 W/m K	0,73 (ohm) mm ² /m	sehr gering

Schweißbarkeit

WIG-Schweißen	geeignet
MAG Massiv-Draht	geeignet
Lichtbogenschweißen	geeignet
UP-Schweißen	geeignet
Laserstrahlschweißen	geeignet
Gasschmelzschweißen	ungeeignet

1.4301 ist mit und ohne Schweißzusatzwerkstoff schweißbar, eine zusätzliche Wärmebehandlung ist nicht erforderlich.

Thermische Behandlung

Weichglühen	nicht möglich
Lösungsglühen	1000 - 1100 °C
Abkühlung	Wasser oder unbewegte Luft
Warmformgebung	1200 - 900 °C
Vergütung	nicht möglich
Spannungsarmglühen	nicht empfehlenswert

Lieferformen:



Drähte, Fittings, Schmiede-/Gussstücke, Bandstahl, Blech-/ Blockzuschnitte,

Fertigteile nach Zeichnung

[Jetzt anfragen >>](#)

HSM Stahl- und Metallhandel GmbH
 www.hsm-stahl.de
 E-Mail: hsm@hsm-stahl.de
 Tel.: +49 9172 69 00 0
 Fax: +49 9172 69 00 - 20

Wichtiger Hinweis:
 Die Angaben über die Beschaffenheit oder Verwendbarkeit von Materialien bzw. Erzeugnissen dienen ausschließlich der Information und stellen keine vertragliche Verpflichtung dar. Die Angaben entsprechen lediglich den Erfahrungen der Hersteller und HSM®.
 Alle Angaben sind ohne Gewähr. Druckfehler, Irrtümer und Änderungen vorbehalten.

Seite 2 von 2

9.3.2 Data Sheet pBN Heater

The screenshot shows the product page for 'Disc heaters PBN/PG with tabs' on the Neyco website. The page includes a navigation menu, a search bar, and a breadcrumb trail: 'SEE ALL > Homepage > Thin films > Refractory materials > Ceramic heaters > Disc heaters PBN/PG with tabs'. The product is categorized under 'THIN FILMS' and 'Ceramic heaters'. A 'Share by email' button is visible. A call to action states 'This product is available in 5 versions' with a 'See our references' button. A 'You have a question?' section provides contact details: 'You can reach us by phone on +33 (0) 41 90 50 50 or send us an email' with a 'Send an email' button. Below the product image is a section titled 'Our standards' containing a table with 6 rows of specifications. The first row is highlighted with a red border. At the bottom, there is a 'Contact us' link and a 'Write to us' button with the phone number '+33 (0) 41 90 50 50'.

Our standards

P/N	Ø Inch (mm)	Resistance (ohm)	V	A	W	Quantity
PCPBNP05	0.50 (12.7)	5-7	15	8	80	Qty
PCPBNP07	0.75 (19.0)	9-15	30	8	150	Qty
PCPBNP10	1.00 (25.4)	9-15	40	10	300	Qty
PCPBNP17	1.75 (44.5)	17-30	110	12	1000	Qty
PCPBNP20	2.00 (50.8)	15-25	110	15	1300	Qty

Can't find the desired product? [Contact us](#)

If you want an offer, or more information on this product, contact us: [+33 \(0\) 41 90 50 50](tel:+33041905050) [Write to us](#)

